Spatially Resolved Nanothermal Transport of Multilayer and Phononic Structures using Scanning Thermal Microscopy

James Anthony Murray Lees

Doctor of Philosophy

University of York

Physics

April 2022

Abstract

Scanning Thermal Microscopy (SThM) is a technique which offers the potential to gain information about material thermal properties but remains under used. Here it was evaluated for use in studying nanothermal transport. Multilayer and phononic structures were examined. This was done using a modified NanoScan VLS-80 atomic force microscope (operated at a spatial resolution of ~100nm and a thermal resolution of <10mK) which allows for relative temperature maps of a surface to be created. COMSOL was used to simulate the heat flow within the sample and the SThM tip/sample response.

Different methods for preparing a multilayered sample for SThM examination were investigated for suitability in measuring the thermal properties of the layers. The ion milled crater was found to be most preferable due to its ability to expose a large surface area for thin layers and the resulting low thermal signal noise (7%). The SThM scans allowed for a qualitative comparison between material thermal conductivities. However, quantitative examinations require further work.

The spatial resolution of the SThM was exploited in the design of Si fishbones, devices constructed of a central suspended Si shaft with attached pillars. This allowed for devices with individual parameter changes which could be used to test for phonon resonance hybridisation where the phonon band structure is changed causing a slowing of group velocity. This was expected to reduce the thermal conductivity which could be measured using SThM. Examinations of the instrument's sensitivity suggest that it should have been able to detect a 7.5% change in temperature gradient which would have been expected from the large thermal conductivity changes suggested by theory work. However, such a change was not seen. A number of reasons for this are suggested as well as possibilities for increasing the chance of seeing the thermal conductivity change in future experiments.

Contents

List of Tables

List of Figures

parameters are a 1CC (1.09nm) and the membrane is 1.63nm thick. The simulations take place at 300K and $\kappa_{\mathrm{mem}} = 10.81\mathrm{W/m.K}$

Figure-6.36: Graph showing temperature change of central point of COMSOL modelled Si shaft at different thermal conductivity values (Bulk Si = 130W/m.K).

Figure-6.37: Graph of comparison between surface and tip temperatures for various shaft κ values.

Figure-6.38: Images of 3D Model with curved shaft and simplified 'block temperature' heater.

Figure-6.39: Graph showing comparison between tip temperature results for the unpowered flat shaft and different levels of bowing.

Figure-6.40: 2D COMSOL simulation of tip model moving across a curved surface. Note that the tip has a larger contact area lower down the tip and becomes hotter at the top as a result.

Figure-6.41: Graph of tip temperature over curved shaft at various shaft κ values.

Figure-6.42: Image of 2D COMSOL Si fishbone model with components labelled.

Figure-6.43: Image of 2D COMSOL model with heated temperature block and curved shaft

Figure-6.44: Image of 2D CSEM image of MARF showing differing κ value regions based on pillar parameters.

Figure-6.45: COMSOL model showing different implemented κ regions on curved shaft.

Figure-6.46: Graph showing comparison between flat and curved shaft on 2D COMSOL model with an applied thermal gradient.

Figure-6.47: Graph showing tip temperature across curved shaft for increasing applied heater temperature on 2D COMSOL model.

Figure-6.48: Graph showing result of 2D COMSOL model of curved shaft with applied thermal gradient at different shaft κ values surface temperature values (Left) and tip temperature values (Right).

Figure-6.49: Graph of 2D bowed shaft COMSOL multi-κ simulation with listed values and regions.

Figure-6.50: Graph of tip temperature over COMSOL simulated shaft examining the difference in 50% thermal conductivity changes between the $\kappa 2$ and $\kappa 3$ regions for three different initial κ values of 150, 80 and 2W/m.K. Note that the non- $\kappa 2/3$ regions remain at 100W/m.K at all times.

Figure-7.1: Representative topography (Top) and thermal (Bottom) scan images of a Si fishbone shaft used for data analysis. Blue boxes show the scan area used for shaft examinations. Note the slight shift in x direction between the two images, this is accounted for in data collection.

Figure-7.2: Representative topography (Left) and thermal (Right) line average across the shaft examination area of Figure-7.1.

Figure-7.3: Representative topography (Top) and thermal (Bottom) scan images of Si fishbone shaft used for data analysis.

Figure-7.4: SEM image of broken Si feather caused by SThM scanning.

Figure-7.5: Optical microscope image of developed Microheater with unremoved Au which causes a short circuit (Left) and burnt out microheater (Right).

Figure-7.6: Image of Si fishbone topography (Top) and thermal (Bottom) scan images with some spin resist still on fishbone.

Figure-7.7: VLS-80 image of topography (Top) and thermal (bottom) of plain silicon area on a chipset #7 fishbone.

Figure-7.8: Graph of 0V MARF combined dataset showing line averaged topography (Middle) and thermal (Bottom) signals.

Figure-7.9: Graph of 0V MARF shaft (Left) and 0V MDF shaft (Right) combined dataset showing line averaged thermal signal with red line showing point where pillar parameters are changed. Note that some peaks on the MDF shaft caused by surface effects have been cut off.

Figure-7.10: Graph of normalised and corrected data of tip temperature showing relative thermal gradient across SoI surface in the same position as fishbones.

Figure-7.11: 6V MARF scan across complete shaft and surrounding Si. Note that the surface being hotter than the tip has resulted in an inversion of the thermal curve, however this is not expected to have changed the Si shaft results.

Figure-7.12: Graph of 1:1 – 5:1 MARF averaged topography at different heater input voltages.

Figure-7.13: Graph of 2V 1:1 – 5:1 raw thermal signal on three scans performed sequentially to then be used for averaging.

Figure-7.14: VLS-80 image of 2V 1:1 – 5:1 scan of topography (Top) and thermal (Middle) as well as comparison between line averaged topography and thermal signal (Bottom).

Figure-7.15: Graph of line averaged thermal signal across the same MARFs at three different times.

Figure-7.16: Comparison between VLS-80 thermal image of 6V 1:1 – 5:1 MARF original scan (Top) and R1 (Bottom).

Figure-7.17: Graphs comparing line averaged thermal signal between original 6V MARF scan (Left) and repeat (Right) taken at different times.

Figure-7.18: Comparison of MARF examinations 0V (Top Left), 4V (Top Right), 3V (Bottom Right), and 0V (R1) shown in order of scans taken. Note the increasing disagreement between the scans.

Figure-7.19: Comparison of Si Fishbone topographies for MARF fishbones showing differing shaft bowing with shaft and pillar limits marked.

Figure-7.20: Graph making direct comparison between recorded tip temperature and height change along an unpowered MARF Si fishbone and surrounding area with shaft changes marked.

Figure-7.21: Graph making direct comparison between recorded tip temperature and height change along an unpowered MARF Si fishbone with shaft changes marked.

Figure-7.22: Graph showing MARF (Top) and MDF (Bottom) examinations across different applied heater voltages.

Figure-7.23: Comparison of 0V MARF scans in atmosphere (Top Left) and vacuum (Top Right) and 0V Shaft only Scans in atmosphere (Bottom Left) and vacuum (Bottom Right).

Figure-7.24: Comparison of 6V MARF scans across Si fishbone and surrounding material in atmosphere (Left) and vacuum (Right) with the barb limits marked in light blue, the shaft limits marked in dark blue, and the pillar parameter change marked in red.

Figure-7.25: Graph comparing thermal signal between two different 'shaft only' shaft scans, MARF and MDF at 6V applied voltage.

Figure-7.26: Graphs comparing COMSOL 0V fishbone thermal signal (Top Left), 0V MARF (Top Right), 0V MDF (Bottom Left), and 0V shaft only (Bottom Right).

Figure-7.27: Comparison of 0V MARF scans in atmosphere (Left) and vacuum (Right).

Figure-7.28: Graph Showing MARF examinations across different applied heater voltages.

Figure-7.29: Graph comparing computations results (Left) and 6V MARF experimental results (Right) of deliberately similar experiments.

Figure-7.30: Graph of 6V MDF thermal results also showing lack of significant difference between the two different regions.

Figure-7.31: Graph of 6V shaft only thermal results showing similar differences in measurements to MDF and MARF examinations.

Figure-7.32: Comparison between line averaged topography and thermal signal for 2V 1:1 – 5:1 VLS-80 scan.

Figure-7.33: 6V MARF Experimental data across barbed area showing regions with different expected κ values and thermal gradients.

Figure-7.34: Graph of normalised effect of varying design parameters of nanowalls in the CASTEP/ShengBTE simulated results of the κ_r. Note that except where mentioned the parameters are a 1CC (1.09nm) and the membrane is 1.63nm thick. The simulations take place at 300K and $\kappa_{mem} = 10.81$W/m.K.

Figure-7.35: Graph showing result of 2D COMSOL model of curved shaft with applied thermal gradient at different shaft values surface temperature values (Left) and tip temperature values (Right).

Figure-7.36: 0V MARF thermal scans across central shaft.

Acknowledgements

I would like to offer my heartfelt thanks to everyone who helped me on this project in ways both big and small without whom it would not have been possible.

I thank my parents who have helped and supported me throughout the project. My friends and colleagues that I have lived and worked alongside including James Lolley and Dan Clarke who helped and supported me through the difficult times of the project.

I would also like to thank my various collaborators. Dr Siew Wai who laid the foundation for this work. Dr Phil Hasnip and Ben Durham who performed the computational work and supporting theory. Dr Adi Scheidemann and Dr Marco Corbetta from Nanoscan for their advice and support with the VLS-80.

A huge thank you to all of those who offered their support and time to this project including Dr Christopher Reardon for his teaching and support with the fabrication, Dr Jon Barnard for his teaching and support in using the SEM, Dr Atsufumi Hirohata for allowing us the use and modification of his instrument, Professor Jonathan Weaver and Dr Phillip Dobson from the University of Glasgow for their support during the initial stages of the project and Tim Ayers, Professor Oleg Kolosov from Lancaster University for the sharing of his electrical designs, Bob Hide and the other members of the University of York Electronics and Mechanical Workshop as well as all others who offered help in smaller, but no lesser, ways. I would additionally like to thank EPSRC for funding this project.

I am also of course incredibly appreciative of the incalculable contribution of my supervisor Sarah Thompson. Her expertise, support, and advice have made this project not only successful but a joy to work on.

Declaration

I declare that this thesis is a presentation of original work and that the work presented, except where explicitly acknowledged in the text or by reference, is my own sole contribution. This work has not previously been submitted for an award at this, or any other, university.

Chapter 1

Introduction

Temperature measurement has always been a useful area of scientific study because of its wide and persistent effects. Temperature is expressed as the inverse of the rate of change of entropy with energy and measures an average of the kinetic energy of the atoms or molecules within a system. It often affects the speed of interactions both physical and chemical as well as modulating many material properties. Therefore it must either be controlled or accounted for in almost every experiment. There is a long history of attempts to measure temperature (1) with the first recorded thermometer being created by Galileo in 1593. Many after him worked on the problem but there were no truly accurate thermometers until 1714 when Daniel Gabriel Fahrenheit invented the thermometer and in 1724 standardised the Fahrenheit scale.

These early thermometers established a principle of thermal equilibrium between the measuring device and its surroundings, meaning they were largely limited by their size. Whilst countless improvements have been made to improve thermometers, and increase their precision, size has continued to prove a key factor. This is especially true when moving into the nanoscale.

In a structure where the sample size is much greater than the mean free path of the heat carriers (electrons/holes or phonons), transport is considered diffusive and can be modelled with Fourier's Law (2). Below this scale however thermal transport becomes ballistic (3) and there is no local thermal equilibrium. This means that traditional thermometry methods are not possible.

This study aims to use Scanning Thermal Microscopy (SThM) as a tool to measure local temperature and temperature differences on very small-scale materials and devices that are just above or partially entering the ballistic regime.

1.1 Motivation

Despite the difficulties, thermal transport and properties on the nanoscale are an increasingly important area of study. The miniaturisation of technologies has led to

the need for a greater understanding of the thermal properties of materials and how heat interacts on these scales.

1.1.1 Hidden Multilayers

Many materials used in assorted technologies are made of multiple stacked thin film layers. This composite design acts to make most of the layers largely inaccessible to analysis techniques. However, measurements of the material as a whole do not provide all of the necessary information for a proper understanding of heat flow within the material.

Products such as Heat-Assisted Magnetic Recording (HAMR) hard drives are just entering commercial production. HAMR is a technology that heavily relies on being able to generate and then rapidly dispel heat from a very localised area (4) and therefore heat transport is a critical design criterion. Despite their use, there is not a full thermal understanding of the various multilayers of the HAMR materials (5).

This means that thin film multilayer materials require a technique that allows for thermal analysis throughout the material, one that is able to examine the effects of the individual layers without the need for creating separate samples which would introduce a number of complicating factors and may not capture all of the relevant interplay between the different layers.

This work proposes a number of different ways in which a sample can be prepared to expose the buried multilayers and how they can then be examined using SThM.

1.1.2 Thermoelectric Metamaterials

Climate change is a serious concern for the whole world and a great many technologies are being developed to help combat it. Thermoelectric devices are full of potential as a way to recover waste heat and turn it into useful energy. However, currently suitable thermoelectric materials struggle with efficiency. The dimensionless 'Figure of Merit' ZT is defined as:

$$ZT = \frac{S^2\sigma}{\kappa}\mathrm{T} \tag{1.1}$$

where S is the Seebeck coefficient, σ is the electrical conductivity, κ is the thermal conductivity and T is the temperature.

Typically considered materials have ZT values of around $0.5 - 1$ (6) and to reach efficiencies above this, materials are being sought after which have a low thermal conductivity but a high electrical conductivity. This means that the material must be both a good electrical conductor but a poor thermal conductor where the two properties are usually co-dependent.

Metamaterials use their composite material and/or geometric structure to create properties not found in the original materials. Much previous work has focused on reducing the thermal conductivity of materials by increasing the phonon scattering (7). However, this tends to also increase the scattering of the charge carries and thus reducing the overall ZT.

In this work a metamaterial using phononic resonance to attempt to modify the device's κ value whilst leaving the σ unchanged is fabricated. The device is then measured using SThM to provide a temperature map of the thermal gradients in order to examine any thermal conductivity changes.

1.1.3 Extension of Nanoscale Techniques

Whilst the use of nanoscale thermal scanning techniques is not new, it is not a widely used technique. This is partially because any measurements which are made are qualitative. In these examinations, techniques are used to attempt to make more quantitative heat transport measurements using SThM.

1.2 Thesis Overview

Chapter 2 examines the technique of scanning thermal microscopy as it currently exists including a number of different methods and some of the considerations which need to be made when performing SThM scans. This is followed by an examination of the probe-sample heat conduction paths and their relative contributions before finishing by examining a number of the different possible analysis methods which can be used to produce quantitative thermal results from SThM examinations.

Chapter 3 is an overview of the different experimental and computational techniques used across the project. This includes a breakdown of the SThM used for

the data collection as well the fabrication technique used to produce the Si fishbone samples. A short description of the computer modelling software is also included.

Chapter 4 examines the theory of thermal transport within the phononic nanostructures used in the project. This includes a consideration of all of the affecting factors for the thermal conductivity as well as results of computational modelling of the expected effect both by collaborators and that of others.

Chapter 5 describes the composition and preparation of multilayer samples for examination within the SThM. The results of such examinations are shown and then compared to see which method is preferable for future samples and are used to attempt to be able to calculate quantitative results for the thermal conductivity of an unknown layer.

Chapter 6 discusses the design, fabrication process and results of the Si fishbone fabrication. It also includes a parallel attempt to model the fishbones and predict their properties using COMSOL simulations.

Chapter 7 presents the results of SThM imaging on the Si fishbones. Examining the difficulties with such examinations, their reliability and considering some of the reasons why the expected effects from the modelling and theory may not have been measured.

Chapter 2

Scanning Thermal Microscopy

2.1 Atomic Force Microscopy (AFM)

Atomic Force Microscopes (AFMs) were first demonstrated in 1986 by Binnig et al. (8) which built on earlier Scanning Tunnelling Microscope (STM) techniques. Rather than using quantum tunnelling currents to determine the distance between a probe and the surface, AFM uses a very sharp tip on a long cantilever (acting as a spring) which is then placed close enough to the surface such that the two interact. Atomic force microscopy is a highly versatile technique that can be used in a variety of ways to measure a large number of different forces. This includes capillary force, magnetic force, chemical bond force and it can even be used to manipulate surface elements (9).

In one of the simpler contact modes, the AFM tip becomes responsive to the van der Waals forces from the sample and is raster-scanned across the surface. This effectively drags the tip across the surface causing the tip to be deflected relative to the topography. This deflection is then measured, typically using a laser diode focused on the back of the cantilever which is then reflected into a quadrant detector as shown in Figure-2.1. This information is then turned into a topographic map of the surface.

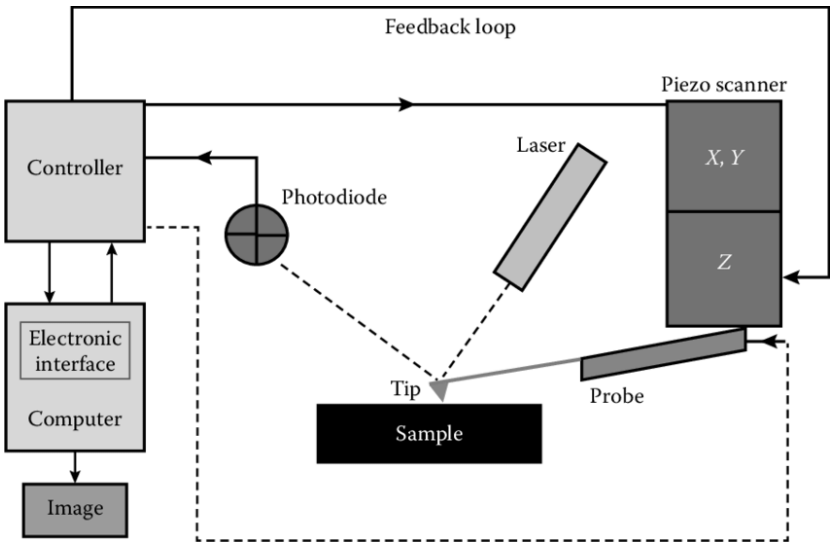

Figure-2.1: Diagram of a simplified standard AFM setup which is used for a basic contact mode topography scan. (Reproduced from reference (10)).

2.2 Scanning Thermal Microscopy (SThM)

Scanning Thermal Microscopy (SThM) further expands the use of atomic force microscopy by the use of a specialised probe. The first demonstration of a thermal scanning technique was coincidentally also published in 1986 by Williams et al. (11). This used a ~100nm thermocouple sensor which used a feedback loop to maintain its height above the surface based on thermal conduction in air between the surface and the probe. This was a limited technique, which did not provide a good image but did prove a useful catalyst for further development of thermal scanning techniques. Many of these were combined with AFM or STM technology to allow for easy surface scanning and have branched into a myriad of different types of SThM probes. Figure-2.2 shows a force curve for an SThM tip onto a surface and the resulting effect on the tip voltage recorded by the tip when contact is made can clearly be seen.

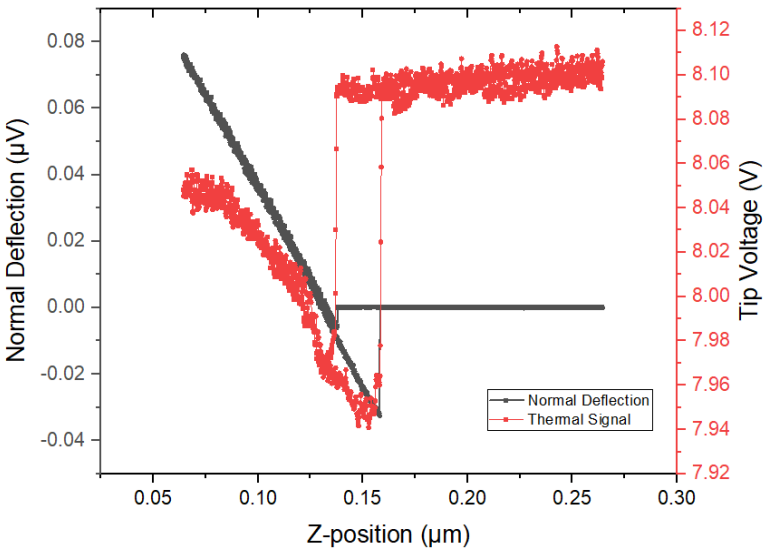

Figure-2.2: Approach curve of an SThM tip onto a Si surface showing both normal deflection and the effect of contact on thermal signal.

2.3 Scanning Thermal Probes and Techniques

There are many different ways that thermal measurements can be taken using SThM. Each of these requires its own electronic setup and type of probes. The three main techniques are (12):

- Thermovoltage
- Thermal Expansion
- Electrical Resistance

Additionally, there are other more experimental methods such as fluorescent particle tips (that use fluorescent materials with a thermally dependent intensity (13)) which are not explored here.

2.3.1 Thermovoltage Method

A thermovoltage-based probe exploits the thermovoltage generated between two electrodes i.e. it uses a thermocouple of some kind. Two materials (such as the tip and sample) are used to form two dissimilar conductors which can create an electrical junction across which the voltage is temperature dependent. This can be done using both contact and non-contact STM or AFM. Thermocouple tips have generally fallen out of use due to fabrication advances favouring thermoresistive methods.

Scanning Thermal Profiler (11)

One of the simplest thermovoltage methods is to fabricate a thermocouple onto the end of an STM tip. When the heated tip is in close proximity to the surface the heat transfer from the tip to the cooler sample through the surrounding gas will cause the tip to cool, altering the voltage reading from the thermocouple. How much the tip cools is dependent on the surface temperature. This technique offers around 0.1K thermal resolution and does not contact with the surface avoiding contact resistance. However, it lacks surface detail and is limited to lateral resolutions of 100nm.

Tunnelling Thermocouple (14)

A multi-wavelength laser is used to heat a sample before an STM tip is brought within tunnelling range of the surface (typically just a few Å). The tunnel junction is then able to act as a thermocouple due to the changing work function of the surface material. Resolution can be on the order of 10nm and it can give subsurface and spectroscopic information. However, it is more of a way of adding temperature measurements to STM and has a limited temperature resolution of ~0.01K.

Wire Thermocouple Probes (15)

Two wires are bonded to form a thermocouple junction which is also an AFM tip. This allows for simultaneous thermal and topographical measurement of a surface. However, such a probe is incredibly difficult to fabricate, and the process has many issues. Additionally, as the probe is so large (being made of a shaped piece of wire often several micrometres in diameter) the heat transfer is overwhelmingly dominated by the gas conduction and as such it has a limited spatial resolution.

Microfabricated Thin-Film Temperature-Sensing Probes (16)

This method uses the AFM probe itself as the thermocouple. The contact potential comes from a slight (2-5nm) gap between the tip and sample, again allowing for simultaneous thermal and topographical measurement. Early fabrication was discovered to be very difficult, and it was found to be easier to adapt a commercially available tip. This method however requires that both the probe and the sample are either electrically conducting or that their surfaces are covered in a thin metallic layer. This limits their use and they have been largely outclassed by modern fabrication of thermoresistive tips.

2.3.2 Thermal Expansion Method

The thermal expansion probes rely on the mechanical expansion of materials when heated, this is exploited to make thermal measurements. Several techniques can be used, however they are largely indirect methods that increase the complexity of interpretation.

Bi-material Cantilevers (17)

Bi-material cantilevers exploit expansion within the tip and are fabricated from two different materials. When heated they bend due to a mismatch of the thermal expansion coefficients of the two materials. The degree of bending is dependent on the temperature cantilever which is affected by that of the surface. AFM optical systems are highly sensitive to tip height changes (with high resolution imaging reaching <1Å) which allows for very small changes to be detected allowing for a good thermal resolution. Even with early design tips, it was possible to reach thermal resolutions of 10µK in 1997 (18). However, as the entire probe is part of the thermal system any experiments must be performed in vacuum to ensure that only tip/sample heat flow is affecting the tip and the analysis of such small changes becomes very important but also incredibly difficult. Additionally, such cantilevers need to be made thin and long which makes them challenging to both manufacture and use.

Scanning Joule Expansion Microscopy (19)

Typically improving resolution for SThM requires using sharper tips. However, this leads to there being a reduced contact area between the tip and sample to allow heat transfer. Scanning joule expansion microscopy attempts to sidestep this issue by not relying on heat transfer. Instead, a sharp tip is placed into contact with the surface and then begins scanning. The sample then has a varying (usually sinusoidal)

voltage applied to it. This causes joule heating which in turn causes the sample to expand. The tip will deflect with the motion of the surface which can then be measured by the system and can be used to determine properties of the surface material. Such a technique is however limited to just conductive surfaces and may have significant issues with multilayers. Additionally, this technique is indirect which increases the complexity of analysis.

Thermoacoustic Method (20)
Similar to the scanning joule expansion method this uses a sensitive tip in contact with the surface. However, in this case, the surface is heated by the application of a laser pulse. The surface is then measured whilst it heats and then cools, therefore expanding and contracting, allowing insight into the thermal properties of the material. Once again, such an indirect method can be difficult to interpret.

2.3.3 Thermoresistive Method

Thermoresistive or electrical resistance probes rely on the idea that as a tip is in contact with a sample, its temperature will change. This change will alter the electrical resistance of the tip which can then be measured as part of a circuit. All resistive metallic probes can be used in two different modes, active mode where the tip is hotter than the surface and passive mode where it is cooler. These two modes allow for testing different thermal properties (21):

Wollaston Wire Probes (22)
These used to be the most commonly used type of thermoresistive probe. Typically, a Pt/Rb core is wrapped in a silver shell, this wire is then bent into a tip shape and the end has the silver etched away to expose an active region for heat transfer. A small, mirrored surface is then placed across the back to allow it to be used as an AFM probe. They have previously been favoured for their relative ease of use and manufacture as well as their high durability. However, the active region is quite large and results in a relatively high spatial resolution.

Nanofabricated Metallic Probes
These work like traditional AFM probes however the tips are made using a resistive metal such as Pd or Pt. The tips are then wired through the cantilever itself allowing for significantly better resolution. Such tips have seen significantly wider

adoption with the development through the QUANTIHEAT project of the KNT-SThM-2an probe (23) which is used in this work.

Doped Si Resistor Probes (24)
By creating a cantilever with a U shape and having a highly doped pair of legs leading to a low-doped resistive element platform which the tip is placed on it is possible to provide an alternative way of joule heating the tip. This is caused by an electrical current flowing through the resistive element. It is notable that the tip is heated indirectly by the cantilever. However the tips can be made much harder and smaller (up to 10nm) than traditional wire tips and can withstand much hotter temperatures.

Near-Field Radiation (25)
By scanning a specially developed highly sensitive tip in non-contact mode over a surface it may be possible to detect changes in temperature of the surface using heat transfer between the tip and sample using only near-field radiation. Such a technique would allow for contact resistance to be ignored. However, due to the very small output of near-field radiation, experiments would need to take place in an ultra-high vacuum environment and sensitive enough tips are not yet available.

2.4 Measurement Considerations

In this project the Kelvin Nanotechnology KNT-SThM-2an was used. This is a nanofabricated metallic probe which was used in contact with the surface. This leads to a number of considerations for a measurement of this type.

2.4.1 Thermoresistive Measurement Method

A measurement system is required to extract the thermal information in the tip. As briefly described in section 2.3.3 for the thermoresistive method this uses the fact that the tip whilst in contact with the surface will change temperature in relation to that of the surface. This then alters the resistance of the tip.

In a nanofabricated metallic probe the tip is supplied with a current through a circuit which can be simultaneously used to heat the tip and measure a change in the tip voltage caused by the altered resistance. As this voltage change is very small this is usually connected to a Wheatstone bridge circuit which is able to amplify the signal. This system is shown in Figure-2.3.

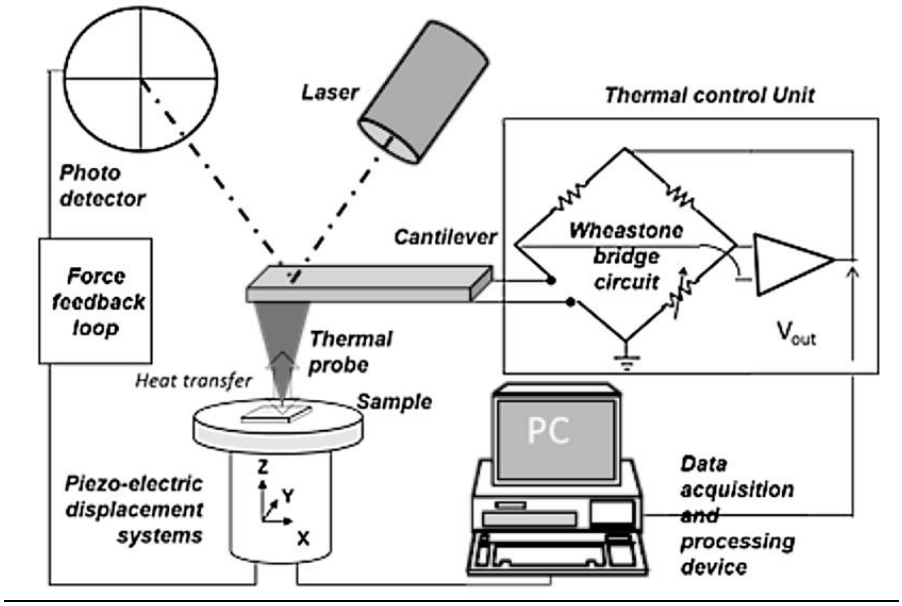

Figure-2.3: Diagram of standard SThM setup which uses a nanofabricated metallic probe and a Wheatstone bridge circuit. (Reproduced from reference (21)).

AC + DC Voltage Supply

Even with a Wheatstone bridge the measurement of voltage changes can be very difficult. To deal with this a dual AC and DC voltage supply was used. This allows for the system stability provided by the DC driving component but also allows for a good signal to noise ratio which comes from the AC component, when used in conjunction with a lock-in amplifier (26).

2.4.2 Contact Resistance

As the tip is in contact with the surface this introduces contact resistance. Contact resistance is the sum of the various resistances of the differing heat transport methods between the tip and the sample. This is discussed in detail in section 2.5.

However, contact resistance is also used as a broader catch-all term for a number of other contributing factors to the tip-surface interaction. This includes factors such as tip-sample contact deformation, sub-tip scale topography changes (also known as roughness) and local thermal property changes caused by impurities or other factors (27).

This results in an ever-changing value for contact resistance which is largely unknowable. This has proven to be a major problem in SThM (28) which has yet to be properly solved. Whilst this is a variable quantity it is not expected to change significantly over small scales (such as those examined within this project). It can therefore be treated as a kind of noise for which averaging data can help reduce its effect on the resulting data and analysis.

2.4.3 Topography Effects

One of the largest considerations that needs to be made in SThM is the effect of topography on the resulting thermal signal. Whilst the temperature and thermal properties of the surface may be independent of the topography, as shown in detecting subsurface thermal features such as buried wires (29), there is a significant effect from the tip geometry.

As shown in Figure-2.4 when a tip is in contact with different surface gradients there will be a different amount of solid-solid contact as well as a change in proximity between the tip and surface for other heat transport methods (discussed further in section 2.5).

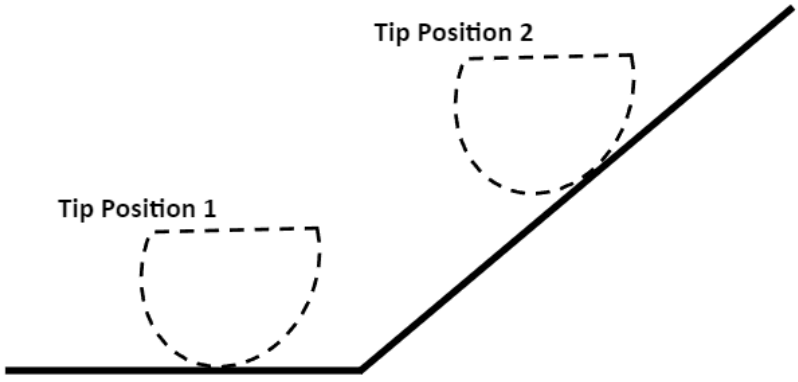

Figure-2.4: Diagram showing different tip/sample solid-solid contact areas caused by topography change of the surface.

This means that as the topography of a surface changes, so too will the contact area between the tip and sample. This changes the heat transfer conditions and can result in the tip heating or cooling independently of the surface temperature. This effect can be seen in Figure-2.5 which shows a calibration grid sample made of square raised sections. The topographical features are clearly visible in the thermal image.

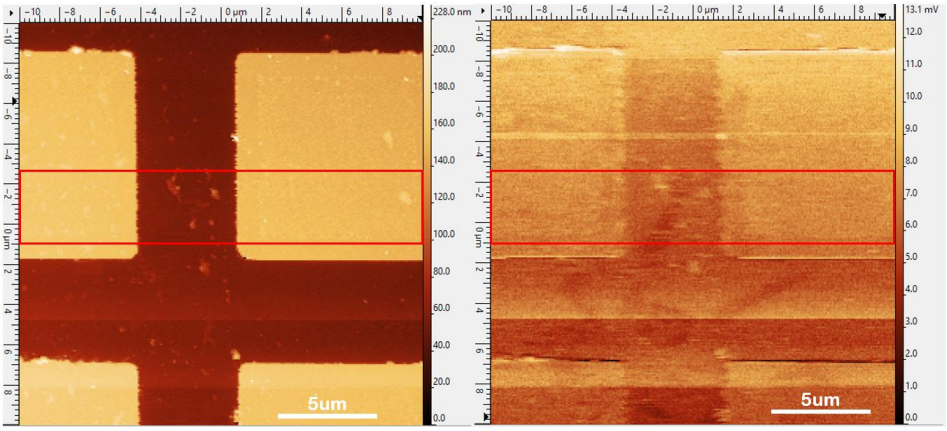

Figure-2.5: Simultaneous images of calibration grid taken on VLS-80 topography (Left) and thermal (Right) with marked red area. Note that topographical features are clearly visible in the thermal image.

The top and bottom surface are made of two different materials which are clearly distinguishable in the image and the thermal to topography comparison in Figure-2.6 but we can also note some of the shape effects around the edges of the squares. Additionally some of the surface detritus can also clearly be picked up by the SThM examination which may be caused by the changing tip-sample contact or the debris being made of a different material.

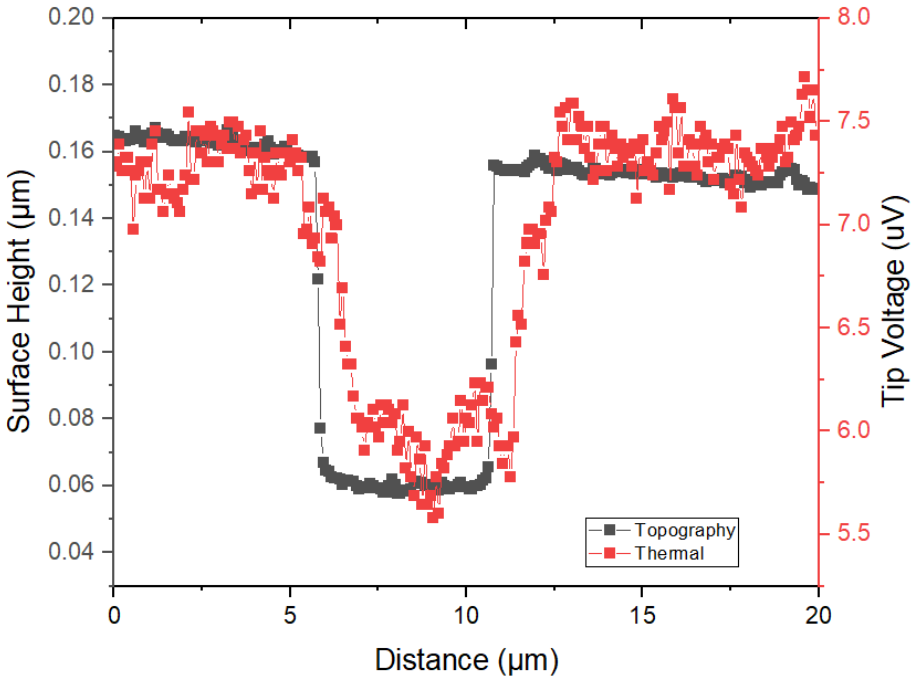

Figure-2.6: Graph comparing topographical and thermal VLS-80 data along the red area marked on Figure-2.5, showing the influence of the different materials used in the calibration sample as well as the thermal response to the topography.

It is noticeable that there is a slight offset between the topography and the thermal signals. This is because the scan is taken from left to right (also known as 'forward'). There is a slight lag in the thermal signal which can result in the two being slightly apart from each other. The amount of difference increases as the speed of the scan does and throughout this project has been accounted for by matching noticeable features (usually debris) between the topography and thermal images.

The direction of the scan also accounts for why the right-hand side of the thermal signal change is longer than the left. This is because the tip's contact with a gradient when travelling up is different to when travelling down due to the tip/surface geometries. This results in an asynchronous result to matching topography. A backwards (i.e. right to left) scan will reverse this effect.

2.5 Probe-Sample Heat Transfer

A tip can be used in two different modes. The 'active' mode is where the tip is heated to a temperature which is greater than that of the surface and thus when they come into contact the surface will cool the tip. The 'passive' mode on the other hand is where the tip is cooler than the surface and any contact will cause the temperature of the tip to rise.

This heat exchange is a complicated process to understand as it consists of a number of different component factors listed below:

- Gas Conduction
- Liquid Conduction
- Solid-Solid Conduction
- Radiation

As shown in Figure-2.7 this is a complex system between the probe (which consists of a cantilever and a tip) and the sample which requires careful examination.

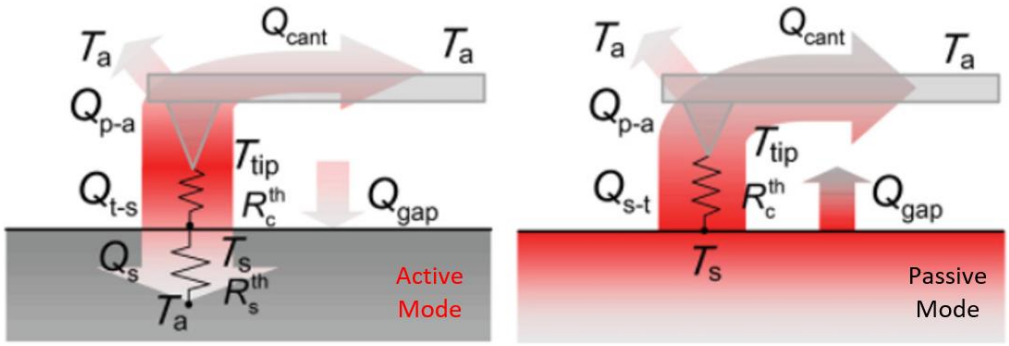

Figure-2.7: Diagram of heat transfer components and direction between tip/sample in the case of active mode where $T_{tip} > T_s$ (Left) and passive mode where $T_{tip} < T_s$ (Right). (Reproduced from reference (12))

where; T_a is the ambient temperature, T_{tip} is the temperature of the tip, T_s is the temperature of the sample, $Q_{p\text{-}a}$ is the heat flow between the probe and atmosphere, $Q_{t\text{-}s}$ is the heat flow between the tip and the sample, Q_{cant} is the heat flow up the cantilever to the larger system, Q_s is the heat flow into the sample, Q_{gap} is the heat flow between the air and sample, R_s^{th} is the thermal resistance of the sample and R_c^{th} is the thermal contact resistance between the tip and the sample.

The key value for determining the heat transfer (Q) within the system is the conductance (G) between the probe and sample. This is the degree to which the heat is able to flow, and the total conductance is the sum of all of these different contributors as proposed by A. Majumdar (22):

$$G_{total} = G_{gas} + G_{liquid} + G_{solid} + G_{radiation} \quad (2.1)$$

In the following section we will explore these different forms of heat transfer.

2.5.1 Gas Conduction

Any experiment not performed in vacuum is subject to heat transfer between the probe and sample through the surrounding gas. The effect of this is clear to see when measurements show a change in tip temperature as it approaches a surface but before it makes any kind of contact. This can be seen in the thermal approach curves shown in Figure-2.8. These show that in air the temperature of the tip begins to drop before the 'snap in' (i.e. when the surface forces cause the SThM tip to make physical contact) which is not seen in the vacuum approach curve.

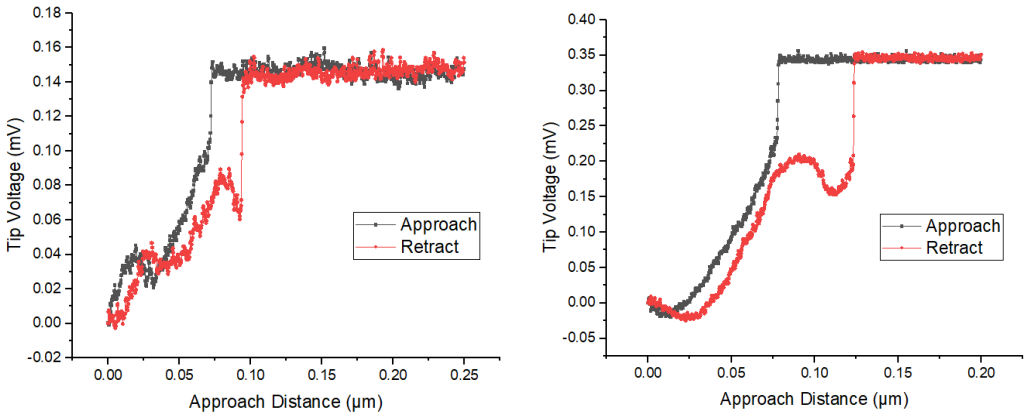

Figure-2.8: VLS-80 thermal approach curves in air (Left) and vacuum (Right) showing tip/sample interaction before physical contact under atmospheric conditions.

There are several methods of gas-based heat transfer. When a tip is more than several micrometres from a surface or is relatively large, such as in the case of a Wollaston wire probe, there can be heat convection where the flux is carried by created air currents. More commonly however the heat transfer takes place at a much smaller distance with diffusion occurring within a few microns of the surface and ballistic transfer below the mean free path of air (Λ_{air} ≈70nm) as shown in Figure-2.9.

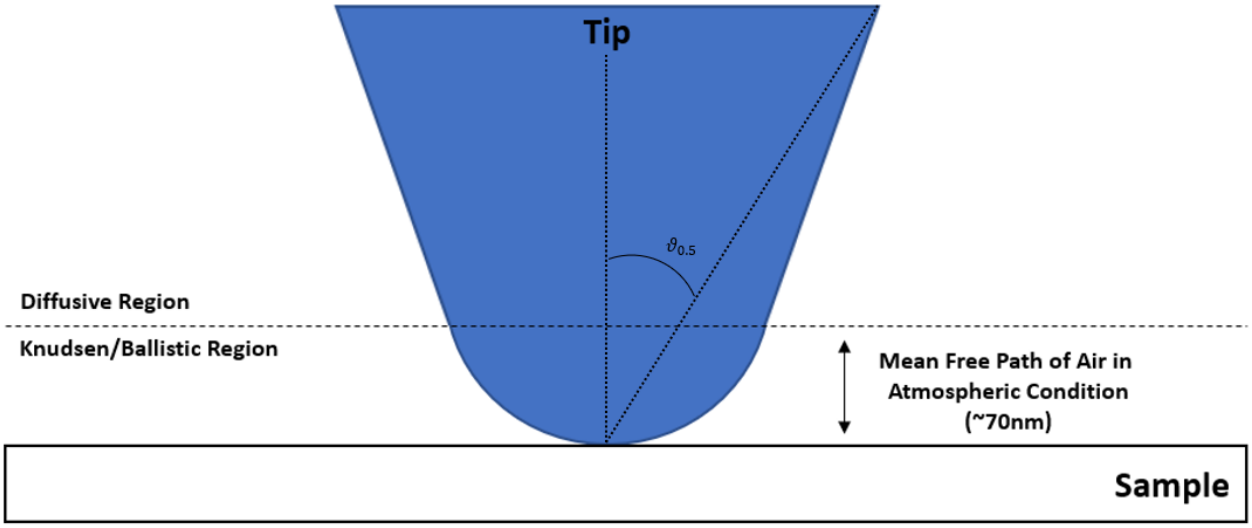

Figure-2.9: Diagram of gas conduction transport areas between tip and sample.

Using kinetic theory, the thermal conductivity of gas is:

$$\kappa_g = \frac{1}{3} C \upsilon \lambda \tag{2.2}$$

where C is heat capacity per unit volume, υ is the rms speed of the molecules and λ is the mean free path for intermolecular collisions. υ can further be defined as:

$$\upsilon = \sqrt{\frac{3k_bT}{m_{mol}}} \tag{2.3}$$

where k_b is the Boltzmann constant, T is Temperature, and m_{mol} is the molecular mass of the gas.

However, when the distance between the tip and the sample, which is defined as z, is smaller than λ_{air} (i.e in the ballistic region) as the collision is now with the tip rather than other air molecules thermal conductivity within the ballistic region as:

$$\kappa_{g,bal} = \frac{1}{3} C\upsilon z \tag{2.4}$$

Local conductance within the ballistic region ($g_{loc,\ bal}$) can therefore be expressed as:

$$g_{loc,bal} = \frac{\kappa_{g,bal}}{z} = \frac{1}{3} Cv \tag{2.5}$$

The local conductance can be converted to be the conductance for the entire ballistic region by multiplying this by the area which is estimated using a cone of half angle $\vartheta_{0.5}$ and a height equal to the mean free path λ:

$$G_{g,bal} = \frac{\pi}{3} Cv\lambda^2 tan^2\vartheta_{0.5} \tag{2.6}$$

It is then possible to simplify this further to:

$$G_{g,bal} = \pi\kappa_g \lambda tan^2\vartheta_{0.5} \tag{2.7}$$

For the diffusive regime, the tip is assumed to continue as a cone. To calculate the area, the entire active length of the tip is given as L and as such the area needs to be integrated between the end of the diffusive region and the active length:

$$G_{g,dif} = \int_{\lambda tan\vartheta_{0.5}}^{L} \kappa_g \frac{2\pi x}{y} dx = 2\pi\kappa_g tan\vartheta_{0.5} \int_{\lambda tan\vartheta_{0.5}}^{L} dx \quad (2.8)$$

where x and y are the limits of the continuum region. This can then be simplified to:

$$G_{g,dif} = 2\pi\kappa_g tan\vartheta_{0.5} \ (L - \lambda tan\,\vartheta_{0.5}) \quad (2.9)$$

equations (2.6) and (2.8) can then be combined to provide a total gas conductance:

$$G_{gas} = G_{g,bal} + G_{g,dif} = 2\pi\kappa_g L tan\vartheta_{0.5} \ (1 - \frac{\lambda tan\,\vartheta_{0.5}}{2L}) \quad (2.10)$$

Gas conduction occurs across the entire active tip, not only in a limited contact area. For this reason, it is often a significant contributor to the overall heat transfer. Especially for larger probes such as a Wollaston wire probe it can provide up to 65% of the transfer at room temperature (30). Consideration also has to be made however for heat-loss from the tip to the environment, especially when using smaller probes in active mode where the tip is hotter than the surface.

2.5.2 Liquid Conduction

In air, when the tip comes into contact with a sample it forms a liquid meniscus around itself due to capillary condensation of humidity as shown in Figure-2.10. This meniscus forms a significant contact area around the tip which is able to transfer heat through the liquid. This contact area is much smaller than seen for the gaseous conduction but can displace much of the ballistic transfer as both forms of conduction cannot happen in the same place.

This meniscus can be seen in the tip-sample force dynamics. When conditions are more humid (and thus more susceptible to forming a meniscus) the 'snap-in' distance for the tip is further from the surface and the force required to remove the tip from the sample is greater (31). Additionally, these effects and the overall heat transfer are lower when performed in vacuum or some other dry gaseous environment such as dry air (32).

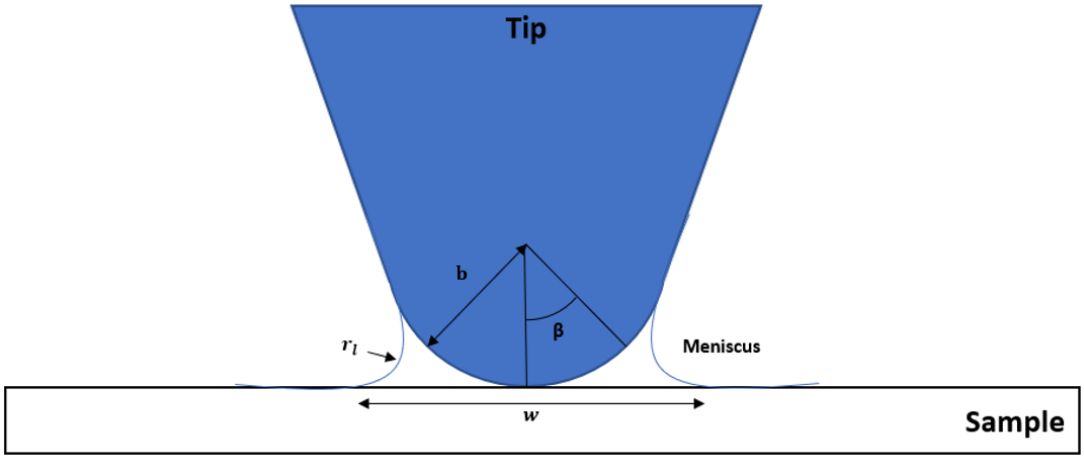

Figure-2.10: Diagram of probe-sample liquid heat conduction showing relevant parameters and approximate formation of a meniscus.

In order to determine the effect of the water meniscus, its dimensions first need to be calculated. Firstly, the radius of the water-film bridge (r_l) can be determined from the Kelvin equation (33):

$$r_l = -\frac{2\zeta V_{mol}}{RTln(\psi)} \tag{2.11}$$

where ζ is the surface energy of the liquid, V_{mol} is the molar volume, R is the gas constant, T is the temperature, and ψ is the relative humidity. For water at room temperature this can be simplified to:

$$r_l = -\frac{1.08}{ln(\psi)}\text{nm} \tag{2.12}$$

The width of the meniscus, w, is much larger than its height so can be approximated to:

$$w \approx 4\sqrt{br_l cos\theta_{cont}} \tag{2.13}$$

where b is the tip radius and ϑ_{cont} is the contact angle. Again, for water this can be simplified to:

$$w \approx 4.16\sqrt{\frac{-bcos\theta_{cont}}{ln(\psi)}} \tag{2.14}$$

In simple calculations we assume that ψ is 0.5 and ϑ is 0 which results in a liquid-film radius r_l of 1.6nm. Therefore for a tip radius b of 100nm the width of the meniscus is 50nm.

We can also then define β as the angle subtended by the edge of the liquid film. The tip can be estimated to be circular through the relationship:

$$\beta = \sin^{-1}(\frac{w}{2b}) \tag{2.15}$$

With this it is possible to estimate the conductance due to the water meniscus using κ_w as the thermal conductivity of the water and z as the separation between the tip and sample using an intermolecular force equation (34) to get:

$$G_{liquid} = 2\pi\kappa_w b[ln\left(1 + \frac{b}{z}(1 - cos\beta)\right) + 1 - cos\beta] \tag{2.16}$$

For larger tips such as Wollaston wire probes the water meniscus is relatively small compared to the active region of the tip so does not constitute the majority of the heat transfer. Smaller nanofabricated tips, such as those being used in this project, are much more susceptible to its effects and it has been proposed to be the dominant contributor in some situations (35). There are however a number of factors from the tip and sample materials which are not considered here. The material properties such as their roughness and how hydrophilic/phobic they are will also factor into the meniscus formation and thus the amount of heat transfer.

2.5.3 Solid-Solid Conduction

In contact SThM there is significant solid-solid conduction. This can be identified by a jump in the thermal signal upon contact. Additionally, the magnitude of this jump is also highly dependent on the thermal conductivity of the sample κ_s.

When considering the tip contact with the surface we must use an estimate of the contact diameter (d) which is the actual contact area between the sample and tip using Hertzian elastic contact theory (36):

$$d = (\frac{6Fr}{E^*})^{\frac{1}{3}} \tag{2.17}$$

where F is the tip-sample force, r is the tip radius, and E* is the effective elastic modulus between the tip and sample which is calculated by:

$$\frac{1}{E^*} = \frac{1-V_{tip}{}^2}{E_{tip}} + \frac{1-V_{sample}{}^2}{E_{sample}} \tag{2.18}$$

where E is the elastic modulus of the material and V is the Poisson ratio.

This gives a value for the amount of contact being made between two stiff surfaces. However, if the stress to a surface is sufficiently high it will cause deformation. At values typically above ~1Gpa for ceramics and ~100Mpa for metals there will be some plastic deformation in the surface which changes how the contact diameter is calculated to:

$$d = (\frac{4F}{\pi H})^{\frac{1}{2}} \tag{2.19}$$

where H is the hardness of the softer material. With the contact diameter established it is possible to calculate the conductance of both the sample and the tip. This is done using the thermal conductivity of the tip κ_{tip} and again assuming the tip is a cone of half-angle $\vartheta_{0.5}$.

$$G_{s,tip} = \frac{\pi \kappa_{tip} d tan\vartheta_{0.5}}{2} \tag{2.20}$$

$$G_{s,sample} = \pi \kappa_{sample} d \tag{2.21}$$

This can then be combined using the surface thermal conductivity κ_{sample} for a total G_{solid} of:

$$G_{solid} = \pi d(\frac{\kappa_{sample}\kappa_{tip} tan\vartheta_{0.5}}{2\kappa_{sample}+\kappa_{tip} tan\vartheta_{0.5}}) \tag{2.22}$$

However, these calculations assume a perfectly flat surface which is receiving perpendicular contact. Additionally, it also assumes a smooth surface and tip. In reality such conditions do not occur and so the conductance is modulated by this. Solid-solid conductance is rarely the dominant method in atmospheric conditions, but it is much more important in those performed in vacuum where it is nearly the sole available heat transfer mechanism.

2.5.4 Near-Field Radiation

Heat is able to radiate out of a surface as infrared light. It is possible for this to be absorbed by the tip providing another mechanism for heat transfer between the two.

The conductance of radiation can be taken from the equation for thermal radiation between two surfaces:

$$G_{rad.s} = \frac{4\sigma_b A T^3}{\frac{1}{\varepsilon_1}+\frac{1}{\varepsilon_2}-1} \tag{2.23}$$

where σ_b is the Stephan Boltzmann constant, A is the area of the surfaces (assuming they are equal), T is the absolute temperature, and ε is the emissivity of each material. From this it is possible to calculate the conductance per unit area:

$$G_{rad.s} = \frac{4\varepsilon_0 c {k_b}^2 \rho_e (1-R) T}{h z^3} \tag{2.24}$$

where ε_0 is the permittivity of vacuum, c is the speed of light, k_b is boltzmann's constant, ρ_e is the electrical resistivity of the metal, R is the reflectivity, h is Planck's constant, and z is the distance between the tip and surface. Once again applying the idea that the tip is a cone of half angle $\vartheta_{0.5}$ the radiative conductance is then:

$$G_{rad} = \frac{16\pi\varepsilon_0 c {k_b}^2 \rho_e (1-r) T tan^3\theta_{0.5}}{hd} \tag{2.25}$$

Generally speaking, the effects of near-field radiation are small enough so as to be unmeasurable. Considering the small tip radius the effect is reduced to the order of 10^{-12} – 10^{-13} W/K (22) which under ambient conditions is negligible. However, it is possible that under vacuum conditions without direct solid-solid contact but within the near-field regime it may be possible to detect. Far-field radiation is also theoretically possible but provides even less of a contribution and would only be noticeable when the tip is significantly far from the surface as to be of little use (37).

2.5.5 Probe-Sample Transfer Contributions

The contribution of each of the different heat transfer mechanisms between a tip and a sample varies depending on the construction of the tip, most importantly its size. For this project KNT-SThM-2an probes were used which have a tip radius of <100nm and a tip height of ~10µm. An approximate calculation of the various conductance paths between the tip in contact with a Si surface using equations 2.10, 2.16, and 2.22 gives the estimate that under standard atmospheric conditions approximately 2% of the heat flow comes from gas conductance, 88% from water conductance and 10% from the solid-solid contact; the near field radiation is negligible. Under vacuum conditions it is assumed that all of the heat flow comes from solid-solid conductance.

The solid-solid contribution is particularly important to note as it means that under vacuum conditions the heat flow drops by an order of magnitude.

2.6 Analysis Methods

SThM outputs a simultaneous topographical and thermal measurement of a surface. This can be used for all standard AFM measurement techniques but also allows for a number of other examinations to be performed on the thermal properties of a sample.

2.6.1 Comparison Method

When a tip is placed in contact with a surface the temperature of the tip changes according to the properties of the material which it is in contact with. The amount which the temperature of the tip is changed by is related to the difference of temperatures and the thermal conductivity of the sample material.

This can be used to determine the temperature difference between different parts of a scan. Or in the case that the whole material is at a single temperature it can be used to examine for differences in the thermal conductivity of a material. This can be for samples such as heated wires buried below a surface or smooth surfaced materials which have structural features which may change their thermal conductivity.

2.6.2 Null-Point Measurements

The comparison method is limited to relative measurements of temperature only. The 'null-point' method attempts to remedy this by being able to provide an absolute measurement of temperature.

This is done by first calibrating the system such that it is possible to correlate a tip's voltage with its temperature (38). Once this has been done, the tip is then approached to the surface producing a thermal approach curve as shown in the force curve of Figure-2.2.

If the tip and sample are at different temperatures, the tip will be caused to either heat or cool as appropriate. The voltage (and therefore temperature) of the tip can then be altered. This process is repeated until the point where upon the tip contacting the surface (as seen in the normal deflection) there is no thermal change which means that the surface and tip are the same temperature. As the system is in equilibrium the contact resistance between the tip and sample are unimportant (39). This allows for the absolute temperature of a point on a sample to be measured.

2.6.3 The Menges-Gotsmann Method

The Menges-Gotsmann method was developed in order to be able to avoid the difficulties in SThM scanning caused by the contact resistance between the tip and sample (40). It uses two scans of a surface. One when the surface is at an ambient temperature and another when the surface is heated (41), typically using some kind of self heated structure.

A comparison can then be made between the two scans. Importantly the contact resistance between the tip and the surface remains the same between the scans regardless of the temperature change. This allows for the thermal effects of the contact resistance to be removed from the images (42). This allows for a relative temperature difference between the heated and unheated surface to be determined regardless of the surface features such as roughness which can hamper SThM examinations.

Chapter 3

Experimental and Computational Techniques

3.1 Establishing SThM in York

The broader techniques of SThM operation were discussed in Chapter 2. Examined here are the specifics of the instrument modified and used at the University of York in this project.

3.1.1 VLS-80 AFM/MFM

The Nanoscan VLS-80 (33) is an instrument designed for high-precision vacuum scanning probe microscopy shown in Figure-3.1. It is built to accommodate a variety of scanning modes such as topographical contact and tapping modes as well as Magnetic Force Microscopy (MFM) which is augmented by the inbuilt magnetic field generators.

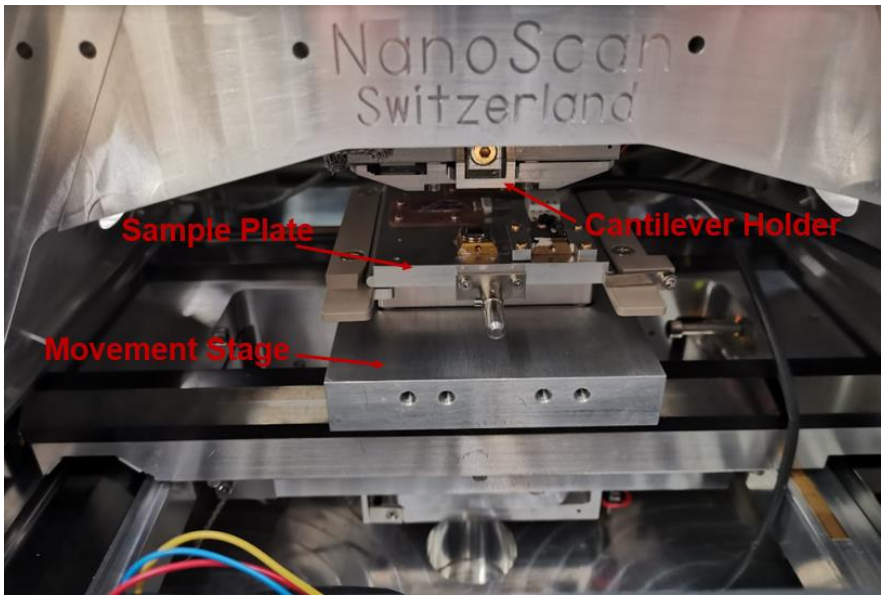

Figure-3.1: Image of the inside of the VLS-80 with sealing chamber removed, revealing the driving mechanism for the sample plate.

Vacuum Capabilities

One of the more specialised capabilities of the VLS-80 is that the chamber can be fully sealed and placed under vacuum as shown in Figure-3.2. The system uses a foreline and a roughing pump backed turbomolecular pump allowing measurement conditions of $<5x10^{-4}$ mbar to be reached in about 10 minutes with maximum vacuum of down to $\sim 6x10^{-6}$ mbar taking around an hour. The roughing pump is also connected to a buffer tank which allows a turbo-only 'quiet mode' which limits vibrational interference from the pumping.

Figure-3.2: Image of sealed chamber of VLS-80 showing externally mounted cameras for positioning the tip.

Sample Plate

The VLS-80 has a large sample plate as shown in Figure-3.3 which is mechanically driven using precisely controlled motors within the chamber. This allows for rapidly scanning between different samples as multiple samples can be mounted at a time without the need for them to be switched out.

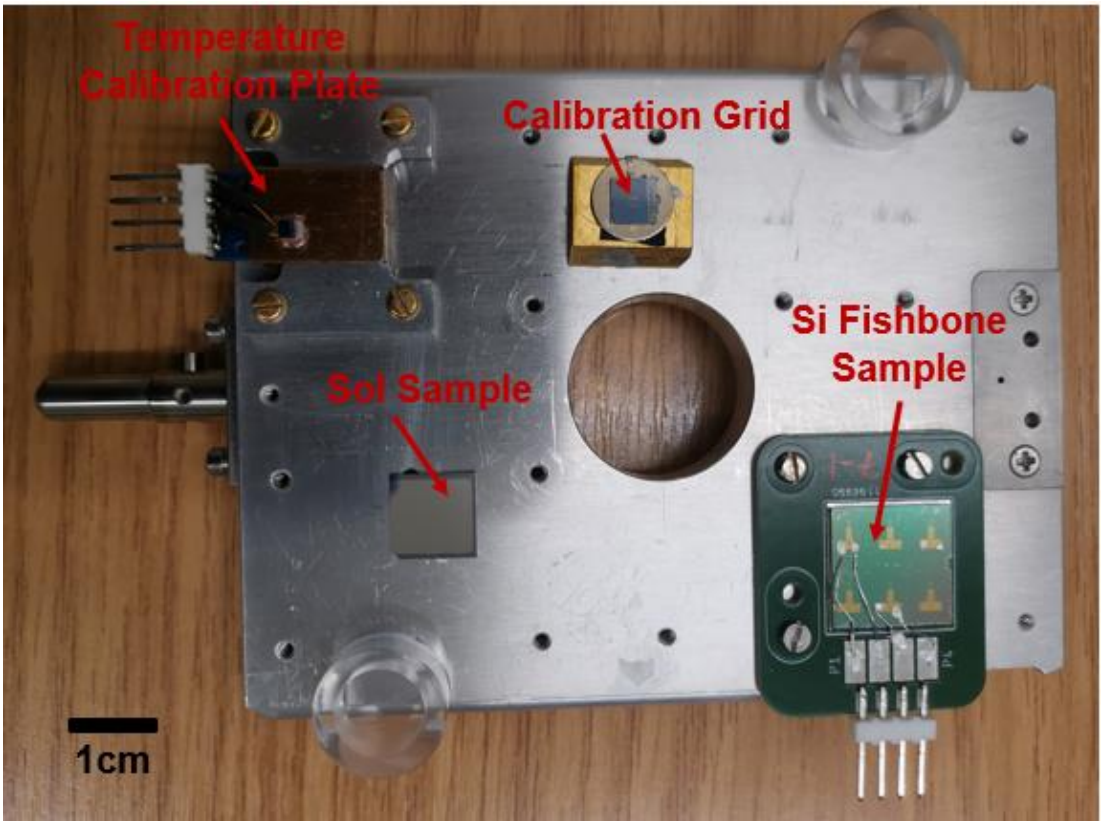

Figure-3.3: Image of VLS-80 sample plate with calibration grid sample, calibration plate and two measurement samples mounted.

3.1.2 AFM to SThM Conversion

The Nanoscan VLS-80 was delivered to the University of York in May 2019 to the laboratory of Professor Atsufumi Hirohata. However, it took until November 2019 for the instrument to become fully functional. It was at this time it became possible to convert the instrument into use as an SThM as part of a collaboration between the University of York and Nanoscan, partly funded by an EPSRC IAA Award. The instrument was typically operated at a spatial resolution of ~100nm and temperature resolution of <10mK.

The wider instrument itself required few changes as it was designed to be adaptable to a number of different circumstances and for future development. However a custom tip holder had to be developed in collaboration with Nanoscan in order to be able to provide power to the tip and extract the signal into an analog to digital converter which could then be recorded. The majority of the additional components were able to be used externally and connected through the wires which were extracted from the system.

SThM Cantilever

KNT-SThM-2an tips shown in Figure-3.4 were used for this project. They were designed as part of QUANTIHeat (23) and manufactured by Kelvin Nanotechnology.

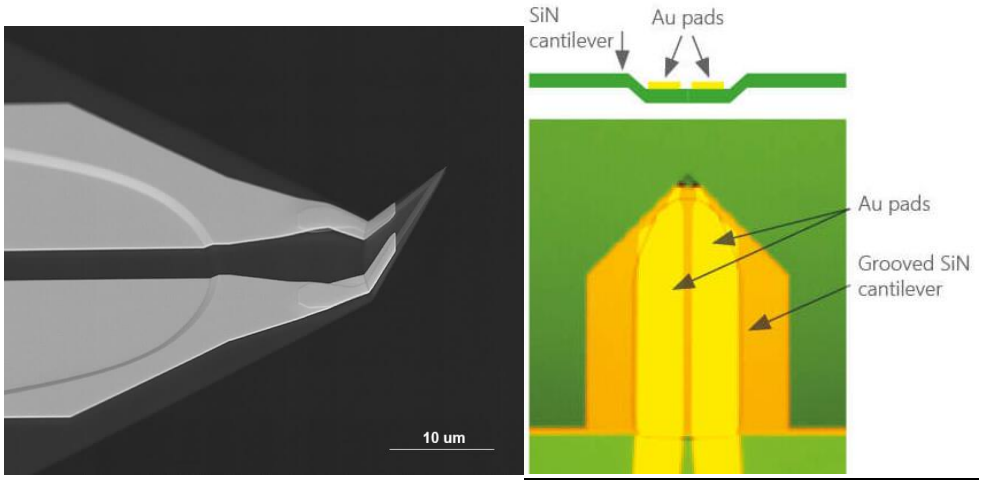

Figure-3.4: SEM image of KNT-SThM-2an probe tip (Left) and schematic (Right). (Reproduced from manufacturer's website (43)).

KNT-SThM-2an tips use a Si_3N_4 cantilever with Au tracks leading to a Pd probe tip of >100nm radius and a spring constant of 0.40N/m. The typical probe resistance is 325Ω and the tip can maintain temperatures of up to 200ºC and a recommended current maximum of 2.5mA DC.

SThM Cantilever Holder

A specialist cantilever holder had to be produced in order to properly use the KNT-SThM-2an tips. This was manufactured by Nanoscan by adapting one of the standard cantilever holders based on prototypes trialled and tested in York. As can be seen in Figure-3.5 this replaces the standard method of holding the tip in place with two Au contacts on top of a PCB board with a mechanically etched depression to allow for easier placement.

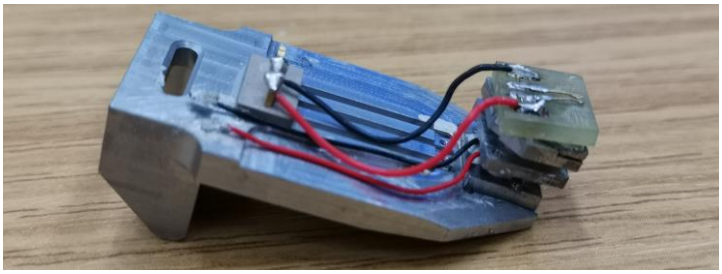

Figure-3.5: Image of custom SThM cantilever holder with circuit wires leading to Au contacts for the SThM tip to be placed under.

These contacts are then connected through wires to connector pins at the back of the cantilever holder which are fed into the VLS-80. It is possible to perform normal topographical operations whilst also powering the tip and allowing the extraction of the tip's bridge circuit voltage to the virtual oscilloscope.

Tip Balancing Circuit

The majority of the additions required to convert the VLS-80 into being an SThM compatible machine came from the addition of an electrical system to power and monitor the circuit running through the tip. This was based on a design from Lancaster University created by the group of Professor Oleg Kolosov. This can be seen in schematic form in Figure-3.6.

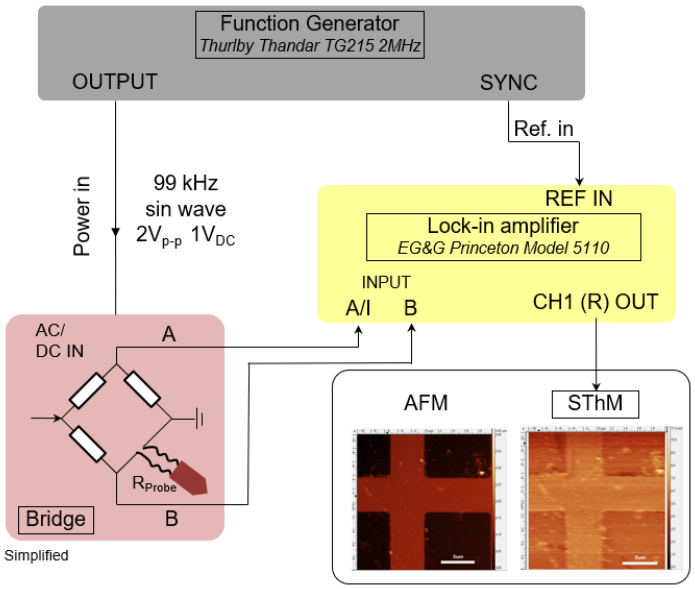

Figure-3.6: Schematics of SThM electrical set-up for VLS-80 including models of components and electrical parameters. (Image made by Dr Siew Wai).

A simplified Wheatstone bridge uses three resistors of known resistance and one with an adjustable resistance. The variable resistor is adjusted until such a point where there is no flowing current, at which point the balance between the tip and bridge is zero. Any small change in the resistance of the tip will then cause an unbalance in the circuit which can be read as a voltage change which is amplified by an operational amplifier. This has the advantage of allowing for measurements of very small resistance changes but is limited by the fact that the output is only obtainable as a relative measurement. The system uses a dual AC and DC sinusoidal

signal sent from a function generator which is fed into a custom Wheatstone bridge circuit which is detailed in Figure-3.7.

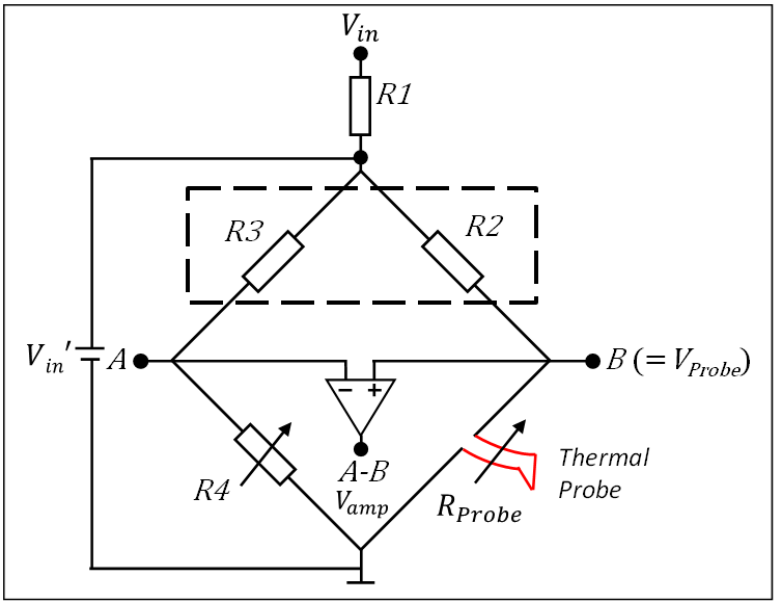

Figure-3.7: Simplified circuit diagram of electronics in the 'Lancaster bridge' which is a customised Wheatstone bridge.

The resulting signal is then fed into a lock-in amplifier where a reference signal is compared to the bridge signal to calculate the difference. This then outputs a recordable thermal signal which is dependent on the temperature of the tip.

Chamber Power

A power cable was present in the machine which was used to power motors which move a permanent magnet within the system (designed for use during MFM examinations). This connection was modified to allow for an external power source to be fed into the chamber. This allowed for the powering of the temperature calibration plate and sample microheaters whilst the chamber was sealed and under vacuum.

3.1.3 Temperature Calibration

As previously mentioned, the use of a Wheatstone bridge circuit limits the output signal in the SThM to a voltage change which is dependent on a relative tip resistance change which is caused by a change in the temperature of the tip. This means that only the temperature difference can be calculated, not an absolute temperature. In order to be able to accurately determine the temperature differences

across a scan the thermal tip must first be calibrated. In short this is done by placing the tip onto a calibration sample and measuring how the thermal signal changes as the calibration plate is heated and cooled.

Calibration Sample

The calibration sample used is made of a peltier heater mounted with a Cu plate and an attached Pt resistance thermometer as shown in Figure-3.8. This is then attached to a brass mounting block which is secured to the VLS-80 sample plate using a custom holder which ensures good thermal contact.

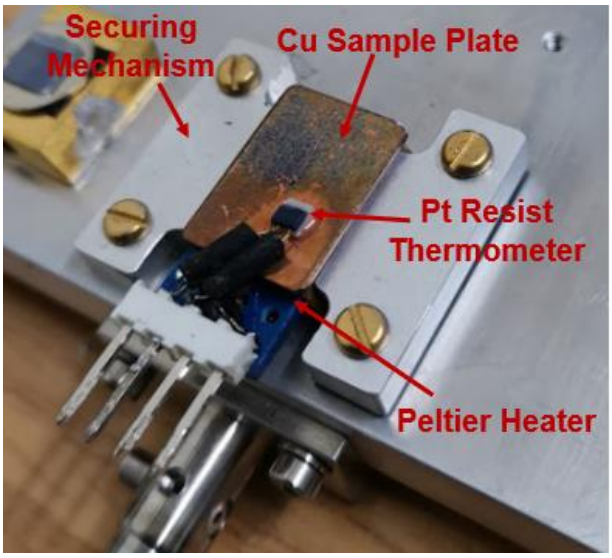

Figure-3.8: Image of calibration sample secured to VLS-80 sample holder.

Whilst the Cu surface is very rough and oxidised as shown in Figure-3.9 the tip can make good contact with the surface. Other, smoother, materials were attached to the top surface of the Cu but the delays in these heating caused significant lag in the temperature rise and did not heat linearly so the bare Cu is used.

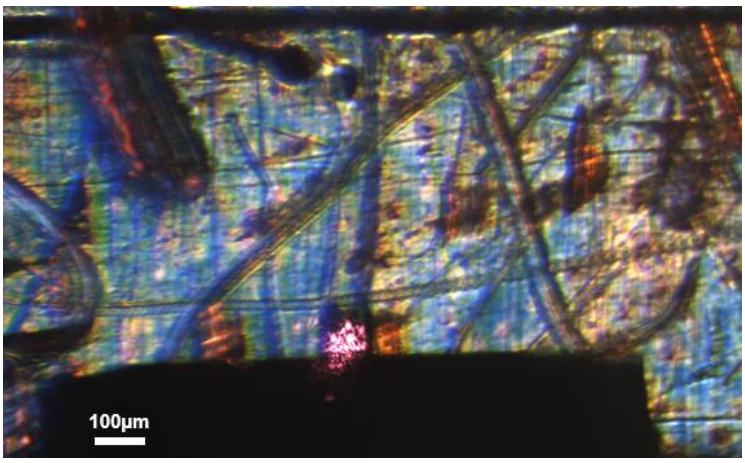

Figure-3.9: VLS-80 top camera view of tip over Cu calibration surface.

York Low Noise Thermoelectric Control System

The York Low Noise Thermoelectric Control System (aka Calibration Control System) was designed and built by Professor Johnathan Weaver of the University of Glasgow and is shown in Figure-3.10. It is designed to be capable of controlling the temperature of the peltier heater within a vacuum SThM system with minimal noise and using no earth loops. It is able to operate off both mains power and a series of large lead acid accumulators. Its operational range is approximately 15-55ºC in atmospheric conditions.

Figure-3.10: Labelled image of the 'York Low Noise Thermoelectric Control System'. Key: 1. Power Out Switch, 2. Read-out Switch, 3. Temperature Read-out, 4, Error Gauge, 5. Power In Cable, 6. Power Out/Signal In Cable, 7. Temperature Setpoint A Dial, 8. Temperature Setpoint B Dial, 10, Signal Out Cable.

The calibration control system allows for two different temperatures to be set (A and B) and the calibration sample to be switched between these. The read-out display shows the current temperature (with an error of ±0.5ºC) of the Cu surface as recorded by the Pt resistance thermometer which is also output as a signal to the computer.

Calibration Protocol

In order to determine the sensitivity of the tip and electronics to the change in temperature, a calibration protocol was developed. First the input voltage to the tip and any other parameters were set and the tip was put into contact with the surface

(effectively performing a 0x0 sized scan which maintains AFM feedback contact conditions) at a low temperature, typically 20ºC.

The surface would then be set to a higher temperature (typically 40ºC) and allowed to heat up and stabilise. The temperature would then be reduced to the lower value and allowed to stabilise once more resulting in the calibration curves shown in Figure-3.11.

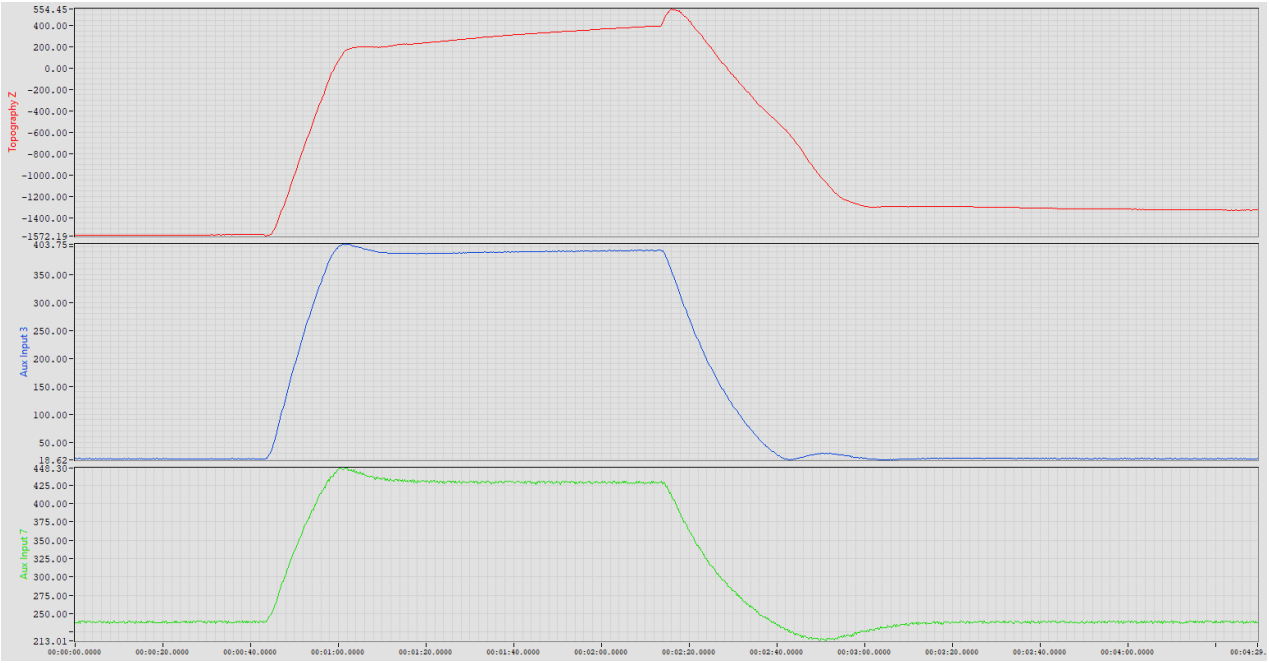

Figure-3.11: Typical air calibration curves showing topography (red), tip voltage (blue) and surface temperature as recorded by Pt resistance thermometer (green).

As the tip is in contact with the surface and is much smaller it is assumed that the tip will equilibrate to the surface temperature. This causes a corresponding resistance change in the tip and thus a voltage change which is recorded. As the surface temperature is changed, so too is that of the tip which results in a voltage change. At any given point it is assumed that the tip voltage is equivalent to the surface temperature so the two are plotted against each other as in Figure-3.12 which shows that within the temperature range the resistance of the Pt varies linearly with the temperature.

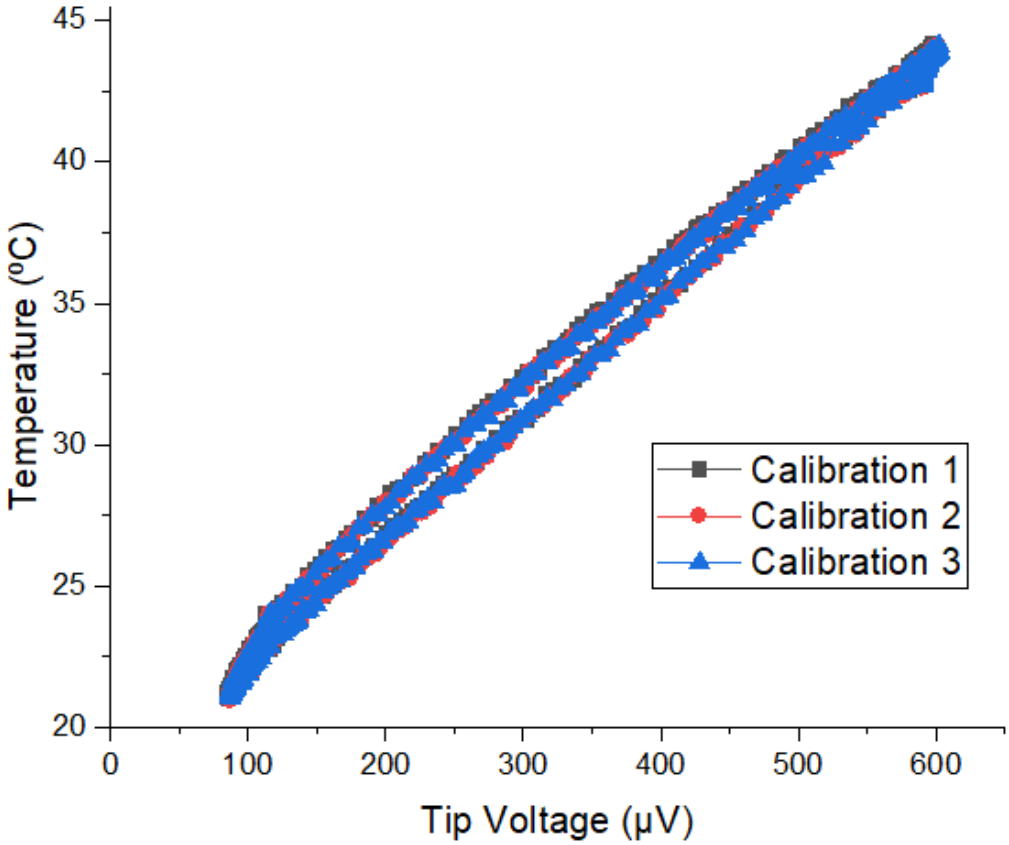

Figure-3.12: Typical calibration curve showing output tip voltage against tip temperature with repeated measurements.

Due to contact resistance it is not possible to be sure that the tip does in fact stabilise at the exact same temperature as the surface but is likely offset. However, as this shift will be constant what can be used is the relative temperature change to relative tip voltage change. This allows for a taking of the gradient from the calibration curve which can be used to convert voltage changes into relative temperature changes.

The calibration generates a significant amount of data points near the highest and lowest temperature from the settling. These areas are noisy and can cause significant error. To correct for this the data is filtered to just the up and down gradients, as seen in Figure-3.13, which are then measured and averaged to give a calibration gradient.

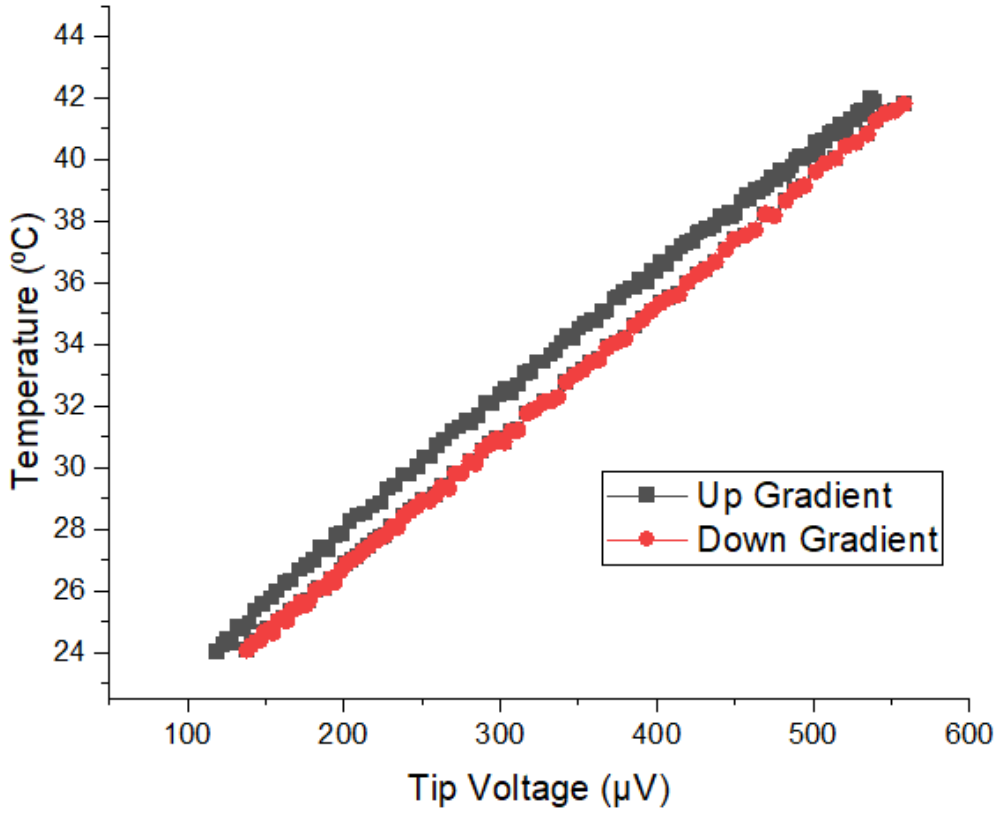

Figure-3.13: Typical calibration curve showing separated up and down gradients.

This calibration curve measurement is performed several times and an average gradient in mK/µV is determined.

Stability of Calibration

It is important to consider how stable the calibrations are. This comes in two different forms. The error on any given calibration scan and how long it takes for the calibration to drift. The agreement between repeated measurements is excellent. Calibrations taken in quick succession have statistical errors of less than a percent and a standard deviation on the order of 2%. The calibration drift however is a significant concern. Over various measurements it was found that the value could range between 27mK/µV and 64mK/µV and significant changes could be noticed within a single day. Because of this significant drift a calibration was taken before each set of scans.

3.1.4 Vacuum SThM

The VLS-80 is able to reach sample chamber vacuum conditions of $<5x10^{-6}$ mbar. This can be desirable for SThM work as it removes the water meniscus, gas

conduction, and the air convection as heat transport methods between the tip and the sample. As previously mentioned, the SThM modifications were made to allow for full vacuum operation. However, attempting to operate the system under vacuum conditions presented a number of significant issues.

Vacuum Calibration

The calibration protocol as described in section 3.1.3 was also used for calibrating the tip under vacuum conditions however as can be seen in Figure-3.14 the results were more variable.

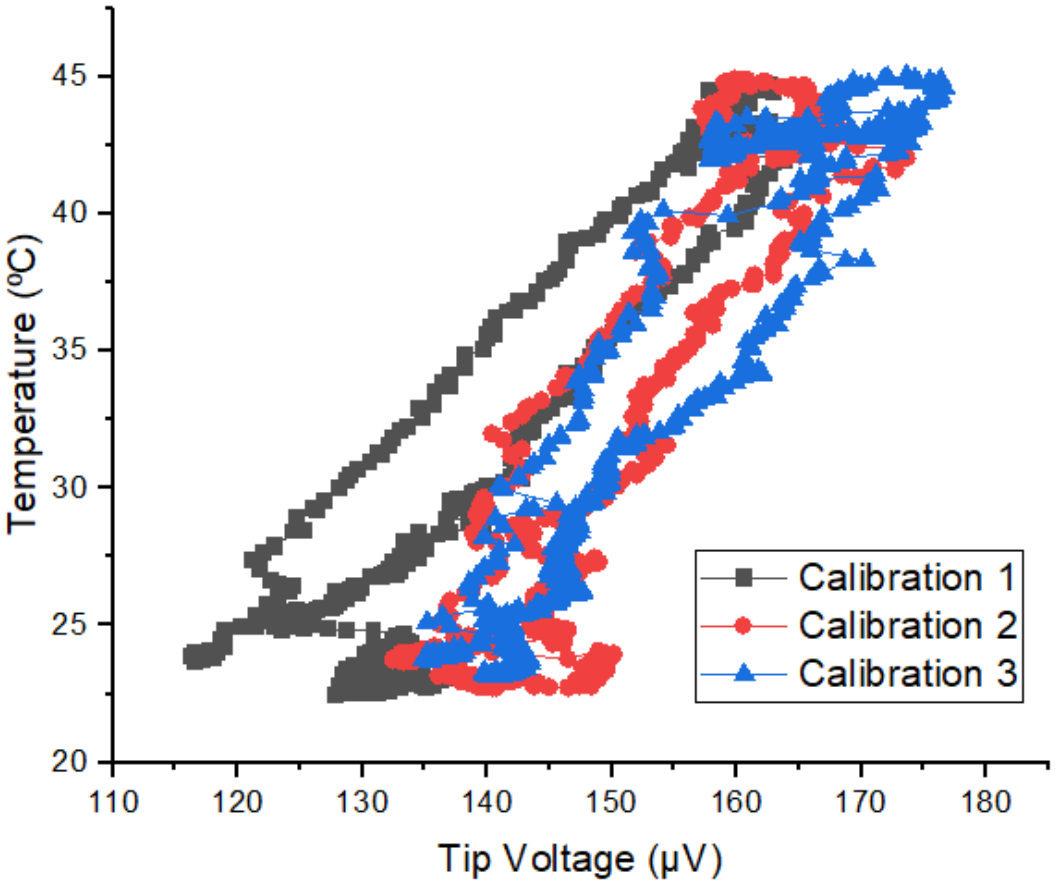

Figure-3.14: Typical vacuum calibration curve with repeated measurements.

Once again, these calibrations could be separated out into upwards and downwards gradients in Figure-3.15 in an attempt to avoid the worst of the uncertainty which comes during the settling period.

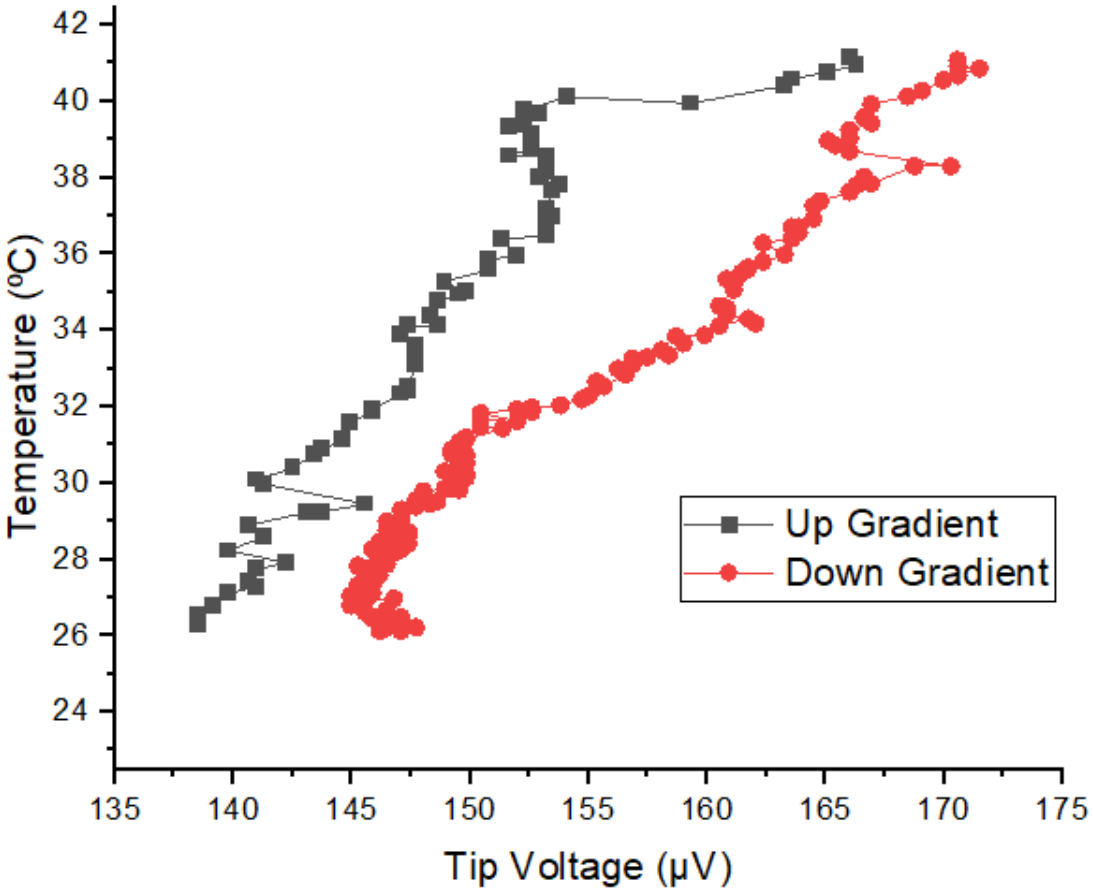

Figure-3.15: Typical vacuum calibration curve showing separated up and down gradients.

Not only were the repeated measurements affected, giving standard deviations of up to 20% but across the measurements there was a larger range of values of the calibration from 274mK/µV to 1094mK/µV across a single day. This made any vacuum measurements that were taken significantly less reliable.

It should be noted that in these measurements the tip is an order of magnitude less sensitive in vacuum. This is due to the removal of the parallel heat flow paths of a surrounding water meniscus and gases which leaves the solid-solid contact as the dominant heat transportation method.

Temperature Control in Vacuum

Another problem when attempting to perform experiments in vacuum is that it was discovered it is difficult to control the temperature within the chamber. This manifested in two main ways.

When performing calibrations, the experiments had to be done quickly and allowed some cooling off time with the calibration plate turned off. This is because the minimum temperature that the calibration was able to reach would rapidly rise. It is thought that this happened as the plate is heated and cooled by a peltier heater. This works by heating one side of the peltier and cooling the other. Under vacuum conditions it is thought that the heated side was not able to properly disperse the thermal energy into the surroundings and would cause the temperature of the cooler side to be raised over time.

Further evidence of this inability to disperse heat is that when microheaters were used in experiments to attempt to provide a thermal gradient they instead heated the entire sample to a stable temperature. This only occurred under vacuum conditions.

3.2 Data Analysis Tools

All of the data taken on the VLS-80 was analysed using Gwyddion (44). The software allows for easy viewing of any of the taken topography and thermal data both as 2D and 3D images.

Gwyddion was used to convert the images into line averaged scans. This was done by selecting an area on an image wherein Gwyddion would average the Y values (either thermal signal or topographical height) for each X point (distance along the sample). These line averaged scans were used at every point of the examinations as the most effective way of examining across a sample.

Gwyddion also offers several other features which were used where appropriate. These include the ability to mask debris (and thus remove them from line averaging), reduce the minimum recorded value to zero and shifting the other data with it, and to perform a topography correction. The topography correction allows for the gradient across the sample caused by imperfection in how the sample is mounted to be automatically removed by considering the line average topography.

3.2.1 Roughness Analysis

At various times in this work the roughness of a surface is referred to. In all cases this roughness was calculated as a root mean square (RMS) roughness over the

entire available material surface area using Gwyddion. The RMS roughness is a measurement of the root mean square average deviation of all the points on the surface from the mean average surface height.

3.3 Fabrication Techniques

Over the course of this work a number of nano and microscale devices were constructed. For this, a number of different fabrication techniques were required which are briefly explained within this section.

The fishbones (examined in Chapter 6 and 7) were constructed on an SoI (Silicon on Insulator) surface using e-beam lithography, a reactive ion etch, and then a wet undercut. The chips also had microheaters constructed on their surface which were fabricated using UV lithography and metal deposition.

3.3.1 E-Beam/UV Lithography

Both E-Beam and UV lithography function using the same principles. First a resist is spin-coated onto a sample. Spin coating allows for the application of a thin, highly uniform layer of fluid onto a surface. This is done in a spin-coating device where the sample is affixed to a rotating plate before having the fluid placed upon it. As the sample is spun, the fluid spreads out into a thin film layer. The thickness of this layer can be controlled by varying the speed and duration of the rotation.

For the production of the microheaters first a 500nm LOR® 7B 'lift-off' layer had to be deposited. This was followed by a 1800nm Microposit® S1818 G2 Photoresist layer. For the production of the Si fishbones a 250nm AllResist® AR-P 6200.13 E-Beam Resist layer was used. These are both lab-standard recipes for lithography.

The surface is then exposed to UV light or electrons which results in either the resist hardening in the case of negative resists or degradation in the case of positive resists (45).

This means that when the sample is placed in a developing agent the location where the resist remains and where it is washed away from can be chosen. What area is exposed can be controlled in a number of ways including the use of masks,

but for small scale fabrications a controllable beam is preferable as it offers greater flexibility.

For the writing of the microheaters, UV Lithography was performed on a 'Kloe® Multifunction Maskless Lithography Equipment: Dilase 650' situated within the York JEOL Nanocentre. The exposure was performed using a 10µm beamline with x10 objective lens, 1.0 optical neutral density filter and a velocity of 2mm/s at a 30µm distance from the focal point.

For the writing of the Si fishbones e-beam lithography was performed on the 'Raith® VOYAGER Electron Beam Lithography System' also at the York JEOL Nanocentre by Dr Christopher Reardon. The machine was operated at 50kV and a beam aperture of 40µm, producing a beam current of 900 pA. A step size of 10nm was used in both x and y directions and a clearing dose for the e-beam resist of 130µC/cm^2 was determined.

3.3.2 Metal Evaporation Deposition

Metal evaporation deposition is performed by heating a metal filled boat within a vacuum. This causes the material to evaporate, and this vapour can then condense on the surface of a sample (46).

This can be used in conjunction with the spin coating and lithography techniques to fabricate metallic features on the surface of a chip. The development of the resist layers following on from the lithography removes the exposed areas creating channels for the metal to be evaporated into where it will remain on the surface.

A lift-off resist (LOR) layer placed during the spin coating can then be easily dissolved in a solvent (in this project Microposit® Remover 1165 was used). This then causes the excess metals to be removed from the surface of the chip. This process is shown in Figure-3.16.

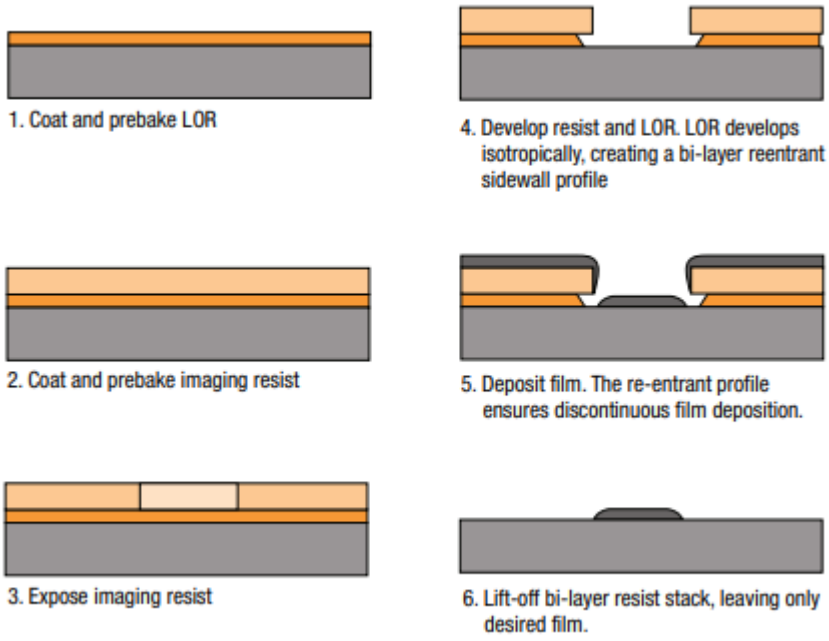

Figure-3.16: Diagram of metal evaporation deposition process on a lithographed resist layer which results in the desired metallic pattern being left on a chip surface. (Reproduced from reference (47)).

3.3.3 Reactive Ion Etching

Reactive ion etching is a process where a high frequency electrical field is applied to a gas. This causes the gas to ionise into a plasma. This plasma is then able to bombard the surface causing an etching process.

Which gases are used is important because the ions are also able to chemically react with the surface which causes increased etching. This allows for much faster etching rates and can be used to make preferential etching in certain materials, as well as allowing for a lower sputtering rate.

This was also performed using the 'Raith® VOYAGER Electron Beam Lithography System' at the York JEOL Nanocentre by Dr Christopher Reardon. Employing a gas mixture of 1:1.2 CHF_3 to SF_6 under a pressure of 0.04mbar. A 30W plasma is generated resulting in an accelerating DC bias voltage, at the stage, of 180V. This resulted in an approximate etch rate of 1.8nm/s which was applied for 2 minutes and 10 seconds to ensure the device layer (220nm Si) was completely etched through. Remaining resist was then removed with solvents.

3.3.4 Wet Etching

Wet etching is the process of immersing a sample into a liquid bath of a chemical etchant. The exposed surface is then etched away. Control over the etching time as well as deliberate surface exposure (though other methods such as reactive ion etching) results in the ability to create patterns of etched material of a desired shape and depth (48).

Hydrofluoric acid (HF) was used by Dr Christopher Reardon because it is the only etchant capable of efficiently etching through amorphous SiO_2 but does not affect Si. However it is well noted for having significant problems with over-etching, where the HF will etch at the material beyond what is desired (49). Control of this over-etching is difficult and was largely compensated for by producing multiple samples.

3.4 Supplementary Techniques

3.4.1 Scanning Electron Microscopy

Scanning Electron Microscopy (SEM) uses a beam of electrons fired from an electron gun down a central column which is then focused by a series of magnetic lenses. This imaging beam can then be scanned over the surface of a sample and the resulting electron scattering can be examined in a number of different detectors to learn about various surface properties including topographical and material information. SEM is a highly effective and relatively quick way of producing high quality images of small-scale devices. It was used throughout this project to quickly examine large numbers of Si fishbones to ensure they had been fabricated as expected.

As shown in Figure-3.17 SEM's typically have a number of in situ detectors which allow for several different types of images. However, only LED was used for examination during the course of this project.

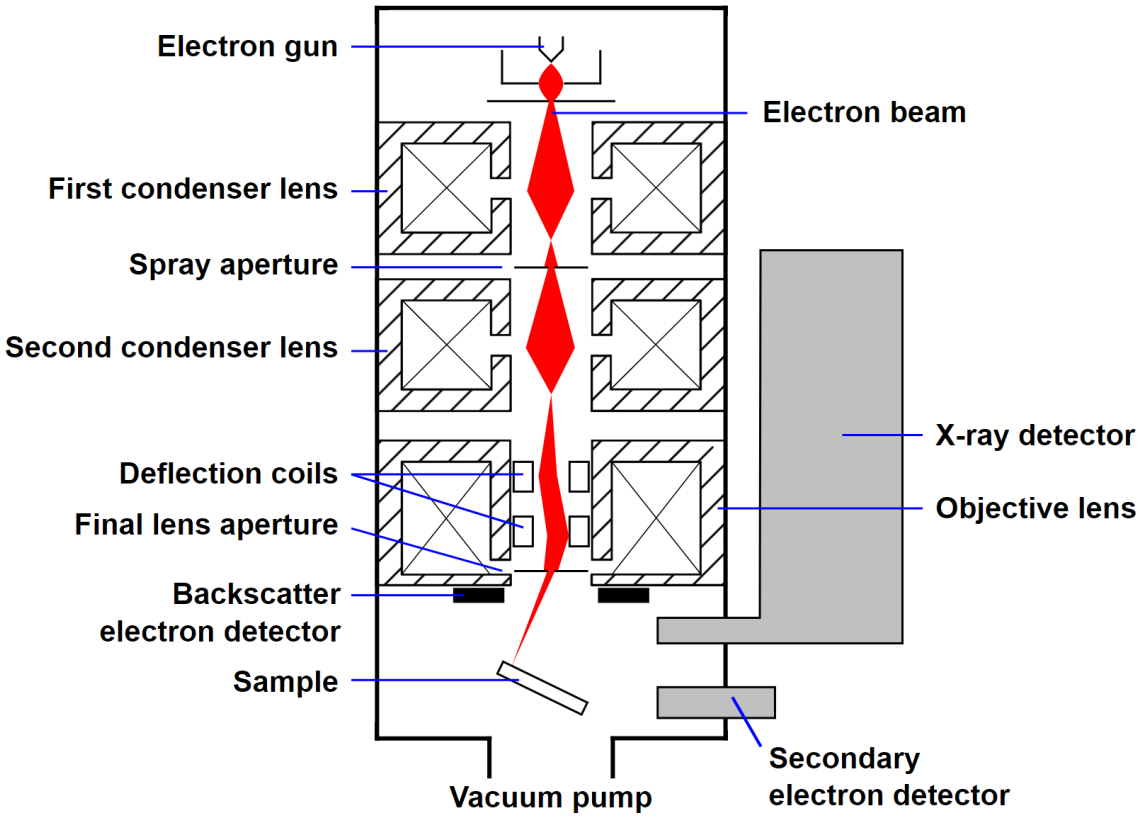

Figure-3.17: Schematic diagram of SEM with important components labelled. (Reproduced from reference (50)).

Low Energy Detection

Low energy detection, also known as secondary electron detection, uses the inelastic electron scattering caused by the sample. Secondary electrons are of much lower energy than seen from back scattered electrons (another form of SEM imaging) and are primarily affected by the topography making it the primary mode for surface imaging.

All of the SEM imaging performed for this project took place on the 'JEOL® 7800F Prime Scanning Electron Microscope' located in the York JEOL Nanocentre. Examinations were typically performed at an approximate working distance of 10mm at 15kV beam strength and imaged using low energy detection.

3.4.2 Contact Bonding

Contact bonding allows for the making of electrical connections on small scale circuits. The technique is widely used on printed circuit boards and integrated circuitry.

There are a number of different ways of producing contact bonds with one of the most common being 'Wedge Bonding'. Wedge bonders use a thin wire (typically Au) threaded through a wedge-shaped tip. The tip is then pressed down to a surface where pressure and ultrasound is used to heat and melt the wire which results in it becoming bonded to the surface.

This bonding process is then repeated at multiple bonding sites before the thread is broken off leaving behind a completed wire. This process is shown in Figure-3.18

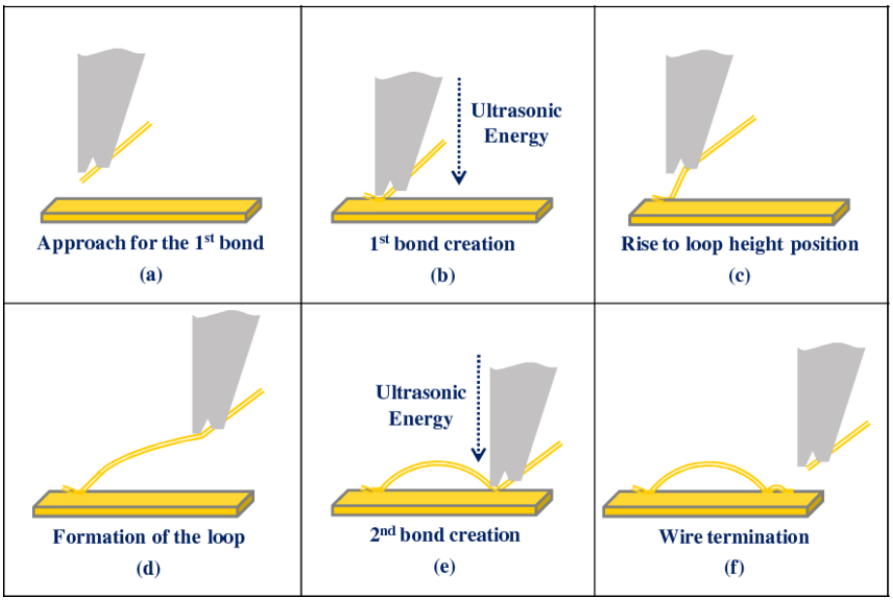

Figure-3.18: Diagram of wire bonding creation process. (Reproduced from reference (51)).

The wire bonding machine used in this project for wiring up some of the microheaters was the K&S 4532/6 Manual Wedge Bonder with a Au wire. However, as this device did not always work, manual bonding using indium (In) wire was performed instead for most devices.

Contact bonding with In wire uses the same technique but takes advantage of the relatively low melting point of In (157ºC) to allow the use of pressure produced by hand to form the contact bonds.

3.5 COMSOL Modelling

COMSOL Multiphysics is a finite element modelling software which focuses on using GUI elements to allow for quick and easy construction of simulations (52).

3.5.1 Basic Function

COMSOL is a broad-use simulation software package and a brief descriptor of the order of how a simulation is constructed is given as this can be different from some more specific simulation programs.

Simulation Construction

First a geometry of some kind is created as the basis for a sample. This is then given physical properties such as thermal conductivity, electrical resistance, and density. These values can be set automatically by importing a material and/or can be individually varied. Any series of different geometric parts and properties can be then put together to match the experimental design.

For this model the experimental samples (or simplified approximations thereof) were created. For the most part the physical constants were defined by the default material values from the COMSOL library. However, where these were known to be different or were deliberately altered (such as the κ value) these were changed.

Applied Physics

Physics modules can then be applied to the system. This allows for only the interactions desirable in the simulation to be included, reducing the complexity of the simulations. For this project a heat transport module was used to model the heat flow through the system and an electrical module was used for the joule heating found in the microheater and the SThM tip.

Study Selection

Following on from the construction of the sample, different kinds of study can be chosen. In this instance the model was simulated as a series of steady state slices over time.

3.5.2 Repeated Project Specific Elements

A number of the project specific elements used in COMSOL were shared between the different experiments and are described briefly here.

SThM Tip Design

As the experimentally recorded thermal data comes from a reading of the SThM tip as opposed to a direct reading of the surface temperature and this interaction is important and complex it was decided to model the tip/sample interaction. Whilst it is possible to recreate the entire tip and cantilever system to form a more accurate tip model this is computationally expensive and was not deemed necessary.

Instead, only a small portion of the broader tip (shown in section 3.1.2) which comes into direct contact with the surface was modelled. The tip consists of a 100nm radius semicircle constructed of an Si_3N_4 core of 40nm radius, an inner layer of 80nm radius Pd and a final outer shell of Si_3N_4 as shown in Figure-3.19.

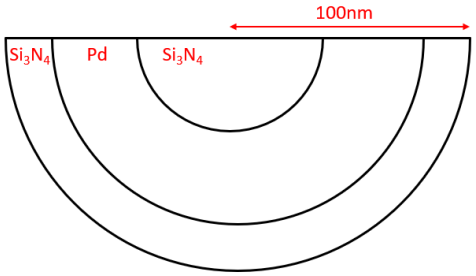

Figure-3.19: 2D side cross-section of simplified COMSOL AFM tip showing different material layers.

A small current is then supplied to the Pd layer which causes some joule heating forming an initial tip temperature. The volume average temperature of the Pd layer is then recorded as it alters due to the tip's contact with the surface. When this tip is expanded out into 3D as shown in Figure-3.20 the semicircle is converted into a hemisphere.

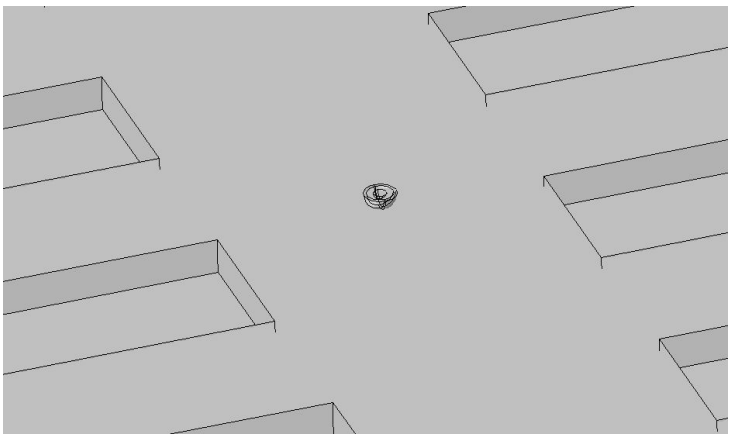

Figure-3.20: Image of 3D COMSOL simplified AFM tip on Si fishbone.

SThM Tip Movement

As with the experiments this tip can then be 'moved' across the surface. This entails a repeated simulation with the tip in contact with a different part of the sample. From each point a different tip temperature can be extracted.

For flat surfaces a simple parameter set of tip position in a straight line across the surface is sufficient. However, for more complex surfaces such as ones which are curved, instead that surface first needs to be mapped out as a series of points which are then used as a coordinate table for the tip to follow.

Chapter 4

Thermal Transport

In this project the SThM is used to examine the relative surface temperature of a variety of materials and is attempted to be used to examine thermal properties. Hence it is important to consider what thermal transport within materials, especially those considered here, is like and how it can be affected.

Thermal energy is a type of energy which is manifest as the movement of particles. The higher the temperature the greater the thermal energy and the more movement is occurring. In gases or liquids where molecules are free to move around the thermal energy is carried by these molecules as they move through the bulk substance. However, in a solid this is not possible due to the constituent atoms being held in place within the structure.

Solid materials transport heat through heat carriers. In metals and semiconductors this can be done through the free electrons (or holes) which are able to act as thermal carriers as well as electrical carriers. In semiconductors and insulators, however, phonons are the dominant method of heat transport. Phonons are a way of quantising a collective vibrational excitation between atoms of a solid structure. These are quasi-particles which help represent how thermal energy can be transported through the structure of a material as a wave (53). Phonons are the primary thermal transport method in insulating materials and are the dominant method in semiconductors. Phononic thermal transport is also present in metals but is typically very small compared to that in semiconductors or insulators.

4.1 Thermal Conductivity

Thermal conductivity (κ) is a measure of a material's ability to transport thermal energy through it. That is to say a measure of how freely the thermal carriers can move through a material. The higher the thermal conductivity value, the better a material is at transporting thermal energy where heat flow is defined as:

$$\dot{Q} = -\kappa \nabla T \tag{4.1}$$

where $\dot{Q}$ is the heat flux, κ is the thermal conductivity and ∇T is the temperature gradient.

A given value for a material's thermal conductivity is made up of the contribution from both phonons and electron/holes with the relevant contribution of each varying between materials. There can also be a number of different conductivities in different directions through a structure depending on materials and anisotropies.

The primary factor on the thermal conductivity for a material is the amount of scattering of the charge carriers. Any form of scattering slows the group velocity of the carriers and thus reduces the conductivity of the material. There are however a number of different factors that cause scattering within a material.

4.1.1 Phonon Dispersion Curves

One way to examine phonons within a material is through the use of phonon dispersion curves. In these graphs such as the one shown in Figure-4.1 each line shows the dispersion of a particular phonon (i.e. a natural mode of the structure) along a wave vector.

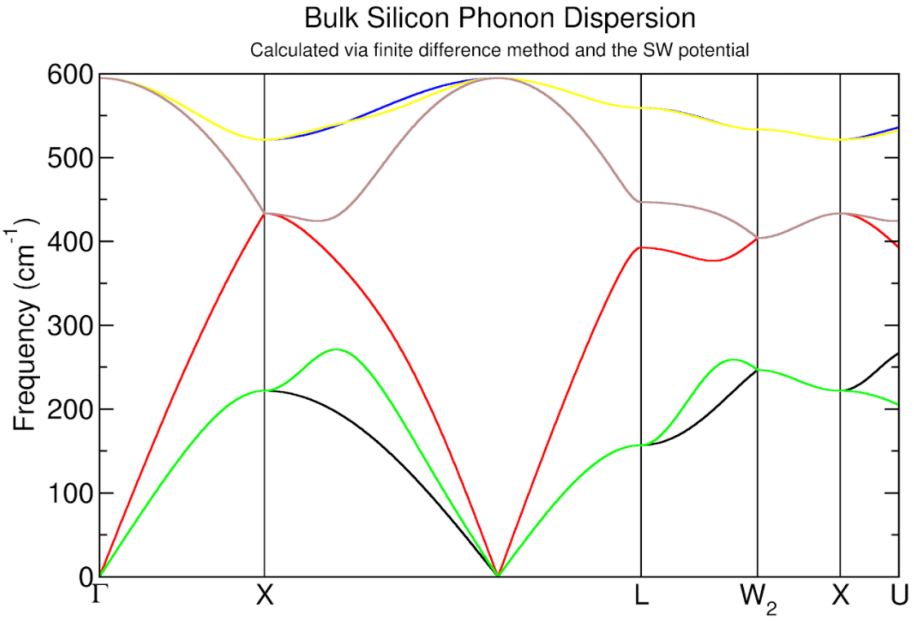

Figure-4.1: Phonon dispersion curves for silicon calculated using the Stillinger-Weber potential. (Provided by Ben Durham).

Each wave vector in the phonon dispersion represents the phase of vibration between a unit cell and its neighbour along an axis of high symmetry in the Brillouin zone as shown in Figure-4.2. At the centre of the zone (Γ) the unit cells are in phase and at the extremity (such as X or L) the unit cells are 180^0 out of phase.

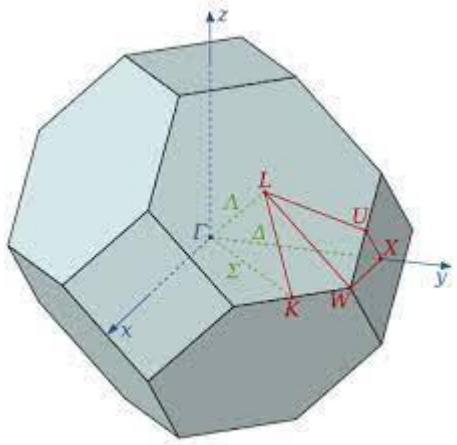

Figure-4.2: Diagram of the Brillouin zone with axes of high symmetry marked. (Reproduced from reference (54)).

Each line within the diagram is a measure of the frequency (or energy though the equation $E = hf$) of an individual natural mode of the cell as the phase changes between the two extremes. Typically, the presence of each atom will result in three natural modes for a total of 3N phonon modes where N is the number of atoms, however some of these can be degenerate meaning that they match other phonon modes. These are some of the main travelling modes which carry energy along the wave vector. In this case they represent the travelling waves of the phonons along the plane of the Si material.

The important feature of the phonon dispersion curves for the thermal conductivity is the group velocity of the phonons. This can be determined from the average gradient of the curves. The greater the gradient of a curve is the higher the group velocity of phonons of that wavelength.

4.1.2 Temperature

The mean free path of a carrier is the average distance which the particle will travel before it undergoes a random scattering event due to a collision with the material structure. As the temperature of a material increases the lattice vibrations increase which increases the chance of scattering and reduces the mean free path. A

shorter mean free path results in more scatter events and thus a lower thermal conductivity as can be seen in Figure-4.3. This same phenomenon can be found for electrical conductivity due to the increased scattering of the charge carrying electrons within metals. However, for semiconductors the electrical conductivity can rise with temperature as more electrons are excited into the conduction band.

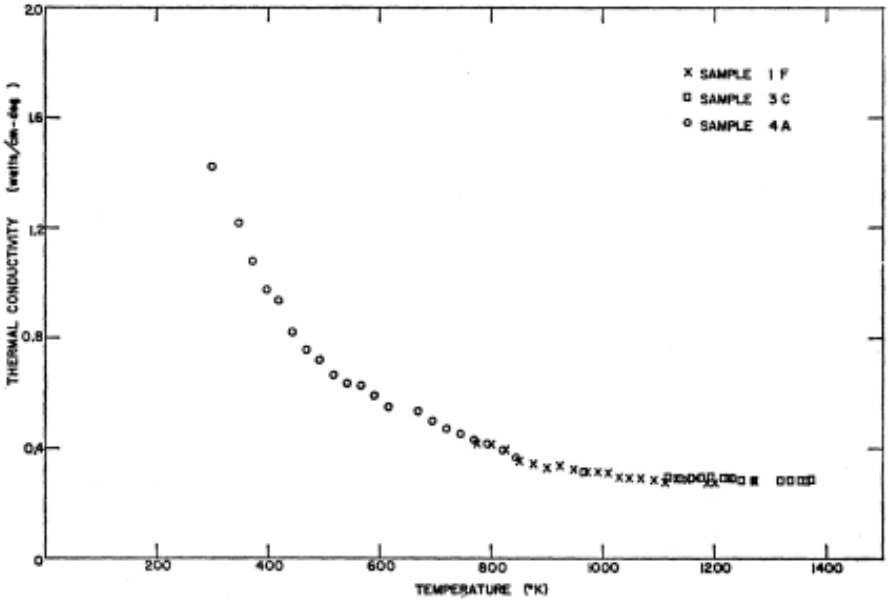

Figure-4.3: Graph of experimental results of silicon showing that thermal conductivity drops as temperature increases. (Reproduced from reference (55)).

4.1.3 Defects, Interfaces and Roughness

Considering a carrier travelling through a material, it is best able to do so through a continuous and regular structure which will result in the longest mean free path. Any change in the structure will cause an increased chance of scattering and thus a lower thermal conductivity. This is why crystalline structures have a higher thermal conductivity than amorphous ones (56).

Crystalline structures can have their thermal conductivity affected by scattering from things like lattice mismatch if the material is not single crystal. Any grain boundaries will have a significant impact. Defects in a structure can be intentional from the material's composition or unintentional as a result of things like oxidisation or contamination which result in potential scattering sites.

Interfaces

Another important scattering site is at interfaces. This could be the material interface with the atmosphere/vacuum or with another material which it is connected to. The change in material results in increased scattering which is represented by an interfacial resistance which is defined perpendicular to the interface as:

$$\dot{Q} = G_I \Delta T \tag{4.2}$$

where $\dot{Q}$ is heat flux, G_I is the interface conductance and ΔT is the temperature difference between the two surfaces. The calculation of this conductance is not however trivial. Typically any attempt to determine the interfacial conductance requires the use of sophisticated computer modelling (57) which replicates an interface and examines temperature differences across the interface.

When considering an atmospheric/vacuum interface the interaction is a little more difficult. In short, for a flat surface a carrier may be able to specularly reflect from the surface back into the material with little impact. A rougher surface instead can cause the phonons to be scattered diffusely causing them to be thermalised at the surface and/or random scattering where the energy is lost and thus reducing the thermal conductivity further (58).

Depending on the involved materials the interface may also become more chemically complicated. Chemical mixing (such as oxide formation) may create a more diffuse interface which is a different material further adding potential scattering sites.

Contact Roughness

The roughness of the material can also be a large factor when considering the tip and the sample contacting each other which prevents thermal transport between the two.

When considering the surface contact between two different layers the material's roughness can result in a significantly smaller contact area and thus lower area for thermal transport between the two materials. As shown in Figure-4.4 this happens due to a mismatch in the atomic scale contact of the two layers.

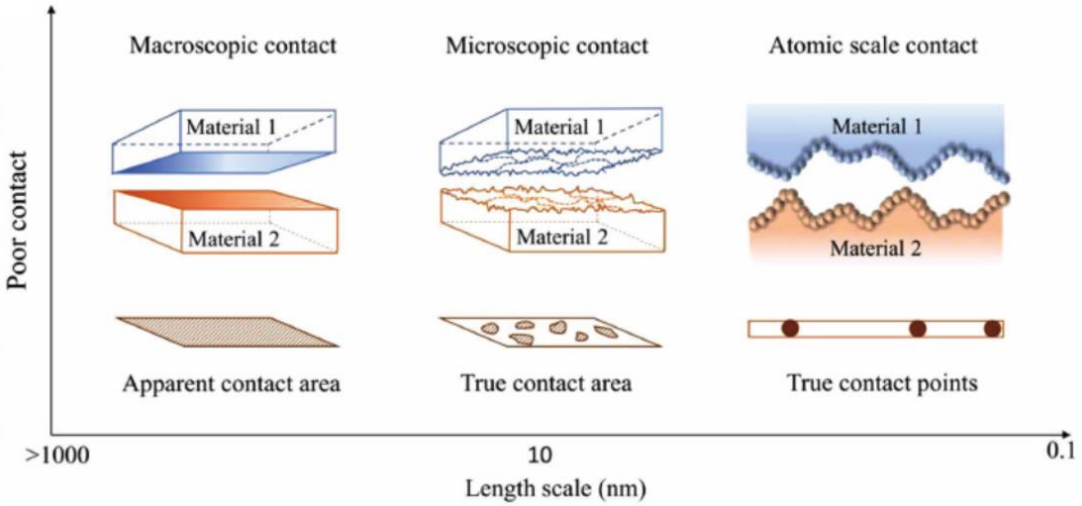

Figure-4.4: Diagram of contact between two solid materials at different length scales showing apparent and true contact. (Reproduced from (57)).

As mentioned briefly in Chapter 2 this non-perfect contact results in less thermal conduction across the boundary because there are fewer contact points which the phonons are able to travel through.

4.1.4 Size Constraints

As a material becomes more and more physically constrained by a reduction in the size this can affect the thermal conductivity. This is because there is an increasing surface-to-volume ratio which results in a greater amount of surface scattering.

As the width of a material is reduced, the chance of the phonon interacting with the edge of the material as opposed to a phonon-phonon interaction increases. As phonon-phonon interactions are more likely to be elastic than one with a defect or interface this reduces the energy present for thermal transport. Additionally, this higher chance of collision will cause a natural reduction in the mean free path.

Significantly constrained materials such as thin films also often have a larger number and density of defects in their structure than bulk materials. This is usually due to how they are constructed, often through sputtering. Once again this increases the scattering. These different factors result in a general decrease in the thermal conductivity of any material as it becomes more geometrically constrained as shown in Figure-4.5.

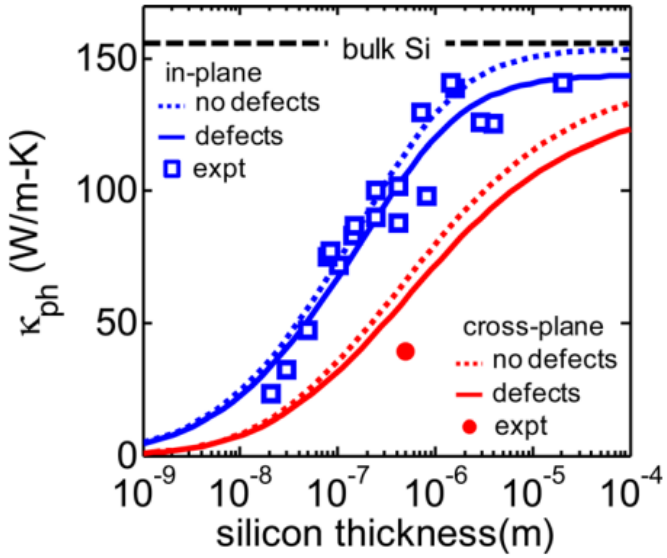

Figure-4.5: Graph of thermal conductivity against silicon layer thickness showing computational model and experimental data. (Reproduced from (59)).

Figure-4.5 is an important collation of information which deserves some further attention. As mentioned, it clearly shows that as the thickness of the Si is decreased both the in-plane and cross-plane thermal conductivities drop. This is important as the material thicknesses used in this project vary between the 10^{-9} to 10^{-6}m range where it is clear that there is a significant effect.

4.1.5 Thermal Conductivity of Used Materials

In this project a range of different materials are used. It is worth considering first what these materials are and their relevant properties. Table-4.1 below shows the thermal conductivity values which were used in the COMSOL simulations which were taken directly from the COMSOL material library.

Material	κ Value (W/m•K)
Al_2O_3	35
Cu	401
HCD	780
SiO_2	1.4
Si	130
Pd	71.8
Si_3N_4	20

Table-4.1: Table of thermal conductivity values used in COMSOL multilayer simulator.

Al_2O_3 – Aluminium Oxide

Aluminium oxide is a ceramic with a relatively high thermal conductivity and low electrical conductivity and dominated by thermal phonon transport. Bai et al. (60) suggest that the thermal conductivity of aluminium oxide could reduce by approximately an order of magnitude when in a thin film state between 1µm and 300nm but at this scale is not size dependent. This might be because the small grain size of the ceramic means that the grain scattering is completely dominant. However, it might be expected that at even thinner layer sizes the thermal conductivity would continue to decrease.

Cu – Copper

Copper is a metal, where electrons are the dominant heat carriers. P. Nath and K. Chopra (61) showed that copper is at its bulk thermal conductivity value up to around 500nm but that producing a thin film to a thickness of 100nm reduced the thermal conductivity by around 75%. Copper also has large grains and is highly susceptible to oxidation. Oxidised copper can be a highly variable material with a number of different compounds depending on the length of exposure. However all of the possibilities have a highly reduced thermal conductivity (on the order of 50-70W/m.K) due to becoming insulators which lose the free electron transport.

HCD – High Conductivity Dielectric

This is a dielectric material notable for its high thermal conductivity from phononic transport which cannot be identified due to a non-disclosure agreement with Seagate. It is often used in a thin film for phononic waveguides and other such devices due to the high phononic transport. Because of these properties there have been considerable examinations into improving the thermal conductivity through methods such as changing the material's structure and doping the material.

SiO_2 – Silicon Dioxide

Silicon dioxide is a widely used insulator which results in very little thermal transport which is carried almost exclusively by phonons. Yamane et al. (62) suggest that silicon dioxide remains around bulk thermal conductivity until around 500nm and begins to rapidly decay around 200nm. However, Schafft et al. (63) suggest this could start occurring much earlier at thicknesses several microns thick.

Si – Silicon

The thermal conductivity effect of the thickness of silicon has already been shown in Figure-4.5. In this project the silicon used is assumed to be single crystal silicon and thus have no grain boundaries except in the case of random defects. Si is dominated by phonon transport which is a key factor in why it has been chosen in this project as it allows for κ modification without significantly affecting electrical conductivity.

4.2 Phononic Thermal Transport

Phononic thermal transport is a complicated process and is usually approached using computational modelling. For this project simulation work was performed by Dr Phillip Hasnip and Ben Durham from the University of York.

For performing the simulations of phononic transport there are a few different types of modelling which can be used in order to simulate the phonon transport in a silicon structure. This can also then be used to examine how this transport can then be changed through the introduction of nanostructures which aim to use phononic resonance to impede the phonon transport and reduce the thermal conductivity of the material.

First principles modelling would use a simulation to effectively solve the Schrödinger equation for the model of the fishbones. However, whilst accurate, this is incredibly computationally expensive and is not appropriate for a first pass at simulating these kinds of structures.

Instead, a simplified approximation of the results of the Schrödinger equation can be used through another kind of modelling such as molecular dynamics. This instead simulates a physical system of particles and examines how they are affected by changes.

For the simulations in this project however a lattice dynamic model using the Stillinger-Weber potential was used. This limits the computation of the modes of a crystal to a low order (in this case 3rd) as opposed to a full molecular dynamic system which models the higher orders. Whilst this means that the simulation is less accurate the majority of the transport contribution comes from the first three

modes. Additionally a full molecular dynamics simulation requires that the entire system be simulated completely periodically. This means that any change in a simulated unit cell must be repeated in the next cell (e.g. the movement of an atom) whereas the lattice dynamics allows for a phase difference between the cells. Constructing the model in this way additionally allows for the structure to have phonons with wavelengths longer than the unit cell which can be a significant restriction for other types of simulation.

Once the interatomic forces have been calculated as a force constant matrix through a lattice dynamic Stillinger-Weber simulation these can then be used in a solver for the Boltzmann transport equation to be made into lateral thermal conductivities for the structure.

4.2.1 Theoretical Models

As the simulation work was performed by collaborators in this section only a basic overview of the processes is included.

Stillinger-Weber Potential

Stillinger-Weber is a method of calculating the interatomic potential energy of atoms within a structure (64). Stillinger-Weber is a force field model whereby the positions of individual atoms and the forces they impose on one another is simulated. Then atoms are moved and the effect this has on the forces between them and other atoms is calculated.

Crucially, the Stillinger-Weber model uses a term based on the distance between two atoms and a term based on the angle between three atoms. This is what allows for the sp^3 angles of the Si atoms to be modelled, creating the silicon diamond structure. Stillinger-Weber was chosen as it is a standard modelling type which offers a good compromise between accuracy and computational cost.

Boltzmann Transport Equation

The Boltzmann transport equation is a statistical model of a thermodynamic system which is not in equilibrium which can be applied to a wide range of different systems. Here it is used as a drift diffusion model to calculate the effect of the change in the phonon modes on the group velocity of travelling phonons.

It is worth noting that this is a semi-classical model so it does not include coherence effects, which are discussed later. However, as the Boltzmann transport equation is only being used to examine the effect along the length of the shaft (which is significantly beyond any coherence lengths) this is not considered to be an issue.

4.2.2 Simulation Method

One method to calculate the thermal conductivity is to solve the linearised Boltzmann transport equation (LBTE) for the phonons in the material (65). Here this was done using ShengBTE code (66), however, this first required calculations of the systems 2nd and 3rd order interatomic force constants (IFCs). The workflow is shown as a flowchart in Figure-4.6.

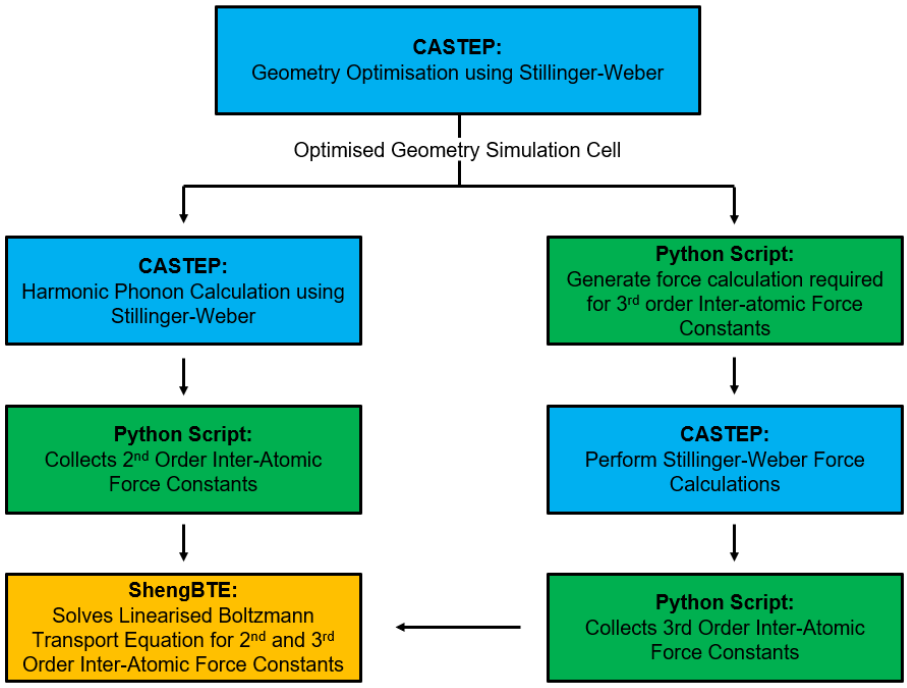

Figure-4.6: Flowchart describing the simulation workflow to take the CASTEP geometric model and output thermal conductivity from ShengBTE. Blue denotes CASTEP simulation steps, Green for custom python scripts and yellow for ShengBTE.

CASTEP (67) is a first principles model for calculating material properties. It is first used to optimise the geometry of the model by finding the structural equilibrium of the system which minimises the interatomic forces. This is done by moving each atom along the three directions until its maximum force on any other atom in the structure is below a set tolerance.

CASTEP can then be used to perform a phonon calculation using the finite displacement method wherein each atom is displaced along each of the three directional degrees of freedom and the resulting force is determined as the 1st order IFC. The movement of a second atom after the first causes a force on the initial atom which results in a 2nd order IFC for the pair, and this is further scaled to a 3rd order IFC for a displacement of three atoms. The 2nd order terms represent the harmonic phonons and the 3rd order the phonon-phonon scattering.

CASTEP then uses an inbuilt Stillinger-Weber harmonic phonon calculation for the 2nd order IFC but for the 3rd order terms another code is first used to determine the symmetry and dramatically reduces the number of calculations required for solving. A cut-off distance is also implemented known as the 'Stillinger-Weber cut-off' beyond which the interatomic forces are assumed to be 0. In CASTEP this value is set as 0.377118nm.

The 2nd and 3rd order IFCs are then collected by a pair of python scripts which then feed into the ShengBTE script. ShengBTE then calculates the lattice thermal conductivity tensor using the LBTE. However, it should be noted that as the Stillinger-Weber does not include any consideration of electrons, the resulting κ is only the phononic contribution.

4.3 Phononic Resonance and Hybridisation

Within the Si fishbone experiments discussed in Chapters 6 and 7 the aim is to increase the figure of merit ZT of the material which is defined as:

$$ZT = \frac{S^2\sigma}{\kappa}\mathrm{T} \tag{4.3}$$

as defined in section 1.1. To do this one of the simplest ways is to reduce the thermal conductivity (κ) of the material. As the fishbones are made of silicon the heat transfer is dominated by the phonon transport.

One of the easiest ways to attempt to reduce the thermal conductivity would be to introduce more defects, interfaces, and roughness to the Si in order to increase the amount of phononic scatter, and indeed this is a method which has been worked on by a number of groups (68) (69). However, increasing the scattering of the phonons

will also increase the scattering of the electrons and thus reduce the electrical conductivity (σ) which will reduce the overall figure of merit. As such it is desirable to attempt to be able to find a method which results in a slowing, scattering or otherwise reduction of the transport of phonons through the silicon without affecting the electron transport.

Nanophononic Metamaterials

Nanophononic metamaterial is a term coined by Honarvar and Hussein (70) for a material which contains nanoscale resonating substructures. These are built onto a semiconducting material in order to reduce the phonon group velocities of the travelling phonon modes as well as populate a large number of localised modes to reduce the thermal conductivity. This notably should have little to no effect on the electrical conductivity of the material.

These resonant structures are designed to cause coupling within the thermal transporting phonon modes. This coupling causes a resonance hybridisation between the phonon mode and the structure which causes the phonon dispersion curves for said mode to be flattened out which implies a reduction in the group velocity (71). This can also potentially cause a totally flat line which would suggest that phonons of said mode would become trapped in the resonant structure as a standing wave and be dispersed. Both of these can cause the desired thermal conductivity reduction.

Increasing the size of the phononic resonators significantly increases the number of atoms within the structure and thus the amount of phonon modes it may be able to hybridise with. Longer structures are also able to support longer wavelengths which are the lower energy modes ($<$150-200 wavenumbers, given in nm^{-1}, at room temperature) which are most important for thermal transport.

Phononic Hybridisation

When two lines on the dispersion curves cross this tells us that the phonon states are degenerate. This means that there is no energy cost to the phonon changing its direction of travel as the wavefunction is equally as viable with any combination of X and Y velocities.

Within these diagrams a flatter curve is better, this is because it has a lower average gradient and thus a lower group velocity. This hybridisation is important

because it results in avoided crossings of the phonon modes. This forces the dispersion curve to reverse direction which causes a significant reduction in the average gradient and thus phonon group velocity.

Phonon Coherence

Phonons are a kind of wave which means that they have assorted wave-like properties including interference (53). Resonant structures are able to create coherent patterns of phonon waves. However, after a number of successive scattering events from defects, boundaries or even some kinds of phonon-phonon scattering, phonons tend to have their phase changed relative to others and thus become incoherent (72).

This is an important factor to consider for the resonant structures, as whilst a larger structure may result in more phonon modes, one which is too large could result in phonon incoherence and thus removing the desired effect. This means that structures should likely be kept below several mean free path lengths in order to avoid incoherence, for Si we can estimate this to be about 3µm.

4.4 Other Computational Work on Resonators

The idea of using nanophononic resonators as a way of reducing the thermal conductivity of silicon is not unique to this group. A number of others have also considered methods of examining such an effect.

4.4.1 Stillinger-Weber Calculations

Mahmoud Hussein from the University of Colorado, Boulder has performed a significant amount of computational work on these kinds of structures. His computational work also uses Stillinger-Weber calculations of the kind used in this project.

Early work by Hussein et al. (73) in Figure-4.7 shows three different nanostructures. In black, a Si membrane 6x6x6 cubic cells in size, in blue, the same membrane with a 2x2x6 cubic cell resonator placed on top, and, in red, the same membrane with a larger 4x4x12 cubic cell resonator. These are then scaled by the scaling factor ‘a’ in all dimensions.

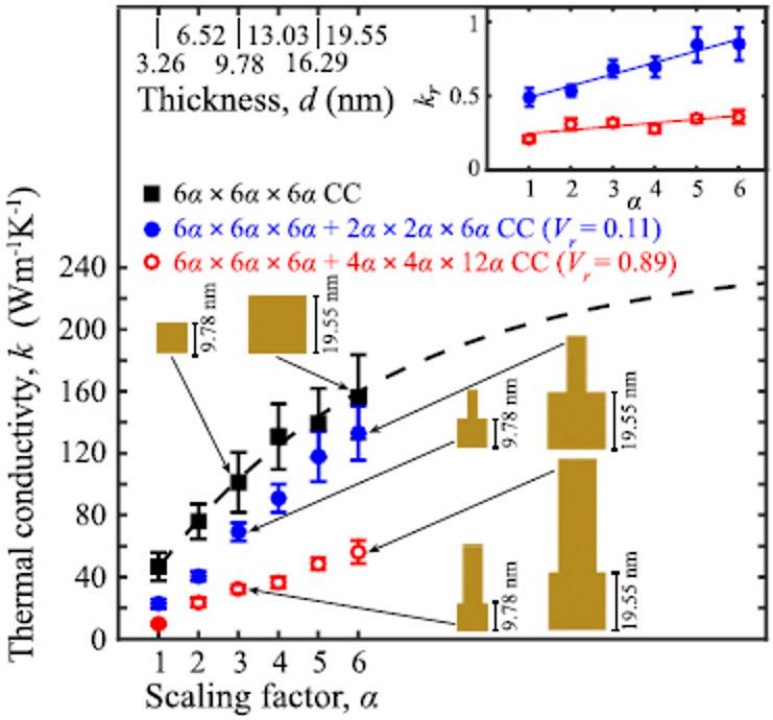

Figure-4.7: Graph of thermal conductivity of pillar on membrane simulations of different pillar sizes (indicated by colours) as the structures are scaled in size. (Adapted from (73)).

Comparing the different structures in Figure-4.7, it is clear to see that the presence of a resonator decreases the resulting thermal conductivity value. Additionally, increasing the width and height of that resonator further reduces the resulting thermal conductivity. However, it also shows that when the structures are increased in scale the thermal conductivity rises. This is shown in the top right which shows κ_r which is the ratio between the thermal conductivities of the membrane with the resonator and the plain membrane. Continuing from this, later work by Hussein and Honarvar (70) found that by further optimising the conditions of the model (such as introducing a second series of pillars on the opposite side of the membrane) they could obtain a two orders of magnitude reduction in thermal conductivity compared to a membrane with no resonators.

One of the major issues with this work is that these simulations scale everything at the same time. This means that it is difficult to pick out the contributions of the different resonator parameters to determine what is causing the thermal conductivity reduction.

4.4.2 Nonequilibrium Molecular Dynamic Simulations

Ma et al. (74) simulated graphene nanoribbons with a series of phononically resonant pillars as seen in Figure-4.8. This was performed using the LAMMPS molecular dynamics simulator (75) which uses a Tersoff potential (76) to calculate nonequilibrium molecular dynamic equations.

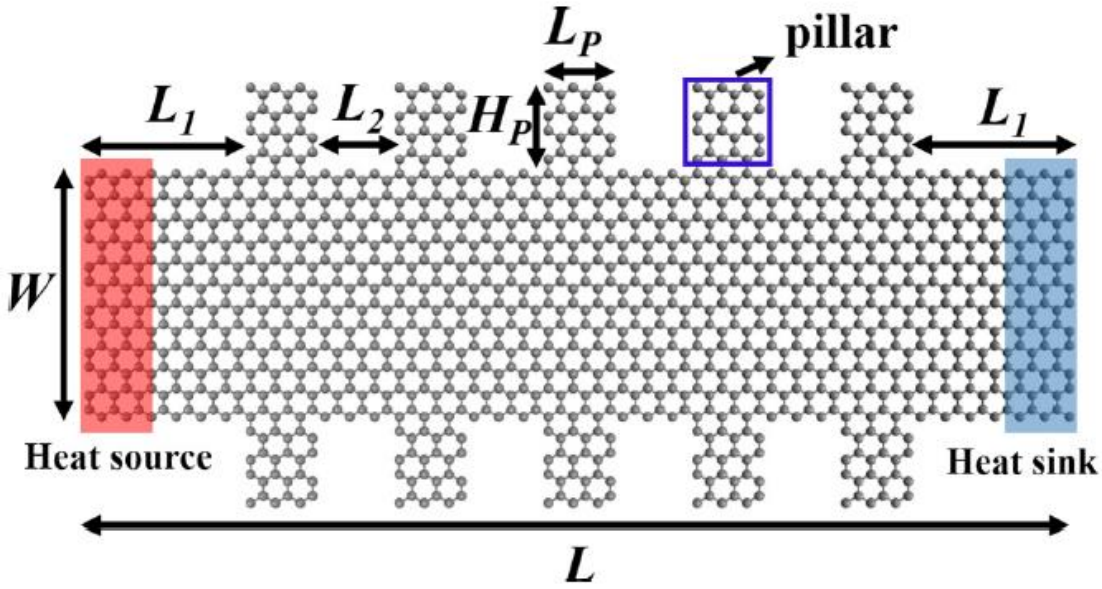

Figure-4.8: Diagram of graphene nanopillared membrane made from a graphene nanoribbon with pillars placed on either side and a heat gradient placed across it. L=80nm, L_1 =1.62nm, L_2=0.87nm, and L_P =0.62nm. (Reproduced from reference (74)).

As can be seen in Figure-4.9 the presence of the pillars on the nanoribbon causes a significant reduction (>55%) in the thermal conductivity. Additionally as the height of the pillars was increased, or the width of the ribbon was reduced this change in thermal conductivity became larger. It is important to note that it is not known if/how much of the thermal conductivity change from the increased width comes from a reduced amount of surface scattering due to less geometric constraint as opposed to less of an influence from the resonators.

This is an important result because it is a completely different method of simulation than that used in this project. This shows similar trends can be seen across the different types of simulations which can increase our confidence in their results.

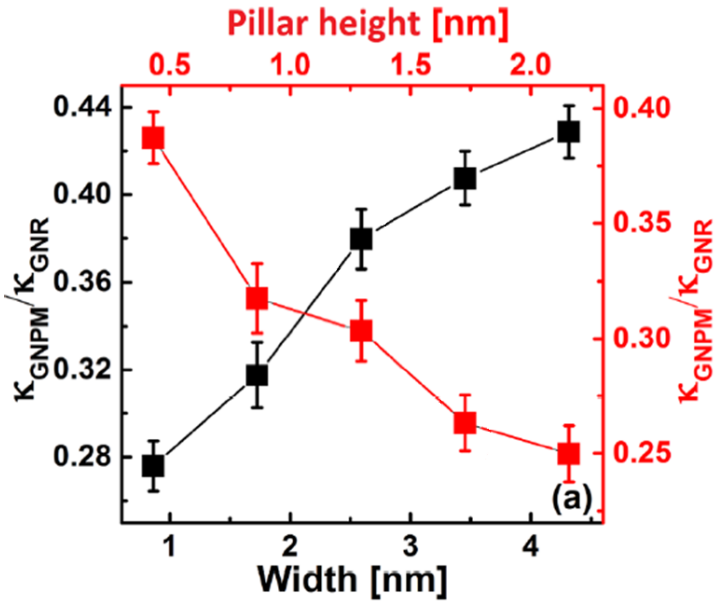

Figure-4.9: Graph of ratio of thermal conductivity change between pillared and non-pillared graphene nanoribbons for changing pillar height and width of ribbon. Y-axes are a κ ratio between the material with the graphene nanopillared material (GNPM) and the plain graphene nanoribbons (GNR). (Adapted from (74)).

4.5 Phononic Resonator Simulations

Simulations were performed by Ben Durham and Dr Phil Hasnip from the University of York using CASTEP (67) and ShengBTE (66) in a separate but related project. The project aimed to perform computational calculations of phononically resonant structures with a similar geometric design to the experimentally produced samples in Chapters 6 and 7. Whilst the scale is very different the trends from the computation were expected to be able to inform experimental results.

4.5.1 Simulated Structures

A model structure was designed to introduce the previously discussed phononic resonators onto the material. This was done as a series of structural pillars outcropping from a membrane surface as shown in Figure-4.10.

The basic structural cell measured 8.7x4.35nm. However it should be noted that this was modelled as a repeating structure in both X and Y directions. This means that the extended structure is not a shaft with pillars like the experimental but rather a membrane with ridges (also called nanowalls) as shown in Figure-4.11.

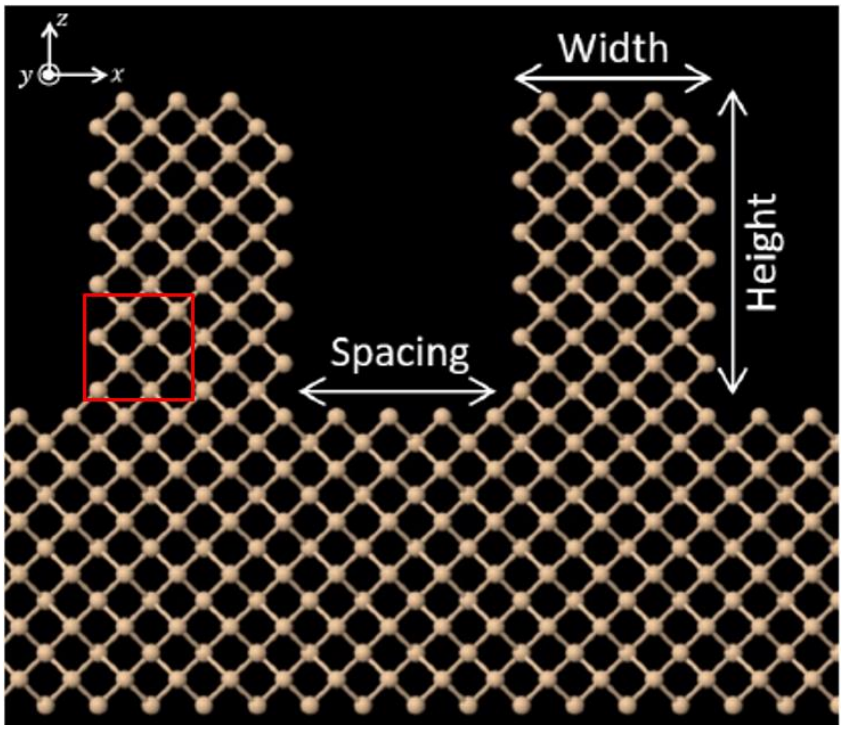

Figure-4.10: Cross-section of CASTEP simulation of Si membrane and resonant structures 2CC wide and 3CC tall designed to induce hybridisation. One cubic cell (CC) is marked in red. (Reproduced from reference (77)).

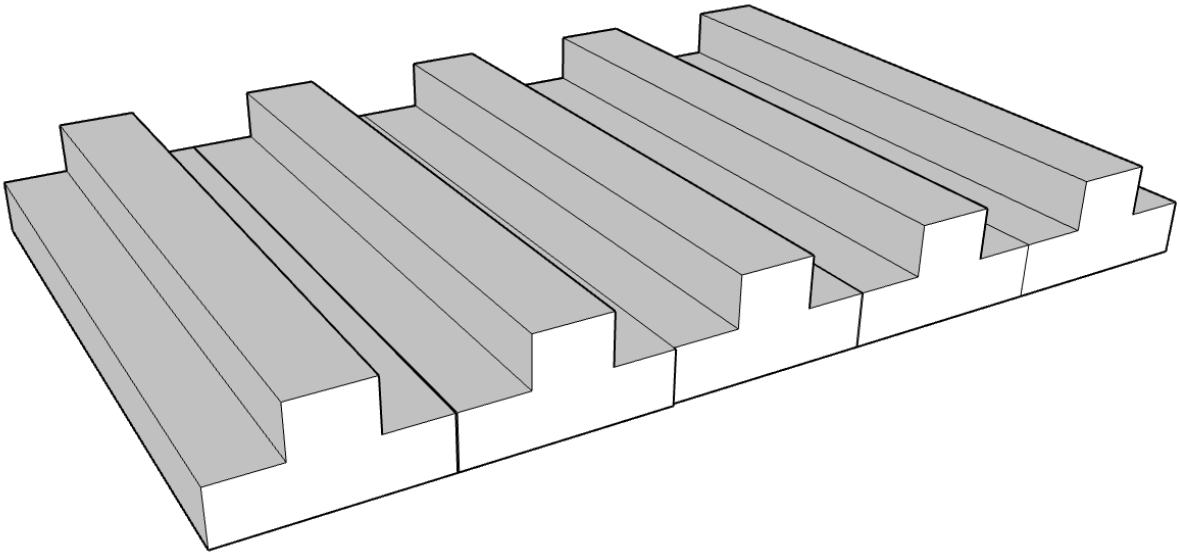

Figure-4.11: Diagram showing the CASTEP model shape as it would appear in 3D projection, i.e. how it is simulated.

Calculations of the 3rd order IFCs scaled at a rate of $27N^3$ where N is the number of atoms. Due to the available resources this limited the simulations to systems of around 300 atoms.

4.5.2 Performed Simulations

Bulk Si Examinations

Before any of the phononic resonator experiments were performed it was thought to first check how the used simulation method results for bulk lattice silicon thermal conductivity compared to experimental data. This is shown in Figure-4.12.

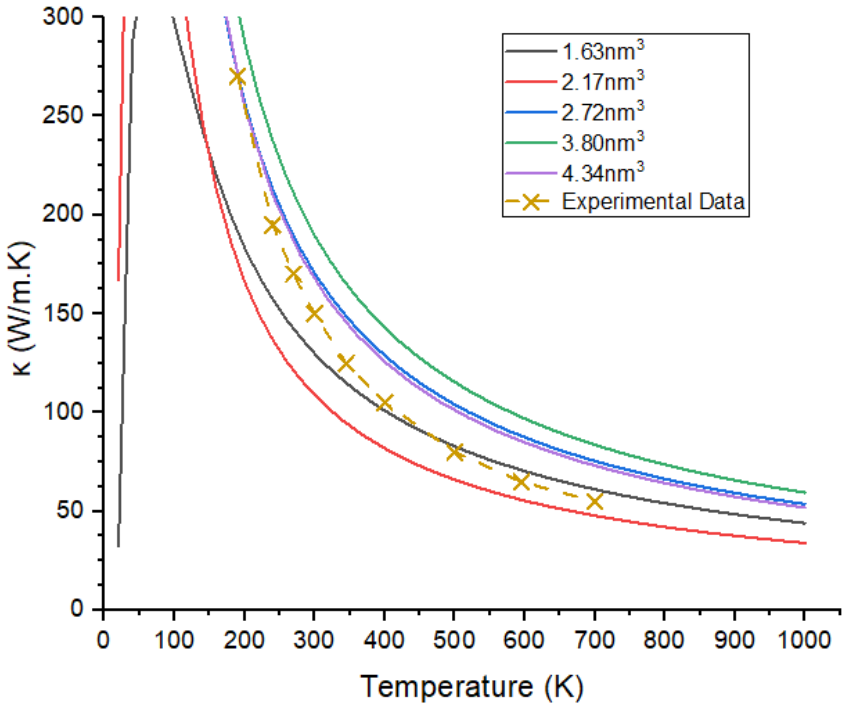

Figure-4.12: Graph comparing CASTEP/ShengBTE simulated results for Si bulk lattice κ of increasing width compared to single crystal experimental data. (Reporduced from (78)).

This shows that the simulations struggle to match the experimental data, likely due to the reduced size and the model assuming a perfect crystal. However the best match is for simulations between 200-300K which is the region where experiments were performed. This further emphasises that the simulated results should not be looked at for accurate κ values but rather trends caused by the resonance structures.

Phonon Hybridisation

The phonon dispersion curve is produced by the CASTEP code and has here been examined as the height of the nanowalls is increased and is shown in Figure-4.13.

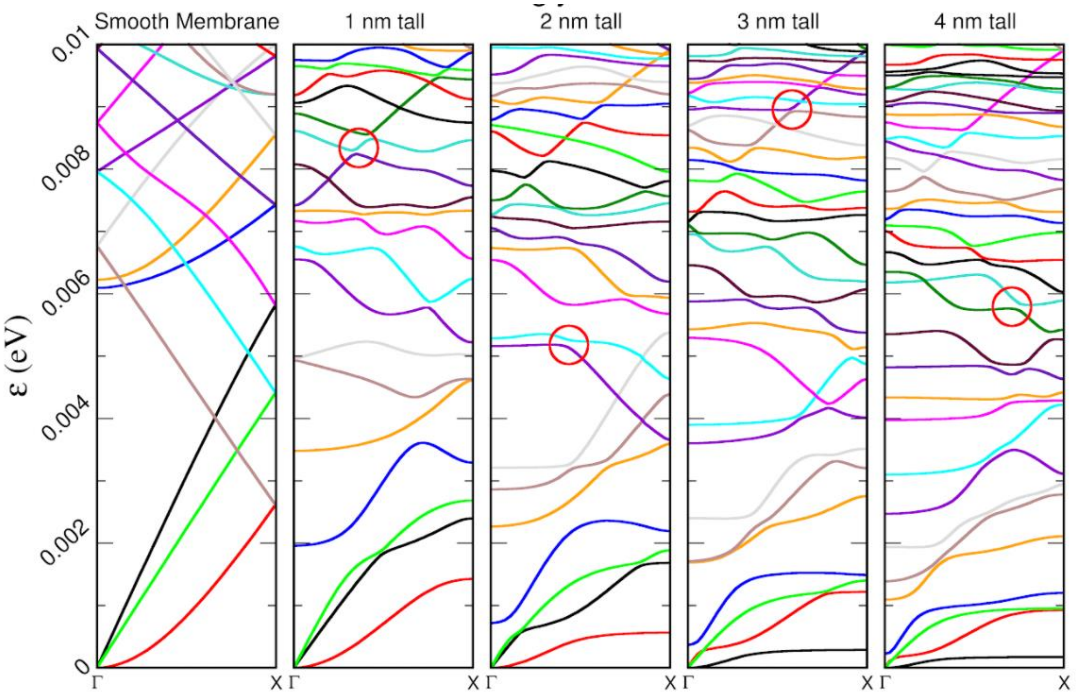

Figure-4.13: Series of phonon dispersion curves for Si membrane with 1.5nm thick Si walls of increasing height. Some of the phonon hybridisation events have been highlighted with red circles. (Reproduced from reference (77)).

It is visually very clear to see that many of the phonon modes flatten as the height of the nanowalls increases. This general decrease in the average gradient of a mode is reflected as a reduced group velocity and thus poorer thermal transport. Also noticeable in Figure-4.13 (and highlighted for ease) are phononic hybridisations where a degenerate state has been avoided resulting in the phonon mode reversing its gradient. This once again results in an overall lower group velocity.

It is notable that within the membrane there is a flexural mode which means that the first mode is not linear as might be expected. As it is caused by the bending of the membrane it is a travelling wave (i.e. quadratic) instead. This is a direct consequence of reducing the dimensions.

Structure-caused κ Reduction

It is clear that the presence of the nanowalls is having an impact on the phonon modes, the ShengBTE code was required to convert this into a measurement of the lateral thermal conductivity (i.e. the thermal conductivity through the membrane down the central shaft).

The thermal conductivity was then calculated for the membrane with increased height nanowalls. The result is shown in Figure-4.14, it should be noted that the shown Y value is κ_r. This is the ratio of the κ of the structure with the nanowalls to

the structure without them. This is because there are a number of different modelling methods which can be used such as Tersoff potential or Callaway-Holland (79) (which simulates phonon scattering as opposed to modes) produce different κ values but generally agree on the scale of change.

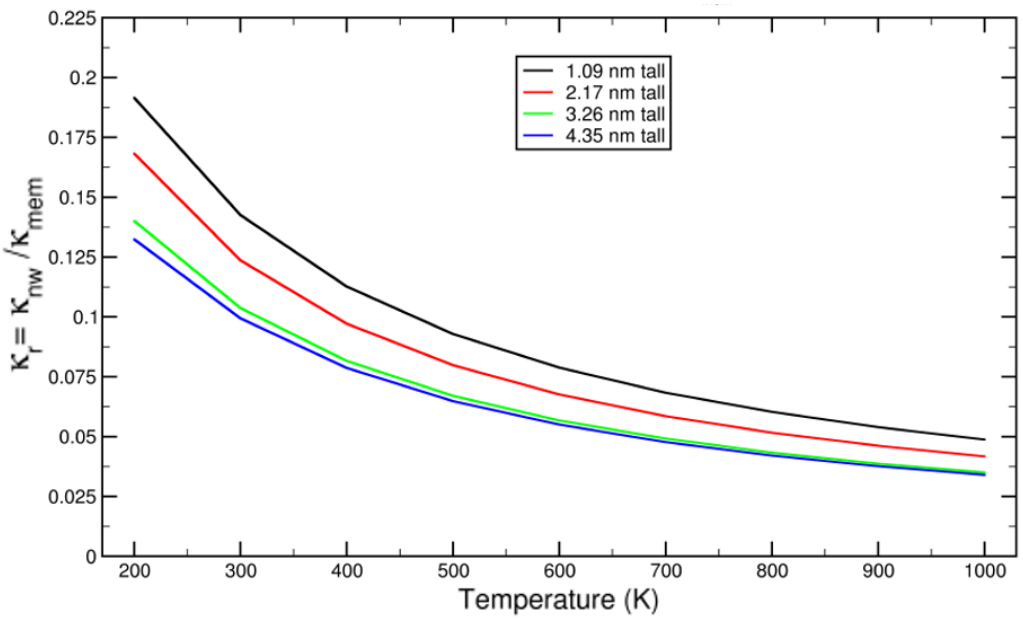

Figure-4.14: Graph of varied height of nanowalls in CASTEP/ShengBTE simulated results of the κ_r over assorted temperatures. (Reproduced from reference (77)).

As can be seen in Figure-4.14 the taller the nanowalls are the more that the thermal conductivity is reduced. This matches with the theory that a taller structure allows for more phonon modes within it which can then affect the central pillar. However it does seem as if the effect is plateauing for the 4.35nm tall structure which could suggest that further increases to height will have diminishing returns to the reduction on κ.

The width of the structures (and thus the amount of the membrane they cover) as well as the spacing between the structures was also varied and the resulting thermal conductivity for those at 300K is shown in Figure-4.15.

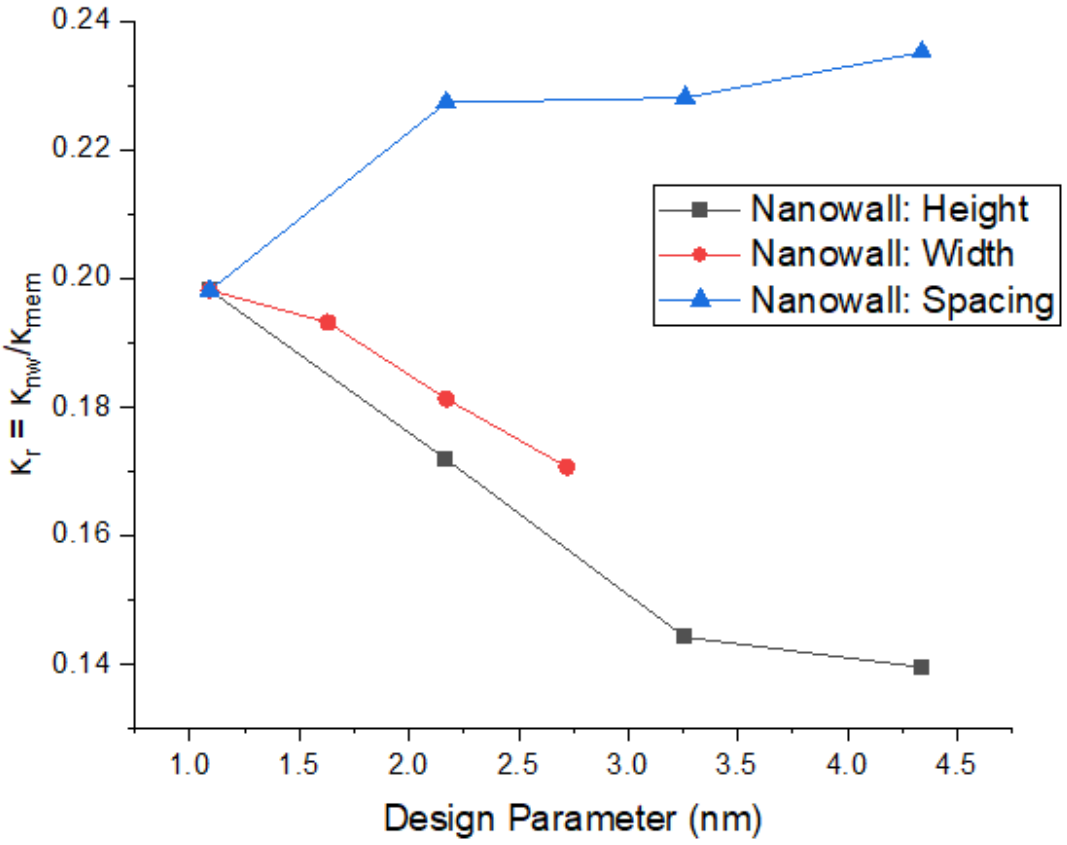

Figure-4.15: Graph of normalised effect of varying design parameters of nanowalls in the CASTEP/ShengBTE simulated results of the κ_r. Note that except where mentioned the parameters are a 1CC (1.09nm) and the membrane is 1.63nm thick. The simulations take place at 300K and κ_{mem} = 10.81W/m.K.

These results show that increasing the height of the nanowalls and the amount of the membrane covered in the nanowalls by increasing the nanowall width cause a reduction in thermal conductivity. They could also suggest that decreasing the spacing between the nanowalls reduces the thermal conductivity further due to being able to fit a higher density of nanowalls. It should also be noted that some early simulations (77) also suggest that these structures cause only a very small change in electrical conductivity in comparison to the seen thermal conductivity changes.

4.6 Other Experimental Work

Before considering how this theory was adapted into experimental work as discussed in Chapter 6 it is important to examine experimental work which has already been performed by others.

As previously mentioned, there is a considerable body of work of groups attempting to reduce the thermal conductivity of Si. Some of these studies take

place examining the thermal conductivity through nanowires (80). In these examinations it was generally found that increasing the geometric restrictions of the wire would increase the scattering and decrease the thermal conductivity. Additionally steps like increasing the surface roughness of the nanowires (81) will also cause further scattering.

These general principles can be broadly applied to Si structures (59) however by increasing the phonon scattering the electron scattering will also increase. This reduces the overall increase to the thermoelectric figure of merit which is the ultimate aim from reducing the thermal conductivity. This is why phononic resonances have been chosen as the mechanism for this project.

4.6.1 Silicon Nanowire Forests

One method of fabricating nanostructures on top of a Si membrane has been to create a large number of pillars on a surface as shown in Figure-4.16. This has been used to create what have been termed Si nanowire forests (82).

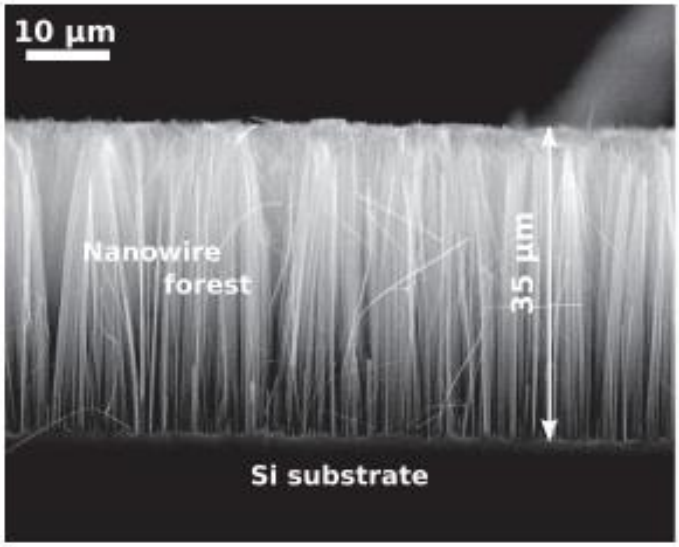

Figure-4.16: SEM image of silicon nanowire forest cross section.
(Reproduced from reference (82)).

As can be seen in Figure-4.17 there is a clear relationship between the length of the nanowires which act as phononic resonators, and the thermal resistance measured. As $R \propto \frac{1}{\kappa}$ this means that longer nanowires result in a lower thermal conductivity.

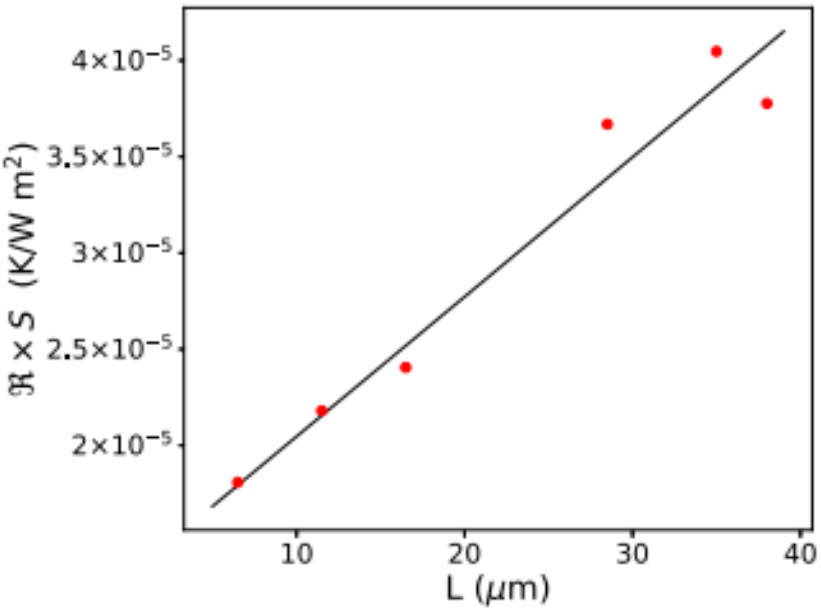

Figure-4.17: Graph showing that an increase in average length of the silicon nanowires within a nanowire forest increases the thermal resistance per unit area of the structure. (Reproduced from reference (82))..

The main issue with attempting to construct these kinds of nanowire forests is that the product is difficult to control and only measurable as a bulk effect. The width of an individual nanowire is highly varied and not homogeneous but was seemingly generally measured on the order of 50-100nm. These structures were measured at thermal conductivities on the order of 5W/m.K (82).

4.6.2 Silicon Fishbones

Some experimental work using highly controlled fabricated Si nanostructures which they called 'Si fishbones' for examining thermal conductivity has been performed by Maire et al. They used a similar fabrication techniques as described in Chapter 3 on SoI to create a suspended platform held up by a series of Si fishbone structures which connected it to the bulk material as shown in Figure-4.18.

The thermal conductivities of the fishbone nanostructure were measured using time dependent thermal relaxation which uses a laser to pulse heat a surface and examines how long it takes to cool. This is directly related to the thermal conductivity of the nanostructures which transport heat away from the heated platform.

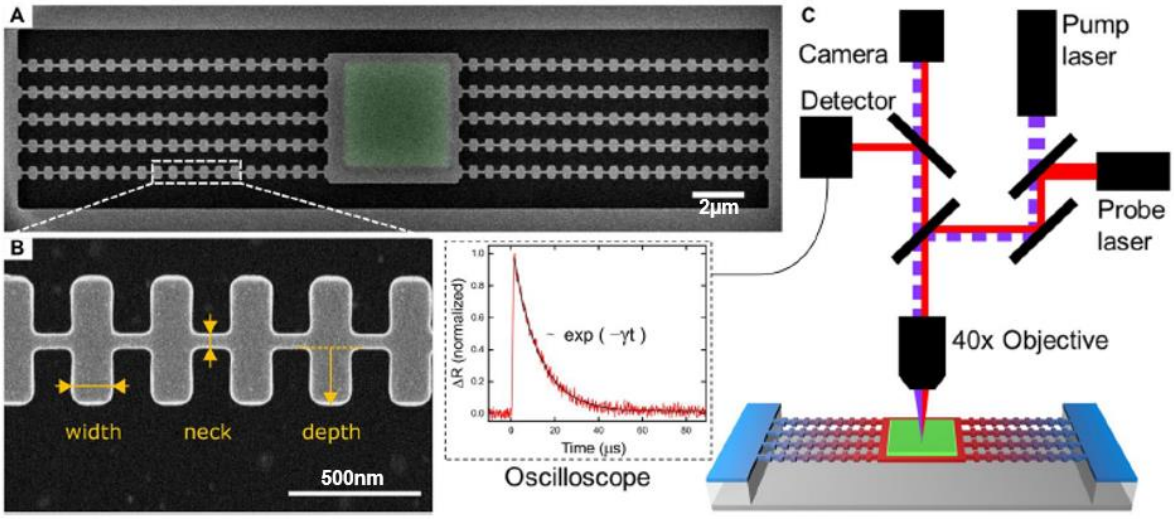

Figure-4.18: Images showing optical image of sample (A), SEM image of fishbone nanostructure (B), and schematic of time-dependent thermal relaxation setup with recorded signal and exponential fit (C). (Adapted from (83)).

A series of samples were made to examine how changes to the parameters of the fishbones affected the resulting thermal conductivity. First the 'neck thickness' was varied as seen in Figure-4.19.

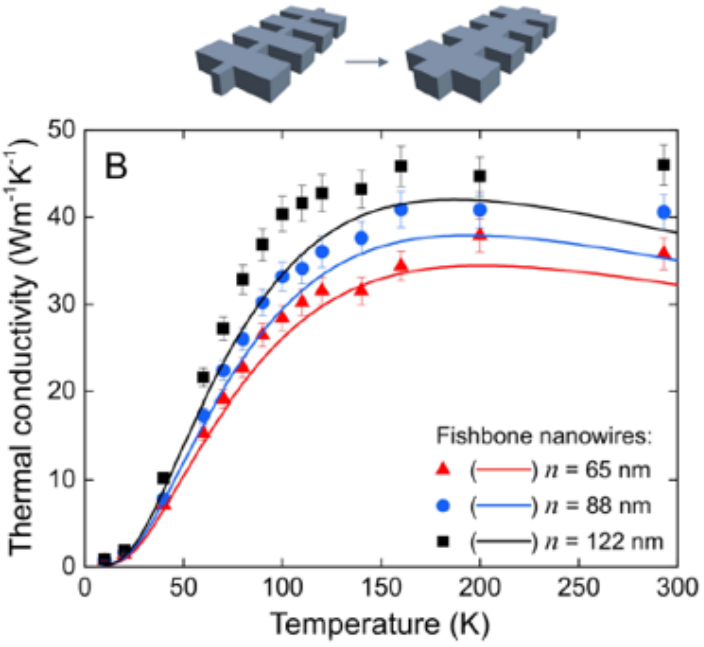

Figure-4.19: Graph of thermal conductivity of Si fishbone structure across various temperatures for multiple neck widths. Experimental data is shown as a series of points and a Callaway-Holland model of the structures is shown as straight lines. Where wing width is 93nm and depth is 190nm. (Adapted from (83)).

This showed that a thinner central neck results in a lower thermal conductivity and shows good agreement with Callaway-Holland modelling (79) which was also performed. It is not clear if/how much this thermal conductivity reduction comes from the increase in surface scattering from the geometric constraint as opposed to an increase in the effect of the wings. The effect of changing the size of the width and depth of the fishbone structures for varying neck sizes was tested as shown in Figure-4.20.

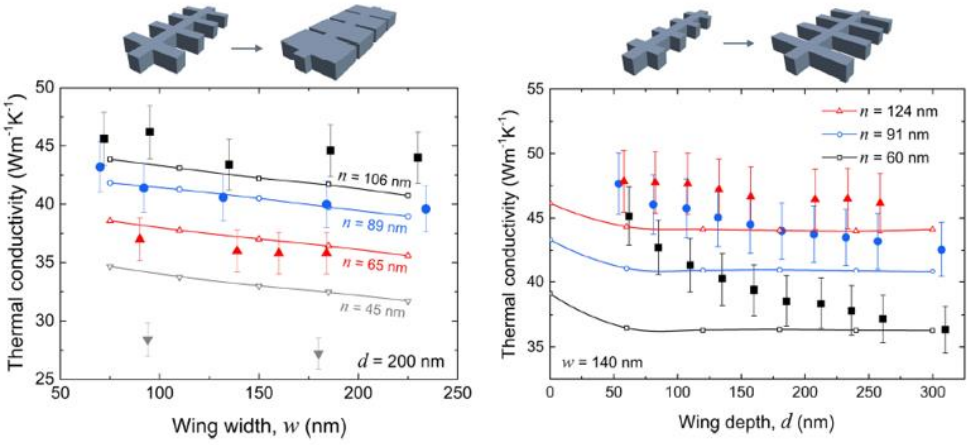

Figure-4.20: Graphs of effect of varying Si fishbone structure at 300K. (Reproduced from reference (83)).

This shows that increased width of the wings (or at least increased central neck coverage) results in a decreased thermal conductivity, as does an increase in the depth of the wings. This would match with the theoretical predictions as the increase in the wing width dramatically increases the fill factor across the neck and the increased wing depth increases the length of the resonators. This allows for a greater amount of phonon modes to form within the resonators due to the height difference and the fill factor increases how much of the neck is influenced by the resonators and allows for more coupling between the resonators. The reductions for these structures are about an order of magnitude less than those seen in the Si forests. This is likely due to the amount of structure coverage.

4.7 Summary

The presented theoretical work performed both by the collaborators from the University of York and those in the literature show a clear mechanism by which resonating structures are able to cause a thermal conductivity change within a material through phonon hybridisation.

It is also shown that thermal conductivity of a material can be affected by a number of factors which are not due to phonon hybridisation and these must be considered when interpreting any results.

This experimental work and the computational modelling can be used to make several predictions for the experiments performed here:

- An increased aspect ratio/height of the resonators will decrease κ
- An increased density/lower spacing between resonators will decrease κ
- An increased fill factor/resonator width will decrease κ

Chapter 5

Multilayer Examinations

Many modern devices use thin multilayer composite materials. Despite this, the specific paths of heat transfer through them is not thoroughly understood, leaving much room for continued examination. This is especially true in the realms of digital storage where the thermal properties of multilayers are becoming increasingly important. In order to examine this a series of multilayer samples were acquired with several goals to accomplish using an SThM scanning technique. Namely:

- Is it possible to resolve different material layers using SThM?
- Is it possible to measure the κ value of unknown layers?

This project aims to evaluate different methods of preparing a multilayer sample which exposes the different layers for examination using an SThM.

This particular project was worked on by a number of people other than myself. Dr Siew Wai designed the samples in collaboration with Seagate who then fabricated them. The SThM scans examined within this chapter were recorded using a VLS-80 at the Nanoscan workshop in Zürich by Dr Marco Corbetta and Professor Sarah Thompson. Ion mill preparation was performed by Dr Matthias Kleine-Boymann of IONTOF.

5.1 Multilayer Composition

The multilayer samples were designed to allow for an examination of the high thermal conductivity dielectric material (HCD) and how it thermally interacts with the rest of the composite layers.

These kinds of materials are used in Heat-Assisted Magnetic Recording (HAMR) read/write heads but here are made with much thicker layers to make examining them with an SThM more possible. HAMR is a technology for allowing a higher density of data storage. This is done by making the grains which store data bits smaller. However as the bits become smaller, they become less stable and more likely to switch polarity. The materials can be made more stable, but this increases the difficulty of deliberate polarity switching when attempting to write new information. HAMR uses a small laser diode to rapidly heat the grains which lowers switching

resistance allowing it to be changed before it cools and locks the polarity once again. This process is required to take place over a very small area in a heating, writing and cooling cycle of less than one nanosecond (4). As such a full understanding of how the heat interacts on a very local scale across the used materials is crucial. This is especially true as the heat needs to be contained laterally (i.e. not causing heating in adjacent bits). Properties such as anisotropy of κ would be highly desirable.

Two different samples were used, n.3 and n.4, which used a combination of Al_2O_3, Cu and HCD layers on a SiO_2-topped Si substrate as shown in Figure-5.1 and Figure-5.2. Note that n.1/n.2 refer to the substrates without deposited layers which are detailed in Table-5.1

Substrate	Used In	Type	Doping Type	Resistivity (Ω.cm)
n.1	n.4	p	B	0.005 – 300
n.2	n.3	n	P	0 - 100

Table-5.1 Parameters of Si substrates used for multilayer samples.

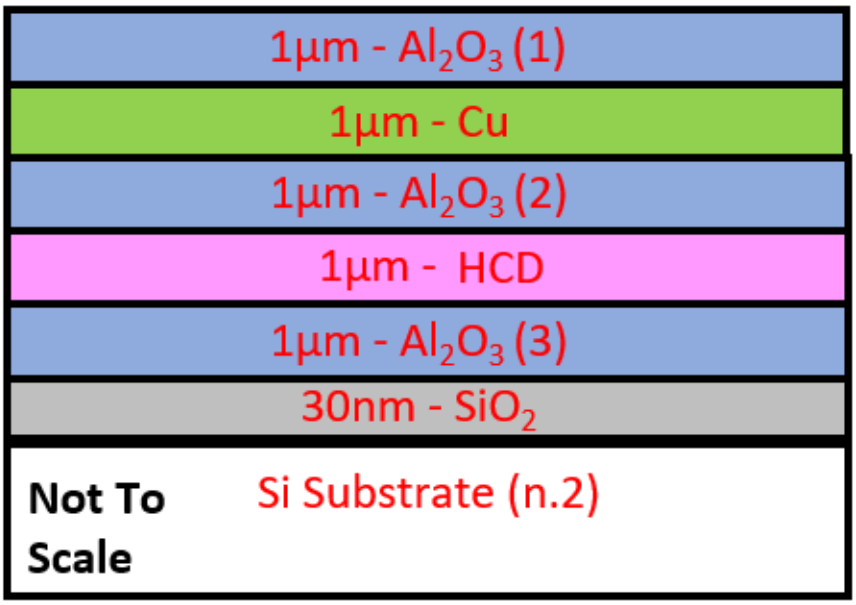

Figure-5.1: Cross sectional diagram of composition of sample n.3. Showing layer material and thickness.

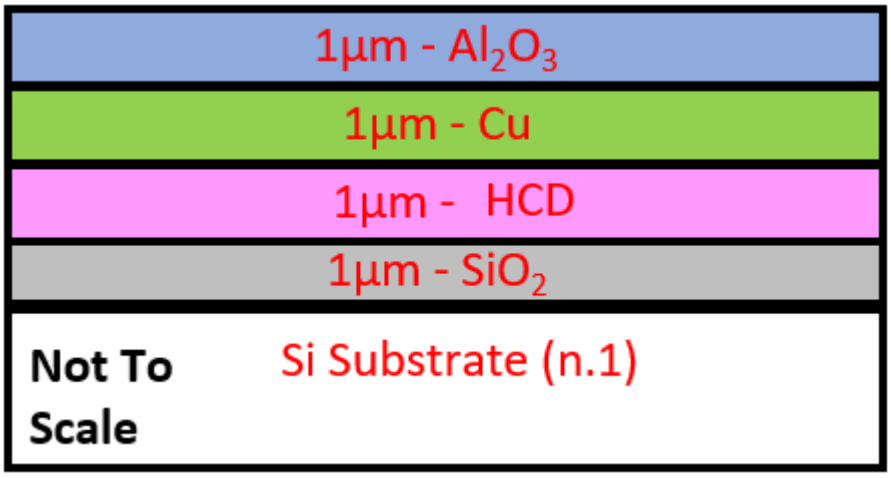

Figure-5.2: Cross sectional diagram of composition of sample n.4. Showing layer material and thickness.

5.2 Multilayer Preparation

By definition, many of the layers in a multilayer material are buried within the sample and are therefore difficult to access. Examination on an SThM requires a flat and exposed surface. The measurements are also limited by the AFM nature of the machine, meaning that if the surface changes are beyond the range of the motor that controls the tip (10µm) it will not be possible to scan at all.

For this project different ways of preparing the multilayers in a way suitable for SThM examination were considered. This involved carrying out some kind of method to first expose the buried layers and then to also ensure that said surface was not too rough for examination. Two methods were tried:

- 'Cut and Polish'
- Ion Beam Milling

5.2.1 Cut and Polish

The simplest way to expose the various multilayers is to cut the sample in such a way that the cross section is visible, much like the images shown in Figure-5.1 and Figure-5.2, which reveals all of the different material layers. This is a standard method of transmission electron microscope sample preparation (84).

This is done here by first cutting out two small chunks of the sample from the wafer in a diamond dicing saw (DISCO DAD-320). These pieces were then stuck together using a Si-based glue at the top surface as shown in Figure-5.3.

The sample was stuck together to allow for the SThM tip to be able to examine the top Al_2O_3 layer of the sample without concern for a sheer edge which would otherwise cause scanning difficulties. Additionally, this allowed for multiple parts of the wafer to be examined without switching samples.

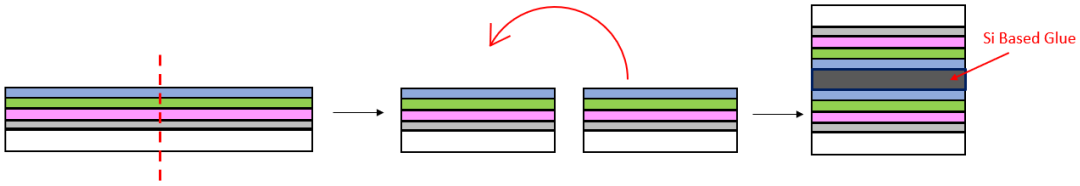

Figure-5.3: Diagram of process of preparing a multilayer with the 'cut and polish' method by cutting the sample and using a silicon-based glue to attach one section to the other.

The completed sample was then placed in a dicing machine which cut through the sample revealing a level cross section across both of the sample halves. This dicing process however left a very rough surface which would not be suitable for use in an SThM. In order to smooth the surface, the cross section was mechanically polished. This was done using a series of lubricated diamond polishing mats of decreasing roughness from 30µm to 0.5µm with each sequentially smoothing the surface. The largest of these were placed on a rotary plate to speed up the initial coarse polish. A final polish using a 0.3µm Si polishing grit was also performed. The full steps for this are set out in Table-5.2 with the visible difference in surface roughness being visible in Figure-5.4.

Size of Polish (µm)	Type of Polish	Lubricant
30	Rotary Plate, Mat	Water
9	Rotary Plate, Mat	Water
3	Hand Polish, Mat	Water
1	Hand Polish, Mat	Oil
0.5	Hand Polish, Mat	Oil
0.3	Hand Polish, Grit	Deionised Water

Table-5.2: Parameters for polishing 'cut and polish' cross section.

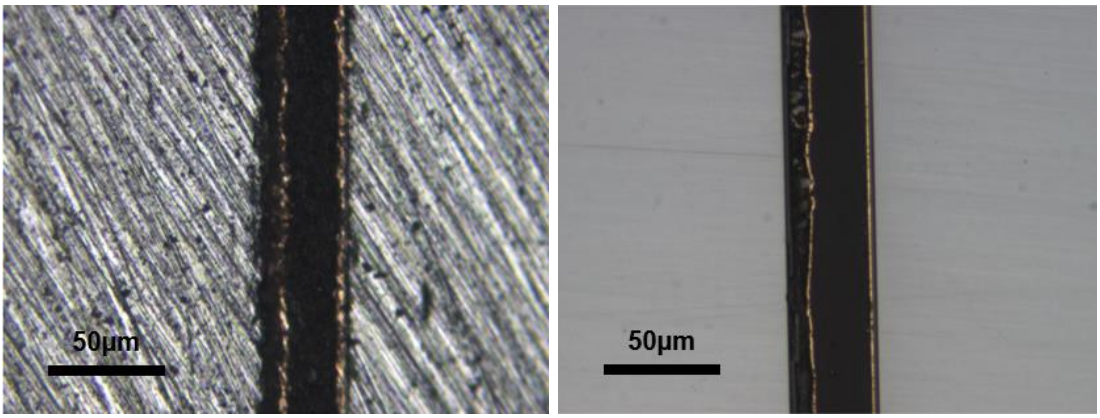

Figure-5.4: Optical image of 'cut and polish' multilayer cross sections post-9µm mat polish (Left) and after all polishing steps in Table-5.2 (Right).

The mechanical polishing results in a significantly smoother cross section with the various layers exposed for examination with an SThM tip as shown in Figure-5.5.

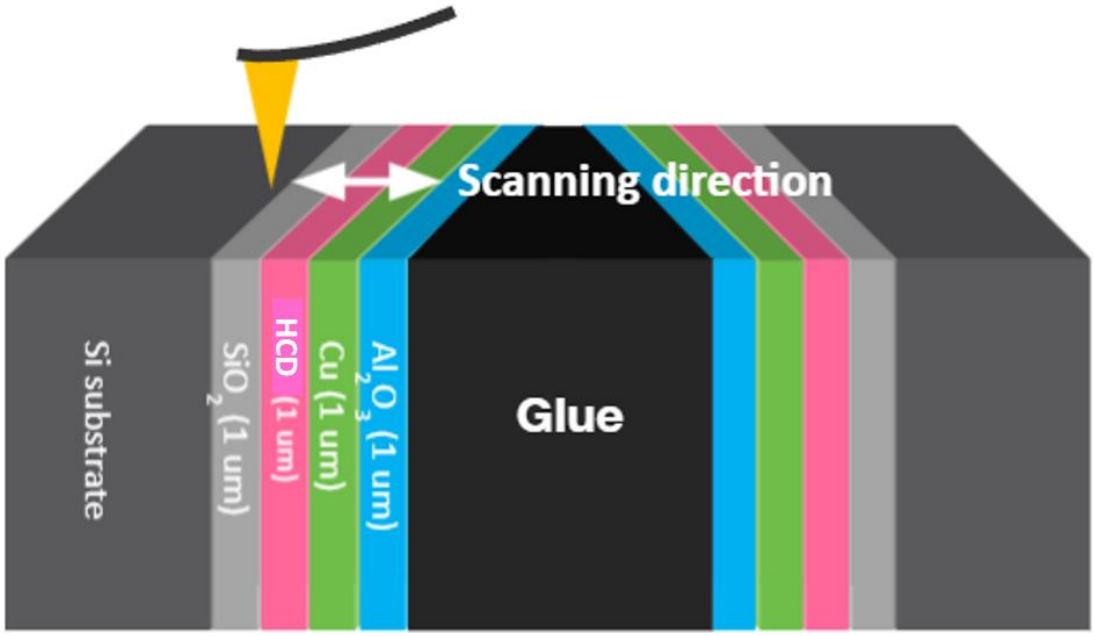

Figure-5.5: Diagram of 'cut and polish' prepared sample and how an SThM Tip is used to examine the surface. (Diagram by Dr Siew Wai).

However, some initial attempts to examine this cross-sectioned surface using SThM revealed that the surface was still too rough, such as in Figure-5.6. Because of this a further surface polishing had to be performed using ion milling.

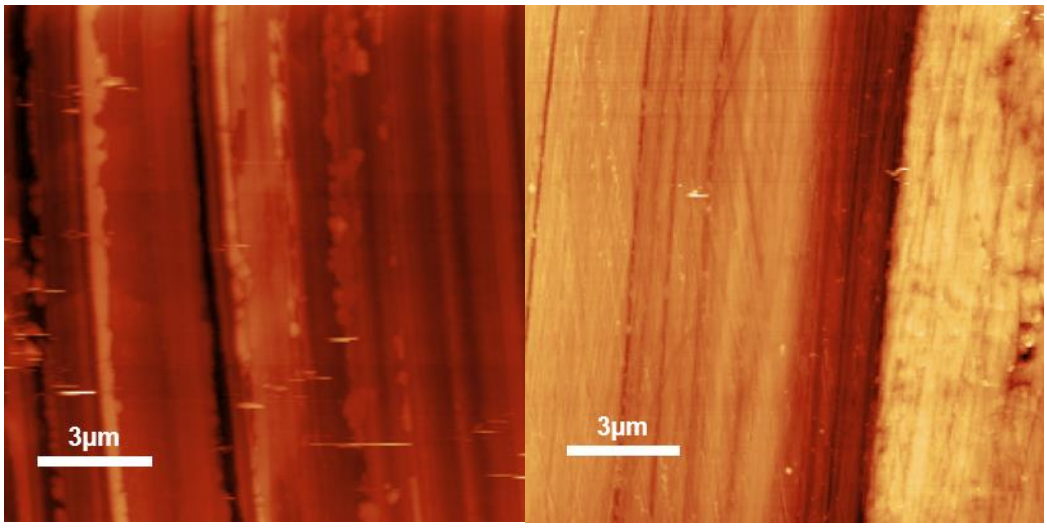

Figure-5.6: Thermal SThM images of two multilayer cross sections as described in Figure-5.5 after mechanical polish only. Note that the individual layers are difficult to resolve, and thus measurements cannot be taken.

5.2.2 Ion Milling

Ion milling uses the process of bombarding the surface of a sample with high energy ions fired from an ion gun. These ions interact with the surface atoms through high energy collisions, causing them to be stripped from the surface through a sputtering process. A similar process has been developed at Lancaster University by the group of Professor Oleg Kolosov (85) although this has considerably less control over the milling parameters.

In this project this technique was used in two different capacities. Firstly, a relatively short and homogeneous exposure was used to continue the surface polishing on the cross section following the previously performed mechanical polishing. Secondly, a longer and more complex procedure was used to mill into the surface in an attempt to further expose the multilayers by creating a gradient crater. All ion beam milling was performed by Dr Matthias Kleine-Boymann of IONTOF in their ToF-SIMS (86) (Time-of-Flight Secondary Ion Mass Spectrometry) instrument.

Ion Beam Surface Polishing

Ion beams are generally directed onto a sample at an angle. This angle allows it to smooth non-regular surfaces. This occurs because any taller features are given a greater exposure and are thus milled more quickly, whereas lower lying areas are blocked from the beam resulting in less milling as shown in Figure-5.7.

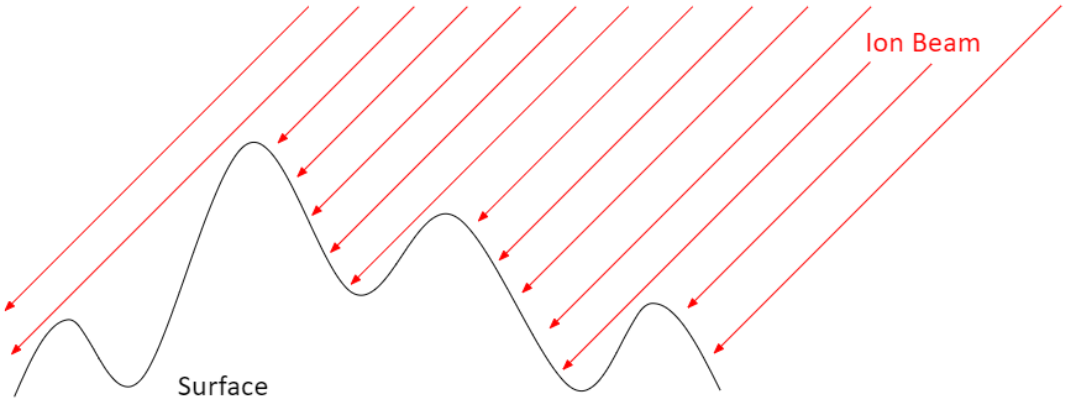

Figure-5.7: Diagram showing effect of ion beam exposure on an uneven surface which results in greater etching of taller features.

Within a multilayer however, the ability to produce a highly flat surface is hindered by the fact that the different materials mill at variable rates under the same exposure. This preferential etching means that longer exposure periods can result in a less even surface than shorter ones. The exposure can also result in ridge patterns caused by the beam.

Ion Beam Drilling

By exposing a material to an ion beam for an extended period it is possible to use the milling to actively drill down into a surface. If carefully controlled in a multilayer this can be used to expose the buried layers. It is possible to change the depth milled into the surface by altering the dose (which is caused by the dwell time) of the ion beam as it is scanned along a surface. By gradually increasing the dose along the X axis it is possible to produce a wedge-like crater which is drilled into the surface. This exposure pattern is shown in Figure-5.8 and an optical image of the result can be seen in Figure-5.9.

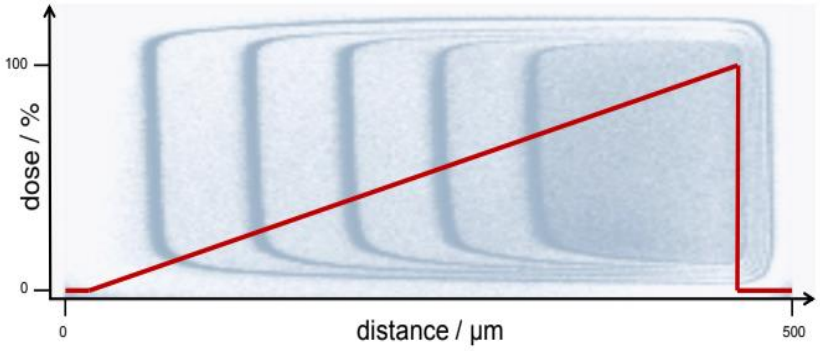

Figure-5.8: Graph and diagram describing increasing dosage use to cause ion mill exposed multilayer. (Image provided by IONTOF).

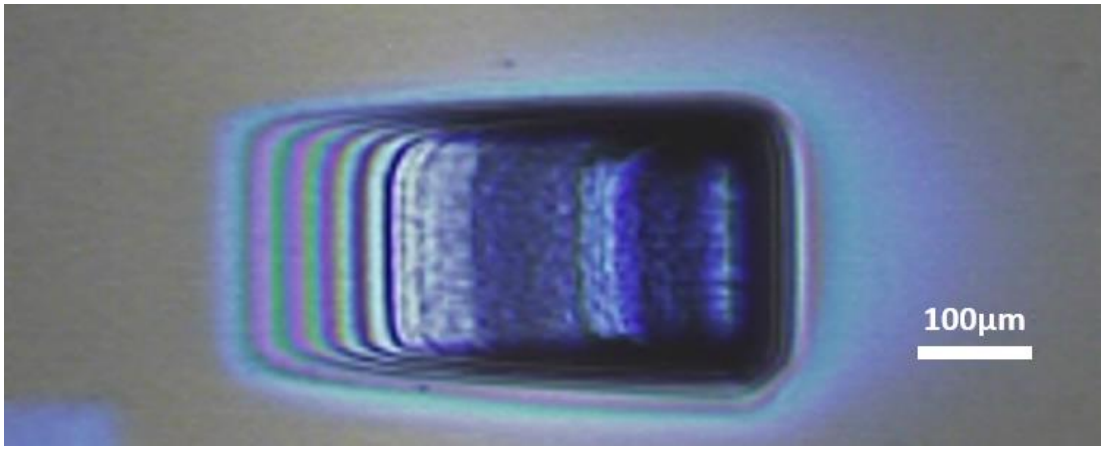

Figure-5.9: Optical image of ion milled wedge crater with steep gradient on left side and shallow gradient on right. (Image provided by IONTOF).

As shown in Figure-5.10 this exposes the surface of the buried layers and so long as the gradient is sufficiently shallow (such that the measured height change does not exceed the AFMs capabilities) they are available to examine using an SThM.

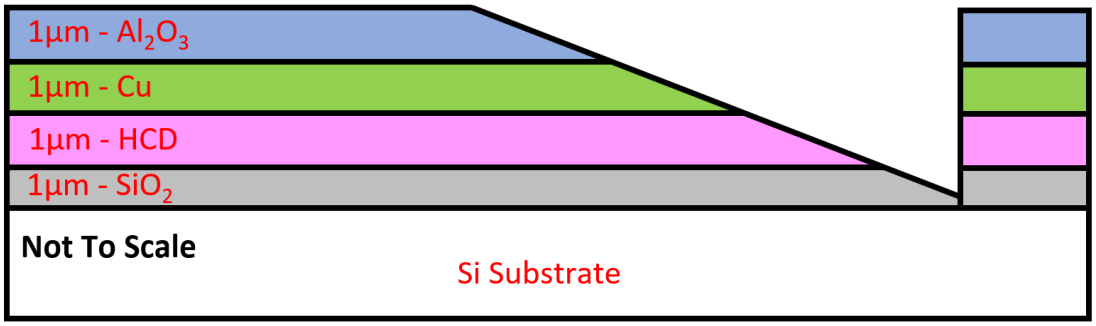

Figure-5.10: Cross sectional diagram of ion mill crater multilayer sample showing how layers are exposed as a surface with a gradient.

Ion Beam Polishing Parameters

A series of experiments were performed on some of the samples as described in Table-5.3. This used samples of either n.3 or n.4 which were mechanically polished (P) or unpolished (UP) before being exposed to an ion beam polish using different parameters.

The different resulting surface topographies were then compared against each other such as in Figure-5.11. This was to see which parameters resulted in the smoothest surface which is most suitable for SThM examination.

Sample	Crater mark	Sputter species	Energy /keV	Sputter current /nA	Sputter time /min	Crater size /µm²
1/1 UP	Not sputtered					
3/3 UP	1	Ar_{1600}^+	20	14.05	10	250 x 250
3/3 P	2	Ar_{1600}^+	20	14.05	2	250 x 250
	3	Ar_{1600}^+	20	14.05	1	250 x 250
	4	Ar_{1600}^+	20	14.05	5	250 x 250
	5	Ar_{1600}^+	20	14.05	0.5	250 x 250
	6	Ar_{1600}^+	20	14.05	0.1666 (10 sec)	250 x 250
4/4 UP	7	Ar_{1600}^+	20	14.05	5	250 x 250
	8	Ar_{1600}^+	20	14.05	10	250 x 250

Table-5.3: Table of ion milling parameters used for ion beam polishing used by IONTOF.

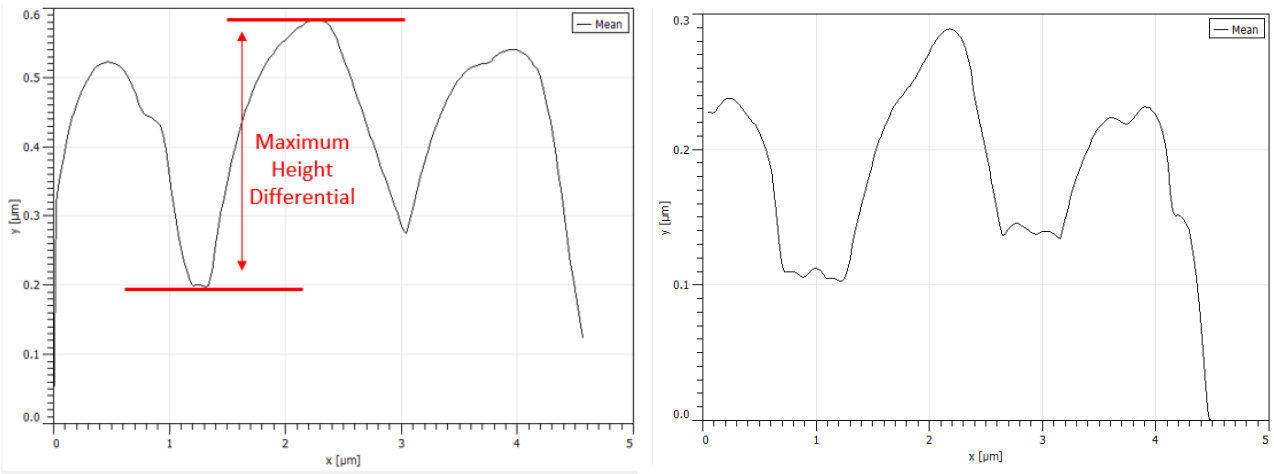

Figure-5.11: Comparison of topography line scan average for crater 2 (Left) and crater 3 (Right) which shows the product of differential etching rates.

The sample which was not mechanically polished proved to be too rough to examine using the SThM. This suggests that even when using a relatively long ion beam exposure an initial mechanical polish is required to produce a smooth surface.

From these examinations it was found that on these particular multilayers an ion mill time of 30 seconds was most appropriate. This is because it is able to polish the surface without the materials becoming more uneven due to the preferential etching. This can be seen in Table-5.4 of the maximum height differential i.e., the largest topographical change recorded between the layers.

Sputter Time /min	Maximum Height Differential (µm)
10	0.4
2	0.2
1	0.45
0.5	0.15
0.1666 (10 seconds)	0.2

Table-5.4: Comparison between 'cut and polish' sample ion beam sputter time and resulting maximum height differential across multilayer surface.

The ion beam milling for the samples examined in the later sections was performed on separate occasions to those produced in Table-5.4. This was done using Ar_{1156}^{+} at 20keV and a sputtering current of 11.88nA over a 250x250µm area for a period of 30 seconds.

Ion Beam Drilling Parameters

The ion beam drilling to form the craters was performed with a more complex array of parameters which can be seen in Table-5.5. The ion beam was directed onto a single point which was defined as a pixel and allowed to dwell on it for a time causing sputtering. Whilst the beam remained the same throughout an entire procedure the dwell time increased throughout the scan (up to the maximum value shown in the table) causing the beam to remove more of the material.

Sample	Wedge mark	Sputter species	Energy /keV	Sputter current /nA	Sputter time /min	Dwell time per pixel /ms	Repeats	Crater size /µm²
1	1	Ar_{1600}^{+}	20	14.050	4	20	1	200 x 400
	2	Ar_{1600}^{+}	20	14.050	2	10	1	200 x 400
	3	Ar_{1600}^{+}	20	14.050	9	50	1	200 x 400
3	1	Ar_{1600}^{+}	20	14.050	17	100	1	200 x 400
	2	Ar_{1600}^{+}	20	14.050	52	300	1	200 x 400
					9	50	1	200 x 400
4	1	Ar_{1600}^{+}	20	14.050	17	100	1	200 x 400
	11	Ar_{1370}^{+}	20	14.658	9	50	5	200 x 400
	2	Ar_{1370}^{+}	20	14.658	9	50	8	200 x 400

Table-5.5: Table of ion milling parameters used for ion mill crater drilling.

Ion Beam Crater Mass Spectrometry

IONTOF also performed a secondary ion mass spectrometry (SIMS) examination of the milled craters as shown in Figure-5.12. This was done at various stages to see how far into the multilayer the mill had exposed. This was used to ensure that all the material layers were available for scanning.

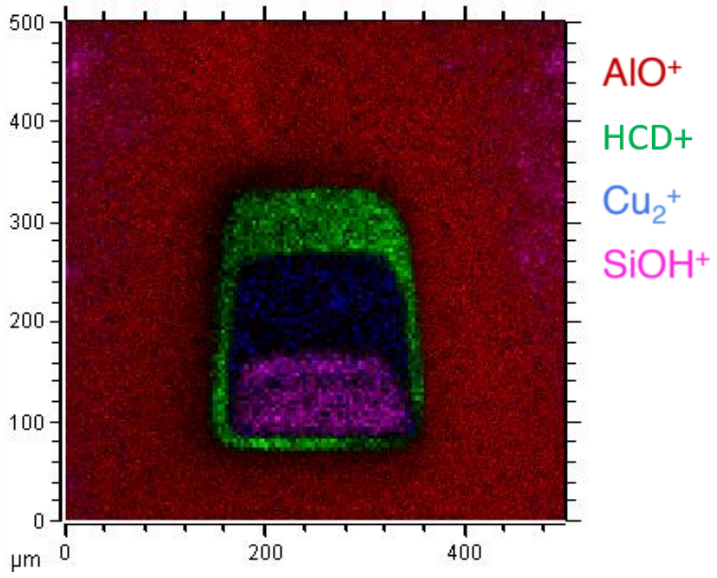

Figure-5.12: SIMS image of ion milled crater with key for different recorded ions from the surface.

5.3 Multilayer COMSOL Modelling

A 2D COMSOL model of the n.4 multilayer was created as shown in Figure-5.13. This used layer thicknesses based on SThM imaging of the surface (which is shown later in Figure-5.23) with the results shown in Table-5.6. This is used rather than the idealised 1µm thickness for all of the metallic layers which was aimed for in production.

Layer	Thickness (µm)	Error (µm)
Al_2O_3 (1)	0.8	±0.2
Cu	1.6	±0.3
Al_2O_3 (2)	0.7	±0.2
HCD	1	±0.1
Al_2O_3 (3)	1	±0.1
SiO_2	0.3	±0.1

Table-5.6: Layer thicknesses of multilayer as determined by SThM measurement.

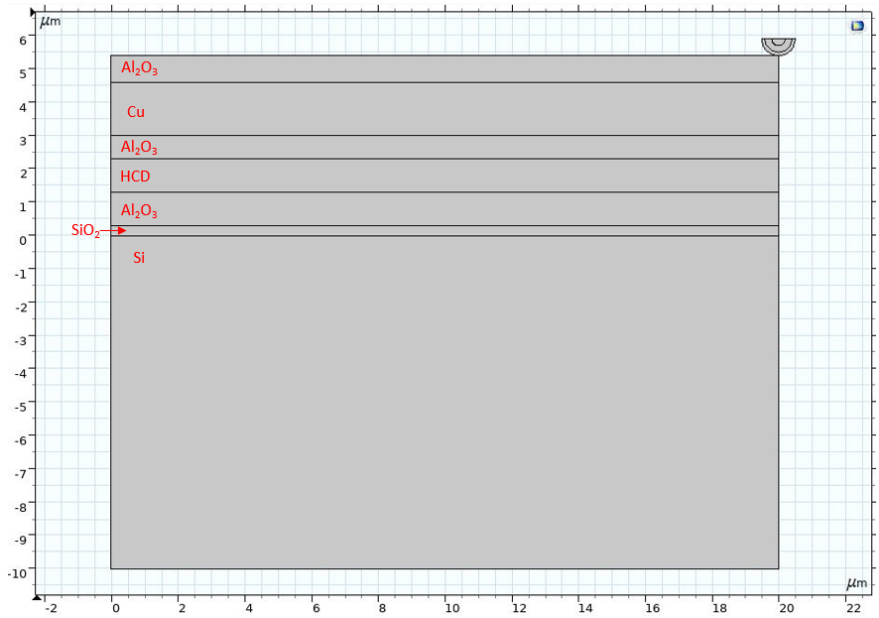

Figure-5.13: Image of cross sectional 2D COMSOL model of n.4 sample showing modelled SThM tip and labelled layer materials.

The model uses a set temperature layer at room temperature (293.15K) at the bottom of the Si layer to simulate the much thicker (1.5mm) Si found in the real sample which acts as a heat sink. A current can then be supplied to the simplified model of the tip which is constructed as described in section 3.3.2. However the model tip can not be given the same current as provided to the physical system due to the difference in tip construction. The tip current was tested until the tip gives a reasonable approximation of the measured tip temperature (~35ºC). The topside edge of the top Al_2O_3 layer as well as the outside edge of the tip both have a heat flux function applied to them. This acts as heat transfer between the surface and atmosphere (set at room temperature) and simulates natural cooling to the atmosphere. However, as the heat flux is an effect applied to the edges rather than a proper simulation of the sample/atmosphere interaction it is not possible for there to be a heat transfer from the surface through the air and then into the tip as would happen in the real system as discussed in Chapter 2.

Despite the presence of cooling to air, the COMSOL results should all be considered as vacuum measurements as there is no opportunity for gaseous or liquid transfer between the tip and the surface. The tip temperature is measured as the average temperature of the tip Pd layer. Each of the layers were assigned thermal conductivity values based on default bulk values within the COMSOL material library which are shown in Table-4.1.

In the first instance, the tip was scanned over the top Al_2O_3 surface with the buried multilayers in a stack below the tip. The isothermal contours shown in Figure-5.14 clearly show the differing heat transport properties of the materials. This is most notable in the SiO_2 layer where many of the contours are located due to the poor thermal conductivity.

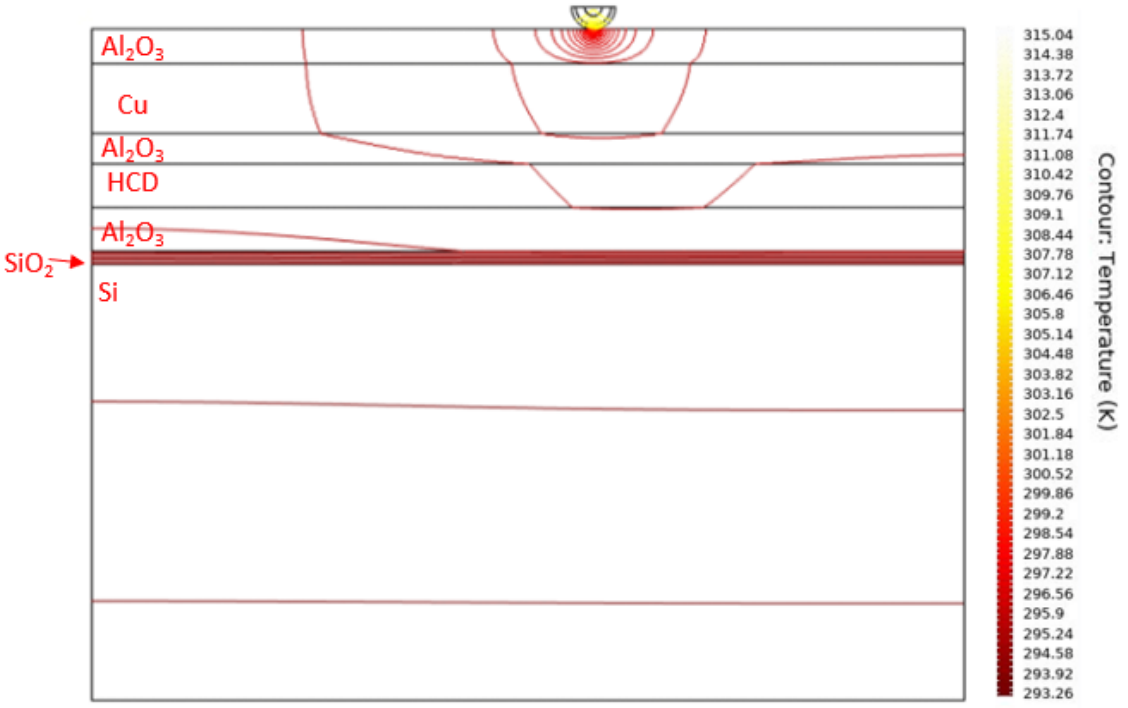

Figure-5.14: Image of COMSOL model of heated tip over multilayer stack showing thermal contours travelling through different material layers.

Scans were then run using different layer thicknesses, including the measured values determined by SThM scanning and the idealised sample thicknesses (where all layers are 1µm thick). As can clearly be seen in Figure-5.15 there is a different overall recorded temperature due to the thickness change of the layers making the cooling to the heat sink less efficient. The curved shape comes from the edge effects as the tip moves closer to the side of the sample.

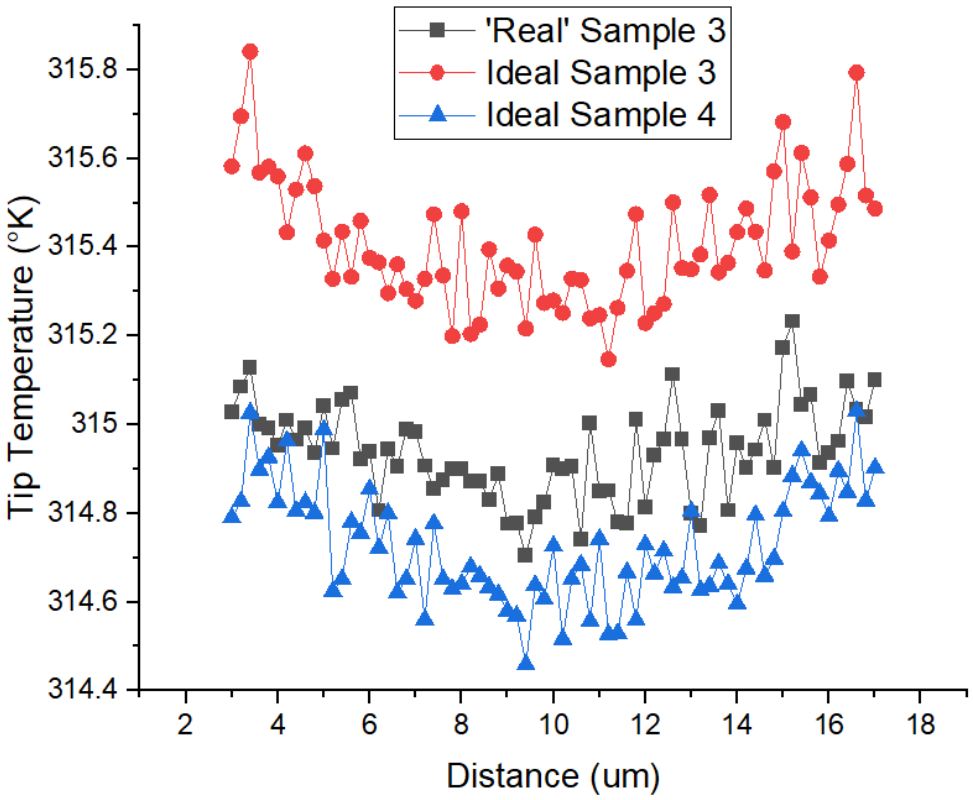

Figure-5.15: Graph of tip temperature for simulated multilayer stacks of idealised n.3 and n.4 samples (i.e., 1 µm layer thickness) and a model using layer thickness measured using SThM scanning detailed in Table-5.6 with extreme edge effects removed.

Within SThM examinations it is very difficult to measure absolute temperature which is being used here. In order to be able to use the change in temperature measurements it would require the construction of a sample where a single factor (such as layer thickness of an individual material) is able to be changed over the length of a scan. Whilst this is a valid method of examining a material property it already assumes complete information on the sample being examined. This means that the method would not be useful in examining a sample with more than one unknown property, e.g. a material of unknown thickness and thermal conductivity. The method would also require direct comparison between two similar samples and thus lacks flexibility.

5.3.1 Cross Sectional Surface

The 'cut and polish' method was simulated by moving the tip and its motion onto the side of the COMSOL model as shown in Figure-5.16 with an added Si layer to simulate the Si-based glue used to attach the multiple samples together.

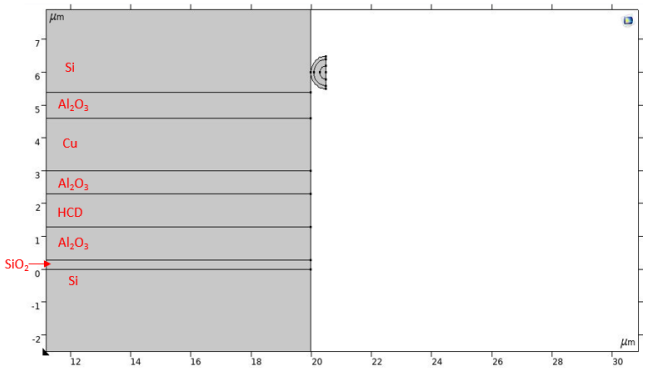

Figure-5.16: Image of COMSOL model of tip passing over 'cut and polish surface with added Si layer to prevent significant edge effects.

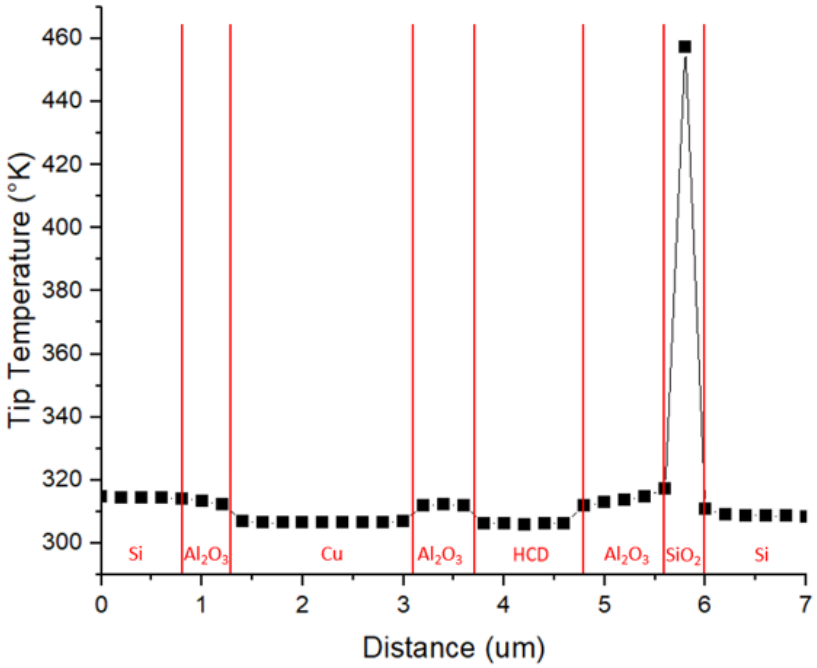

Figure-5.17: Graph of COMSOL measured tip temperature along 'cut and polish' multilayered surface model.

Once again, the tip can then be moved along the surface with the tip volume average temperature measured as shown in Figure-5.17. From here a number of very clear distinctions can be made. The different layers are clearly visible in the tip temperature, which is the area average temperature of the Pd layer of the tip when said tip is in contact with that part of the surface. This follows the expected results

of the values from Table-5.7 where the layers with higher κ value result in a lower tip temperature due to their better thermal transport. We can also however see that the temperature does not remain completely constant and is affected by the surrounding layers.

This method shows potential for the relative thickness of each layer to be determined as well as the relative thermal conductivities of the layers. The SiO_2 layer is a clear standout with its very high and visible peak despite it being thin compared to the other layers. However, it should be noted that this model does not include any consideration of the realistic surface terrain which can be seen in Figure-5.24 which may significantly impact the thermal measurements.

5.3.2 Crater Surface Gradient

Whilst a simple flat surface may match the ideal of the 'cut and polish' a more detailed model is required for the ion milled crater surface. This can be done by creating a sliced gradient down the surface exposing the various multilayers and changing the path of the tip to follow this new edge. Figure-5.18 shows an example of this kind of single gradient slice which is based on a measured overall average of one of the ion milled craters at a 3% decline.

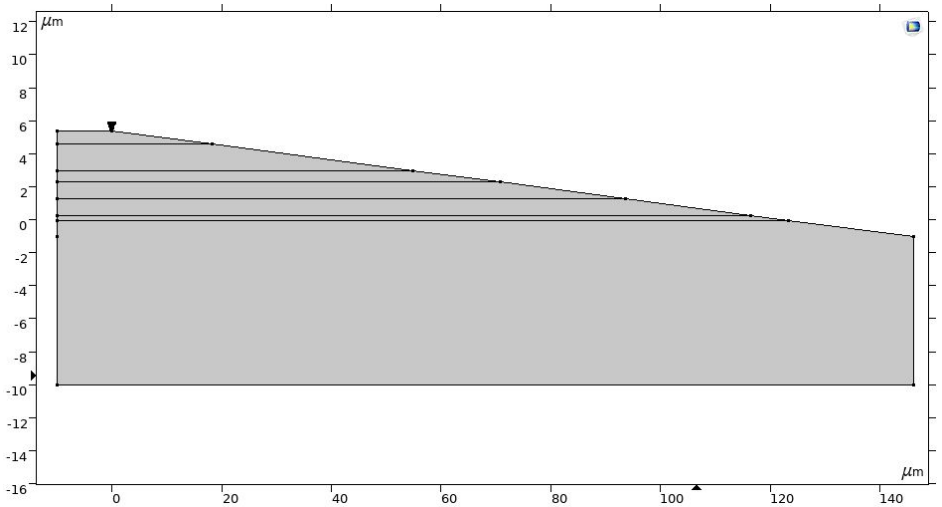

Figure-5.18: COMSOL model of sloping surface showing 3% decline with scaling.

However, despite the linear increase in the milling dosage applied to the surface along the crater's length, this does not result in a single gradient surface as seen in Figure-5.18. This is because of the preferential etching. This results in softer materials such as Cu having a steeper gradient than harder ones such as Al_2O_3. The COMSOL model was adjusted to attempt to match the different gradients for each

material as measured from a sample and noted in Table-5.8. The sample topography is shown in Figure-5.19 which also shows the resulting match between the model and sample topography.

Layer	Width (µm)	Height (µm)	Gradient
Al_2O_3 (1)	20	0.5	0.025
Cu	9	1.05	0.117
Al_2O_3 (2)	18	0.85	0.047
HCD	6	1.1	0.183
Al_2O_3 (2)	16	0.85	0.053
SiO_2	1.5	0.3	0.200

Table-5.7: Table of parameters used to construct multilayer model gradient surface derived from surface measurements.

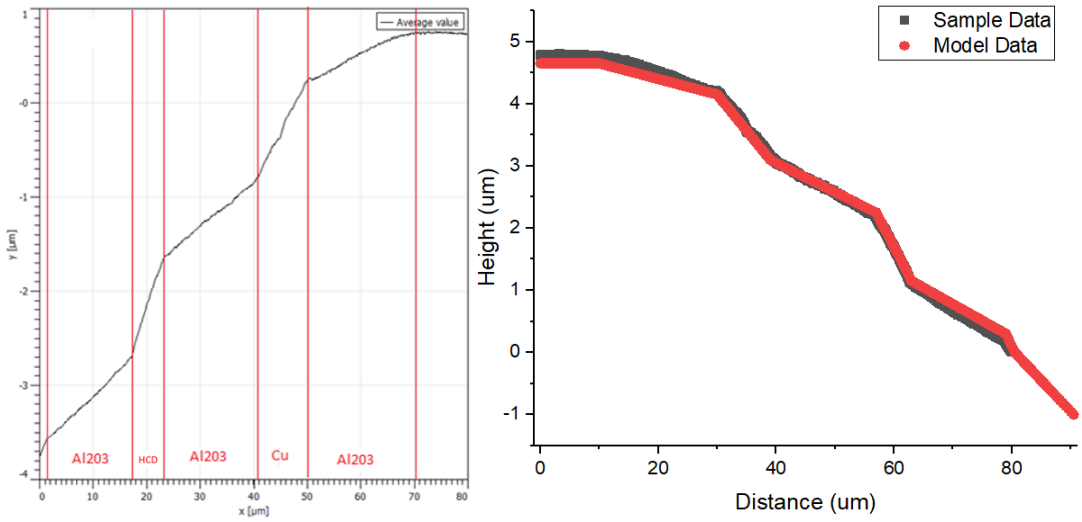

Figure-5.19: Topographical line scan average of AFM scan of ion milled crater 80x2µm, 1024x26 pixel resolution measured crater gradients (Left) and match between experimental topography and simulated COMSOL surface (Right).

This topography was then used to construct the model seen in Figure-5.20, producing the correct layer thicknesses and exposed gradients. The pathing of the tip was then modified such that it would follow the surface gradient as it changed across the model. This allows the tip to be able to simulate some of the effects that the changing topography has on the resulting thermal signal.

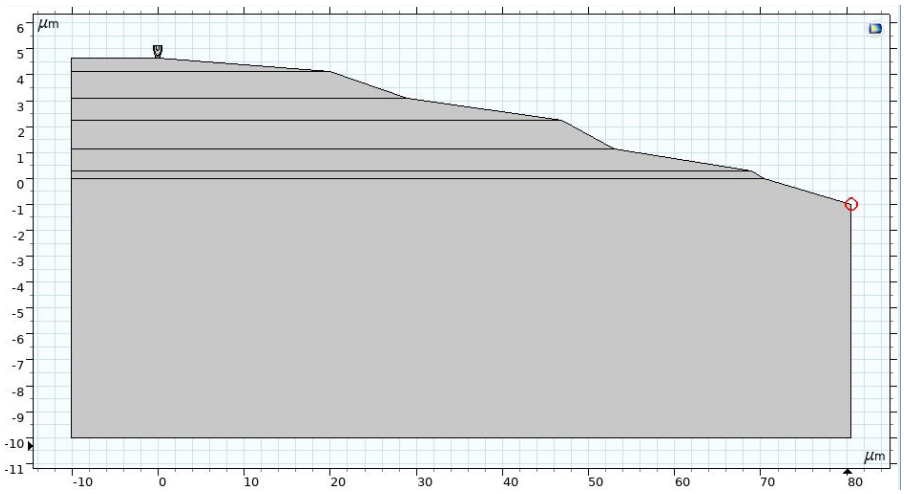

Figure-5.20: Image of sloping gradient COMSOL model of ion milled crater with realistic multilayer gradients applied. Note 1:3 scaling in X.

The resulting graph of tip temperature in Figure-5.21 looks very similar to the previously obtained graph Figure-5.17 obtained from the 'cut and polish' both of them showing the same temperature difference between layers and the same features such as the SiO_2 peak.

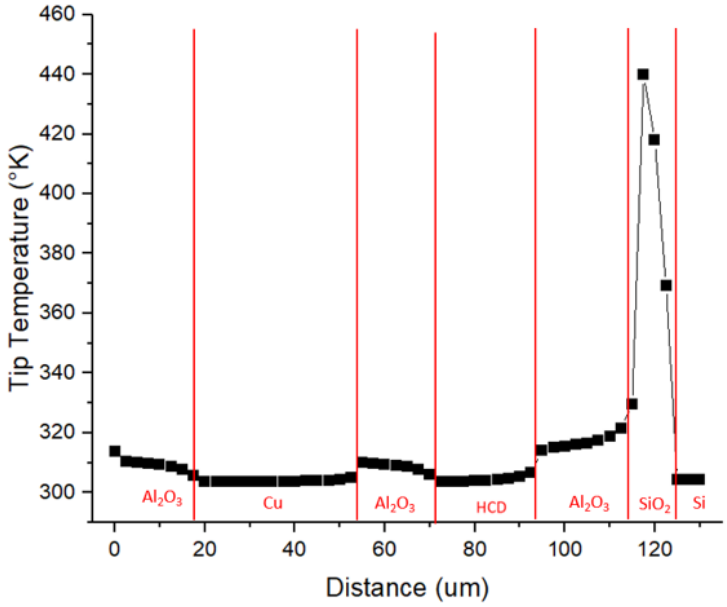

Figure-5.21: Graph of COMSOL simulated tip temperature when scanning over ion milled crater model.

There are two main differences between the models. The first is that they both offer different heat paths from the tip into and through the sample. As shown in Figure-5.22 the 'cut and polish' sample has the tip in contact above a single material which is flanked by others. This means that the tip temperature measurements are

mostly of a single material but there are larger edge effects caused as the material thins and the influence of the material under it becomes stronger. The ion milled crater on the other hand has a more immediately complex heat path as there is a greater impact in the local area from other materials.

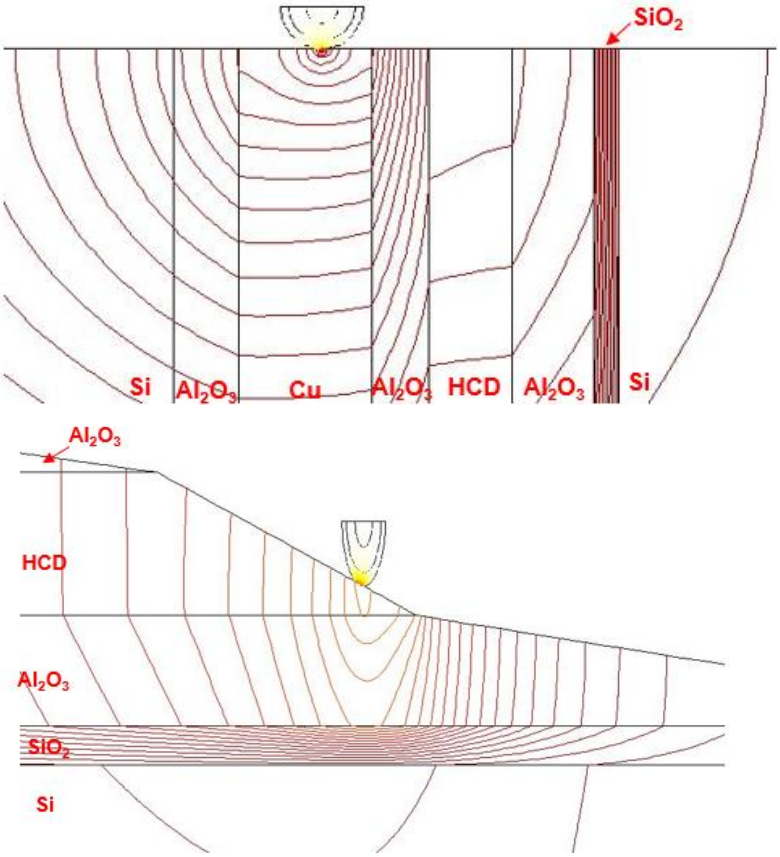

Figure-5.22: Representative diagram showing tip/sample heat path for 'cut and polish' sample (Top) and for ion milled crater sample (Bottom). Note that the ion milled crater has been compressed along the X axis at a 1:3 ratio to allow for easier examination.

The second difference is that the milled surface has a much greater exposed scanable surface per layer. This allows for more data points to be taken across the surface at the same sampling rate and fewer of these data points will be significantly impacted by edge effects. Hence better averaging and reduced noise.

5.4 Multilayer SThM Examinations

With the samples prepared, they were then examined in the VLS-80 using SThM. The resulting graphs Figure-5.17 and Figure-5.21 from the COMSOL

modelling whilst showing some difference around edge effect produced similar results. This means that under ideal conditions the two methods give largely indistinguishable results. A preferential technique then is best determined by an examination of the experimental results. SThM scans were performed by Professor Sarah Thompson and Dr Marco Corbetta at the Nanoscan workshop before the VLS-80 was delivered to York.

5.4.1 Resolving Layers

Cut and Polish

Determining the difference between the layers in the 'cut and polish' n.3 sample is a complicated matter. As can be seen in Figure-5.23 the different layers are visible to the eye in both the topography and thermal images. However, the interfaces are not clean and of varying thicknesses. The oxidation of the materials also further complicates the ability to distinguish between materials. Generating a graph using the line averaged values as in Figure-5.24 can also be used to make an approximate calculation of the layer thicknesses and to qualitatively examine their relative thermal conductivities to each other. However, the exact edge of the layers remains difficult to determine.

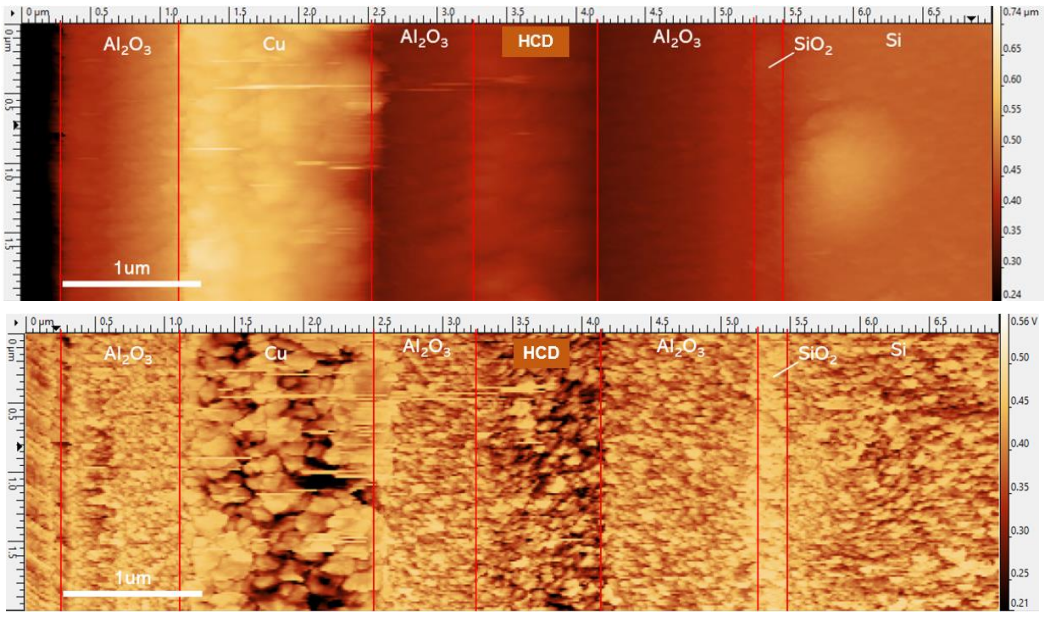

Figure-5.23: SThM images of 'cut and polish' sample topography (Top) and thermal (Bottom). Taken at 7x2µm^2 512x146p, 6 sec/line 30nm setpoint.

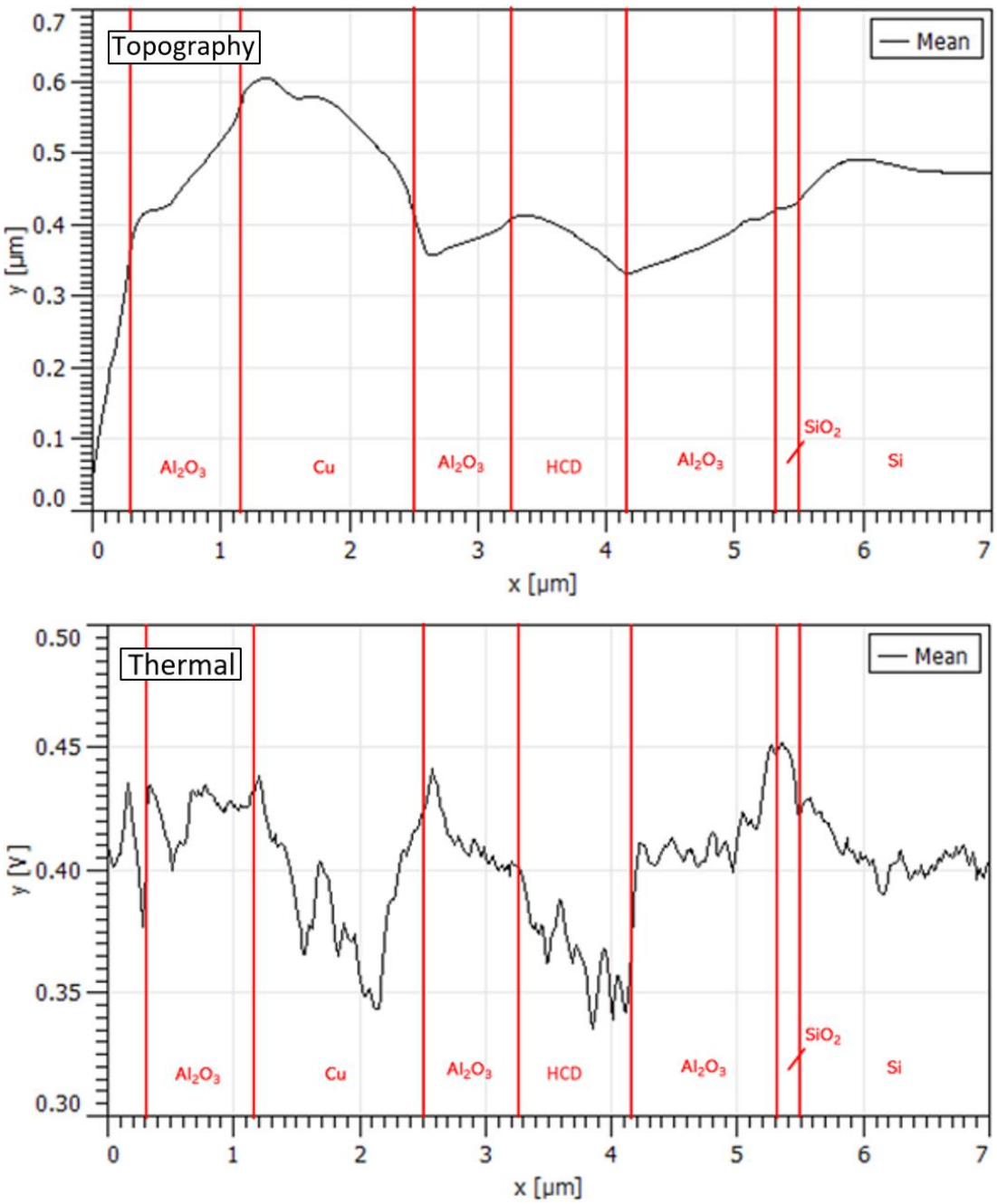

Figure-5.24: Line averaged graphs of topography (Top) and thermal (Bottom) of 'cut and polish' sample taken from SThM images in Figure-5.23. Material positions determined by looking for significant thermal and topographical changes.

Other observations can be made from examining the images and average line scans. The different grain sizes from within the materials can be seen clearly within both the topography and thermal imaging and used to determine surface roughness. The average line graphs, whilst somewhat rough due to the grains, can also be used to make some qualitative statements about the relative thermal conductivity between the different material layers.

Ion Beam Crater

The ion milled crater design may at first seem less easy to determine the different layers by eye in Figure-5.25 but this is largely due to the aspect ratio of the image. A closer examination shows a very similar image to that seen in the 'cut and polish' although as it is taken over a longer scale the resolution is poorer making it so that whilst the grains are still visible in both the topography and thermal they are less distinguishable. This could however be solved by taking longer and higher resolution scans or shorter scans of specific areas for testing.

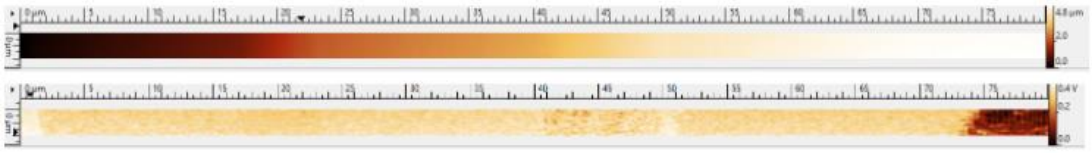

Figure-5.25: SThM images of ion beam crater topography (Top) and thermal (Bottom). Taken at 80x2µm^2 1024x26p, 5sec/line, 30nm setpoint.

As can be seen in Figure-5.26, the line averaged graphs make determining the different layers relatively simple. The layer thicknesses can easily be determined from the height changes across the exposed layer widths in the topography which are marked by gradient changes. A qualitative comparison of relative material thermal conductivity can also be made from the thermal graph.

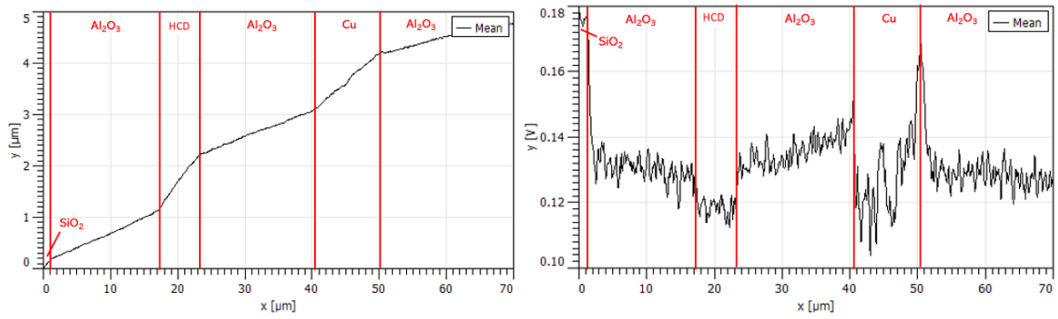

Figure-5.26: Line averaged graphs of topography (Left) and thermal (Right) of ion milled crater sample taken from SThM images in Figure-5.25.

5.4.2 Surface Examination

When considering the surface suitability for SThM examination there are a number of important factors. The size of the available scanning area is important but so too is the roughness of the surface and also the macro surface features (i.e. those significantly larger than the tip).

Macro Smoothness

A simple comparison between macro smoothness of the two different methods can be made by examining the recorded topographies as seen in Figure-5.27. This shows that the ion milled crater has much greater overall topographical changes but that these are typically flat (though at a gradient) as opposed to the peaks and troughs seen in the 'cut and polish' surface. This is further explored in the roughness analysis.

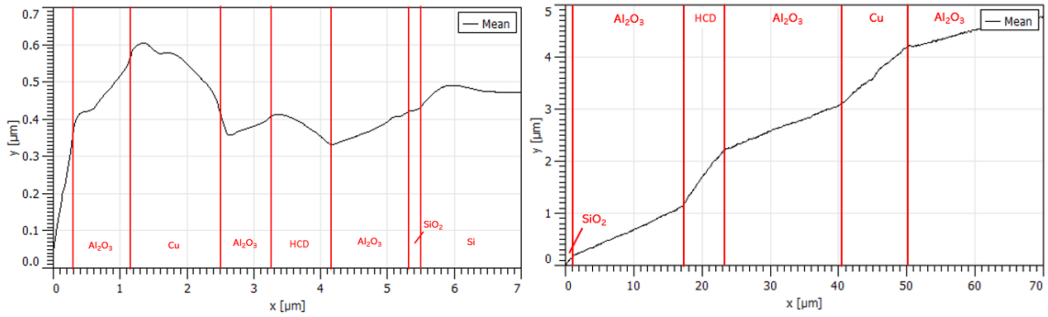

Figure-5.27: Line averaged topography graphs for 'cut and polish' (Left) and ion milled crater (Right).

Ridge Features

Throughout the ion beam milled crater samples, across all materials, a series of ridges were seen. As shown in Figure-5.28 with a variable height depending on the material and a width of around 30nm these features were created by the ion-beam milling process. These ridges are a well-known side effect of ion beam milling and fabrication (87).

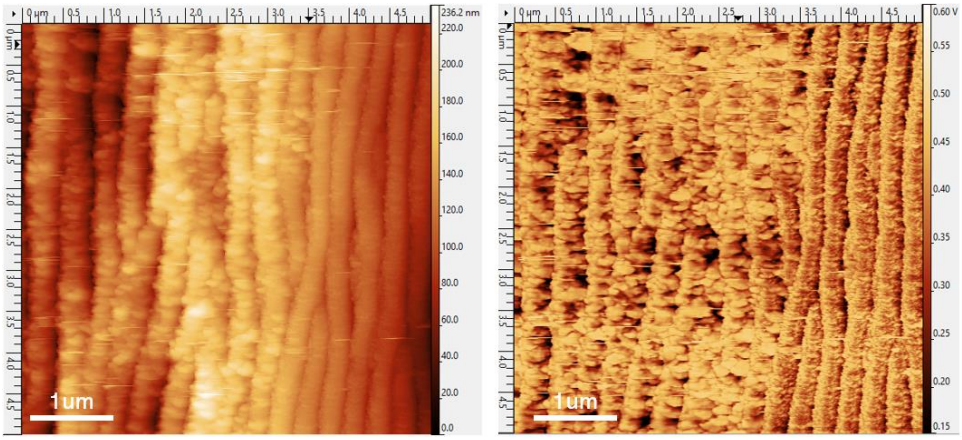

Figure-5.28: Example SThM images of ion-beam produced ridge features at the Cu-Al_2O_3 interface, topography (Left) and thermal (Right). Taken at 5x5um^2 512x512p, 1.4sec/line, 30nm set point.

As can be seen these ridges are of a significant size compared to the tips resolution and have a noticeable effect on the recorded thermal signal. These ridges make up the bulk of the surface roughness measurement for the crater sample.

Roughness

The RMS roughness (as discussed in Chapter 3) was measured across all the recorded image scans of the samples and averaged to provide an overall average layer roughness for their respective methods. This information is shown in Table-5.9 and Table-5.10.

Layer	RMS Roughness (nm)	Error (nm)
Al_2O_3 (1)	41.5	±6.8
Cu	66.7	±1.5
Al_2O_3 (2)	34.6	±6.6
HCD	32.5	±7.2
Al_2O_3 (3)	31.9	±7.8
SiO_2	18.8	±4.9

Table-5.8: Table of RMS surface roughness of cut and polish layers.

Layer	RMS Roughness (nm)	Error (nm)
Al_2O_3 (1)	81	±13
Cu	156	±18
Al_2O_3 (2)	87	±12
HCD	99	±22
Al_2O_3 (3)	82	±11
SiO_2	31	±11

Table-5.9: Table of RMS surface roughness of ion beam crater layers.

This comparison clearly shows a smoother surface for the cut and polish which does not suffer from the ion milling induced ridges on the milled crater.

Surface Oxidation

One major concern with these techniques is that when layers become exposed, they are prone to oxidation. The oxidation will then change the composition of the surface layer and affect its roughness.

In order to mitigate the oxidation problem, the SThM examinations were performed within only a few days of the surface layers being exposed. Even after the relatively short time period the Cu surface had become partially oxidised causing it to affect the interfaces and provide a rougher surface than might be expected after the milling. A further attempt to examine the same samples three months later showed a highly oxidised surface layer which proved too rough to be able to examine in the SThM, this effect was most notable on the Cu surface.

The VLS-80 was designed to be able to function as an in-situ analysis machine to go with the IONTOF developed ToF-SIMS machine. This would allow for a sample to be prepared and examined without exposure to air and thus any oxidisation.

5.4.3 Method Comparison

It is clear both of the preparation methods are able to expose the multilayers and result in surfaces which are examinable using SThM however there are a number of differences between the two.

The 'cut and polish' samples have on average smoother surfaces (38nm RMS) across the different materials compared to the ion mill (86nm RMS). This is due to the presence of the ridges which are caused by the ion milling. However, the preferential etching on the flat surface of the 'cut and polish' has resulted in larger uneven macro changes as can be seen in Figure-5.27. These two different kinds of surfaces will both have some kind of effect on the thermal reading of the tip, but they are not easy to numerically quantify and compare.

The major advantage the ion milled crater has is that the wedge shape exposes a significantly larger surface area of each material which can be examined by the SThM. This is because the 'cut and polish' method is limited by the thickness of the layer whereas the crater exposes along a gradient creating a greater examinable material width for the same thickness. Not only does this allow for better averaging of results but it reduces the influence of edge effects. These factors lead to a clearer delineation between the different layers as can be seen in Figure-5.29, which is helpful for identification and examination of said layers.

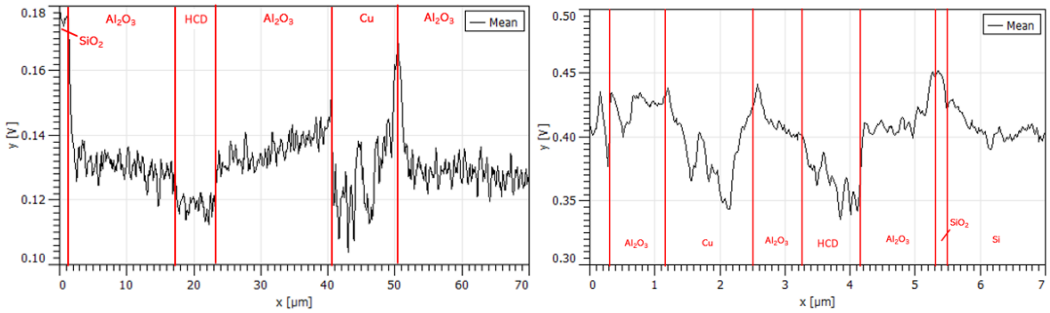

Figure-5.29: Side by side comparison of thermal line average for 'cut and polish' (Left) and ion milled crater (Right). Note that the graphs are laterally inverted.

It is possible to create an even shallower gradient by slowing down the rate at which the dosage is increased whilst milling the surface and increasing the physical length that is milled. This could then be used to examine very thin layers which would not be thick enough for meaningful analysis using the 'cut and polish' method.

Examining the thermal line average graphs in Figure-5.29 also allows for a comparison between the thermal signal which is used to determine thermal properties. It is clear that the error across the ion milled crater is significantly smaller and gives better results. Because of the more clearly delineated layers, the surface and the ability to expose surface areas of materials that are not strictly limited by the layer thickness, the ion milled crater method is the preferable sample preparation technique despite the rougher surface. However, it must also be considered that the technique requires access to uncommon ion beam milling facilities and experimentation to determine appropriate parameters.

5.4.4 Comparison to Modelling

The experimental results of the thermal examination of the ion milled crater can be compared to the COMSOL model version of the same as seen in Figure-5.30.

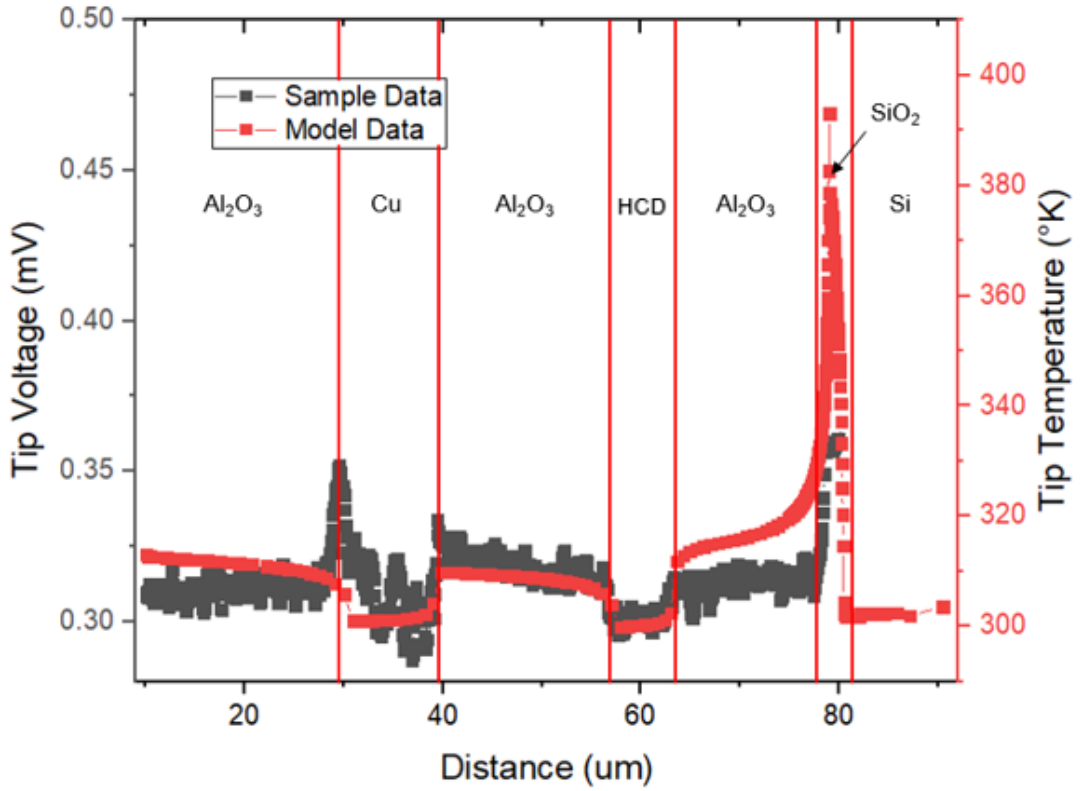

Figure-5.30: Graph comparing thermal signal from ion milled crater sample and tip temperature on crater gradient COMSOL model.

These two data sets seem to match relatively well showing similar sized changes in thermal signal which indicate qualitatively that they show similar relative thermal conductivities. No calibration curve was taken on this measurement and as such a direct comparison between the relative tip temperature changes of the model and measurement cannot be made. Instead the average voltage/temperature of each layer (excluding the SiO_2 peak and its effects) were measured and the scales for each of the measurements set to best fit for each layer.

One of the largest differences is the much higher peak seen in the model data for the SiO_2. This is likely due to the edge effects caused by the interfaces which are not properly simulated in the COMSOL model. This large peak in the SiO_2 also clearly affects the nearby Al_2O_3 making the modelled temperature higher than is seen on the experimental data because the heat path is much more restricted in the model with the heat not being able to escape to atmosphere which causes the tip to heat to unrealistic temperatures due to its arbitrarily high temperature when not in contact with a surface. The SiO_2 peak in Figure-5.30 already includes a higher sampling rate than the rest of the material as the changes take place over a very small distance.

To attempt to further examine the extreme change in the thermal signal the modelled gradient of the SiO_2 was decreased from 0.2 to 0.03. This increases the exposed surface area from 1.8µm to 12µm however as can be seen in Figure-5.31. This only further exacerbated the problem showing that the modelling here is far too idealistic.

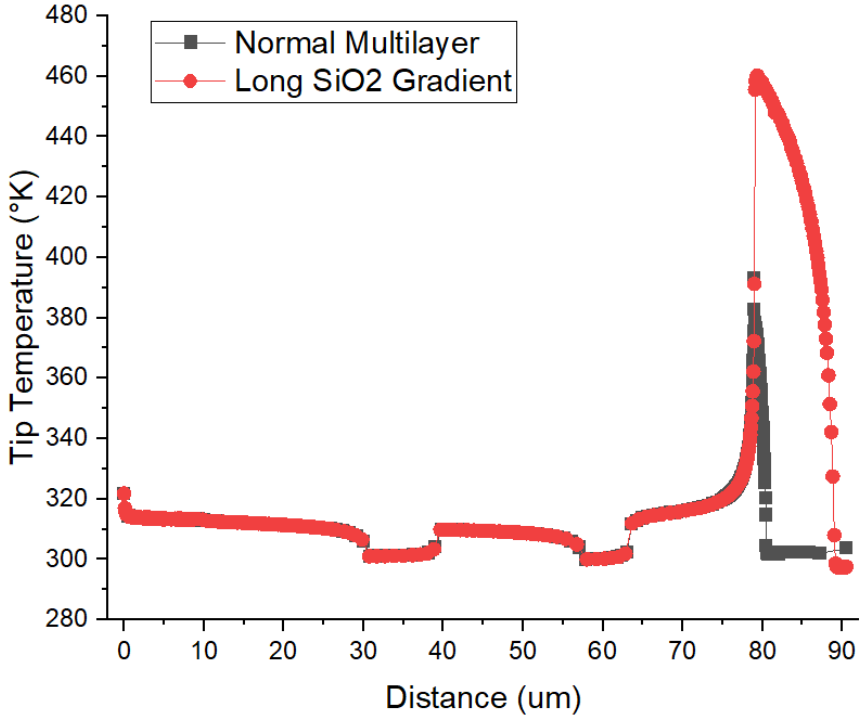

Figure-5.31: Graph comparing COMSOL tip temperature on previously examined multilayer and multilayer with greater exposed SiO_2 surface.

The model data is also much cleaner than that of the sample. This is because the model does not simulate the surface roughness or irregularities such as the ridges seen in the real sample. This is especially obvious in the Cu surface which is very rough and suffers from some oxidation leading it to be significantly rougher and composed of a different material from its model counterpart.

Another potential issue comes from the fact the used values for κ within the COMSOL model are the default values provided by COMSOL which are based on bulk determinations. The actual values within the multilayer are likely to be different as the materials are within the thin film regime which can result in a changed κ value (88). As mentioned in Chapter 4 this is because as the material becomes thinner the average grain size decreases and the amount of grain boundaries increases causing more scattering.

5.5 Determining Thermal Properties

The SThM data was then examined to try and make statements about the materials which were examined within the multilayers.

5.5.1 Qualitative Thermal Conductivity Comparison

Determining a qualitative, and relative understanding of the thermal conductivity of the layers is possible from a simple examination of the thermal scans. For example, by examining Figure-5.29 it is possible to conclude that the SiO_2 has a significantly lower κ value than any other material and that Cu and HCD have a higher thermal conductivity than Al_2O_3.

Examining Figure-5.29 and applying a zeroed correction to the graph we can determine an average thermal voltage for each layer as well as the relative difference between them as shown in Table-5.11 and Table-5.12.

Material	Thermal Voltage (µV)	Error (µV)	% Error	Relative Value
SiO_2	449	±24	5	1
Al_2O_3 (1)	409	±37	9	0.91
HCD	363	±62	17	0.81
Al_2O_3 (2)	408	±38	9	0.91
Cu	390	±66	17	0.87
Al_2O_3 (3)	423	±31	7	0.94

Table-5.10: SThM recorded average temperature for 'cut and polish' sample layers including error and relative thermal conductivity value.

Material	Thermal Voltage (µV)	Error (µV)	% Error	Relative Value
SiO_2	353	±19	5	1
Al_2O_3 (1)	313	±20	6	0.89
HCD	302	±17	6	0.86
Al_2O_3 (2)	319	±18	6	0.91
Cu	313	±32	10	0.89
Al_2O_3 (3)	317	±19	6	0.90

Table-5.11: SThM recorded average temperature for ion milled crater sample including error and relative thermal conductivity value.

This gives an average thermal error for the 'cut and polish' sample of 11% and the ion milled crater of 7%. However, the relative value is only a very rough approximation, and a more quantitative method is required. It is desirable to be able to determine the absolute thermal conductivity value of an unknown layer or layers by using the presence of some known layers within the composite sample.

It is clear to see however that there is a significant difference between how the tip interacts with the different layers. The soft metallic Cu shows not only its relatively high thermal conductivity but also how much rougher the surface is topographically through the thermal signal. It is important to note that it may be possible to see the multilayer structure affecting the heat transport as the different Al_2O_3 layers show a clear difference depending on what materials they are sandwiched between. However as these changes are less significant than the error no definitive statements can be made.

5.5.2 Comparison Method

In their paper 'Determination of the Thermal Conductivity of Diamond-like Nanocomposite Films Using a Scanning Thermal Microscope'(89) F.Ruiz et al. propose the following method for determining the relative contribution of a sample to heat flow to the tip.

Assuming that the tip is heated in atmospheric conditions that heat flow from the tip to the air Q_{air} is given by:

$$Q_{air} = \frac{{V_{air}}^2}{R_{op}} \tag{5.1}$$

where V_{air} is the tip voltage and R_{op} is the probe's resistance at the operating Temperature T_{op} which is defined by:

$$R_{op} = R_{amb}\left[1 + \alpha(T_{op} - T_{amb})\right] \tag{5.2}$$

where R_{amb} is the probe's resistance at ambient conditions, T_{amb} is the ambient temperature and α is the coefficient of resistance. Then when the probe tip is placed into contact with the surface the total heat flow from the tip Q_{total} is:

$$Q_{total} = Q_{air} + Q_s = \frac{{V_{total}}^2}{R_{op}} \tag{5.3}$$

where Q_s is the heat flow between the tip and the sample. We also know that:

$$Q_s = -\kappa_s r_c (T_{op} - T_{amb}) \tag{5.4}$$

Where κ_S is the sample's thermal conductivity, r_c is the contact radius of the tip, T_{amb} is the tip temperature in ambient conditions and T_{op} is the operating temperature of the tip when in contact with the sample.

Using equation (5.4), it is then possible to use the ambient tip conditions as a zero point and then plot the recorded change in heat flow for the tip across a number of materials with a known κ value as in Figure-5.32.

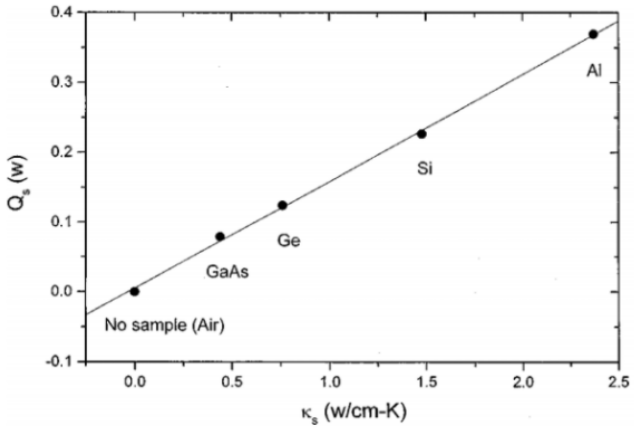

Figure-5.32: Graph comparing thermal signal from ion milled crater sample and tip temperature on crater gradient COMSOL model. (Reproduced from reference (89)).

From here a material with an unknown κ value could be measured using an SThM tip. This would provide a Q_s value which could then be compared to the line of best fit of the known values giving an estimated thermal conductivity.

5.5.3 Multilayer Thermal Conductivity Attempt

The previously mentioned method of κ determination in section 5.5.2 was attempted to be used on the multilayer data. However due to the circumstance of the taken data a number of concessions needed to be made.

Unlike in the experiments performed in the F.Ruiz et al. paper no recordings of the ambient tip conditions were made. This meant that a different baseline had to be chosen. The SiO_2 was used due to it being the smoothest surface in all cases and also the material with the most confidence in its given κ value being similar to the actual value.

As previously noted, the used values for thermal conductivity of the materials are taken from bulk values provided by COMSOL which likely do not match the thin film form of the materials found within the multilayers. For some materials this may make a significant difference however the actual thermal conductivity of the thin layer of SiO_2 is not expected to be significantly different due to its already low value of 1.4 W/m·K.

It was the recorded tip temperature on the SiO_2 surface that was used as a T_{amb} in the calculations. Considering this, one of the thermal images of the VLS-80 recorded multilayer surfaces was examined and a thermal voltage average across each material was recorded and converted into a T_{op} by using the recorded calibration.

Q_{air} was then calculated using equation (5.4) with κ_s as the given value of 1.4 W/m·K and the estimated tip radius contact area of the KNT-STHm-2an probe (from the manufacturers website (43)) r_c of 100nm. Q_s was then calculated for the other materials using their recorded average tip temperatures to determine a Q_{total} and removing the SiO_2 baseline as shown in equation (5.3). The determined relative Q_s values were then plotted on the graph shown in Figure-5.33 against their given thermal conductivity values taken from Table-5.7. It should be noted that the large errors come from the combination with the error of the SiO_2.

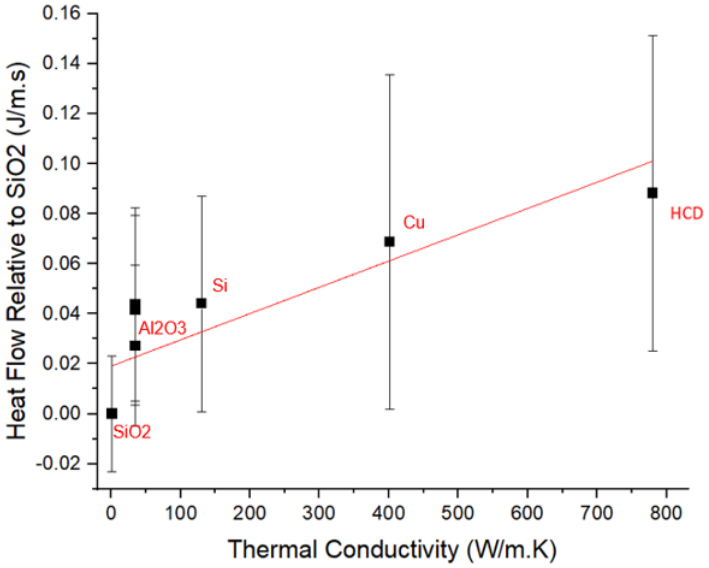

Figure-5.33: Graph of determined Q values for materials in multilayer against given κ values with line of best fit.

It is fairly clear that Figure-5.33 is a poor graph and any attempt to determine a thermal conductivity using the line of best fit would not produce a good result. The surface roughness also results in a very high error which significantly impacts the reliability of the results. Even when averaging the thermal signal over the results of a number of different samples as in Figure-5.34 which reduces the error significantly the resulting graph and line of best fit still provide poor values for unknown κ materials.

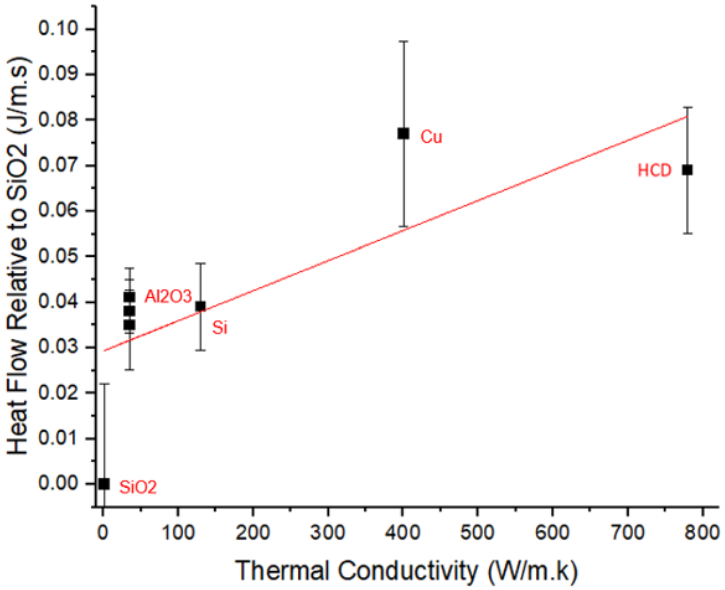

Figure-5.34: Graph of determined averaged Q values for materials across multiple examinations of multilayers against given κ values with line of best fit.

Given that the Cu layer is significantly oxidised resulting in the surface being the roughest, as well as the likeliest to have a significantly changed κ value, the graph in Figure-5.35 was constructed without the Cu. Whilst this significantly improves agreement the fundamental SiO_2 layer remains significantly out of proportion which questions the validity of the results.

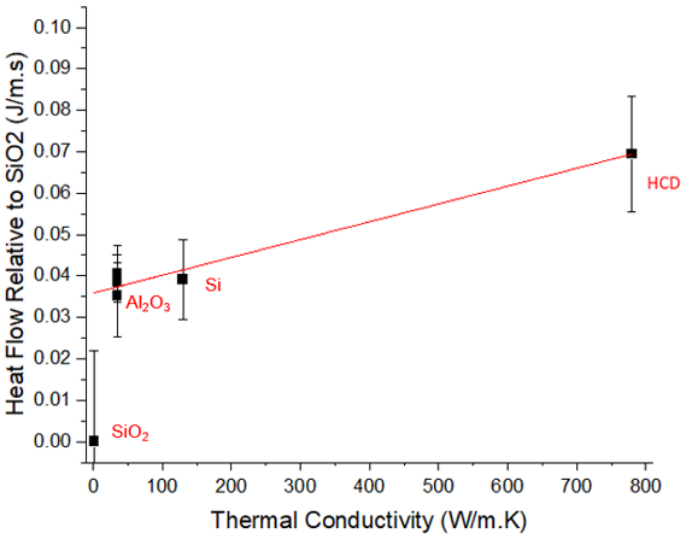

Figure-5.35: Graph of determined averaged Q values for materials across multiple examinations of multilayers against given κ values with line of best fit with Cu excluded.

In examining these graphs, we must look at a number of factors which might account for why it is so wildly out of proportion. As already considered, the actual thermal conductivity values of the materials within the multilayer likely do not match the used values in the model shown in Table-5.7 which are taken from bulk. The thin film nature of the layer can reduce the thermal conductivity of materials by over 50%, especially those with initially high κ values.

The potential presence of complicating oxides and other material combinations caused at interfaces may have an impact. It is clear that even materials which are supposedly the same have significant differences which may be due to their location within the larger multilayered sample. The Al_2O_3 (2) which is sandwiched between the HCD, and Cu layer is consistently recorded at a lower thermal voltage (and thus Q_s) than the other Al_2O_3 layers, however as this change is within error it is difficult to make definitive statements

Using SiO_2 as the baseline could also introduce other issues not considered here. It has been assumed that this would simply shift the graph as the heat flows are all relative. This might not be the case, and this could be introducing complicating factors. For example, in air the contact with the atmosphere is total and unchanging which is not the case when scanning the SiO_2 surface due to the roughness of the sample and the ridges caused by the ion milling..

For future examinations a number of factors are important to consider to try and ensure a better ability to determine unknown κ values. Primarily the use of an ambient atmosphere reading to serve as a more suitable baseline through the measurement of force curves and the inclusion of at least two well characterised materials with known thin film thermal conductivities within the multilayer which can be used as proper references. These materials should also have similar values for roughness so that contact resistance remains similar across the sample. Further attempts at examining the surface through methods such as discussed in Chapter 2 should also be considered.

5.6 Summary

Both of the proposed preparation methods of 'cut and polish' and ion milled crater were able to create viable samples for SThM examination and an initial set of optimal parameters was found for later iteration.

Both of these methods were matched to COMSOL modelling which showed a close correlation displaying the importance of understanding how the multiple layers interact with each other within the material.

Despite the fact that ion milled crater provided a rougher surface the fact that it has fewer macro topographical features and a larger available examinable surface area per layer resulted in almost half the thermal error in the 'cut and polish' sample. This means that it is the preferable preparation method.

The attempts to use the collected results to be able to identify the thermal conductivity of an unknown layer were not successful. This was mostly due to a lack of an air comparison and well characterised reference materials which can be improved upon in any future experiments.

Chapter 6

Silicon Fishbone Setup

As previously discussed in Chapter 4, it is theoretically predicted and some experiments (83) have shown that it is possible to decrease the thermal conductivity of a material by introducing resonant nanostructures. This causes phonons to hybridise into standing waves which impede the flow of heat carrying phonons (70). In this project it was decided to use pillars as the resonant nanostructure coming from a central membrane as shown in Figure-6.1 due to their simple yet stable design which allows for easier fabrication, analysis and simulation.

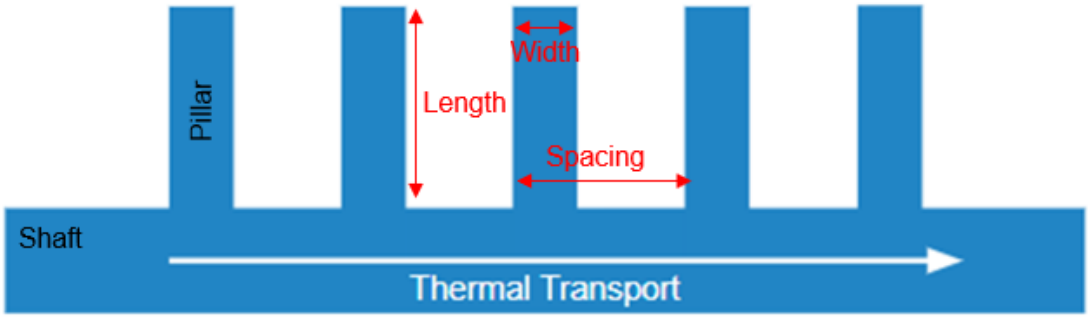

Figure-6.1: Diagram of nanostructured pillars on membrane design used as the basis for designing a material with a reduced thermal conductivity. Important structure parameters are labelled.

Also as discussed in Chapter 4, most other groups examining this area attempt to produce similar materials using some kind of large-scale production to cover a surface (83) or examining individual nanowires (81). However, in this project a different approach was taken with the creation of Si Fishbones.

6.1 Fishbone Design

The Si fishbones instead are created as a 2D pattern of pillars pointing outwards from a central shaft as can be seen in Figure-6.2. These pillars are constructed at a series of lengths, widths and densities.

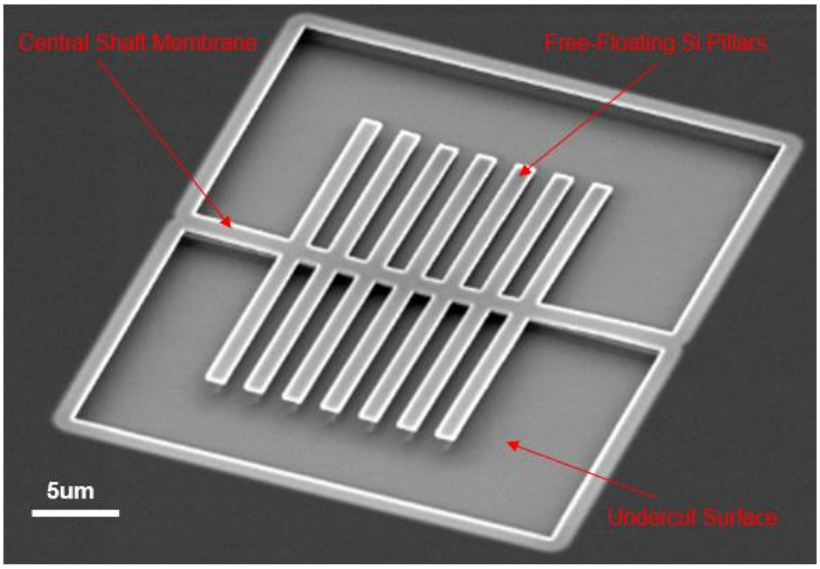

Figure-6.2: SEM image of a Si fishbone used in this project with relevant components labelled.

This Si fishbone design allows for two major advantages. Firstly that the parameters of the individual pillars (such as their length, width and the spacing between them) can be fully controlled, and secondly that the central shaft where the expected change in thermal conductivity will occur is open to examination in an SThM as shown in Figure-6.3. This enables the measurement of the temperature of and thermal gradient across the shaft which is expected to change as the κ of the shaft changes.

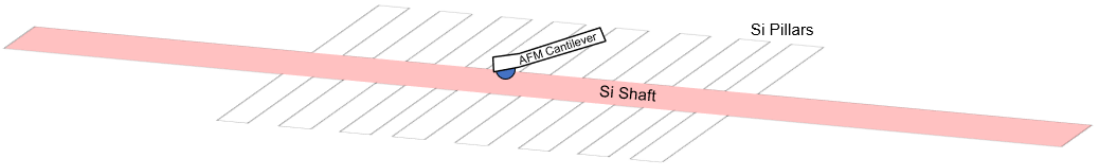

Figure-6.3: Schematic diagram showing SThM tip position in relation to Si fishbone with scanned area (i.e. central shaft only) shown in red.

Across the following sections the fabrication limits of the various pillar parameters are examined. This is then followed by how these limitations informed the design of Multi-Aspect and Multi-Density Fishbones (MARFs and MDFs) as well as how these fishbone samples were provided with a temperature gradient using a microheater. The final part of this section is then dedicated to the experimental parameters used in the creation of the experimental chipset used in the examinations.

A similar design has been experimented on before by Maire et al. (90), however the single shaft design allowed by the shift from time-domain thermoreflectance to SThM measurements allows for more localised examination.

6.1.1 Experimental Chipset Design

The theory suggests that in order to maximise the resonance (and thus give the largest κ reduction) the pillars want to be as tall and as thin as possible (73), whilst remaining below the phonon coherence length. This means that a high aspect ratio is desirable. A number of preliminary chipsets were made to determine the fabrication limits of the fishbones that were produced using e-beam lithography, a reactive ion etch, and an HF undercut as described in Chapter 3.

Dosing

In creating the Si fishbones, e-beam lithography was used to expose the Si fishbone pattern. The dosing refers to the area dose which is defined by:

$$Area\ Dose = \frac{It}{A} \tag{6.1}$$

where I is the beam current, t is the dwell time and A is the dose area with the area dose given in C/cm^2.

The 'clearing dose' is the minimum area dosage required to fully expose the pattern. A series of dosage values were tried in order to fully expose the Si fishbones; these results can be seen in Figure-6.4 where the leftmost three rows of fishbones are visibly not fully exposed.

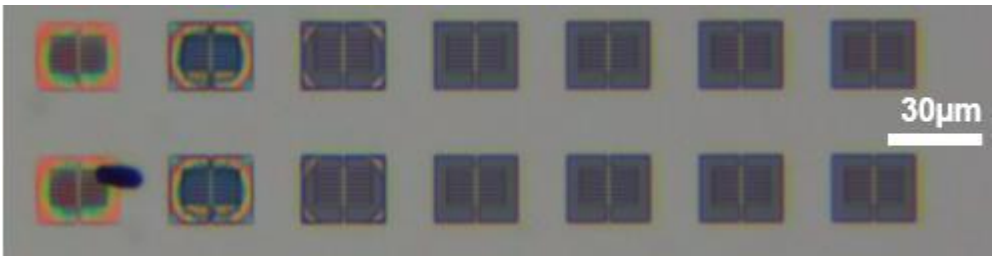

Figure-6.4: Image of ion etching dosing test to determine clearing dosage on large Si fishbones with applied area dosage increasing from the left to right.

Using this experiment it was established that the clearing dosage for the fishbones was $130\mu C/cm^2$ which was used on all further fabrications.

Pillar Width Tests

The fabrication of the pillars using a 1µm width was found to be reliable and repeatable. Attempts were then made to reduce the width of the pillars as much as possible.

It is important to note that for pillar widths below 1µm, proximity effects become significant. This is where the resulting width of the pillar is smaller than that specified in the lithography. This occurs because the electron spot is roughly gaussian and the dosage is cumulative, causing the etch to bleed slightly beyond the specified edge. This results in the pillar being thinner than the value given to the machine. Whilst this occurs at all etch sizes it only becomes significant for distances below ~1µm. Further experimentation could have been performed to correct or reduce the proximity effect but as it resulted in thinner pillars with a higher aspect ratio this was not changed.

However, this effect can result in the complete removal of a feature as is shown in Figure-6.5. The small nubs on the side of the central shaft were programmed into the e-beam lithography machine to be 1µm long and 100nm wide pillars (which is the size of the blue rectangle). Due to the proximity effect the pillars were completely removed giving a lower limit on the possible pillar width.

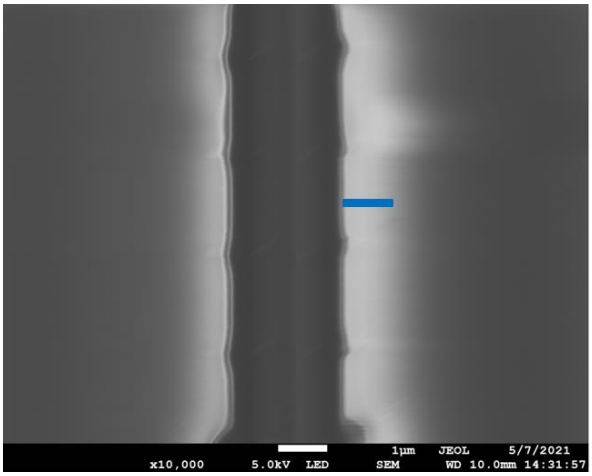

Figure-6.5: SEM image showing a failed attempt to fabricate 100nm wide 10:1 pillars on a central Si shaft with projected size marked in blue.

Given these constraints the smallest fabricated width of the pillars was a fabrication value of 200nm which resulted in a physical width of ~115nm as shown in Figure-6.6.

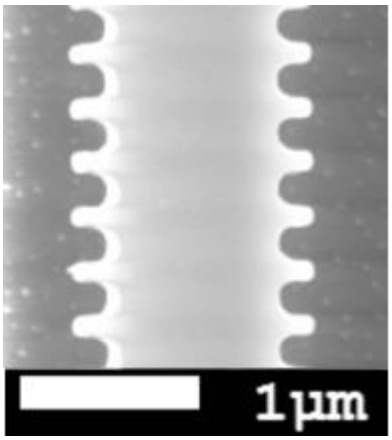

Figure-6.6: SEM image showing ~115nm width, 200nm length Si pillars.

Pillar Length and Phonon Coherence Limitations

Experiments were then performed to determine the maximum fabrication length of the pillars. The initial concern was at what length they would either become too fragile and break or would bend under their own weight so as to contact the undercut surface.

Some early tests using 1µm wide pillars to construct fishbones up to lengths of 30µm resulted in the weight of the pillars causing the central shaft to bend. It was also seen that the individual pillars could bend and become pinned to the undercut SiO_2 by surface forces. These effects are both seen in Figure-6.7.

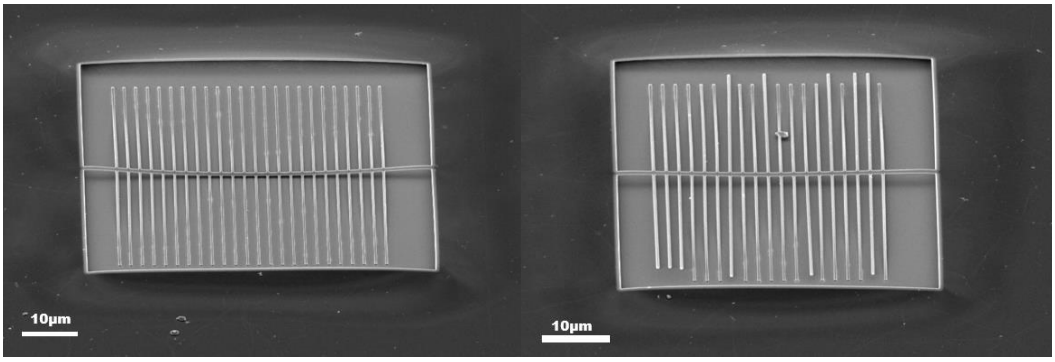

Figure-6.7: SEM images of 30:1 aspect ratio Si fishbone showing bending shaft (Left) and 20:1 aspect ratio Si fishbone showing mixture of pinned and unpinned pillars (Right).

This pinning will likely prevent (or at least lessen) the ability of the pillars to resonate and thus limit the fishbones thermal conductivity reduction capabilities. Such bending was not seen in experiments using thinner pillars which had the same aspect ratio (and thus were also shorter) such as in Figure-6.8.

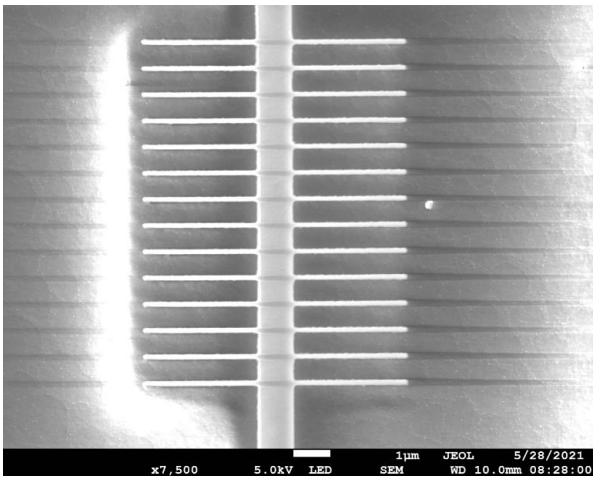

Figure-6.8: SEM image of 115nm wide, 3µm long, 600nm density 26:1 aspect ratio Si fishbone.

However, it was later realised that the phonon coherence length (the distance above which phonons will become incoherent and thus the hybridisation attempts from the pillars will not occur) set an upper limit for the pillar length regardless of pillar width. The exact distance for the loss of phonon coherence is not known due to various factors such as geometric constraints which can affect the mean free path of the phonons within the Si. This was given a conservative estimate of around 3µm based on the bulk value (91).

Maximum Aspect Ratio

As previously mentioned, the higher the aspect ratio is the more phonon modes the pillar can produce and the greater its theoretical effect on the membrane's thermal conductivity. However, the given fabrication limit on the width is ~115nm wide and the phonon coherence length limits the pillars' maximum height to 3µm. This means that the maximum achievable aspect ratio for the Si fishbones used in this experiment is 26:1.

Pillar Density Tests

Within this section the density of the pillars across the shaft is discussed. However, rather than using the actual density values (e.g. 0.5 pillars per µm) it is easier to consider the period between the start of one pillar and the start of the next. This includes both the width of a single pillar and the distance before the next pillar begins as this also factors in the width of the pillar. i.e. A shorter period results in a higher pillar density so long as the pillar width remains unchanged.

As predicted in the theory it is expected that the more pillars there are within a given area the greater the resulting κ change is expected to be. Therefore a density as high as possible is desirable. A series of samples were created using the minimum pillar width of 115nm. These were produced between periods of 2µm and 300nm (i.e., 1 pillar per 300nm is 300nm period). Two of these at different densities are shown in Figure-6.9.

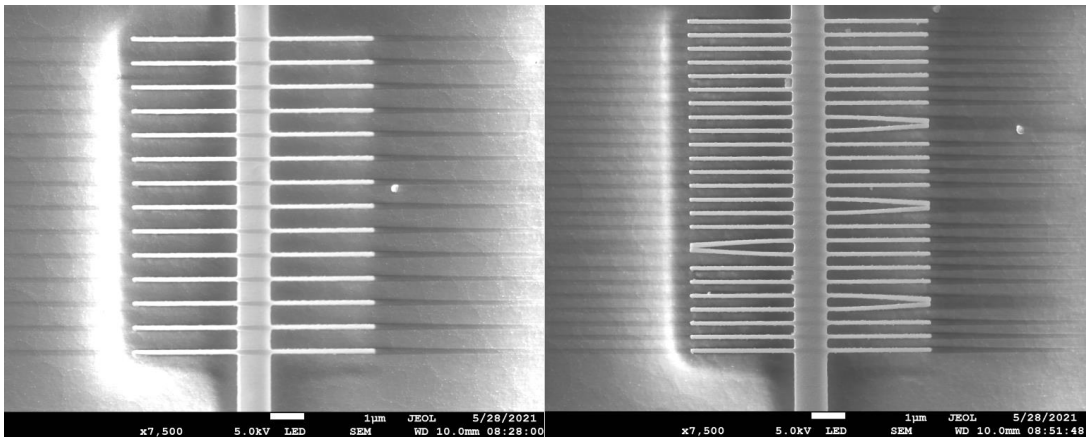

Figure-6.9: SEM Images of 15:1 aspect ratio pillars at 700nm period (Left) and 400nm period (Right) which also shows pillar pinning.

As can be seen in the 400nm period image, when pillars get close enough to each other the pillars can stick together. The distance at which this begins to happen is dependent on the length and width of the pillars. However, for the maximum aspect ratio pillars (i.e. 26:1 at 115nm width) this begins to occur at the 400nm period. It is thought that much like when the pillars pin to the undercut surface this will reduce the ability of the pillar to resonate, reducing the available phonon modes and thus the κ reducing effect of said pillars. This pinning of pillars together is thought to occur during the HF undercut step as surface tension of the drying HF pulls the features together. The amount of pinning is varied, with one structure displaying near total pinning and another identical structure displaying almost none. One clear factor in the amount of pinning seen is that the longer pillars result in an average of more pinning at the same density.

At the lowest used period of 300nm and fabrication aspect ratio of 26:1 an examination across multiple feathers showed that an average of 29±1.5% of the pillars would be pinned. Despite the fact that the pinning may have reduced the pillar resonance effectiveness, the density of pillars on the membrane at 300nm period allows for a significantly higher number of pillars (and thus theoretically

greater effect). The shortest period which exhibits no pinning has ~60% fewer unpinned pillars present.

Chosen Pillar Parameters

These experiments have established a minimum pillar width of 115nm, a maximum length of 3µm and a minimum pillar period of 300nm. The combination of these parameters can be seen in Figure-6.10.

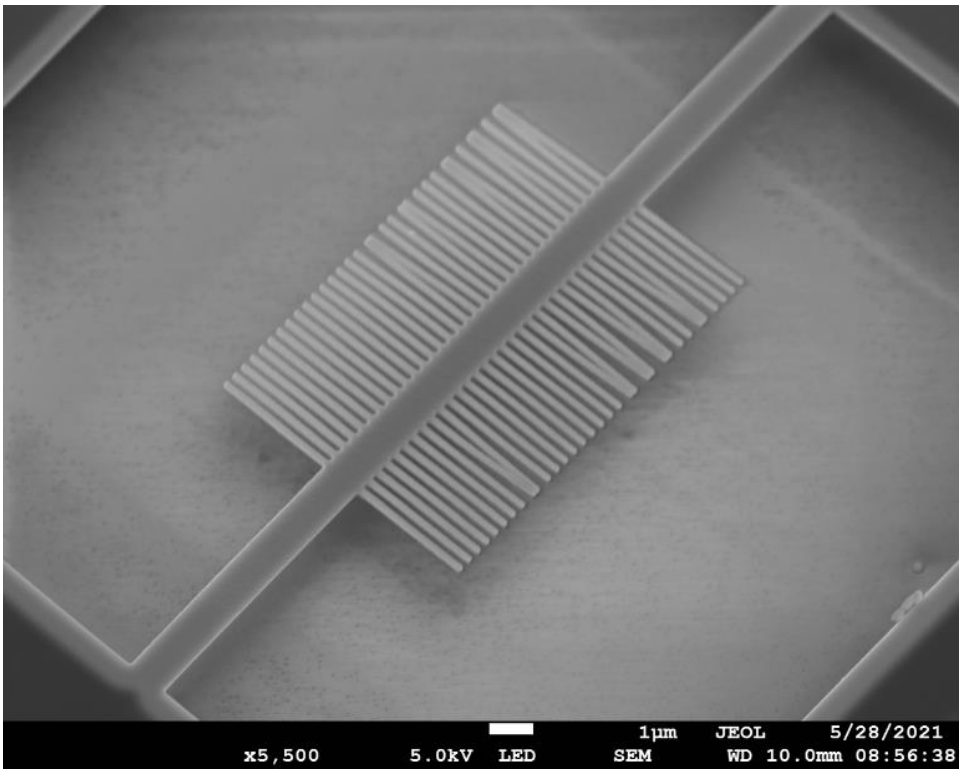

Figure-6.10: SEM image of a 115nm wide, 3µm long, 300nm density 26:1 aspect ratio Si fishbone representing the best fabrication feather.

6.1.2 MARF and MDF Designs

With the fabrication parameters established it can be considered how best to use these in an experimental setting. When performing various preliminary examinations, it was realised that due to changes in the calibration it could be difficult to compare results between two different SThM images.

As such it was decided to fabricate multiple kinds of pillars on an individual shaft. The idea being that each set of pillars would affect the central shaft's thermal conductivity a different amount. That way there should be a clear difference between the thermal gradient measured on one part of the shaft compared to the

other which can be measured in a single scan. If the heat flow through each part of the shaft is fixed then differences in the conductivity will give rise to differences in the thermal gradient.

Two different types of fishbone were created. Multi-Aspect Ratio Fishbones (MARFs) and Multi-Density Fishbones (MDFs) where the pillar aspect ratio and density respectively are changed halfway along the fishbones. Both of these are shown in Figure-6.11 and SEM images of the fabricated feathers are shown in Figure-6.12.

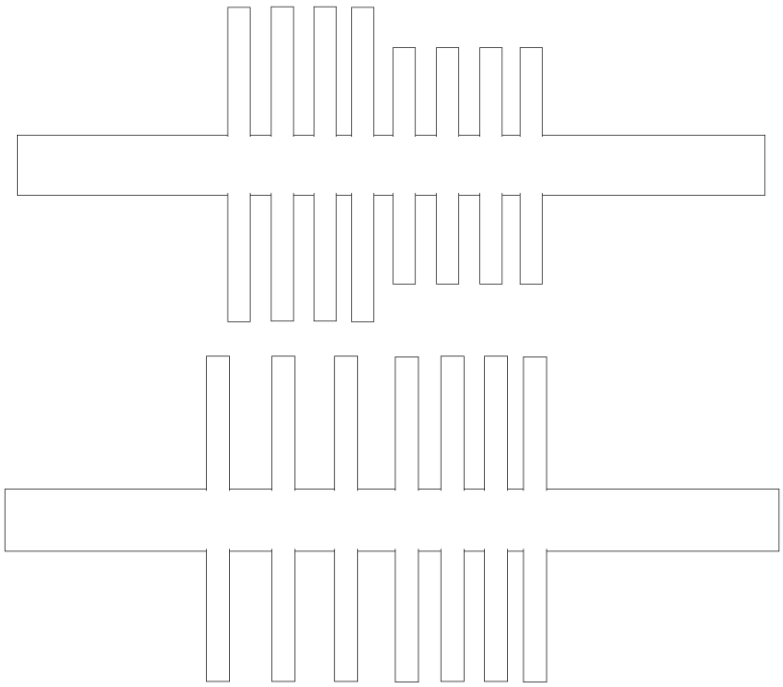

Figure-6.11: Schematic diagram of a multi-aspect ratio fishbone (Top) and multi-density fishbone (Bottom).

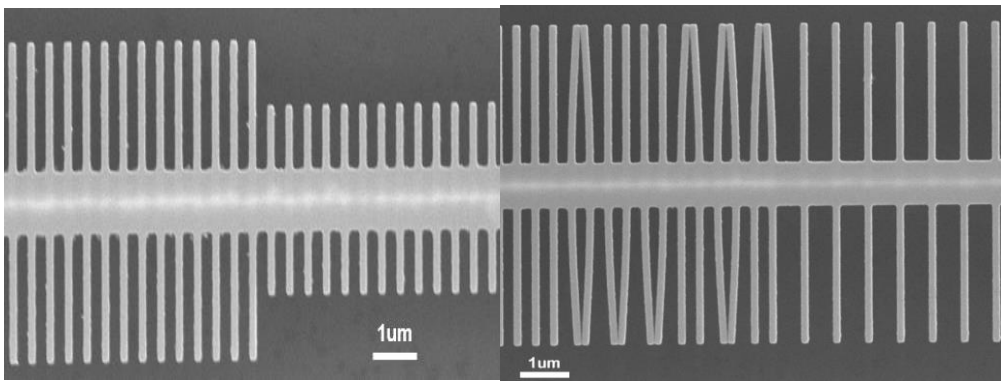

Figure-6.12: SEM image of MARF Si fishbone (Left) and MDF fishbone (Right). Note pinning in the higher density area

6.1.3 Microheater Design

The microheaters were designed to provide a temperature gradient across the SoI chip and thus also across the Si fishbones. This would allow for measurement of a change in thermal conductivity by measuring how the thermal gradient varies across the shaft.

As can be seen in Figure-6.13 the heater consists of a small heating element of approximately 210x250µm size made of 10µm wide wiring which follows a three-loop meander pattern which produces the heat. This is attached to a larger winged structure which provides two large connection pads which wires can be easily bonded to. The entire microheater is constructed using UV lithography and metal evaporation deposition to produce a 100nm thick Au heater layer on a 5nm Ni adhesion layer.

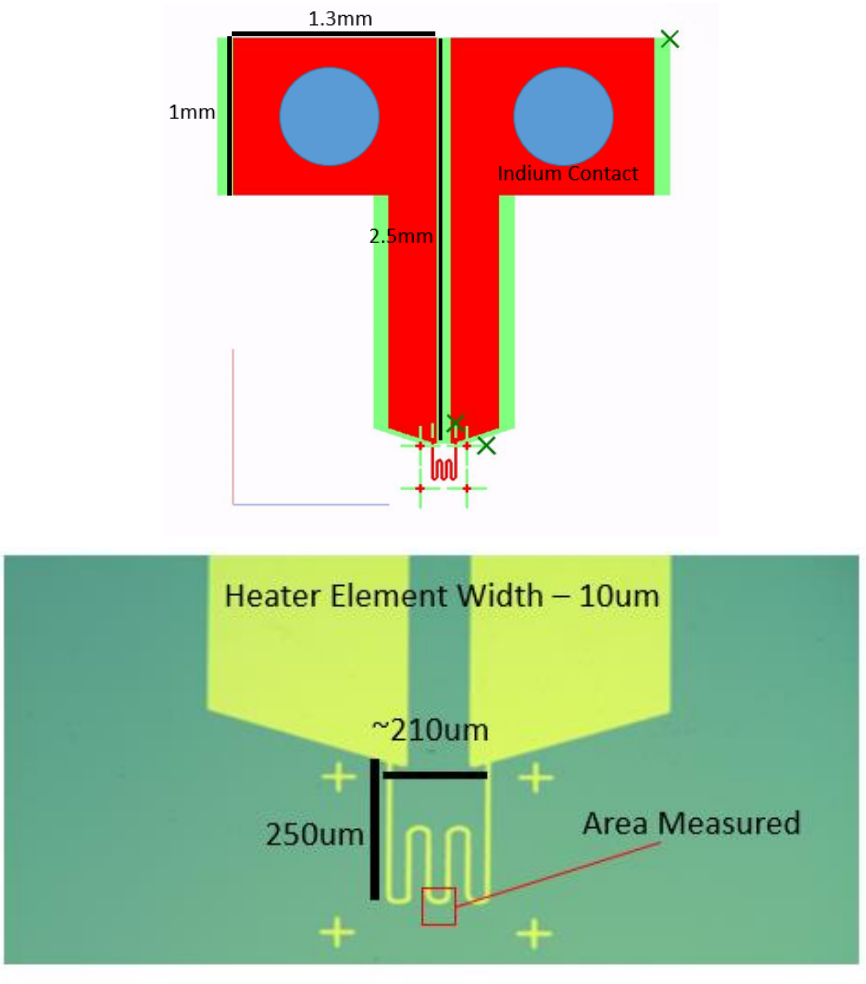

Figure-6.13: Diagram of full heater including space for wire bonded contacts (Top) and optical microscope image of microheater element (Bottom) with scan area for Figure-6.14 marked for reference.

An AFM topographical examination of the heating elements show a depressed surface with significantly ridged edges as well as a thin layer of deposited Au around the element as can be seen in Figure-6.14. These effects are caused by the lift off process where the excess Au is removed from the surface and cannot be easily avoided. However, it is not thought that this will cause any substantial issue with the heating which would affect the experimental results in this experiment.

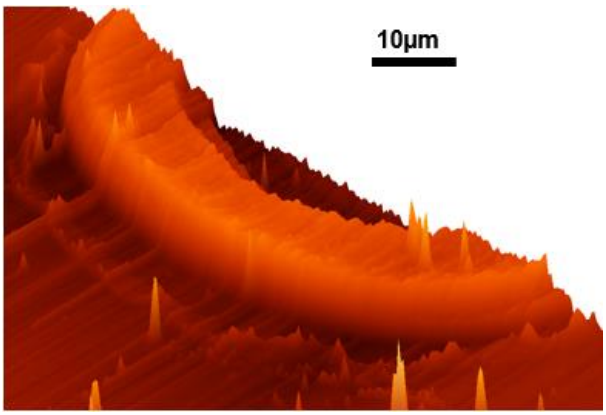

Figure-6.14: 3D representation of topographical AFM scan of heating element and surrounding Si.

An SThM examination of the heated element performed in collaboration with Professor Weaver and Dr Dobson at the University of Glasgow was performed using a Veeco Dimension 3100 AFM converted for use as an SThM. As shown in Figure-6.15 there is a clear and measurable temperature gradient coming from the heater.

It should be noted that the heaters used in this initial examination were constructed on a pure Si substrate as opposed to the SoI substrate used for the feather construction. Whilst this will change the exact temperature gradient it is not expected to make any significant difference to the overall trend.

A calibration had been performed and gave a conversion calculation of:

$$T(^0C) = 0.0735 * V(mV) + 250.1 \qquad (6.2)$$

where T is the temperature in celsius and V is the recorded tip voltage in millivolts. This allows us to convert the images into absolute temperatures as used in Figure-6.15.

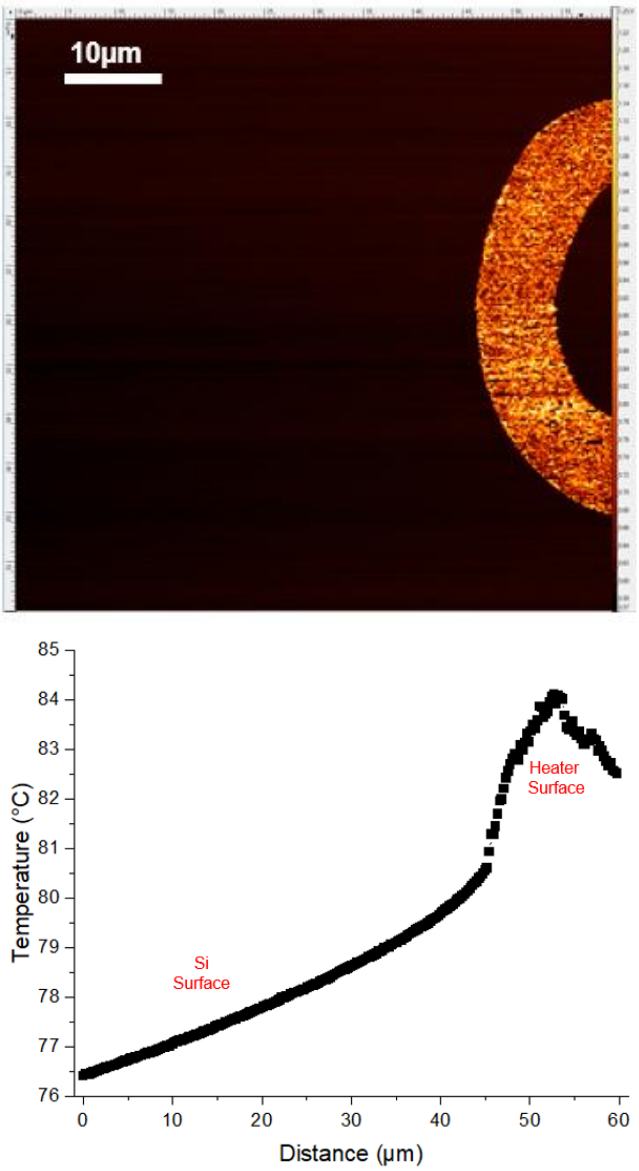

Figure-6.15: Thermal SThM image of microheater element and surrounding Si surface with 8V applied to heater (Top). Whole image line averaged thermal graph of SThM image (Bottom).

We can see that in the 40µm immediately beyond the heater the temperature drops by 2.8K giving a gradient of 79.3 ± 0.4mK/µm. Corresponding data sets were taken for an applied voltage of 2V and 5V which gave respective approximate linear gradients of 18.3mK/µm and 41.3mK/µm. This information as well as the average temperature of the scanned heater element are shown in Table-6.1.

Applied Voltage (V)	Average Heater Temperature (ºC)	Approximate Linear Thermal Gradient (mK/µm)	Error In Linear Thermal Gradient (mK/µm)
2	37.1	18.3	±0.0
5	43.7	41.1	±0.1
8	83.3	79.3	±0.4

Table-6.1: Average surface temperature reading and immediate gradient for microheater under different applied voltages.

Considering the rapid decay of the temperature it seems clear that the temperature gradient is not linear despite the low error in the gradients. This can already be seen from the 8V graph in Figure-6.15 and is further confirmed in the COMSOL modelling detailed further in the chapter which shows that there is a log normal decay across the Si surface.

However, examinations taken on the scale of the Si fishbones both close to the heater and away from it can be approximated as linear. This can be seen in Figure-6.16 which were taken later on SoI samples with constructed microheaters.

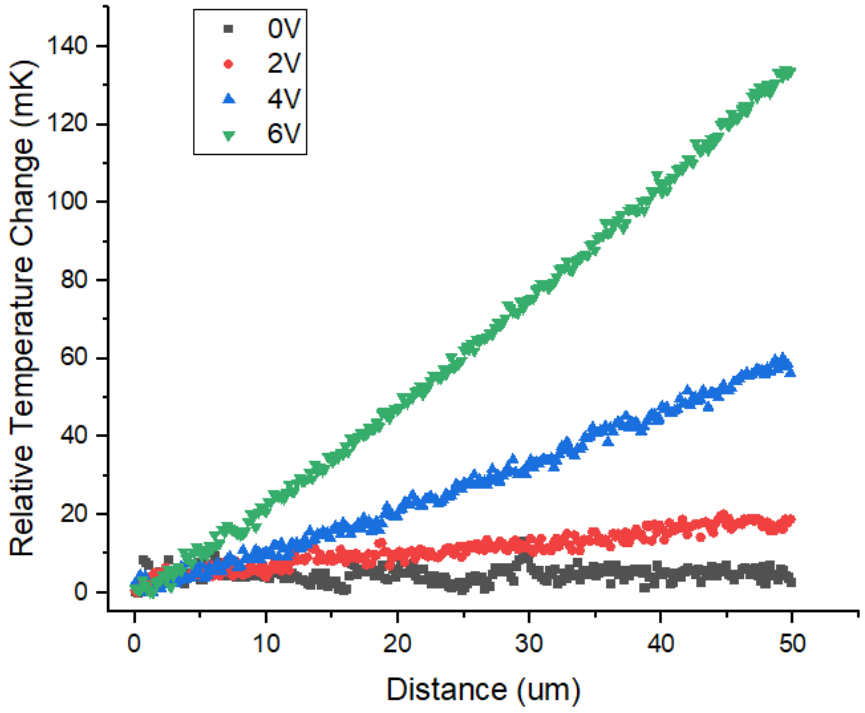

Figure-6.16: Graph of SThM measured relative temperature change of pure SoI surface next to Si fishbones at different applied voltages to the microheater showing near linear temperature decay.

It is important then that the Si fishbones are placed as close to heaters as practically possible and where possible those in the nearest proximity to the heaters are used for experimentation. This is not only because the surface will be hotter, which is desirable, but also that the temperature gradient will be larger which increases the chance of changes in thermal conductivity being seen.

Temperature Stability

After some initial experimentation it was found that in order for the sample to reach a steady state the heaters would need to be switched on for at least an hour or more. In addition, individual scans could take upwards of an hour to perform with multiple scans performed in succession.

This necessitated that the heater needed to be able to remain on and thermally stable for a period of days. This was possible, however in order to be active without breakage for an extended period a maximum voltage input of 6V was used.

6.1.4 Chipset #7 Design

The bulk of the examination work was performed on Chipset #7 which included MARFs, MDFs and also a set of control shafts with no pillars. The overall layout of the chipset can be seen in Figure-6.17.

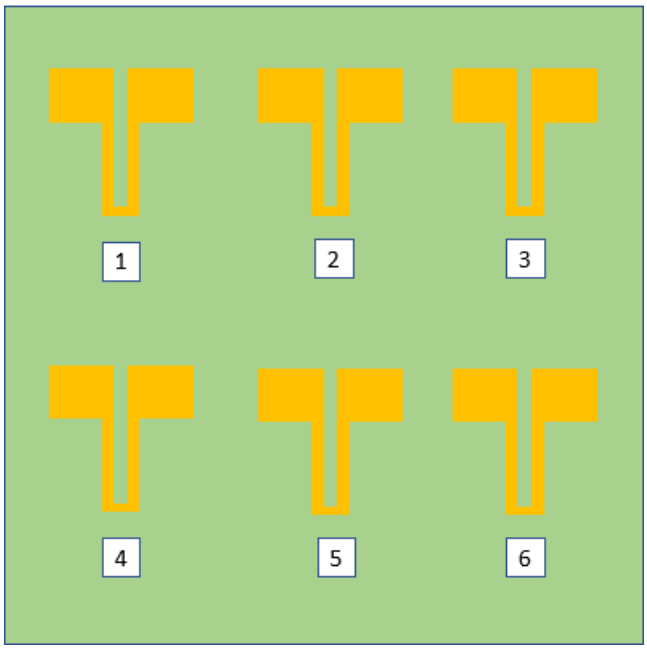

Figure-6.17: Diagram of Chipset #7 layout with marked heater positions which are described in Table-6.2.

These heaters had different experimental sets of fishbones placed in close proximity as shown in Figure-6.18. Each set of fishbones next to a heater is made of a 4x4 or 5x4 (for the MDF experiments) array of fishbones resulting in 104 fishbones per device. Several of these full chips were fabricated in order to account for potential heater or fishbone failures.

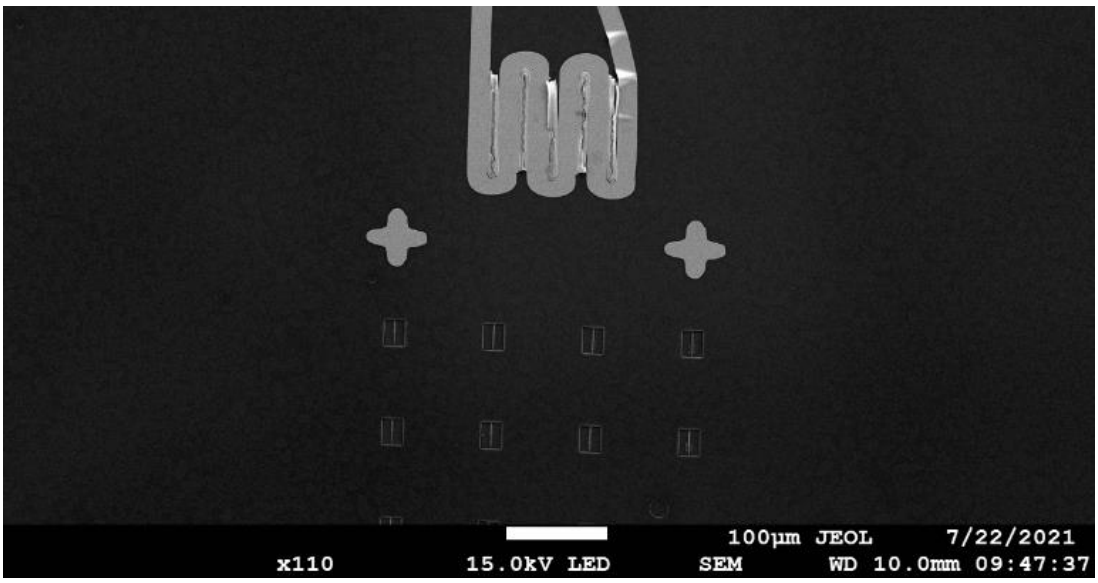

Figure-6.18: SEM image of (damaged) heater in proximity to the Si fishbones.

In order to ensure that only the desired pillar parameters were changed, all of the fishbones were standardised at a shaft length of 26µm and a shaft width of 1µm. They were surrounded by a 20µm wide undercut window, and the pillar parameters were dictated by the experimental setup as dictated Table-6.2.

Heater Position	Fishbone Type	Testing
1, 2 (Repeated)	MARF	Aspect Ratio
3	0-MARF	Pillars/No Pillars
4, 5 (Repeated)	MDF	Density
6	Shaft Only	Control

Table-6.2: Table of heaters in relation to experimental fishbones in proximity.

These different types of fishbones allow for different experiments to be performed. The MARF fishbones test for the effect of altering the aspect ratios on the κ of the shaft and the MDF fishbones test for changing the density. The shaft only fishbones were designed as a control.

Multi-Aspect Ratio Fishbones

For the MARF tests a 400nm pillar density (i.e. one pillar per 400nm) was chosen for all fishbones and the aspect ratios used were 1:1 - 5:1, 5:1 - 5:1, 10:1 - 5:1 and 15:1 - 5:1, with the change halfway along the shaft. The fishbones were laid out as shown in Figure-6.19 which shows the different aspect ratios across the X axis and the repeated fishbones in the Y.

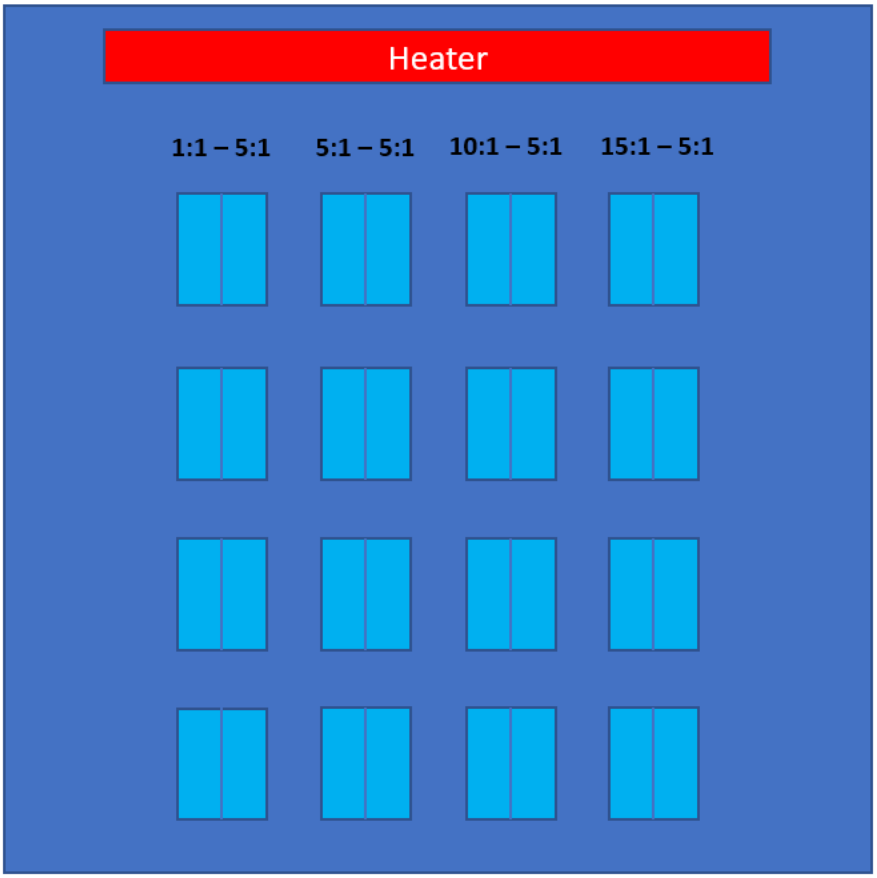

Figure-6.19: Diagram of heater and Si fishbone layout as used for the MARF examinations.

It is important to note that as mentioned earlier the fabrication aspect ratios used in the design of the fishbones do not match that of the physical structures. This is because the fabrication is imprecise at such a scale and the proximity effect causes more of the material to be removed than intended. This results in a pillar width of 115nm as opposed to the fabrication value of 200nm. However, the length was still determined based on a multiplication of the fabrication width. Table-6.3 shows a conversion between the input fabrication aspect ratios and the experimentally measured aspect ratios for chipset #7.

Fabrication Aspect Ratio	Experimentally Determined Aspect Ratio
1:1	2:1
5:1	9:1
10:1	18:1
15:1	26:1

Table-6.3: Table of fabrication aspect ratio conversion to experimentally measured aspect ratios.

0-MARF Fishbones

Heater 3 and its 0-MARF fishbones uses the same idea as the MARFs but instead of having a 5:1 on one side of the fishbone it uses a 0:1 (i.e., no pillars) as a control measure. Again, these pillars are at a density of 400nm, and the used aspect ratios were 1:1 - 0:1, 5:1 - 0:1, 10:1 - 0:1 and 15:1 - 0:1 in a layout that closely matched Figure-6.19. The top two rows of feathers were fabricated with the pillars on the top half of the shaft and for the bottom two rows this was reversed as shown in Figure-6.20.

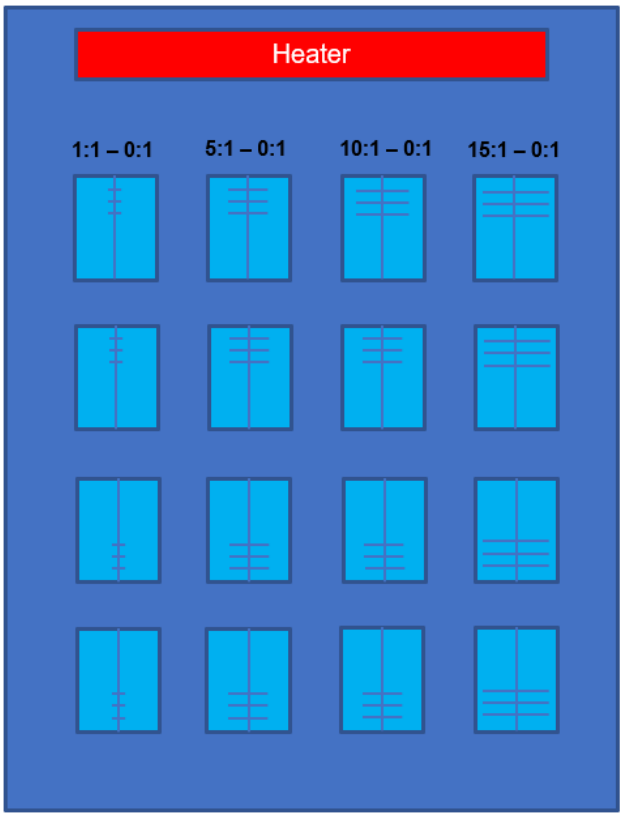

Figure-6.20: Diagram of heater and Si fishbone layout, also showing changing direction of Si fishbones.

Multi-Density Fishbones

As with MARFs the MDFs have a split in the middle where there is a change in the pillars. Instead of changing the individual pillar geometry the pillar density is changed. All of these pillars use a fabrication width of 200nm (and thus a measured width of 115nm) and a length of 3µm (i.e. aspect ratio of 26:1). The periods used are 2000nm - 700nm, 1000nm - 700nm, 700nm - 700nm, 400nm - 700nm, and 300nm - 700nm.

Once again, the proximity effects are important to consider here. Whilst the period of the pillars (i.e. number of pillars per length) remains the same, the fill factor and the distance between each pillar is changed. Table-6.4 shows the expected period from the fabrication parameters and the averaged measured period from chipset #7.

Fabrication Period (nm)	Fabrication Separation (nm)	Approximate Real Separation (nm)	Approximate Fill Factor (%)
2000	1800	1885	5.8
1000	800	885	11.5
700	500	585	16.4
400	200	285	29
300	100	185	39

Table-6.4: Table of conversion between fabrication period values and the resulting measured periods. Including the resulting fill factor.

Shaft Only

The 'shaft only' fishbones have no pillars on them but are otherwise the same size as the other shafts at 26µm length and 1µm width within a 20µm wide undercut window. This is to allow for a controlled comparison with the fishbones.

This can be used to determine if the observations for the MARF and MDF experiments are due to the presence of the pillars or some other factor inherent in the shaft or tip.

6.2 Fishbone Fabrication

The Si fishbones were created using lithography and etching as described in Chapter 3. Briefly, a Silicon on Insulator (SoI) chip had a series of microheaters produced by using spin coating and UV lithography to create a masking layer. The removed segments of the mask then allow for a metallic deposit to be made directly onto the chip surface with the rest being later removed resulting in the desired metallic microheater remaining.

The chip then has another round of spin coating and then undergoes e-beam lithography and a reactive ion etch to produce the Si fishbones which are then undercut with a wet etch. This produces a chip as shown in Figure-6.21.

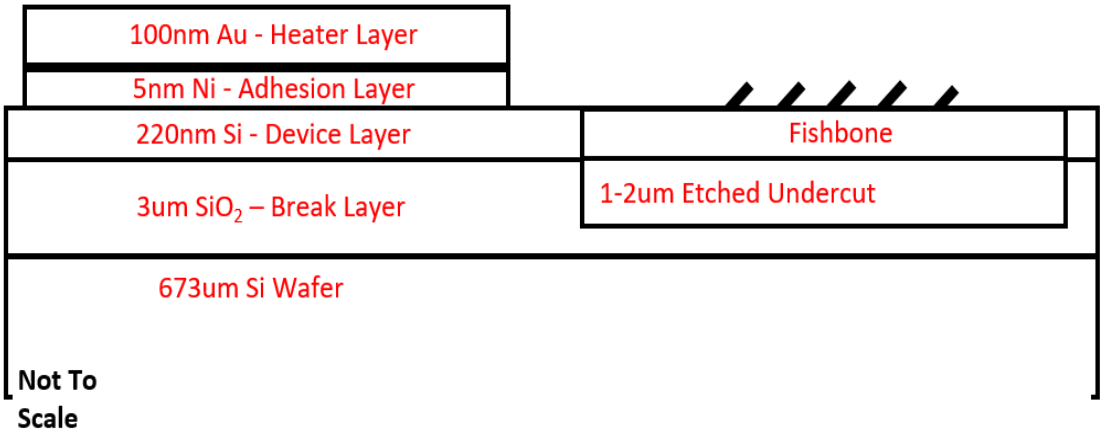

Figure-6.21: Cross sectional diagram of SoI chip layers (including microheater composition).

In order to power the microheaters a chip was designed with the assistance of Mr Timothy Ayers from the University of York Electronics Workshop. This consisted of a PCB board with lead-free solder coated copper plates and was manufactured by Eurocircuits. The mounting has precision screw holes which allow for consistent mounting onto the VLS-80 sample plate and connectors which allow for up to two heaters to be wire bonded at the same time as shown in Figure-6.22.

These mounting devices could then be securely attached to the VLS-80 sample plate through the use of screws and a cable attached to the power pins.

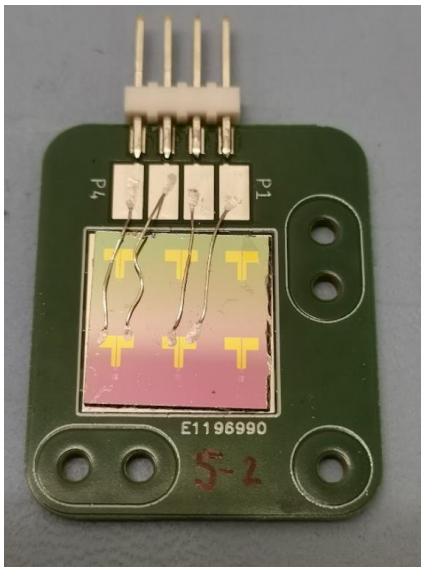

Figure-6.22: Image of SoI chip 5-2 on PCB mounting device.

6.2.1 Shaft 'Bowing'

It was found upon examination that there was a degree of surface raising (described as 'bubbling') around the Si fishbones and that the central shaft of the fishbones was bowed. This can clearly be seen in Figure-6.23.

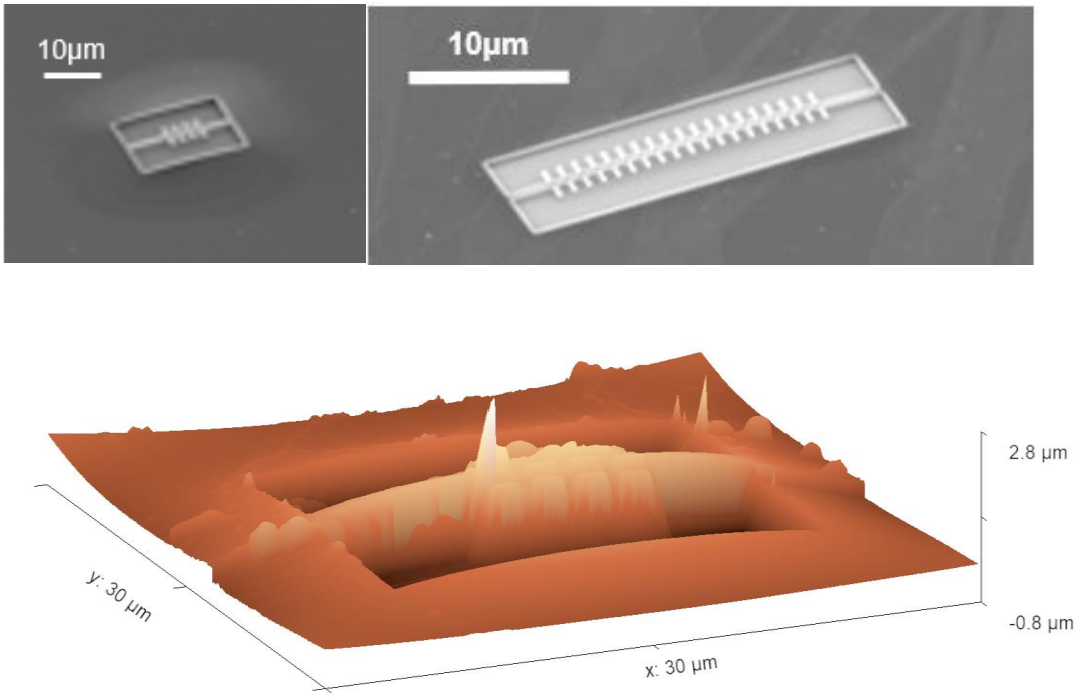

Figure-6.23: SEM Images showing surface bubbling (Top Left) and shaft bending (Top Right) as well as VLS-80 topographical image of Si fishbone (Bottom) showing surface bubbling and shaft bowing.

This effect occurs due to inherent stress within the silicon layer. The HF etches isotropically and thus whilst etching downwards it also etches outwards beyond the desired Si window determined in the e-beam lithography. This results in a section of the device layer with no SiO_2 below it which then pulls upwards due to stress as shown in Figure-6.24. This upward pulling also then affects the Si Fishbone causing it to bow between the two raised surfaces.

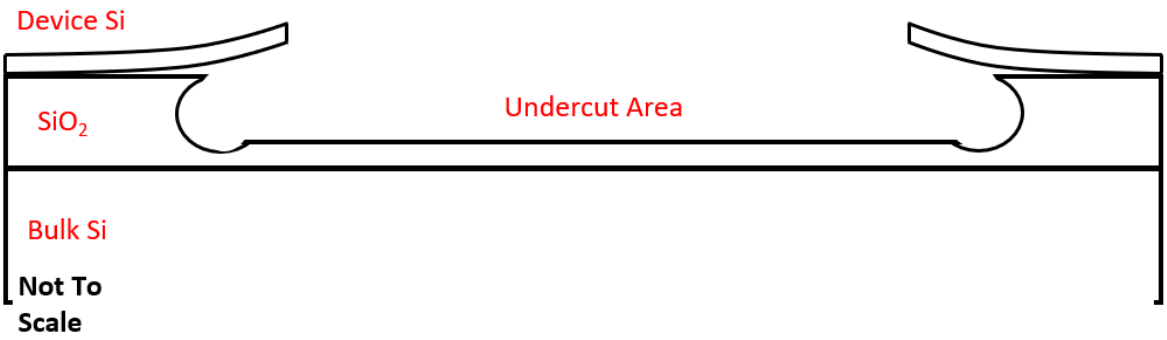

Figure-6.24: Diagram of anisotropic over etching of the HF which results in undercut device Si which then causes surface bubbling and shaft bowing.

The amount of over etching that occurs is due to the grain structure of the underlying SiO_2. Additionally, the amount of time the feather was submerged in the HF wet etching was a factor in the amount of undercut but this was only controlled to the precision of a second over an etch only tens of seconds long. This and an unpredictability with the silicon stresses ultimately results in varying and uncontrollable under etching, and thus the exact degree of surface bubbling or shaft bending is essentially random.

The shaft bowing is important because it affects how the tip interacts with the surface and thus its thermal readings. Figure-6.25 shows two different measurements of the shaft. The first is of the topography of the shaft and its surrounding material. This shows the effects of the surface bubbling. The second image is the topography of just the shaft which is relatively flat compared to the bubbling as a whole but remains curved.

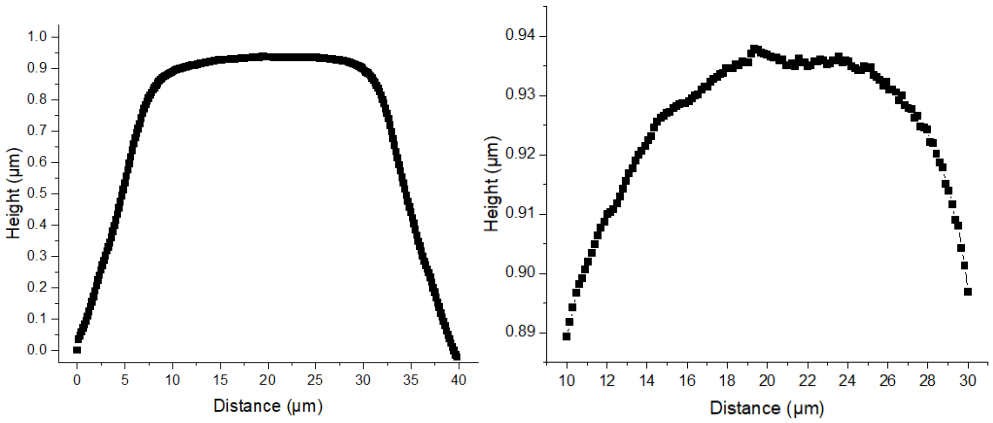

Figure-6.25: Topography graph of shaft average topography of full MARF fishbone (Left) and central pillared area only (Right). Note the different X and Y axis units.

In order to control for the shaft bowing several copies of each chipset were made and the one that displayed the least amount of bowing and bubbling was chosen for experimentation. The result of this was that the measured range of the bowing that was seen across the shafts used in experiments gave a maximum curve height of the shaft around 100nm whilst the surface bubbling leading up to the shaft were of height differentials of between 0.5-1.3µm.

6.3 Fishbone COMSOL Modelling

In the first instance it was decided to try and completely recreate the Si fishbone sample in the finite element program COMSOL (52). This was used to examine the effect of the microheater across the surface of the Si chip. However, it was found that this kind of simulation was too large for any more complex COMSOL simulations, largely due to the several orders of magnitude difference between the thickness of some of the different elements. Simpler and more specific COMSOL models (including being converted to 2D) then had to be made to test the effects of thermal conductivity change on the measured tip temperature and the effects of having a curved shaft.

As COMSOL does not include the ability to simulate the phonon hybridisation it was instead used to model the temperature in the case of no change in the thermal conductivity and to simulate the impact that different values of κ, which may be produced by the phonon activity, would have. It can be used to simulate the 'shaft only' fishbones as well as have thermal conductivity changes applied to the shaft.

6.3.1 3D COMSOL Model Construction

The model, shown in Figure-6.26,,is constructed of a base layer of Si 550µm thick with a 3µm thick SiO_2 layer on top and a further 220nm layer of Si to closely match the real sample. However, it should be noted that whilst the model attempts to replicate the layer thicknesses the experimental Si substrate thickness is over 1mm compared to the model's 550µm. The width of the model is also only 500x500µm compared to the actual chip which is 15x15mm

Here only the heating element of the microheater has been modelled due to size constraints as well as providing the majority of the actual heating of the sample. As with the real sample the heater consists of a 5nm Ni adhesion layer and a 100nm Au layer making 10µm wires with the three-loop meander pattern.

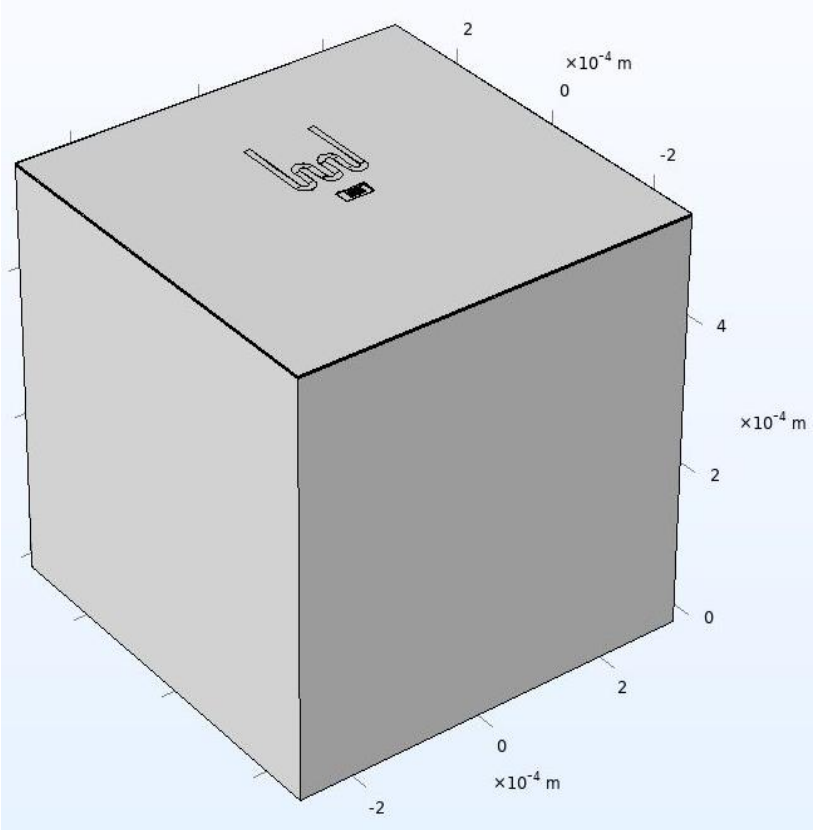

Figure-6.26: 3D COMSOL model of microheater and Si fishbone.

A rectangular hole is then cut out with a depth of 2µm through the top Si layer and the SiO_2. Here a Si fishbone is inserted on a level with, and of the same thickness as the device layer, over the hole as can be seen in Figure-6.27. The size of the hole and all the parameters of the fishbone are individually variable.

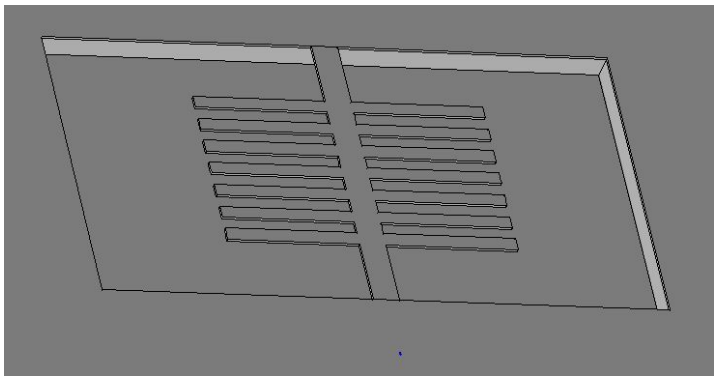

Figure-6.27: Image of 3D COMSOL Si fishbone suspended above Si window.

Model Heating and Cooling

A current is supplied to the end of the Au wires which causes joule heating in the meander. The bottom face of the bulk Si was set to a constant value of room temperature (rT=293.15K) to simulate cooling from the bulk material.

6.3.2 3D COMSOL Model Results

Modelling the fishbones revealed a number of important factors to consider. This includes the overall temperature profile of the sample caused by the heater, the tip-sample interaction, and the resulting temperature changes seen from differences in thermal conductivity.

Surface Temperature

Modelling the surface heating was very important in understanding how to perform and interpret an SThM scan of the surface. The performed SThM scans (such as the previously discussed heater scans like Figure-6.16) are limited by the SThM scan range and are too small to be able to provide a full picture. At the scale of individual scans the gradient can appear linear, but it is not clear that this is the case across the entire sample.

As mentioned only the heating elements were able to be simulated due to the physical constraints of the model. It is unclear if the way COMSOL model heats the model matches the physical sample. Additionally, it is not known if the 'arms' of the microheater are also heated in the physical sample whilst in the model they remain cool and this could reduce the overall temperature and the temperature profile of the heater. Despite this it was not expected that this would be a large difference especially as only the temperature change was of interest rather than the absolute temperature.

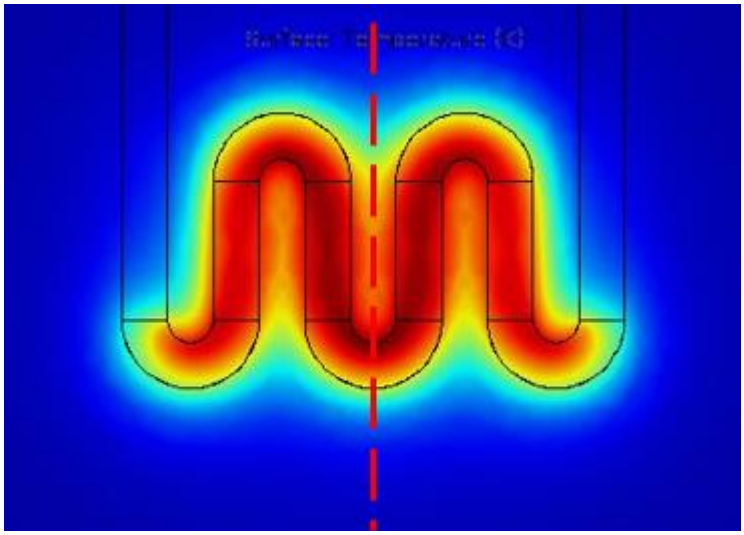

Figure-6.28: Temperature map of joule heated heating element in arbitrary units with central line marked.

Figure-6.29 shows the surface temperature across the complete model as measured in a line which passes through the centre of the heater as marked in Figure-6.28, henceforth referred to as 'central line'. The applied joule heating voltage is based on approximations of the experimental heater and results in heater temperatures between 60-70ºC.

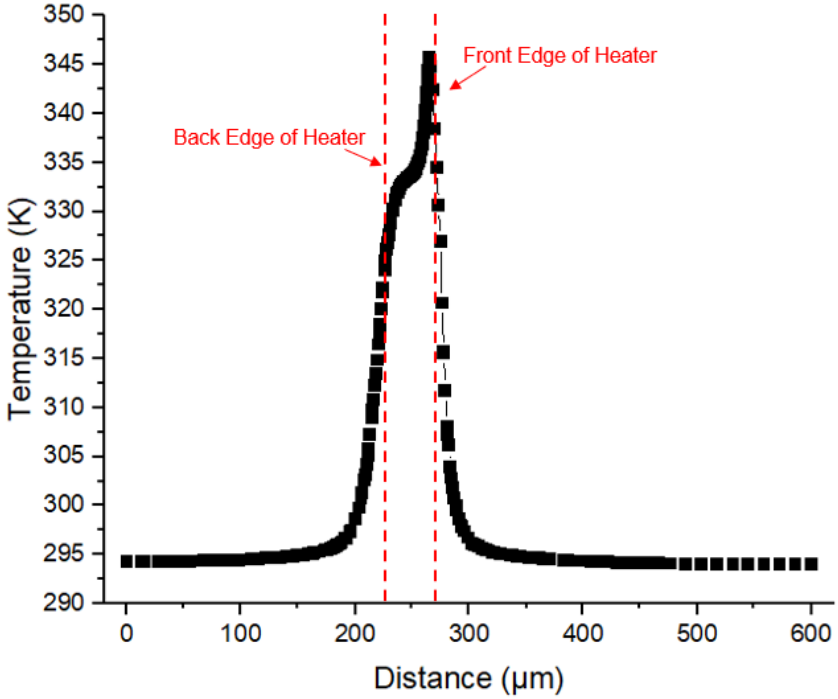

Figure-6.29: Graph of surface temperature across central line of joule heated sample.

This shows the presence of the heater but importantly also shows the steep temperature drop-off beyond the heater which starts as a near-linear decay as seen in the experimental work performed in 6.1.3. However, this rapidly drops off after only a short distance as shown in Figure-6.30 which can be approximated as a log normal decay curve.

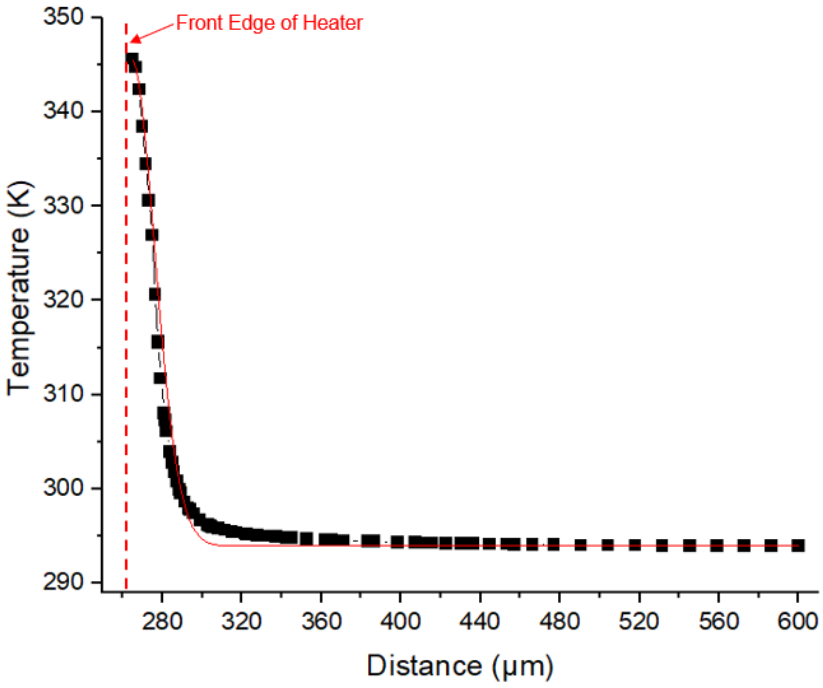

Figure-6.30: Graph of central line surface temperature from peak into following SoI with fitted log normal decay curve shown in red.

Both the steep, near linear, temperature drop-off after the heater and the approximately linear gradient further away from the heater seen in the experimental work are visible here.

Until this point the model had been run under vacuum conditions. In an attempt to simulate the presence of air a heat flux was applied to the top surface of the heater and Si. This is a standard method for COMSOL. However as can be seen in Figure-6.31 this only made a very small difference (<1mK) to the resulting temperature. Whilst the absolute temperature used at this point is arbitrary the shown temperatures are similar to that seen in some of the earlier heater experiments and is thus somewhat realistic. It would be expected that the introduction of air cooling would result in a larger temperature reduction than what is seen in the model.

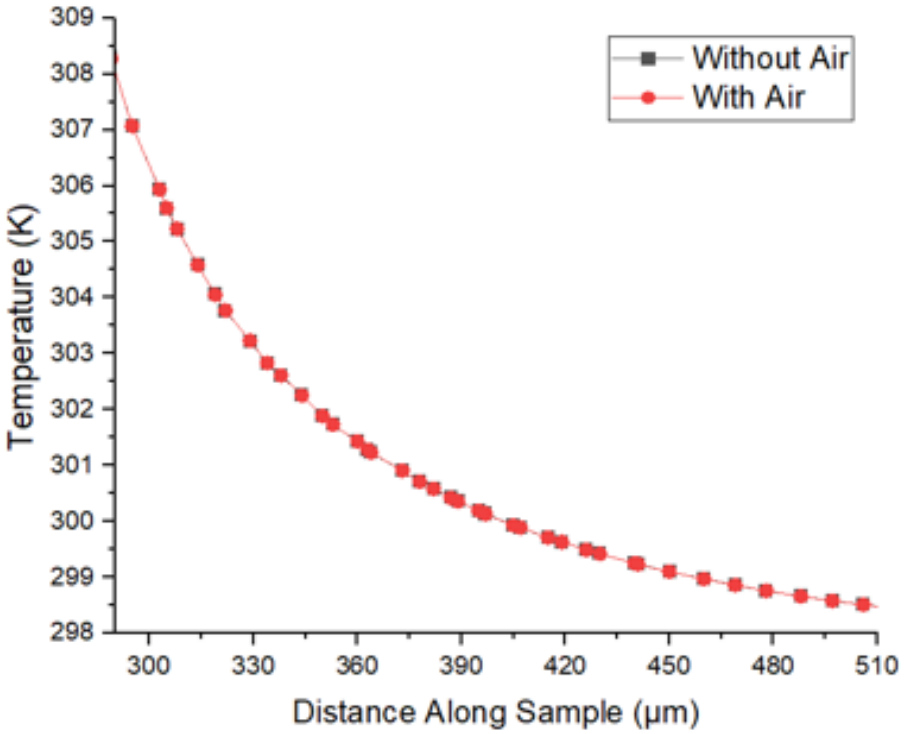

Figure-6.31: Graph of central line temperature from heater edge with and without air flux applied.

The heat path can be seen in Figure-6.32 which shows the heat maps for the area of the heater and the Si fishbones as both a surface map and cross section. In this we can see that the majority of the heat is contained within the device and SiO_2 break layer.

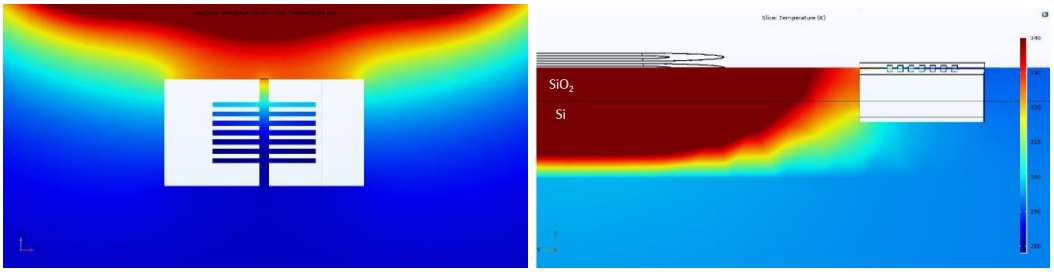

Figure-6.32: Heat maps of SoI surface (Left) and cross section (Right).

Several further attempts to understand the heating and atmosphere interaction through the modelling were made. This included adding a physical layer of air on top of the model rather than relying on the heat flux parameters as well as replacing the joule heating with a single applied temperature to the heater components.

However, these all made little difference with the maximum average difference between air and vacuum values being 3mK.

Applying non-realistic heat flux conditions (such as 0K atmosphere) would also have little impact on the surface so long as it was connected to the bulk. However the shaft which was not directly connected to the cooling plate could be significantly impacted by the introduction of the extreme flux resulting in unrealistically low temperatures. This suggests that the way the cooling from the rest of the sample was implemented (i.e. through the bottom side of the sample being permanently set to RT) had unintended consequences and does not properly represent the physical sample.

Effect of κ Change on Central Shaft Measurements

In order to understand the expected results from a change in κ this effect was simulated in the model. This was done by changing the assigned thermal conductivity value of the shaft and pillars as a whole.

For these measurements an extreme level of heat flux was applied to the shaft (i.e. the atmosphere was set at 200K). This was done in order to compensate for the difficulties with the air conduction model and allow the shaft to cool a visible amount. As such only the seen trend should be considered.

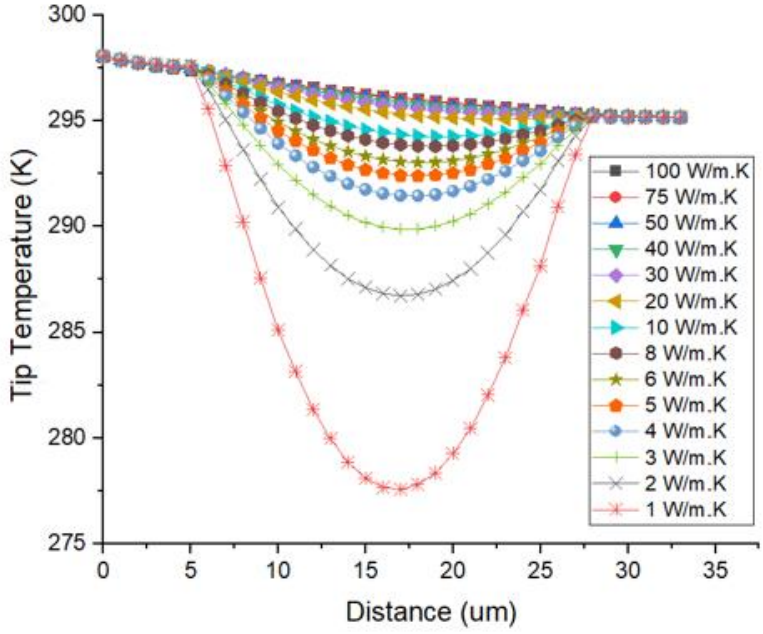

Figure-6.33: Graph of tip temperature across Si shaft for varying shaft κ values.

As shown in Figure-6.33 as the κ of the shaft was lowered, so too was the recorded average tip temperature at 1µm intervals across the central line of the suspended shaft. This is caused by the lower heat flow through the material which makes the temperature drop along the shaft. However, as this effect becomes very large the shaft becomes cooler than the opposite side. This leads to the far side of the shaft also being heated by the surrounding material as shown in Figure-6.34 This results in a near mirroring of the effect on both sides which results in the near-parabolic shape which can be seen in Figure-6.35.

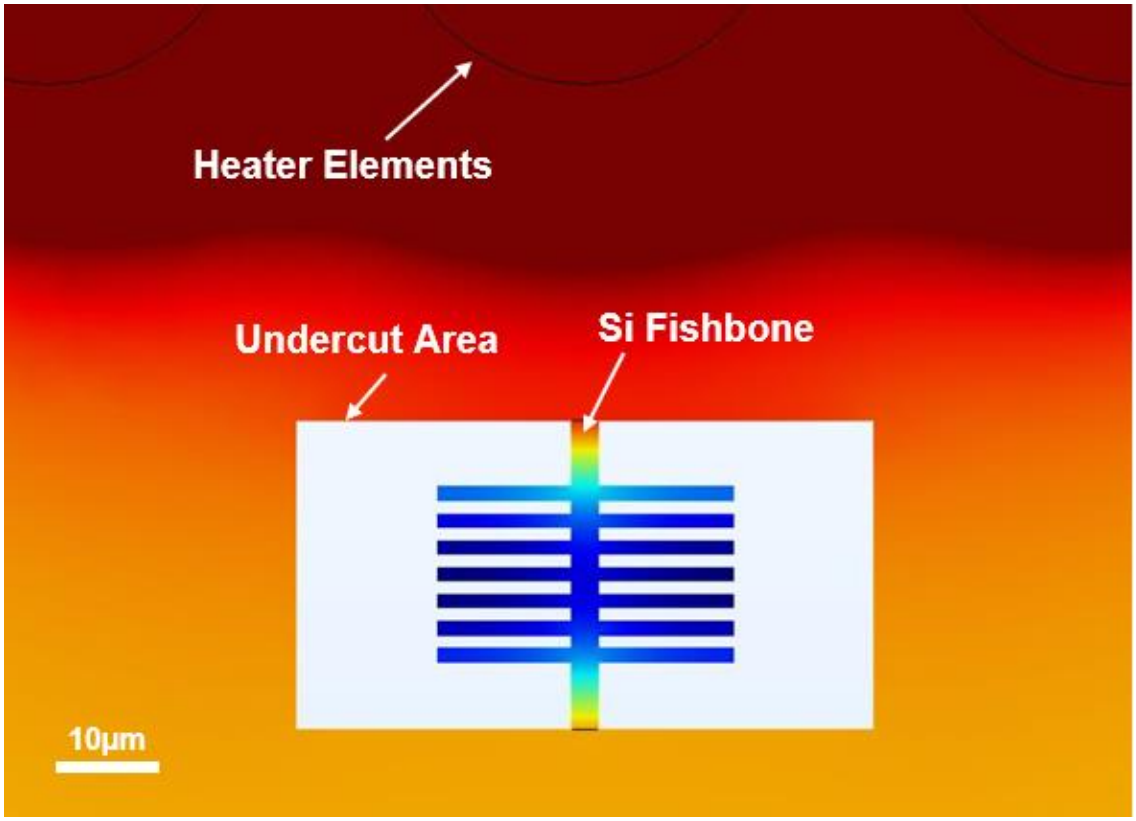

Figure-6.34: Heatmap of Si surface showing fishbone with very low thermal conductivity being heated from both ends.

Additionally, as shown in Figure-6.35, a 50% reduction in the thermal conductivity from 100W/m.K to 50 W/m.K results in only a minor change in the surface temperature (of ~0.17%) with a maximum change of around 0.2K. However, the same 50% reduction from 2W/m.K to 1 W/m.K causes a much larger maximum change of around 6K (or ~3.5%).

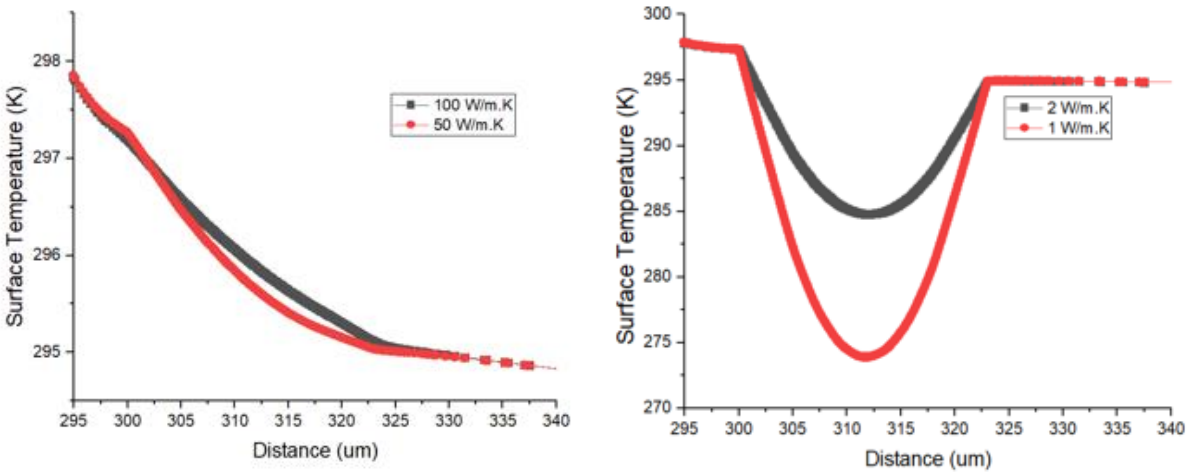

Figure-6.35: Graphs comparing surface temperature thermal gradients across Si fishbone at 100-50 W/m.K (Left) and 2-1 W/m.K (Right).

It is clear that the temperature change and the change in thermal conductivity are not linearly related. Using the data from Figure-6.33 and comparing the temperature change at the central point of the shaft Figure-6.36 was created. From this we can clearly see that the temperature change scales as the thermal conductivity decreases. This confirms that the initial thermal conductivity of a material is an important consideration. Materials with lower thermal conductivities will only require smaller changes to have a noticeable effect on the thermal gradient.

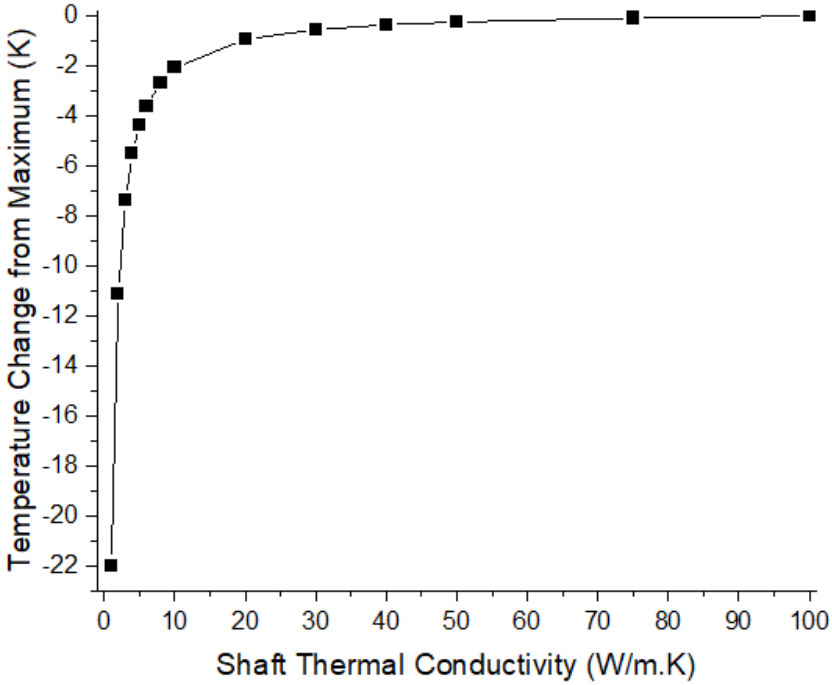

Figure-6.36: Graph showing temperature change of central point of COMSOL modelled Si shaft at different thermal conductivity values (Bulk Si = 130W/m.K).

We must also consider the relationship between the surface temperature (which is the more intrinsic value) and the recorded tip temperature. This is because the tip/surface temperature relation is not straightforward. It needs to be considered how much of the measured effect from the thermal conductivity change is in the surface temperature of the shaft and how much comes from the change in tip/surface heat transfer.

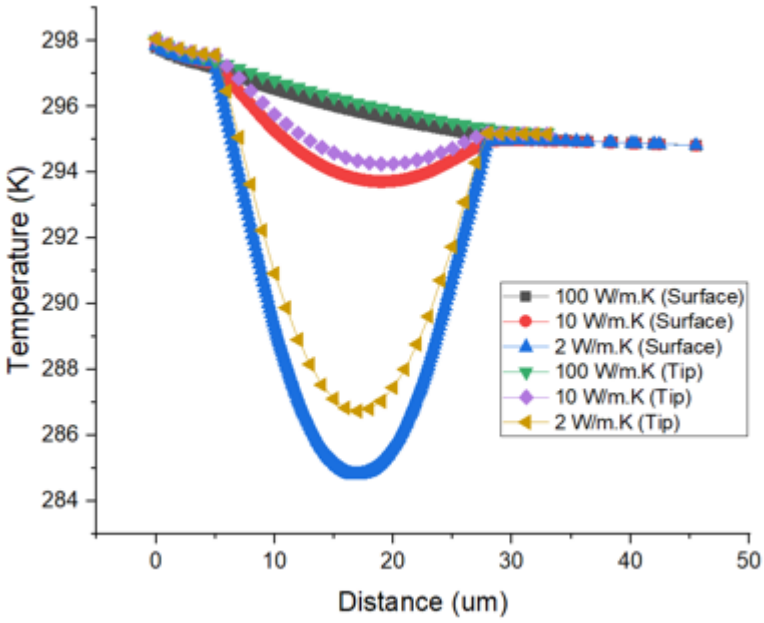

Figure-6.37: Graph of comparison between surface and tip temperatures for various shaft κ values.

Figure-6.37 shows a comparison between the surface and tip temperatures for different shaft thermal conductivities. Here the tip is hotter than the surface and is cooled by it. The graph also shows that when the thermal conductivity drops not only does the temperature of the shaft, and thus the tip temperature, but that the reduction of thermal conductivity results in the tip being cooled less efficiently. This can be seen by the increasing gap between the tip and surface temperature.

Bowed Shaft Creation

As previously discussed, it was found that during the fabrication of the Si fishbones a significant bowing shape was introduced into the shaft structure. As discussed in Chapter 3 it is known that these kinds of topography effects can significantly change the interaction between the tip and the shaft and thus the resulting tip temperature. Therefore the model was refined to make the central shaft curved in a parabolic fashion as seen in Figure-6.38. It should be noted that whilst

the degree of the curve is based on an average measurement of measured bowed shafts, the one in the model is a parabola where the fabricated curves are less regular.

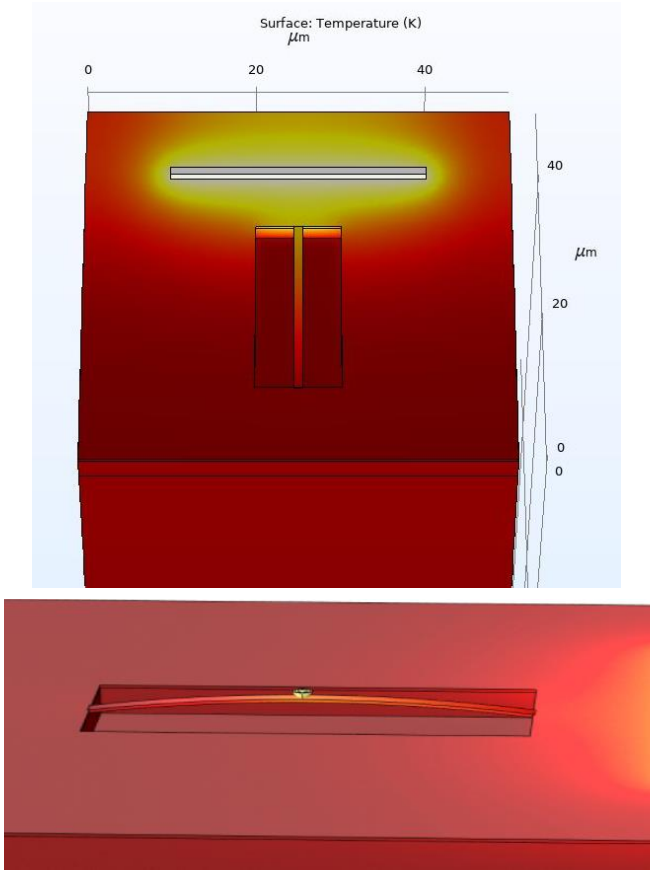

Figure-6.38: Images of 3D Model with curved shaft and simplified 'block temperature' heater.

Adding the bowed shaft and the necessary steps to allow the tip to properly follow the surface as discussed in chapter 3 made the model more complicated. In order to allow the simulation to run, a number of simplifications needed to be made to the model.

Examinations found that the pillars did not make any difference to the thermal gradient across the shaft. This is because there is no simulation of the phononic hybridisation nor an impact from the surface area causing an increased loss of heat to the air due to heat flux. The pillars were removed to help simplify the model. Additionally, the joule heated meander heating element was replaced with a simple Au block on top of the SoI surface which was at a set temperature.

These changes were tested first on the original model (i.e., without a curved shaft) and found that whilst it changed the absolute temperature it did not change the thermal profile recorded along the central line away from the heater in the area the Si fishbones are located.

Additionally, the scale of the sample as a whole had to be reduced. The total size was reduced from 500x500x500µm to just 50x50x100µm in order to allow the simulation to be able to function. This significantly smaller amount of space changes the heat transport throughout the sample as there is now less lateral space for the heat to disperse into. The main difference however is that there is significantly less material between the bottom cooling plate (present to simulate the bulk material) and the surface. This led to a reduction in the recorded absolute temperature but not a change in the more important thermal profile.

Curved Shaft Examination

It is also important to note how the tip interacts with the curved sample. The model is designed such that the very bottom of the tip is always placed in exact contact with the surface. On a flat surface this means that the contact always remains the same but on a curved surface the physical geometry of the tip can change the contact area.

In the case of a tip moving across a shaft with no temperature gradient applied to it and an active (i.e. hotter) tip the recorded tip temperature will form an upward curved pattern. This is because as the tip moves to the centre of the shaft the heat paths to the bulk Si become longer, leading to less effective tip cooling. This is true for both ends of the shaft leading to the hottest tip temperature being in the middle of the shaft as shown in Figure-6.39

As can also be seen in Figure-6.39 when a bowed shaft is used instead of a flat one this causes the central peak to become sharper. This is because near the edge of the curves where the gradient is highest there is a larger contact between the tip and sample (which is higher than for the flat surface). Conversely at the central point along the shaft the gradient is at its lowest and there is the least amount of tip-sample contact which results in a lesser heat flow and thus a hotter tip as shown in Figure-6.40.

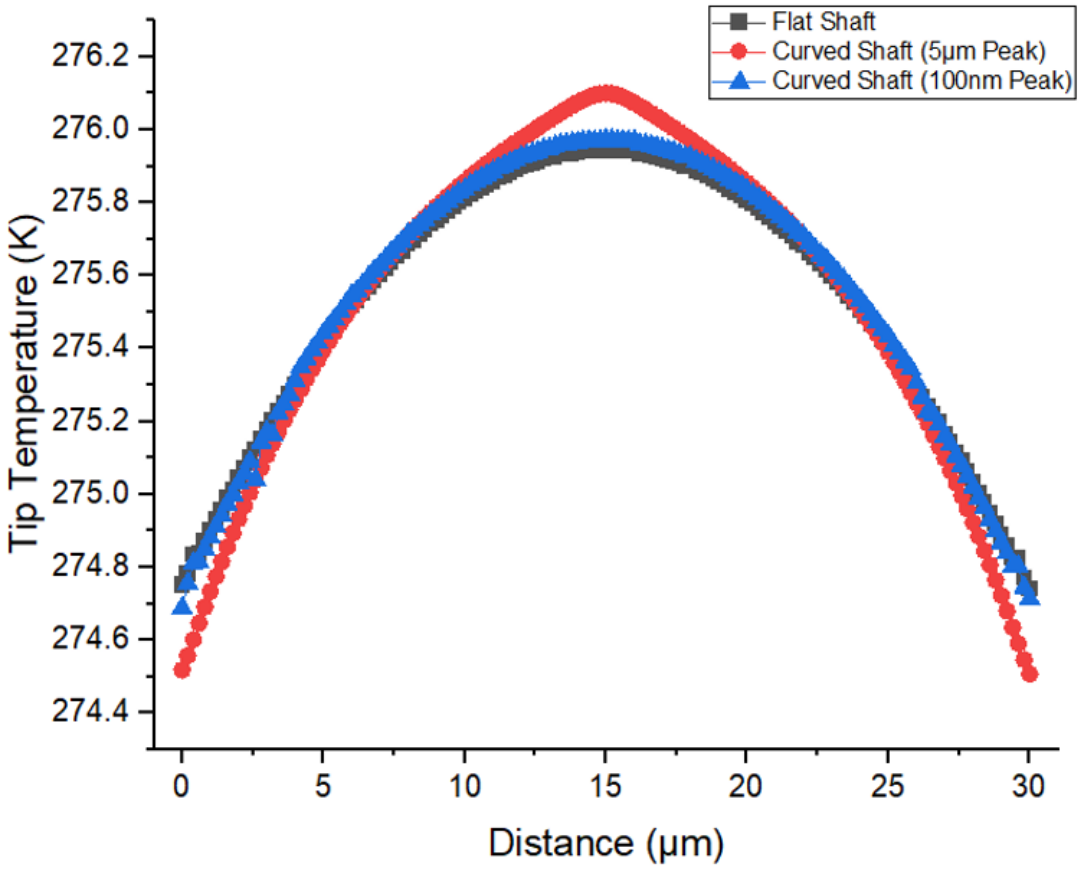

Figure-6.39: Graph showing comparison between tip temperature results for the unpowered flat shaft and different levels of bowing.

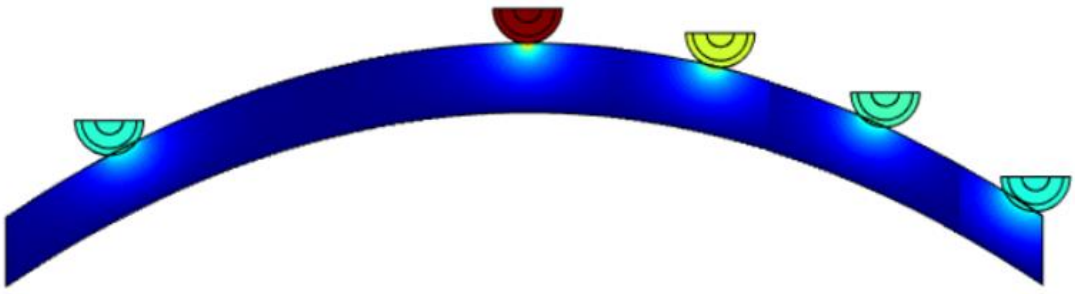

Figure-6.40: 2D COMSOL simulation of tip model moving across a curved surface. Note that the tip has a larger contact area lower down the tip and becomes hotter at the top as a result.

However as also seen in Figure-6.39 when the curve of the shaft is reduced to levels which match the experimental results across the barbed areas of the shaft this difference is only very small.

Using a bowed shaft with no applied thermal gradient the thermal conductivity value of the shaft was once again changed and the tip temperature across the central line measured. As might be expected from the previous results this showed that a decreased thermal conductivity value caused an increase in tip temperature as seen in Figure-6.41. However, it is notable that this tip temperature rapidly rises to unrealistic values. This is because the only way for the tip to disperse heat is through the tip/sample contact, rather than into the atmosphere or the larger cantilever structure as it would in a realistic situation. As this heat path is heavily restricted the tip temperature can quickly rise as the temperature is at an arbitrarily large value when not in contact with the surface.

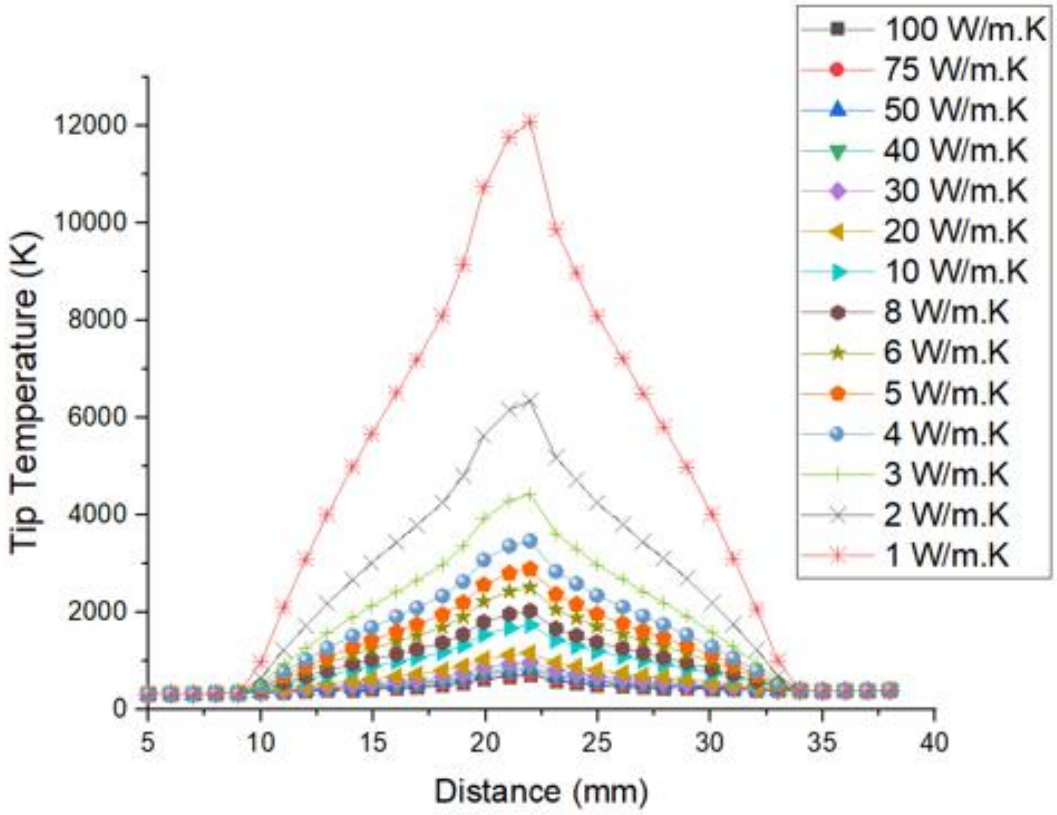

Figure-6.41: Graph of tip temperature over curved shaft at various shaft κ values.

Model Limitations

Despite the previously made simplifications to the model, it still struggled to run properly, frequently crashing or getting stuck running the simulation. It seems that this issue stemmed from the difference in the geometric elements (such as the tip at 100s of nm and the bulk Si at 10s of µm) and how this interacted with the simulation mesh. Though it is unclear exactly how, this prevented the simulation from running.

6.3.3 2D COMSOL Model Construction

With the complexity of the model causing a significant issue it was clear that it was not possible to move forward using the model as was. It had been established that the heater provided a measurable thermal gradient across the Si shaft and that the thermal transport could be significantly decreased if the thermal conductivity was reduced.

Moving forward it was decided to simplify down to a 2D model which would be able to handle the further experimentation of multiple thermal conductivity values on the Si shaft. The 2D model could be constructed to reflect the 3D model, however the major difference is the lateral heat spreading. The cause for concern is that the heat flow outwards into the sample may not be properly considered. COMSOL does use some simple functions to simulate the depth of a 2D sample, but it is unclear how well they simulate the larger model.

2D Model Design

The model was built as a cross-section of the previously used 3D model. As can be seen in Figure-6.42 it consists of the bulk Si layer which is topped with the 3um SiO_2 layer and the 220nm Si device layer from which the simplified shaft (i.e. without pillars) is also constructed over a removed undercut. The tip is modelled with the standard SiN_3 and Pd composition.

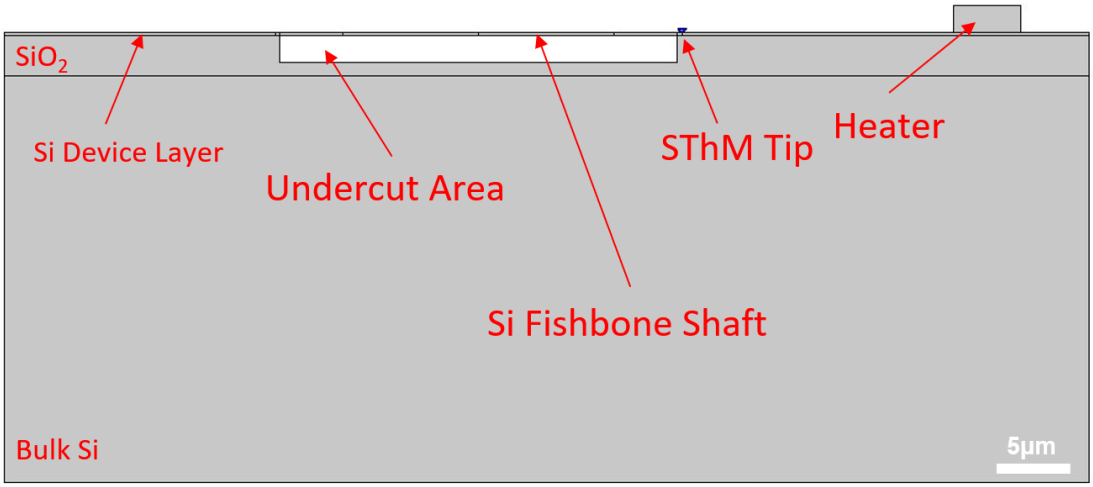

Figure-6.42: Image of 2D COMSOL Si fishbone model with components labelled.

This model is heated by a heater block which can be set at any given temperature as with the 3D model. This and a curved shaft which the tip was able to follow were also implemented into the model as seen in Figure-6.43.

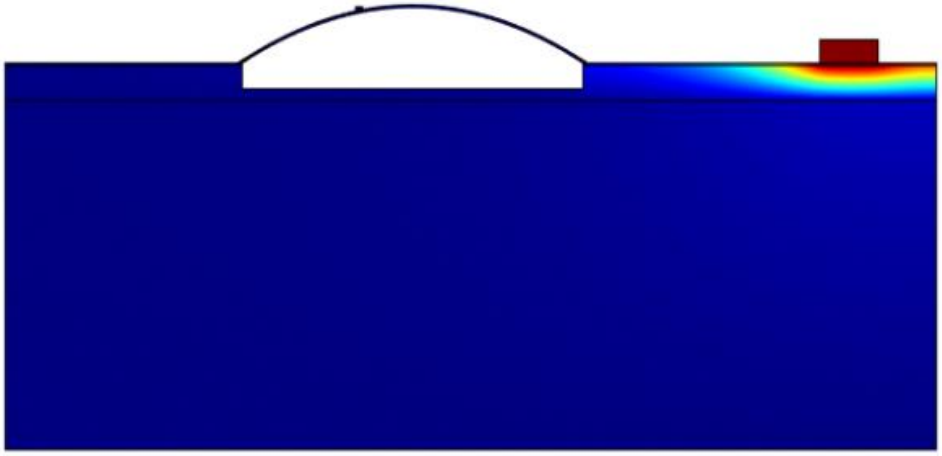

Figure-6.43: Image of 2D COMSOL model with heated temperature block and curved shaft.

Simulation of MARF/MDF

Multi-Aspect Ratio Fishbones (MARFs) and Multi-Density Fishbones (MDFs) are detailed in section 6.1.2. However, in brief they consist of a fishbone structure where the pillar parameters change along a single shaft in order to implement multiple κ values.

As shown in Figure-6.44 and Figure-6.45 this would be expected to result in four different regions which have three different κ values. This was then implemented into the COMSOL model by splitting up the shaft and allowing for each section to have a different κ value assigned to it.

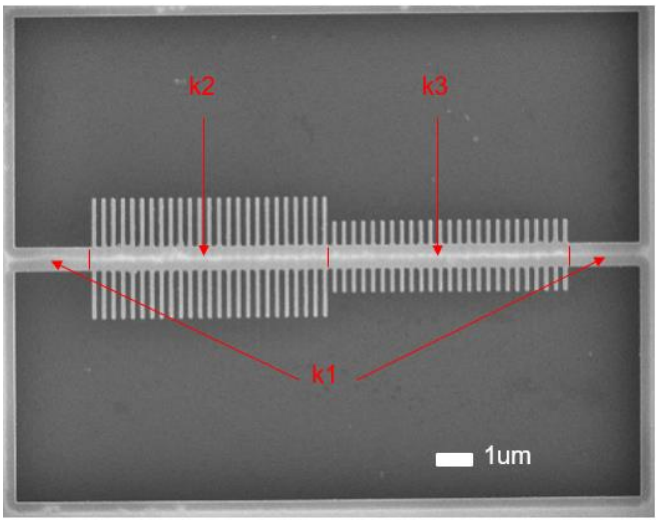

Figure-6.44: SEM image of MARF showing differing κ value regions based on pillar parameters.

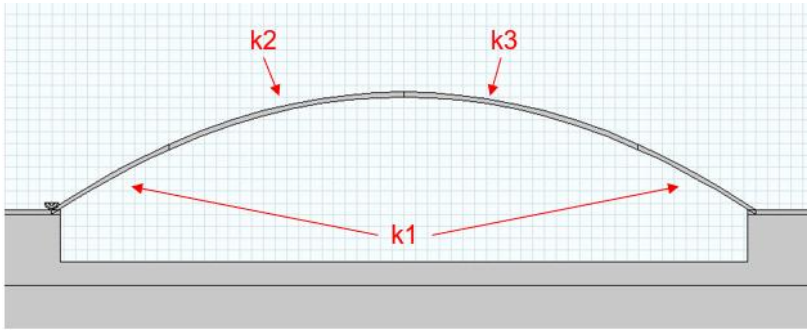

Figure-6.45: 2D COMSOL model showing different implemented κ regions on curved shaft.

6.3.4 2D COMSOL Model Results

The previous 3D model had not been able to handle both a curved shaft and an applied thermal gradient. This meant that the comparison between a 5µm peak bowed and flat shaft with an externally applied thermal gradient from the heater had to be performed using the 2D model.

As shown in Figure-6.46 this does result in a different measurement between the two shafts. However, this difference is much smaller than that seen in the unpowered shaft in Figure-6.39. This suggests that the presence of a thermal gradient may be a far more significant factor than the curvature of the shaft and reduces its overall effect on the recorded tip temperature.

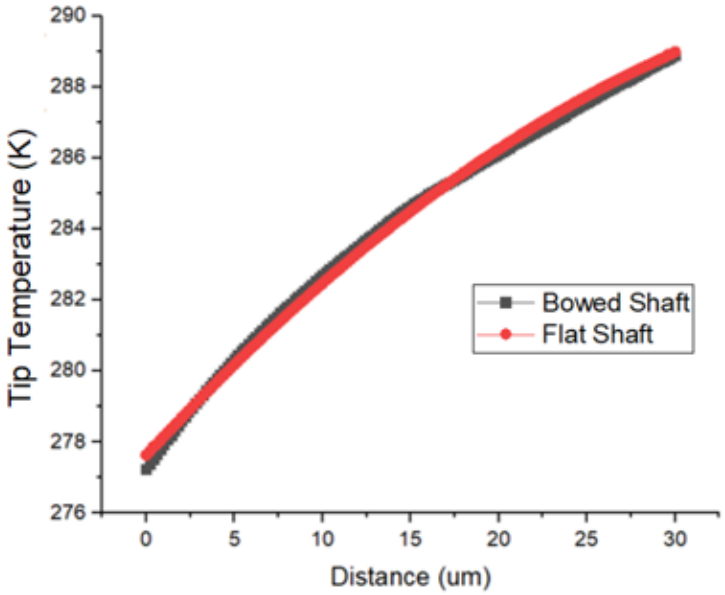

Figure-6.46: Graph showing comparison between flat and curved shaft on 2D COMSOL model with an applied thermal gradient.

This idea was then tested by taking the bowed shaft and applying increasingly high temperatures to the block heater. As shown in Figure-6.47 it can be seen that as the temperature increases, the effect of the curved surface on the thermal signal is reduced.

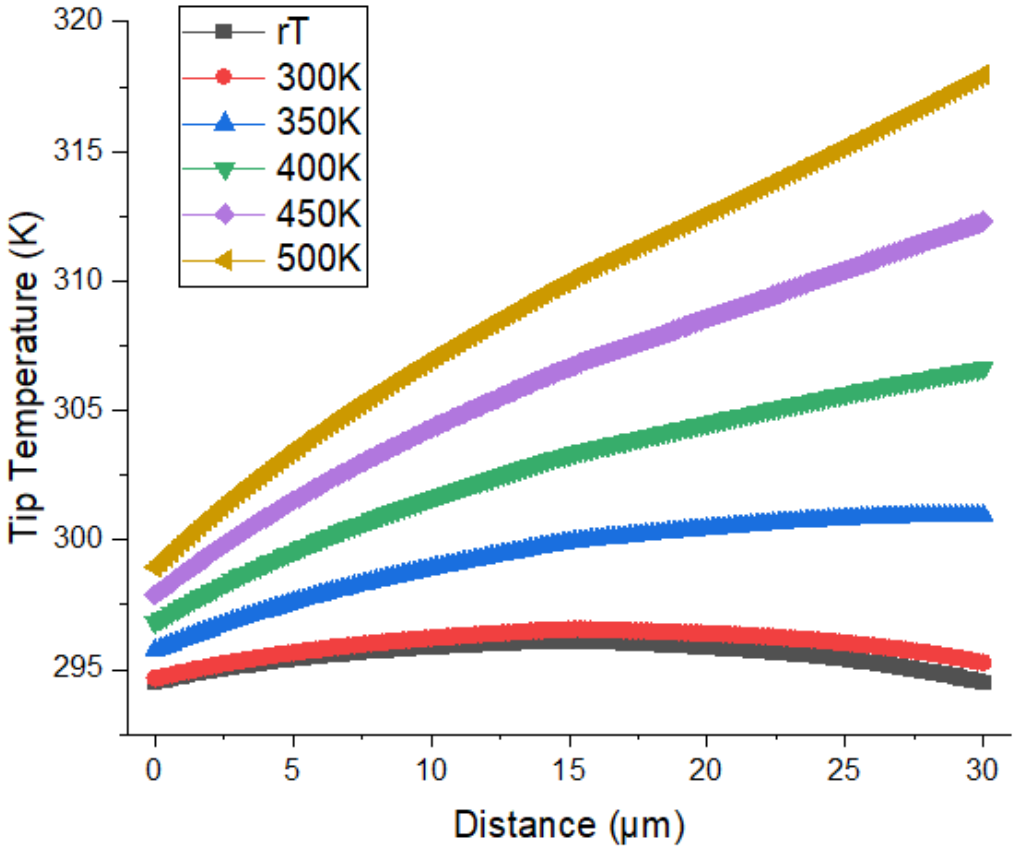

Figure-6.47: Graph showing tip temperature across curved shaft for increasing applied heater temperature on 2D COMSOL model.

It is important to consider the difference between the changing thermal conductivity effect on the surface and on the tip/surface interaction. In this case unlike those shown in Figure-6.35 the surface was not subjected to extreme flux conditions and effectively took place under vacuum conditions. This is why the surface examinations seen in Figure-6.48 do not show the negative parabola seen previously. However we can see that the surface temperature is affected. It is slightly higher at the part of the shaft closest to the heater (i.e. the right-hand side) because the heat cannot be as effectively transported down the centre. This clearly shows that a lower thermal conductivity results in an increased thermal gradient despite the applied heater temperature remaining constant at 400K.

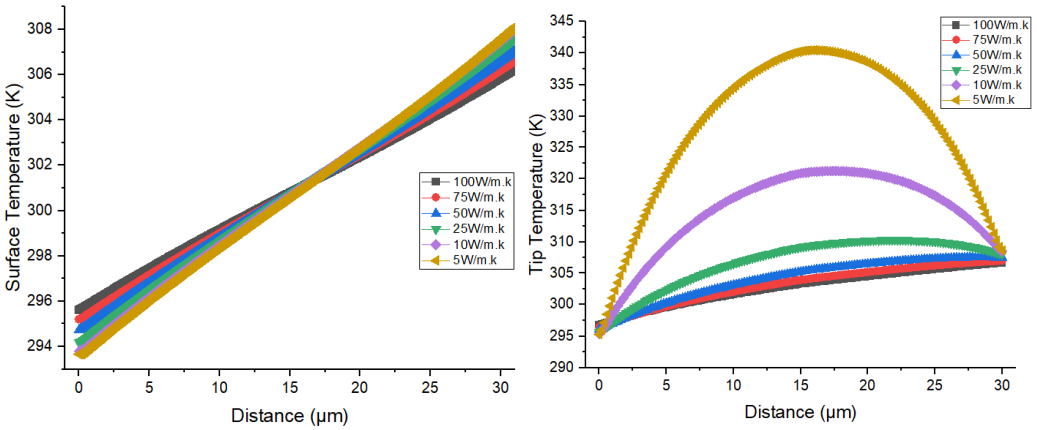

Figure-6.48: Graph showing result of 2D COMSOL model of curved shaft with applied thermal gradient at different shaft κ values surface temperature values (Left) and tip temperature values (Right).

From examining Figure-6.48 we can see that the largest influence on the tip temperature comes from the tip/sample interaction rather than the surface temperature. The tip is hotter than the surface and is cooled by it, as the thermal conductivity decreases the tip temperature rises.

However, as we can see that the surface temperature does not change significantly the change seen in Figure-6.48 must be the result of the shaft being less able to cool the tip. This also explains why the tip reaches its maximum temperature towards the centre of the shaft as it is the furthest point away from the bulk material which is able to better cool the tip.

MARF/MDF COMSOL Simulation

The different regions of the shaft were then assigned different thermal conductivities. To simulate some of the SThM examinations a series of κ regions designed to mimic a set of MARF or MDF fishbones were created. The κ values used were not based on measured outcomes of the experiments. The $\kappa 1$ region on either side of the shaft was set at a constant 100W/m.K, the $\kappa 2$ region was set at a constant 80W/m.K and the $\kappa 2$ region was varied. The results of this experiment are shown in Figure-6.49.

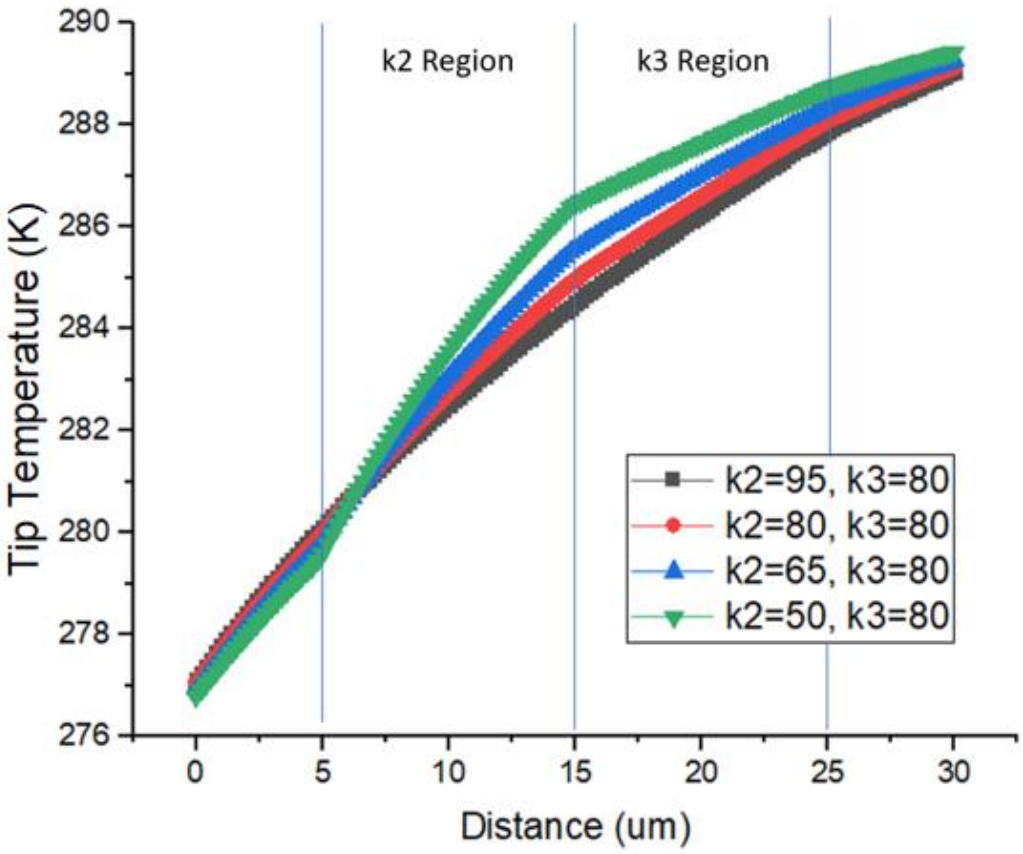

Figure-6.49: Graph of 2D bowed shaft COMSOL multi-κ simulation with listed values and regions.

Figure-6.49: shows a very clear and important result. Given a large enough change in the thermal conductivity across a shaft with an externally applied thermal gradient it should be visible in the tip temperature measurements. This is something which can be experimentally looked for.

As previously examined with Figure-6.48 the surface temperature of the shaft itself seems not to be the major contributor to the visible difference but rather the tip/sample interaction. The scale of change is also important to consider, the difference is most notable at the largest change but as previously suggested by Figure-6.41 it seems reasonable to assume that this scales as the thermal conductivity value lowers.

This means a 50% change in thermal conductivity for an initial thermal conductivity of 150W/m.K (aka bulk Si) might be difficult to determine but the same percentage reduction for a much lower thermal conductivity (e.g. SiO_2 at 1.4W/m.K) would be significantly easier to see. This is shown in Figure-6.50.

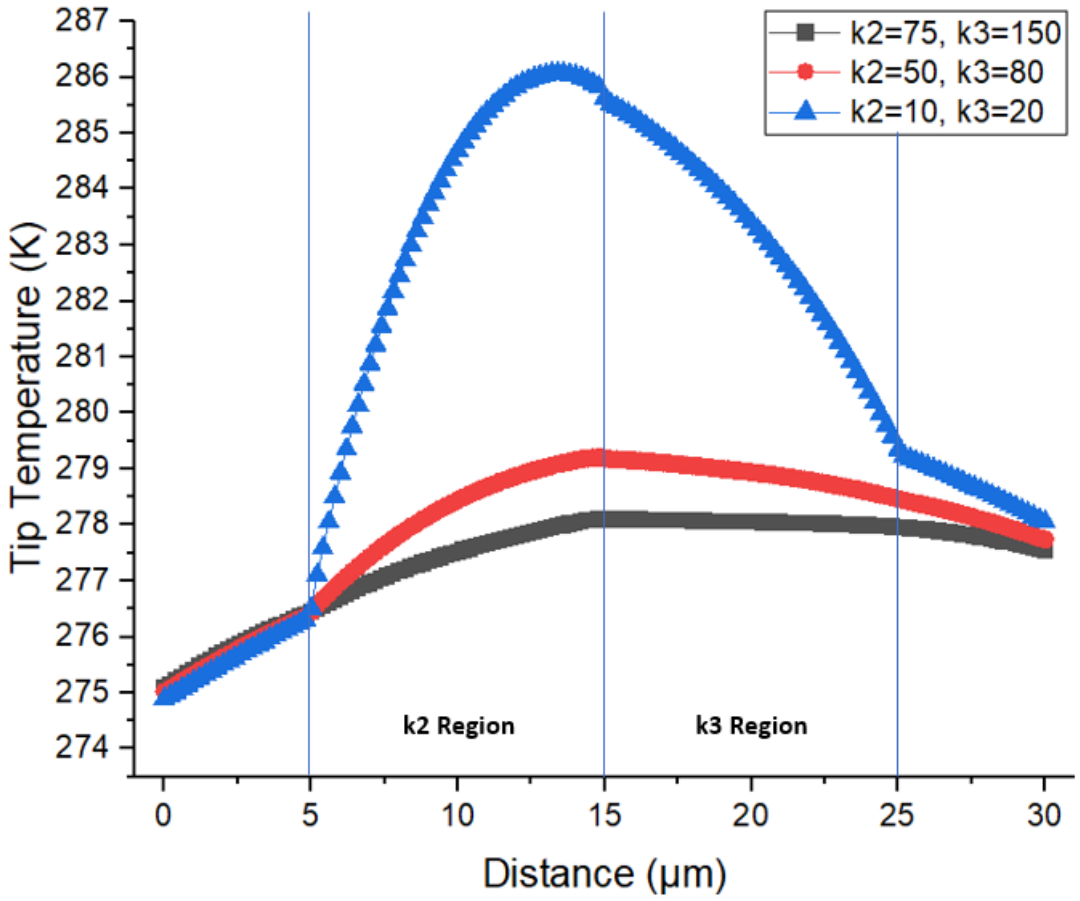

Figure-6.50: Graph of tip temperature over COMSOL simulated shaft examining the difference in 50% thermal conductivity changes between the κ2 and κ3 regions for three different initial κ values of 150, 80 and 2W/m.K. Note that the non-κ2/3 regions remain at 100W/m.K at all times.

6.4 Summary

The fabrication of the Si fishbones was highly successful, able to produce higher aspect ratio pillars than had been expected at 26:1 with a length of 3μm and a width of 115nm. Some pinning of the pillars to each other was found, especially at higher pillar densities. However a tradeoff point where the amount of additional available pillars was greater than the loss through sticking pillars was found and used.

The microheaters were shown to experience a decaying temperature across the sample surface that was approximately linear on the scale of the fishbones allowing for easier examination. The chipset #7 design has also been laid out showing the

different fishbones created for examination and how they can be compared against one another.

The COMSOL modelling was able to match the experimental results of the heater however when attempting to model the fishbone structure it struggled to work with the various sized elements and required significant simplification. Despite this there are very clear results in that the topography of the shaft is highly important to the thermal results and that changes in the thermal conductivity along the shaft should be visible in the SThM measurement.

Chapter 7

Silicon Fishbones Experiments

The Si fishbones were examined in the VLS-80. Whilst a number of sets were created and examined, the data presented here are largely limited to that collected from the chipset #7 fishbones. This is because the previous designs and examinations were used to inform the creation of chipset #7. This was to give the greatest chance at being able to examine the effects of phonon resonance induced thermal conductivity change.

7.1 Fishbone SThM Imaging

An issue with the scanning of the Si fishbones was that the movement of the tip along the pillars could cause the fishbone to break off. The full mechanism for this is not understood but it likely occurs because the downward force of the tip causes the shaft to twist and snap. Therefore, an alignment procedure had to be performed to ensure that only the shaft and a small amount of the pillars (used to ensure correct positioning) were scanned by the tip. The resulting shaft scans are similar to the representational topography and thermal scans in Figure-7.1. The scanning parameters used in all the scans were standardised using the parameters shown in Table-7.1. The AC and DC voltages are the voltages supplied to the SThM tip. The setpoint represents the force with which the tip is pushed into the surface, P is the proportional gain and Ti is the integration time constant of the controller which controls the tip feedback loop.

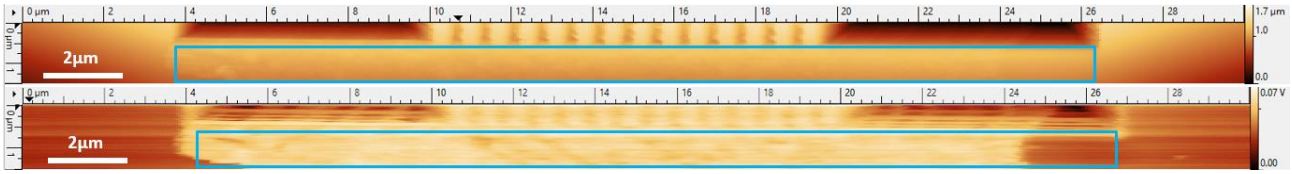

Figure-7.1 Representative topography (Top) and thermal (Bottom) scan images of a Si fishbone shaft used for data analysis. Blue boxes show the scan area used for shaft examinations. Note the slight shift in x direction between the two images, this is accounted for in data analysis.

Scan Conditions	
Scan Size (µm)	40x1.5
Pixel Count	256x256
Tip Velocity (nm/s)	10000
AC Voltage (V)	2
DC Voltage (V)	1
Vacuum?	No
Setpoint (mV)	1000
Proportional Gain (nm/mV)	0.06
Integration Time (ms)	1
Time to Run	34:11

Table-7.1: Relevant VLS-80 parameters for the Si fishbone shaft scans.

The area of the scans which cover just the free-floating shaft above the undercut SiO_2 surface (which is marked in blue on Figure-7.1) are then converted into a line averaged graph which is used to compare shafts. This was done to avoid the largest topographical changes which would impact the thermal signal. These were then normalised to the temperature of the right-hand side (which would be expected to be most consistent across the various scans) as shown in Figure-7.2.

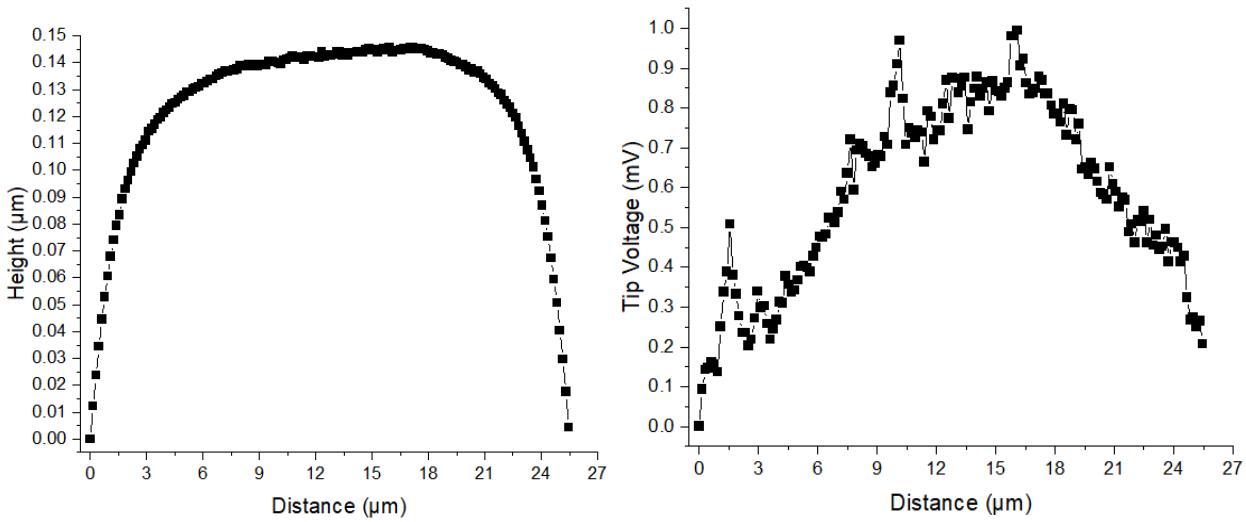

Figure-7.2: Representative topography (Left) and thermal (Right) line average across the shaft examination area of Figure-7.1.

It is important to note that in all scans the heater was always located on the right-hand side of the fishbones due to power cable positioning requirements within the VLS-80. As such the expectation is that when a thermal gradient is applied the right-hand side will be at a higher temperature which then decreases across the fishbone moving right to left as shown in Figure-7.3

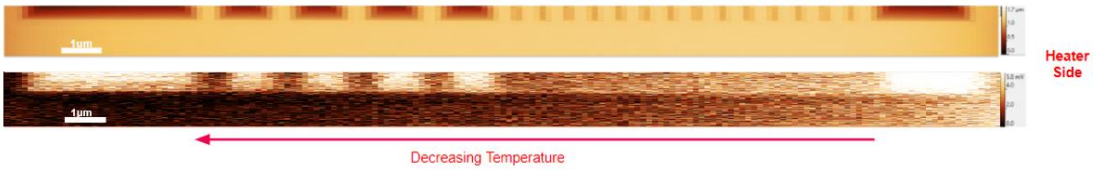

Figure-7.3: Representative topography (Top) and thermal (Bottom) scan images of the Si fishbone shaft used for data analysis.

7.2 Impediments to SThM Imaging

When attempting to examine the fishbones there were a number of issues which complicated the procedure. Whilst the fabrication and imaging process were greatly improved over the course of the project, some issues persisted through to chipset #7 (particularly heater issues) which hampered the full suite of experiments and restricted what was possible to perform. All created chips suffered from a number of issues across the complete set however enough fishbones and heaters remained in working order across the multiple chips to be able to complete the comparative experiments.

7.2.1 Fishbone Breakages

Some of the Si fishbones were broken. Much of this occurred during the fabrication process and it is not fully understood how any particular fishbone broke. In chipset #7 the fabrication success rate was ~90%.

Even with the proper alignment of the tip some fishbones were broken when attempting to scan them. The scanning can result in significant damage to the shaft and pillars such as in Figure-7.4 or even the complete removal of a fishbone.

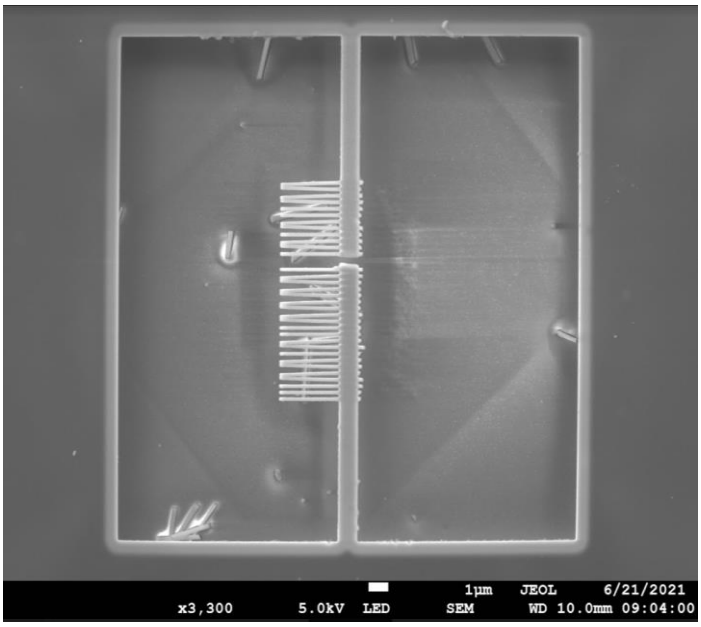

Figure-7.4: SEM image of broken Si feather caused by SThM scanning.

Such operational breakages were rare, occurring less than 5% of the time, however each one prevented further comparative work on an individual shaft.

7.2.2 Heater Breakages

The heaters were also found to fail sometimes. This happened in two main ways. Firstly, the fabrication method sometimes resulted in a microheater which was not built as designed. This was usually caused by the Au not being fully removed from the surface as shown in Figure-7.5. It could also occur that the entire heater structure would be removed from the surface. It is not understood why these failures occurred and despite modifications to the fabrication (such as increased surface cleaning) results seemed to vary. Chipset #7 suffered complete failure of heater production on several chips. On chips that were usable the average fabrication success rate for the heaters was around 70%.

The second method of failure was that a fully functioning heater kept at a stable voltage could burn out. The operational time for the microheaters could extend into days at a time and an individual heater could be used for a total time of several weeks. This could cause damage to the microheaters as also shown in Figure-7.5.

Figure-7.5: Optical microscope image of developed microheater with unremoved Au which causes a short circuit (Left) and burnt out microheater (Right).

7.2.3 Remaining Resist

On occasion during the fabrication process some of the fishbones would not be cleaned completely of the covering AR-P 6200.13 resist. This resulted in the thermal fishbone scans being distorted by the presence of the resist material as can be seen in Figure-7.6. It is notable that this is not visible in the topographical image due to the resist layer's relative thinness compared to the topography of the surface but is clearly visible in the thermal image.

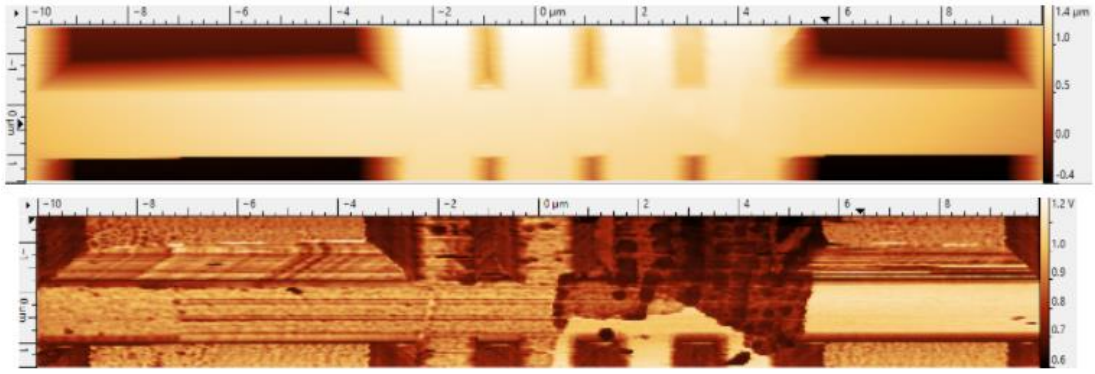

Figure-7.6: Image of Si fishbone topography (Top) and thermal (Bottom) scan images with some spin resist still on the fishbone.

Further evidence of this remaining resist or perhaps some other kind of debris could be found all over the wider chips. This resulted in a significant amount of thermal noise which can be seen surrounding the fishbones at any point as shown in Figure-7.7. This was found across all samples.

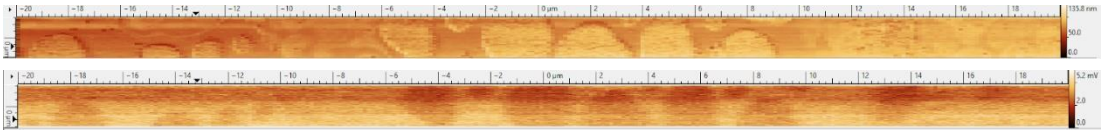

Figure-7.7: VLS-80 image of topography (Top) and thermal (bottom) of plain silicon area on a chipset #7 fishbone.

7.3 SThM Results

A large set of SThM scans of fishbones from chipset #7 were then taken. Due to various breakages of fishbones and in order to keep as consistent a set of measurements as possible, the second line of fishbones (approximately 250µm away from the heater) were measured in all cases. At this distance, according to the earlier COMSOL modelling, we would expect temperature gradients of around 1.6mK/µm. Table-7.2 details the different input heater voltages that measurements were taken at for the various kinds of fishbones. It is worth noting that due to a combination of heater and fishbone damage the 0-MARF fishbones (i.e. those where only half of the shaft had pillars) were not able to be examined.

Heater Volts	MARF	MDF	Shaft Only
0V	Y (R)	Y	Y (R)
2V	Y	Y	N
3V	Y	Y	N
4V	Y	Y	N
5V	Y	Y	N
6V	Y (R)	Y	Y
0V Vacuum	Y	Y	Y

Table-7.2: Table of systematically performed SThM examinations of Si fishbones where (R) shows that this was repeated.

All of these scans were taken using the same parameters as detailed in section 7.1. Each fishbone was scanned three times and a set of data of the line average value across the shaft taken. The data from the three scans was then averaged to produce a graph of the topography and thermal signal for each fishbone.

These individual fishbone examinations were then combined with the other fishbones of their type (i.e., MARF, MDF) as shown in Figure-7.8.

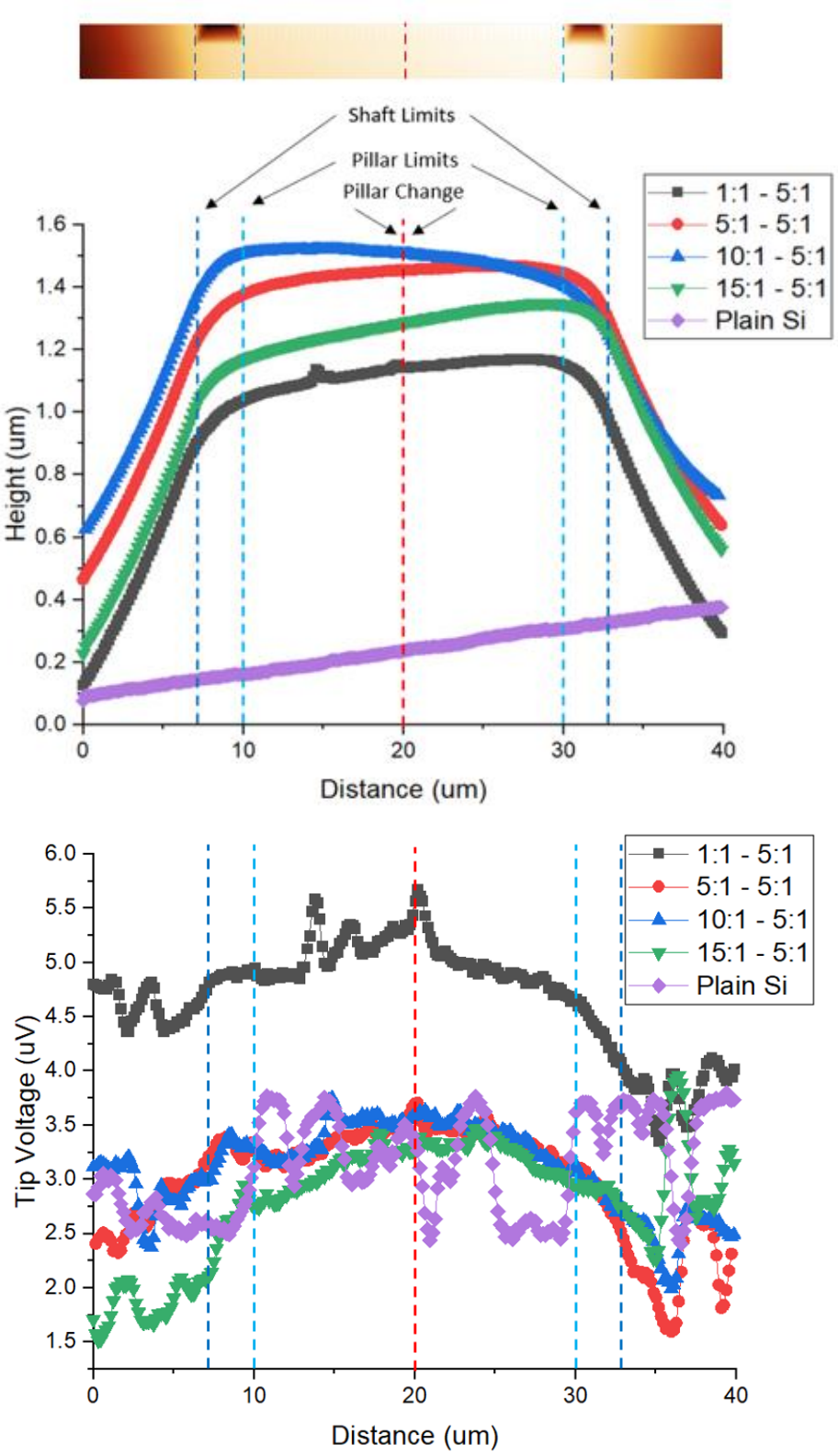

Figure-7.8: Graph of 0V MARF combined dataset showing line averaged topography (Middle) and thermal (Bottom) signals along with topography image of shaft (Top)

This was then reduced further to just the exposed shaft which was above the undercut area and is covered by pillars (as marked by the pillar limits in Figure-7.8) shown in Figure-7.9. These were normalised to the right hand side.

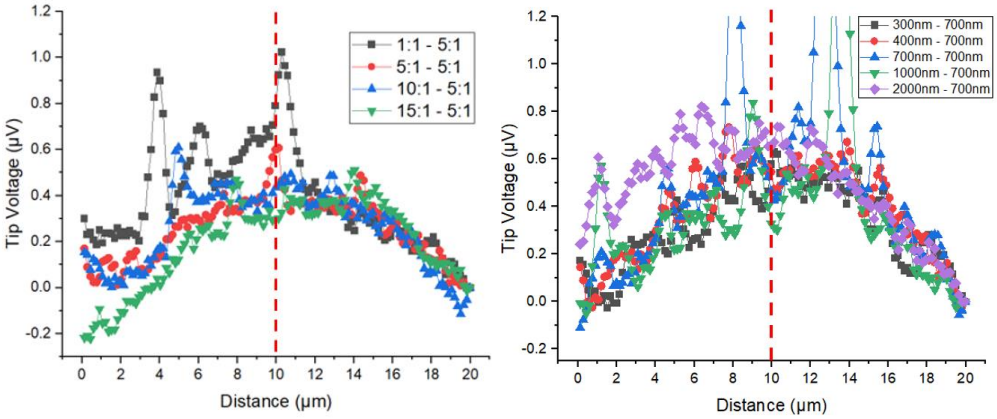

Figure-7.9: Graph of 0V MARF shaft (Left) and 0V MDF shaft (Right) combined dataset showing line averaged thermal signal with red line showing point where pillar parameters are changed. Note that some peaks on the MDF shaft caused by topography effects have been cut off.

These data sets were produced for all of the scans listed in Table-7.2 and representative examples are included within the analysis where appropriate. Before considering comparative analysis of the fishbones, it was important first to ensure that the system was working as expected. Therefore SThM examinations were performed on a bare SoI surface which had not had fishbones constructed upon it.

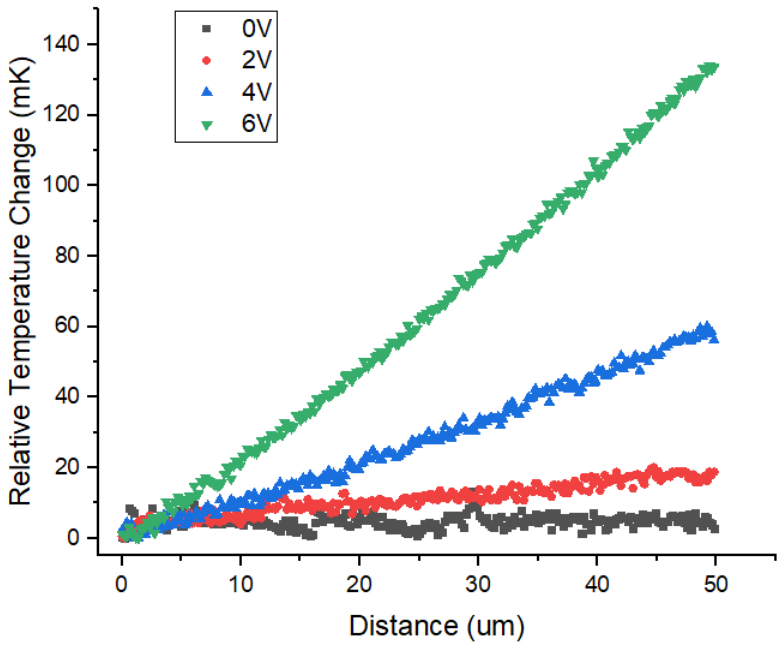

Figure-7.10: Graph of normalised and corrected data of tip temperature showing relative thermal gradient across SoI surface in the same position as fishbones.

Figure-7.10 shows the recorded line average temperature of a series of SThM scans taken on the bare SoI in the position where fishbones would be in the fully fabricated sample. This was performed for different input voltages to the heater and

as can be seen higher voltage (which causes a higher heater temperature) resulted in greater thermal gradients.

It is important to note that this data was converted into real temperatures using the calibration, but that these are relative temperatures. The temperature changes that are recorded are real, but the shown values do not represent an absolute temperature. It is not at this stage possible to extract an absolute temperature from VLS-80 examinations.

The COMSOL simulation using an average heater temperature of 67ºC calculated a temperature gradient value for the area by the fishbones of 1.62±0.01mK/µm. The experimental measurements are shown in Table-7.3. These show the COMSOL model matches well for the kind of temperatures being used in the experiment. This shows a small statistical error from the data but there may be a much larger systematic error or reproducibility issues.

Input Voltage (V)	Measured Thermal Gradient (mK/µm)	Error (mK/µm)
6	2.68	0.02
4	1.18	0.01
2	0.38	0.01

Table-7.3: Table of measured thermal gradients at the position of heaters across a series of input heater voltages.

It should be noted that when looking at a 6V scan such as in Figure-7.11 the measurements show significant temperature drops caused by the steep topography of the surface bubbling. The temperature in this case likely drops rather than rises as previously seen because the surface is heating the tip so the lesser contact results in less heating rather than less tip cooling. However, importantly this does not affect the results seen within the range of the shaft so no special considerations need to be made.

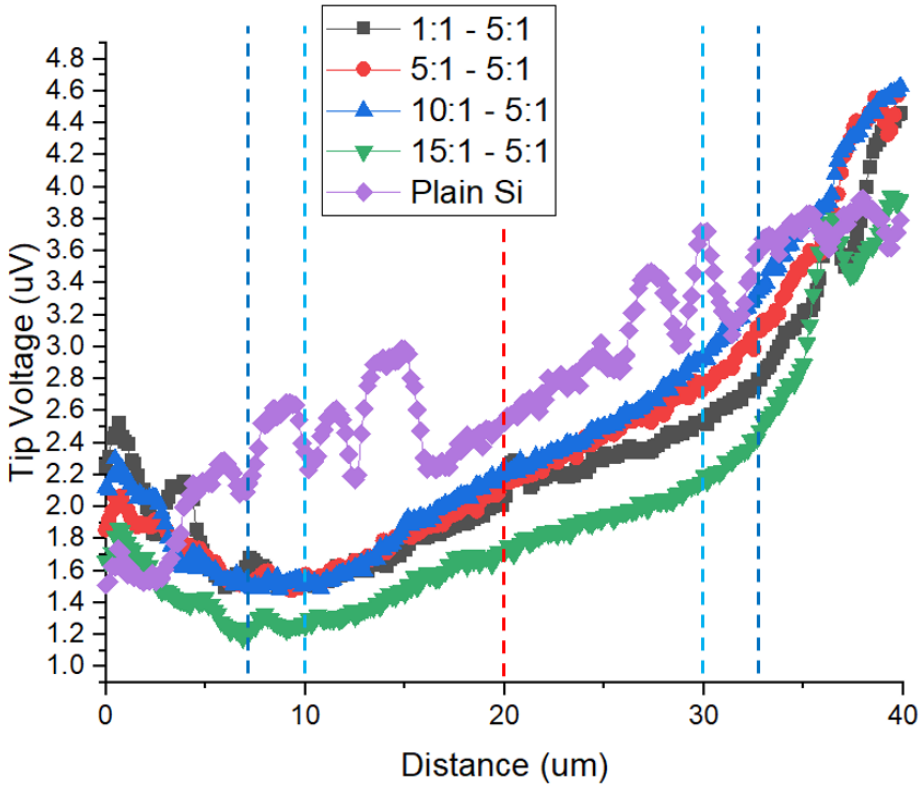

Figure-7.11: 6V MARF scan across complete shaft and surrounding Si. Note that the surface being hotter than the tip has resulted in an inversion of the thermal curve, however this is not expected to have changed the Si shaft results.

7.3.1 Reproducibility of Scans

The reproducibility of the scans is an important consideration when attempting to examine and interpret the recorded data. A number of different ways of considering the reproducibility of the measurements are discussed here.

Topography Reproducibility

It had been initially worried, considering the ability of the SThM tip to damage the fishbones and the pillars, that the scanning process might be causing the shaft topography to change. This could be from the tip causing the shaft to flex or deform or in some way altering the pinning of the pillars which could change the thermal response.

However as can be seen in Figure-7.12 not only does the topography remain unchanged across all of the performed scans it is also unchanged when altering the temperature of the applied heater voltage. This suggests that during a normal scan the SThM tip does not affect the topography.

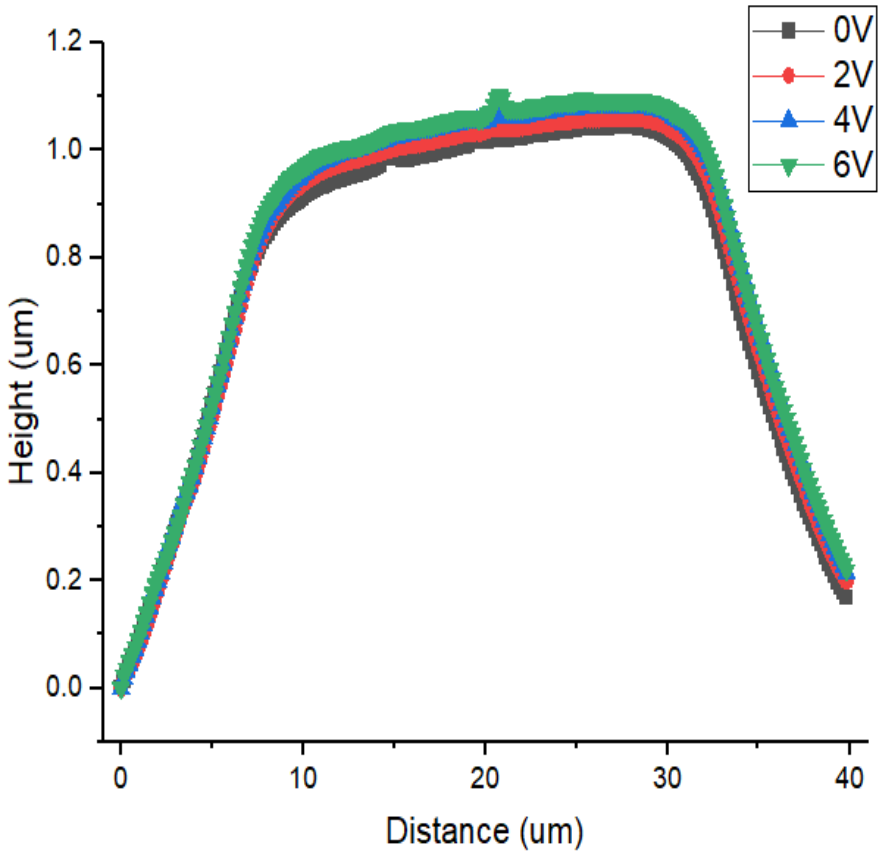

Figure-7.12: Graph of 1:1 – 5:1 MARF averaged topography at different heater input voltages.

However it should be noted that the topographies in Figure-7.12 are not an exact match. This occurs due to cantilever heating from the surface. Where there is a hot surface as the tip scans the cantilever as a whole is heated. This heat causes the cantilever to bend slightly. This is a well-known effect which is exploited for use in bimetallic probes (92). This is why the height is raised a little and that this is dependent on the increasing heater voltage. It should be noted that this is separate to the plane raise which results in a difference between the height on the left to on the right which can also be seen in the 0V scan and is due to the mounting of the sample not being completely level.

Sequential Repeat Reproducibility

The main type of data used from the images is the thermal line averaged scan across the shaft area. This comes from the average across three different scans which are all taken sequentially. It is important to understand how reproducible these kinds of scans are.

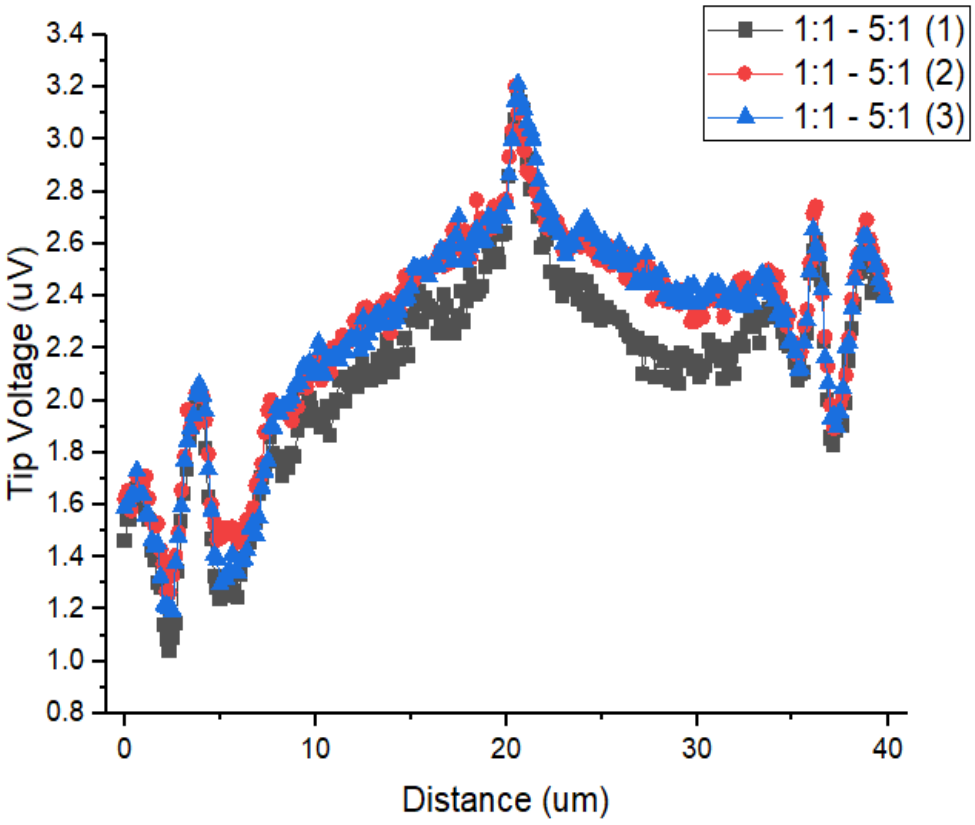

Figure-7.13: Graph of 2V 1:1 – 5:1 raw thermal signal on three scans performed sequentially to then be used for averaging.

As can be clearly seen in the representative Figure-7.13 there is a good amount of agreement between the sequential scans. All of the major features remain in the same place and there are similar scale changes in the tip voltage at each point. It is notable that the first taken scan is not as similar as the second two, it is suspected this is because the tip voltage had not fully equilibrated during this first scan.

The averaging across different scans remains important to examine for eliminating scan artefacts (such as tip changes or bad contact), however it is clear there is not a huge difference between the sequential scans.

If we examine the individual images and the topography as in Figure-7.14 we can see that the central thermal peak seems to be caused by some kind of surface effect which is perhaps a piece of debris.

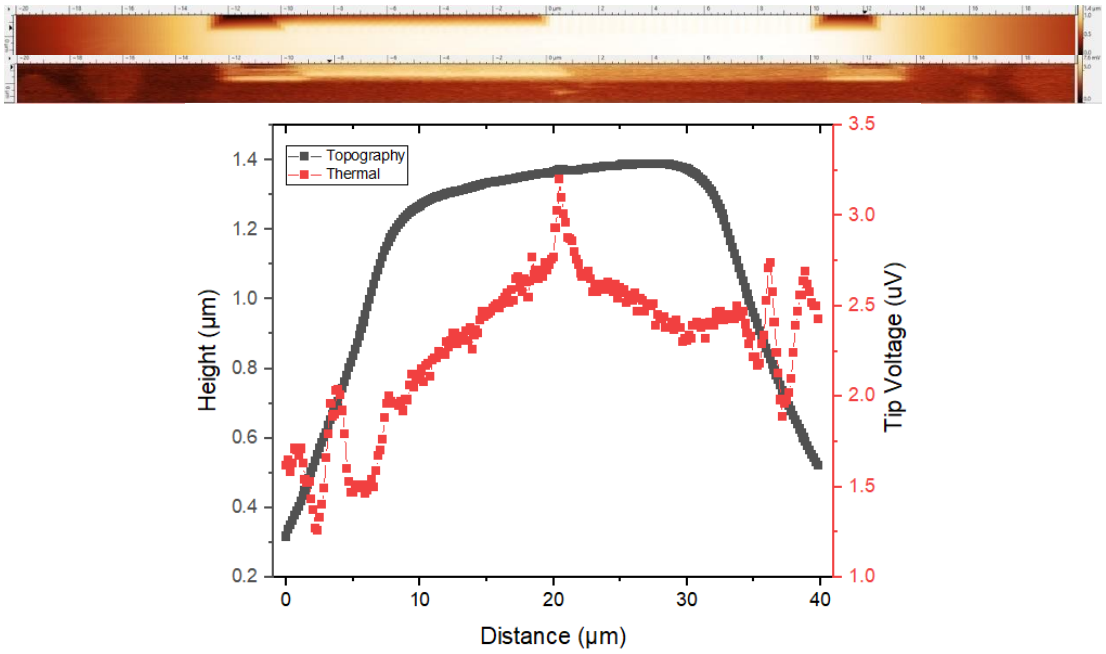

Figure-7.14: VLS-80 image of 2V 1:1 – 5:1 scan of topography (Top) and thermal (Middle) as well as comparison between line averaged topography and thermal signal (Bottom).

Complete Scan Repeat Reproducibility

There are however greater concerns when the scans are performed at another point in time. The graphs in Figure-7.15 show the 0V MARF line averaged scans that were performed on each of the different fishbones at three different times, weeks apart. These measurements used different calibrations and in the case of the second repeat a different SThM tip after the first had broken.

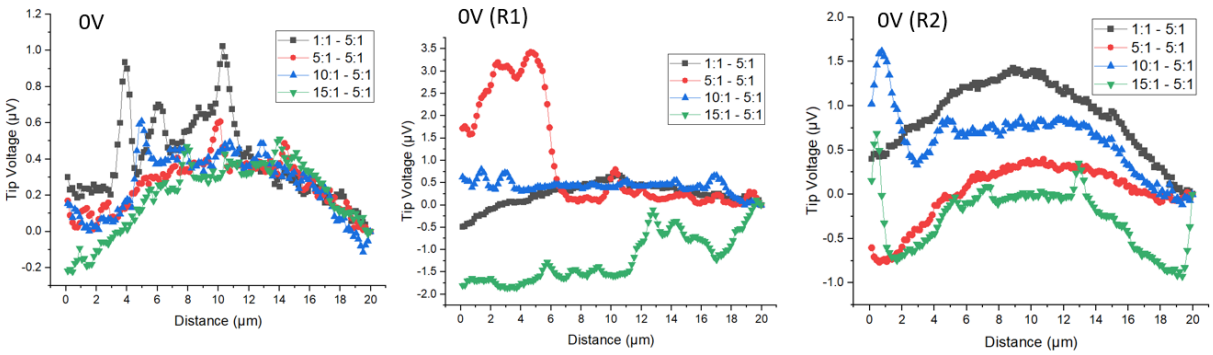

Figure-7.15: Graph of line averaged thermal signal across the same MARFs at three different times.

It is clear from Figure-7.15 that these repeated scans are dissimilar from one another and that crucially this is seen in the shape, not just the values. The second repeat was carried out because of how different the first repeat was but even just

comparing the original and the second repeat it is clear that the recorded thermal signal is very different.

It is not clear why these scans are so different, but there are a number of possible contributing factors. Firstly there is a clear difference in the absolute values of the tip voltage changes recorded between the samples. This is not a major concern as different calibration values were recorded for each set of measurements.

The larger concern is that the shape of the measurements is completely different. As shown in Figure-7.16 the thermal image is completely different despite being taken at the same point, showing that this is not an error in the averaging or analysis.

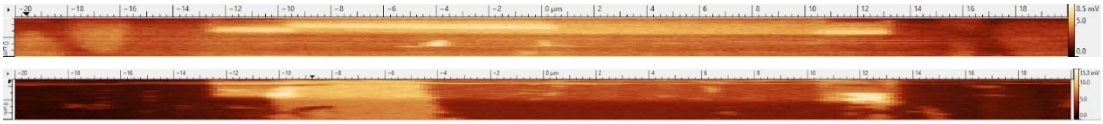

Figure-7.16: Comparison between VLS-80 thermal image of 6V 1:1 – 5:1 MARF original scan (Top) and R1 (Bottom).

The second repeat the thermal image returned to something more similar to the original and followed the more expected curved pattern. This suggests that what was seen in the first repeat was not an inherent change in the material but could come from some kind of debris or tip change. A second set of repeated measurements of the MARFs with an applied voltage of 6V also showed a similar pattern where the seen result is changed in the repeated scan as shown in Figure-7.17.

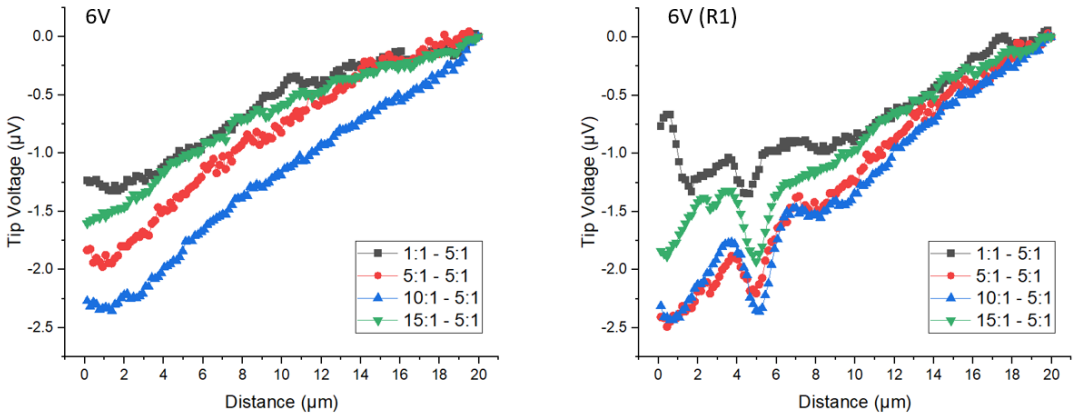

Figure-7.17: Graphs comparing line averaged thermal signal between original 6V MARF scan (Left) and repeat (Right) taken at different times.

An important consideration can be seen in Figure-7.18 where some of the combined MARF scans are shown in chronological order. From this it seems that the disagreement between the different graphs increases over time. As the repeated measurements were some of the last sets of scans to be taken this could mean they suffer the largest effect.

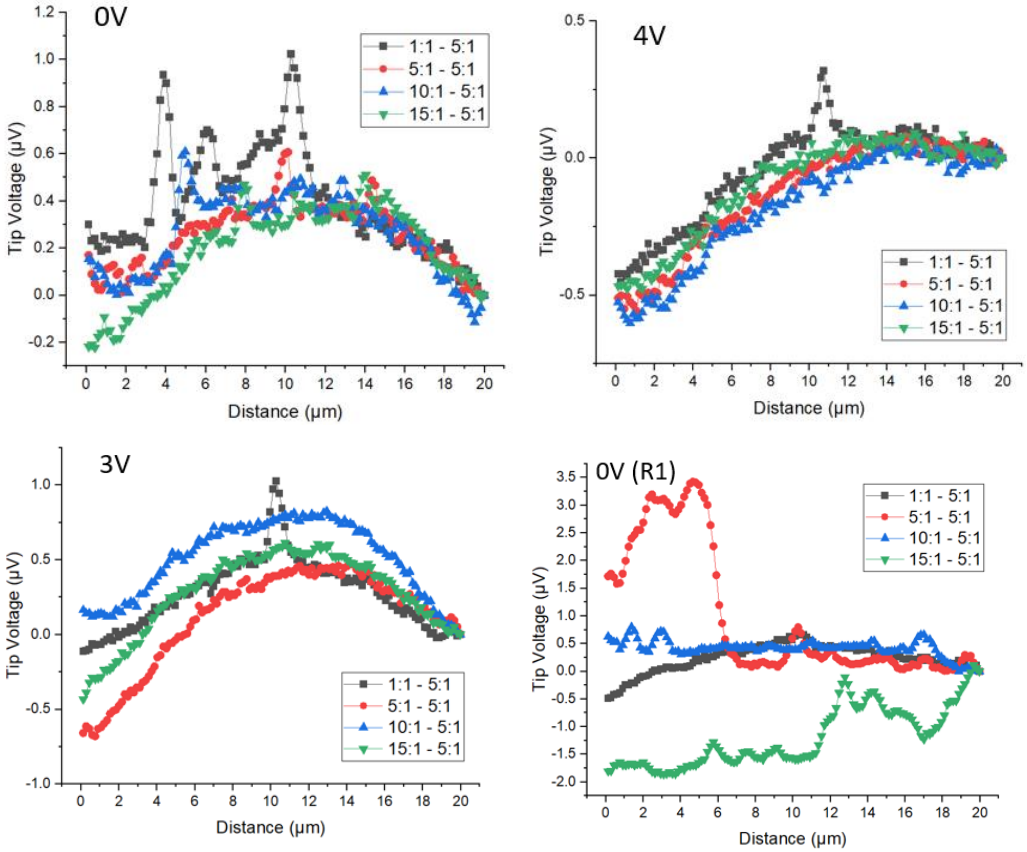

Figure-7.18: Comparison of MARF examinations 0V (Top Left), 4V (Top Right), 3V (Bottom Left), and 0V (R1) (Bottom Right)shown in order of scans taken. Note the increasing disagreement between the scans.

The reason behind this effect could come from the degradation of the SThM tip. As the tip scans it can become worn down (93) resulting in it becoming uneven and less sharp. It is not clear precisely how this would result in this effect. Two possibilities are that as the tip becomes more irregularly shaped this results in the contact becoming less stable and resulting in more noise or that the changed tip means that the calibration changes more quickly and this results in a calibration drift which is not properly accounted for.

7.3.2 Effect of Topography and Si Bowing

It is well known that the topography has a significant effect on the thermal output of the SThM as discussed in Chapter 2. This is especially important in these examinations due to the presence of the shaft bowing.

When the topography of different fishbones is examined as in Figure-7.19 it can be seen that they are similar but vary due to the Si bowing by up to 0.1µm. It is likely that this will have a noticeable effect on the resulting thermal signal.

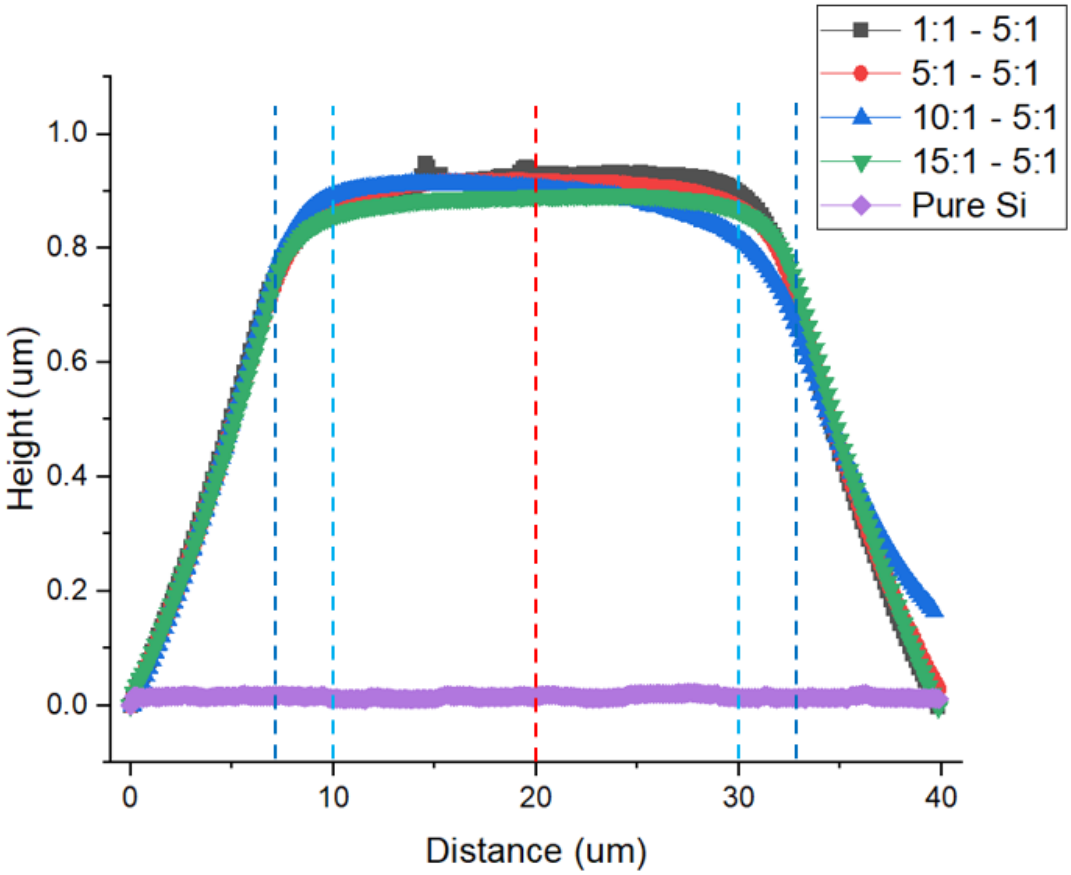

Figure-7.19: Comparison of Si fishbone topographies for MARF fishbones showing differing shaft bowing with shaft and pillar limits marked.

The effect of the topography on the recorded thermal measurement is examined in Figure-7.20. As can be seen there is a large topographical change immediately surrounding the Si fishbone. This is also reflected in the thermal signal which changes significantly as the change in gradient alters.

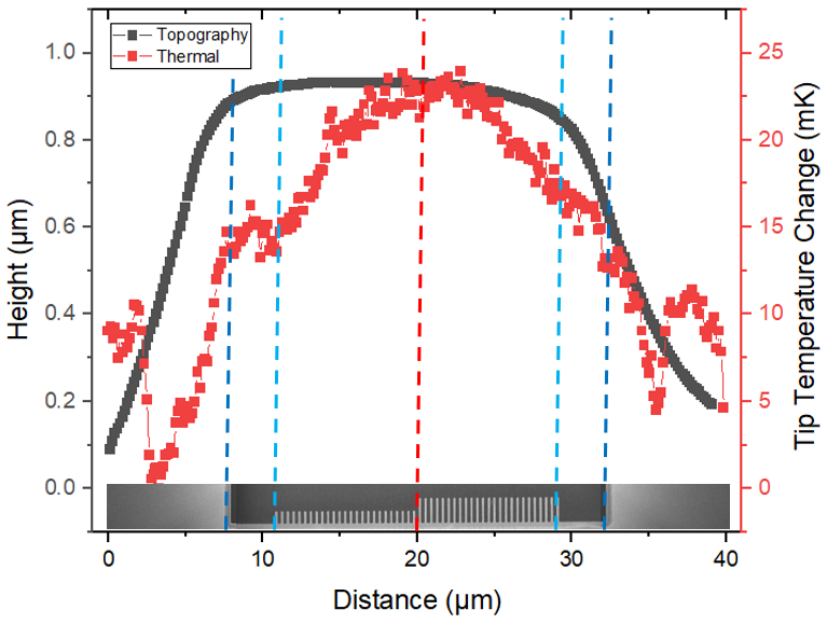

Figure-7.20: Graph making direct comparison between recorded tip temperature and height change along an unpowered MARF Si fishbone and surrounding area with shaft changes marked.

Figure-7.21 shows the same information as Figure-7.20 however it is reduced to just the length of the fishbone. From here again we can see that the majority of the topographical change is limited to the area without the barbs as opposed to the central part of the shaft.

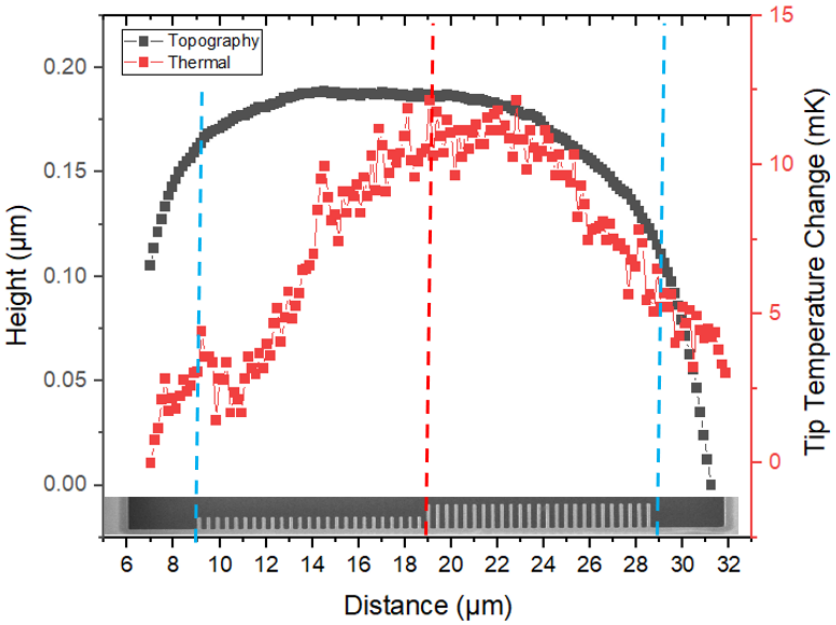

Figure-7.21: Graph making direct comparison between recorded tip temperature and height change along an unpowered MARF Si fishbone with shaft changes marked.

Whilst the central region of the fishbone which contains the barbs is relatively flat there is a much larger seen curve in the thermal data. Earlier COMSOL examinations performed in chapter 6 shows that this is to be expected due to the tip being less efficiently cooled by the surface.

The COMSOL modelling also predicted that any of these topographical effects which are seen by the tip would become 'washed out' as the applied gradient across the surface was increased. As shown in Figure-7.22 as the applied voltage to the heater is increased the amount of visible curving in the thermal data is reduced.

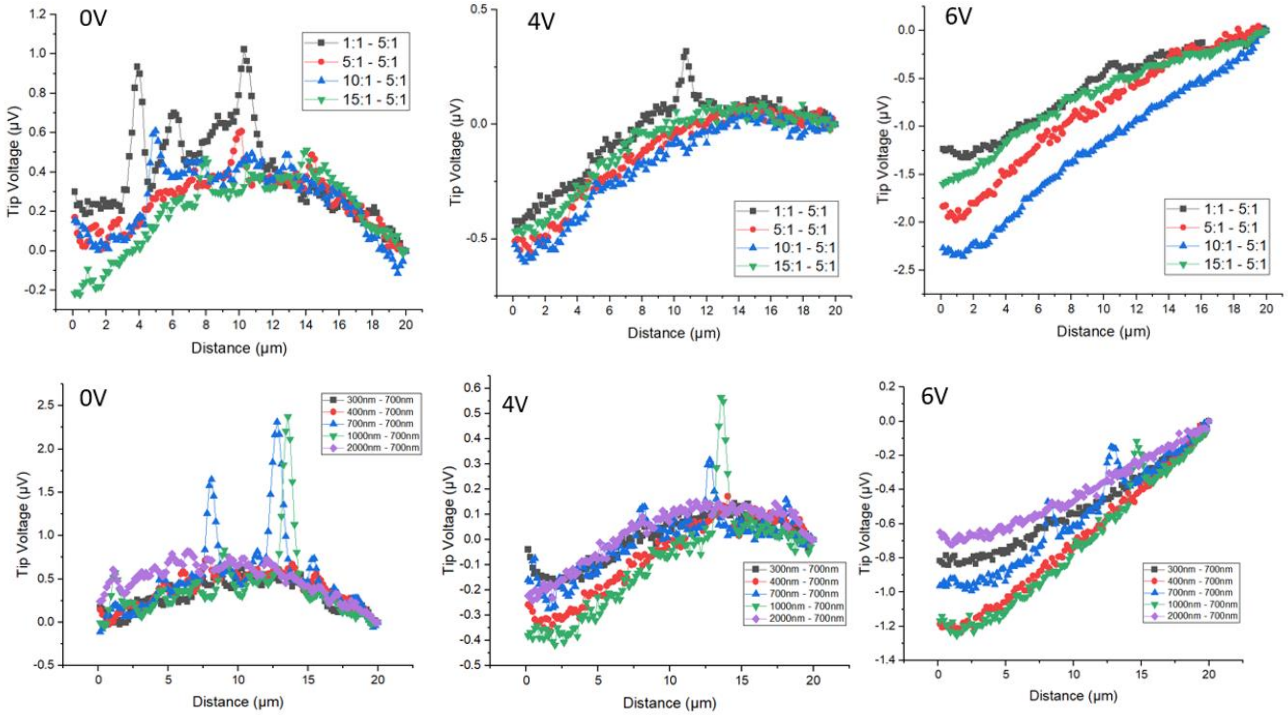

Figure-7.22: Graph showing MARF (Top) and MDF (Bottom) examinations across different applied heater voltages.

7.3.3 Vacuum Examination Attempts

As discussed in Chapter 2 performing SThM examinations under vacuum conditions confers a number of advantages. Primarily it removes the gas and liquid conduction heat paths between the tip and sample, meaning that only the solid-solid conduction heat flow needs to be considered. However, this also results in a smaller effective tip size and a less sensitive instrument.

A number of scans were taken which allow for a direct comparison of fishbones in atmospheric conditions and in vacuum. These showed that the topography did

not change between the scans however there was a clear difference in the thermal images which can be seen in Figure-7.23

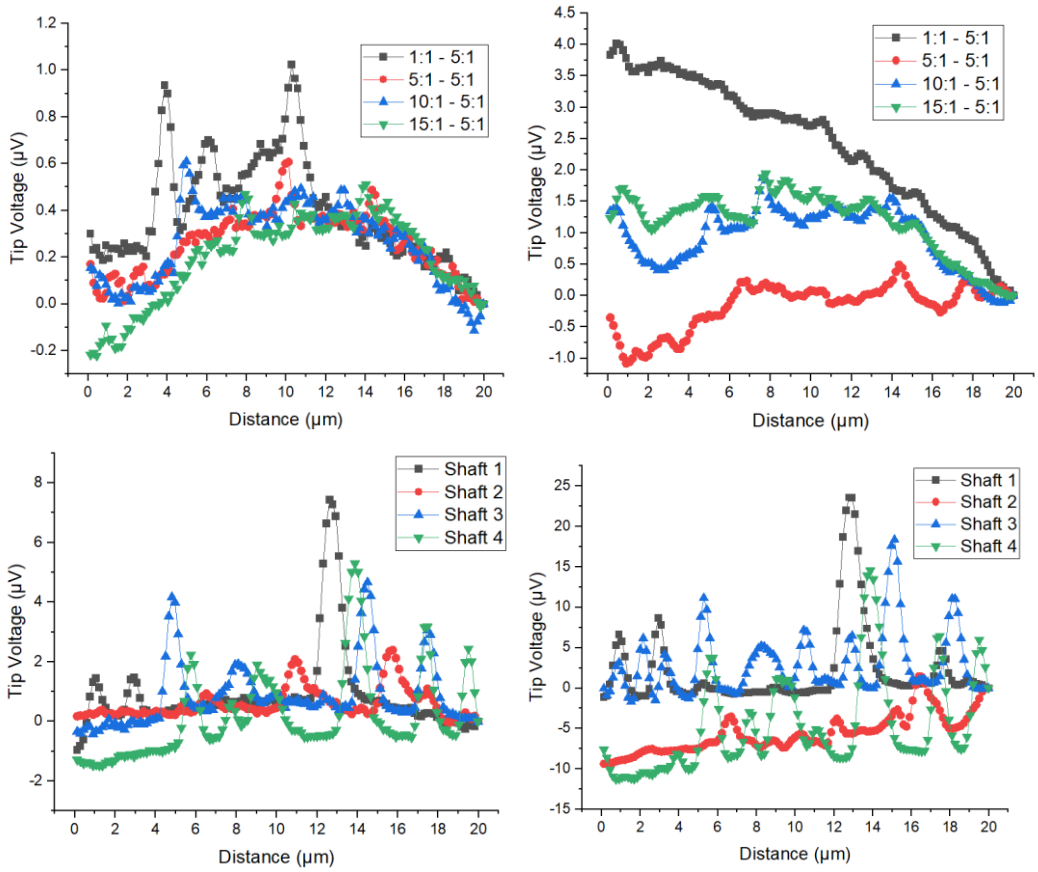

Figure-7.23: Comparison of 0V MARF scans in atmosphere (Top Left) and vacuum (Top Right) and 0V shaft only scans in atmosphere (Bottom Left) and vacuum (Bottom Right).

These comparisons reveal a number of things. Firstly, whilst still present the overall curve caused by the topography is less prominent in the vacuum scans. This is likely due to the smaller effective radius of the tip which will be less influenced by the large-scale change. On the other hand, this smaller tip makes the thermal signal more responsive to the localised changes which may be caused by defects, debris, or other effects.

Examining the difference between the MARF and shaft only images in atmosphere it is interesting to note that the MARF feathers appear to show more of the thermal bowing than seen in the shaft only scans. However, the topography shows little difference beyond the normal variations suggesting that this could be some kind of thermal effect.

The vacuum images also appear to be more vulnerable to varied results with the MARF 1:1 – 5:1 fishbone being particularly difficult to interpret.

Measurements Using Heaters

The vacuum examinations were limited to those that did not use a powered heater. Whilst various attempts were made to examine the fishbones under vacuum conditions with the heaters powered this proved to be unsuccessful.

This was because the heaters did not act in a way that was expected once subjected to vacuum conditions. Once the heater is supplied with a voltage and allowed to reach a steady state (as is also done in atmosphere) it is clear that the whole sample has become heated, and the expected thermal gradient cannot be recorded. This can be seen in Figure-7.24 which compares a 6V applied voltage across a Si fishbone in air and in atmosphere.

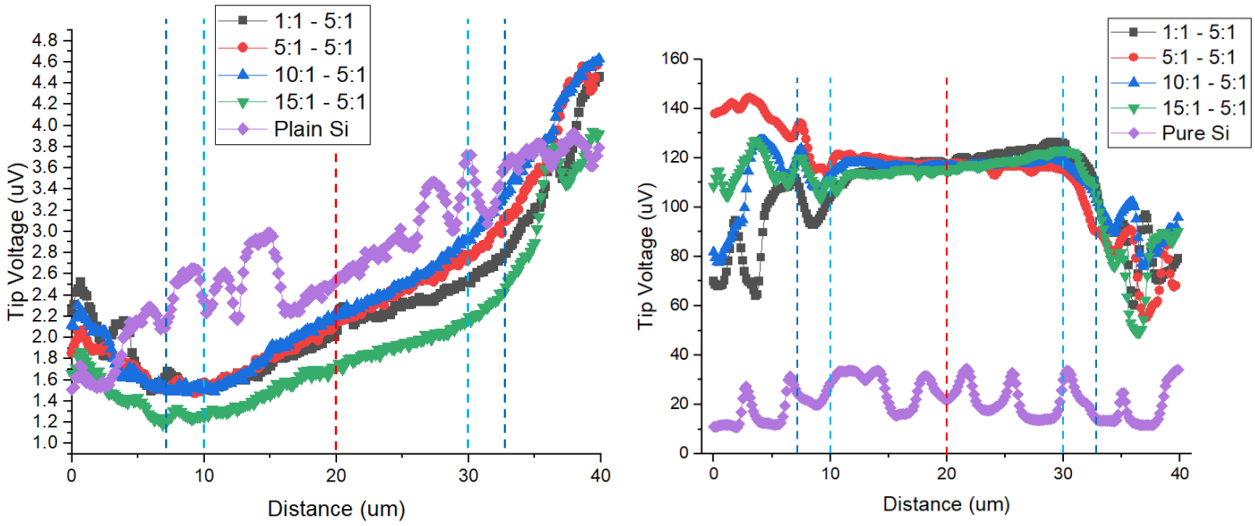

Figure-7.24: Comparison of 6V MARF scans across Si fishbone and surrounding material in atmosphere (Left) and vacuum (Right) with the barb limits marked in light blue, the shaft limits marked in dark blue, and the pillar parameter change marked in red.

The shafts themselves have a clear and relatively linear negative thermal gradient. The graph under vacuum conditions does not show this inversion and it seems likely that the tip is hotter than the surface. This may be due to the tip being hotter as it is not able to cool to atmosphere, that the surface does not reach as high a temperature, or a mixture of the two.

It seems that under vacuum the entire sample reaches a single stable temperature rather than forming a thermal gradient. This is seen across the heated vacuum measurements. The central shafts show no or little thermal gradient. More convincingly, comparing the plain Si (i.e. Si surface at the same position as the feather but far enough away to be unaffected by surface bubbling) in air and vacuum shows that both exhibit features from the topography which are a similar scale compared to the thermal features on the fishbones allowing them to be compared. However, in atmosphere there is a clear thermal gradient which is not present under vacuum.

Further to this upon repressuring the chamber and opening it shortly after having a stabilised heater in vacuum the VLS-80 sample plate and chamber were noticeably warm to the touch. This suggests that the heater is able to warm a surprisingly large area to a significant degree under vacuum. It is not clear why this is the case. It may be due to an inability for the sample to cool sufficiently to make up for the loss in cooling to atmosphere. A significant redesign of the heater and or the heat paths from between the chipset and the rest of the system is likely required.

7.3.4 Pillar vs No Pillar Examinations

One of the largest differences which might be seen from the phononic resonators is the difference between there being no resonators at all in the shaft compared to any of the MARF or MDF scans. In Figure-7.25 two of the shaft only thermal gradients at 6V have been plotted against the two largest MDF and MARF change scans in order to compare.

From this examination there does not appear to be a significant difference between the shaft only scans and the MDF/MARF scans. Whilst the shaft only scans do show the highest thermal gradient the MARF and MDF have thermal gradients both above and below at least one of the shaft scans. It should be noted that the shaft scans are significantly noisier than the other scans. This is most likely due to the particular shafts not being as clean rather than any inherent difference due to the lack of pillars.

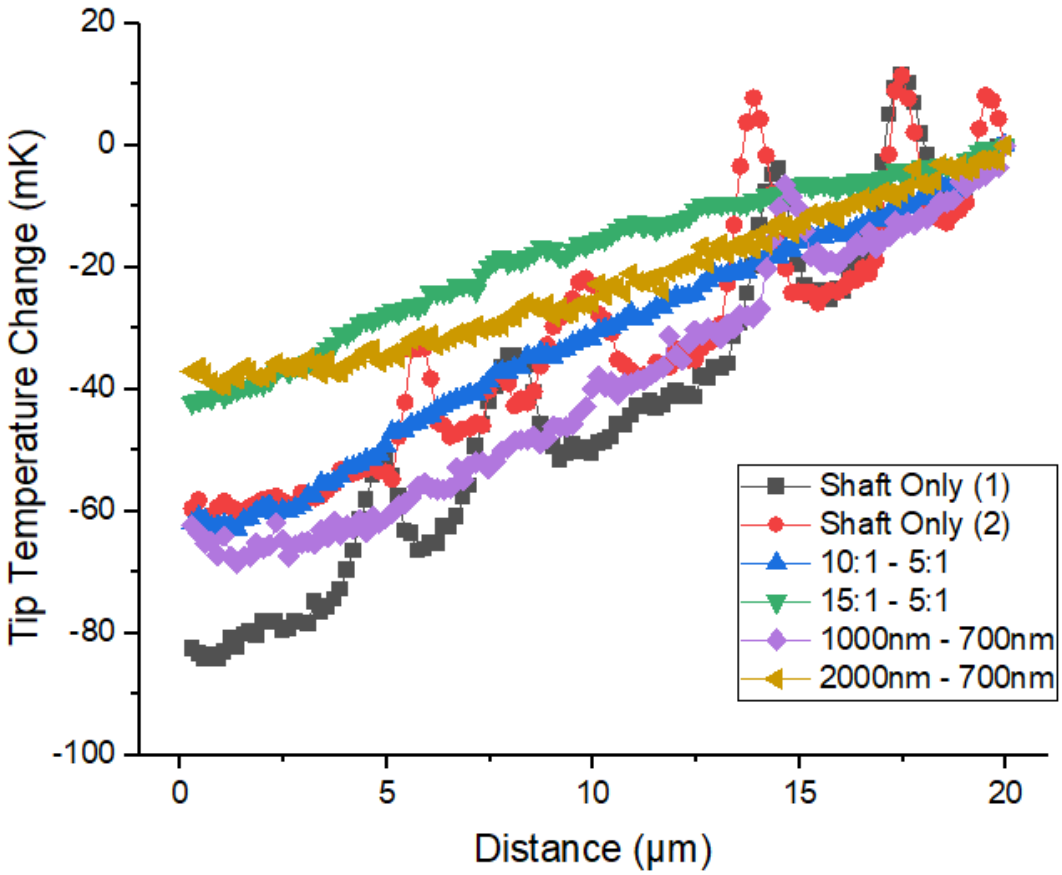

Figure-7.25: Graph comparing thermal signal between two different 'shaft only' shaft scans, MARF and MDF at 6V applied voltage.

7.4 Comparison to Modelling

The experimental data can then be compared to the COMSOL modelling to try to examine and explain the various seen results.

7.4.1 0V Thermal Shape

The parabolic shape seen in the COMSOL modelling for the thermal signal from the fishbones is clearly seen in the 0V examinations of the MARFs, MDFs, and shaft only examinations as shown in Figure-7.26.

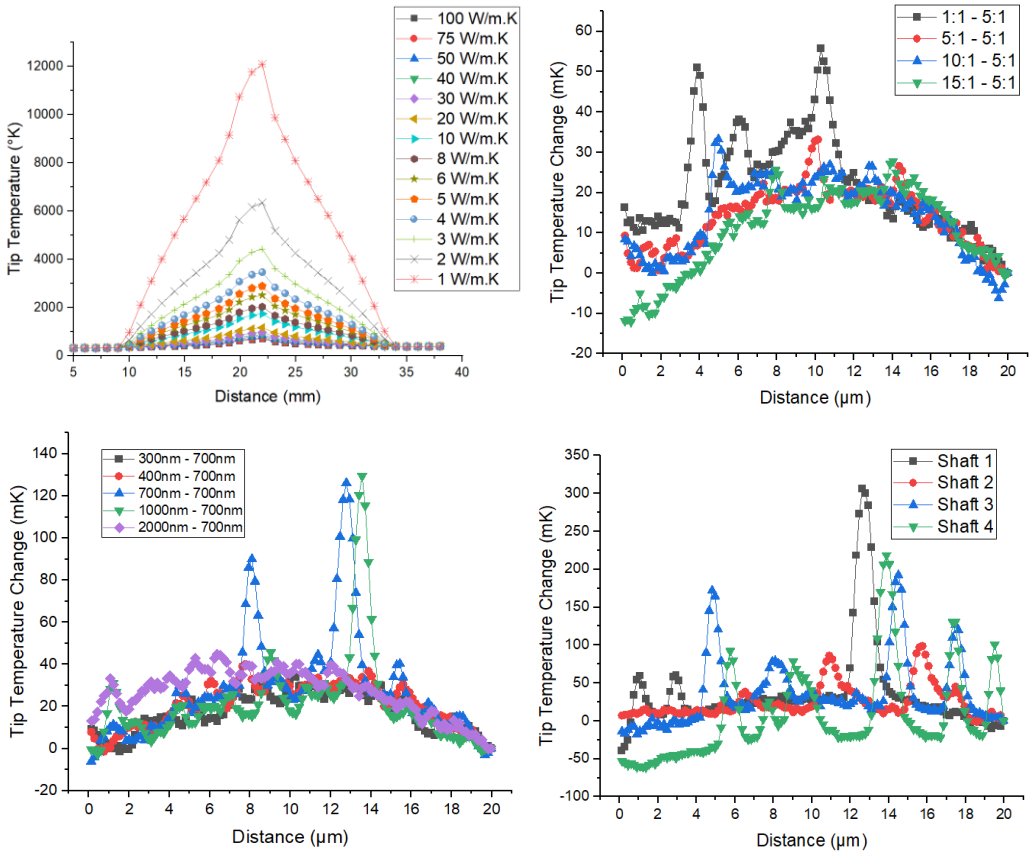

Figure-7.26: Graphs comparing COMSOL 0V fishbone thermal signal (Top Left), 0V MARF (Top Right), 0V MDF (Bottom Left), and 0V shaft only (Bottom Right).

The COMSOL modelling also shows that this shape comes from a combination of the topography and the way that the tip cooling is less efficient in the centre of the shaft due to the increased distance from the bulk. These two different contributors are difficult to pick apart.

One way to attempt to examine the contributions is to examine the difference seen between air and vacuum scans such as in Figure-7.27. Under vacuum conditions the heat transfer between the tip and the sample becomes significantly less as the heat paths are reduced to only solid-solid conduction. This accounts for the messier line scan as there are higher variances in the tip/sample contact during the scan which in atmosphere are made up for by the water and gas conduction.

When placed under vacuum it is clear to see that the curved nature of the thermal data is reduced. This could suggest that the tip/sample contact over the curved surface is a greater contributor than the change in the heat path through the shaft due to distance from the bulk material.

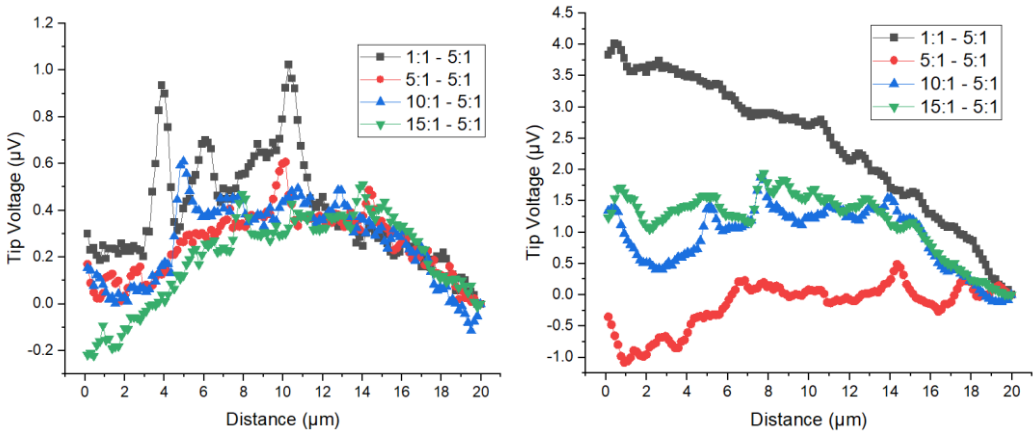

Figure-7.27: Comparison of 0V MARF scans in atmosphere (Left) and vacuum (Right).

7.4.2 0V Topographical Effects from Gradients

The COMSOL experiments which showed the tip temperature across the curved shaft for increasing applied heater temperatures on the 2D COMSOL model in Figure-6.46 suggested that as the temperature of the heater was increased, and thus the thermal gradient across the surface was also increased, that this would 'wash out' the curve seen in the thermal image caused by the topographical bowing and/or tip cooling changes. A physical experiment was carried out under similar circumstances. Figure-7.28 shows as the voltage applied to the heater (and thus the temperature) was increased the curve seen in the data becomes reduced until it follows a straight line from the gradient.

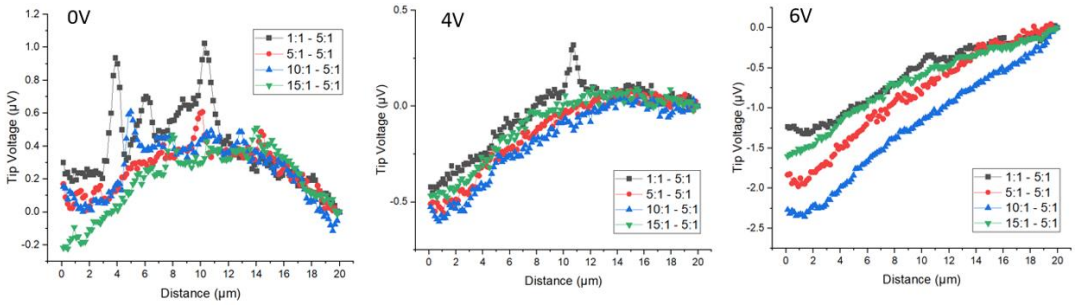

Figure-7.28: Graph showing MARF examinations across different applied heater voltages.

7.4.3 MARF/MDF Examinations

The COMSOL simulation work showed a very significant result that suggested that the MARF/MDF fishbones should display a clear thermal gradient change given a significant enough thermal conductivity change. Notably it was also seen

that this was not due to just an actual temperature change in the surface temperature but rather mostly because of the interaction between the tip/sample.

However, in Figure-7.29 which compares the 6V MARF results to the COMSOL simulation of the shaft with multiple κ values this change is not seen. There is no clear and obvious 'break' in the graph which shows that the tip is now measuring an area with a different thermal gradient.

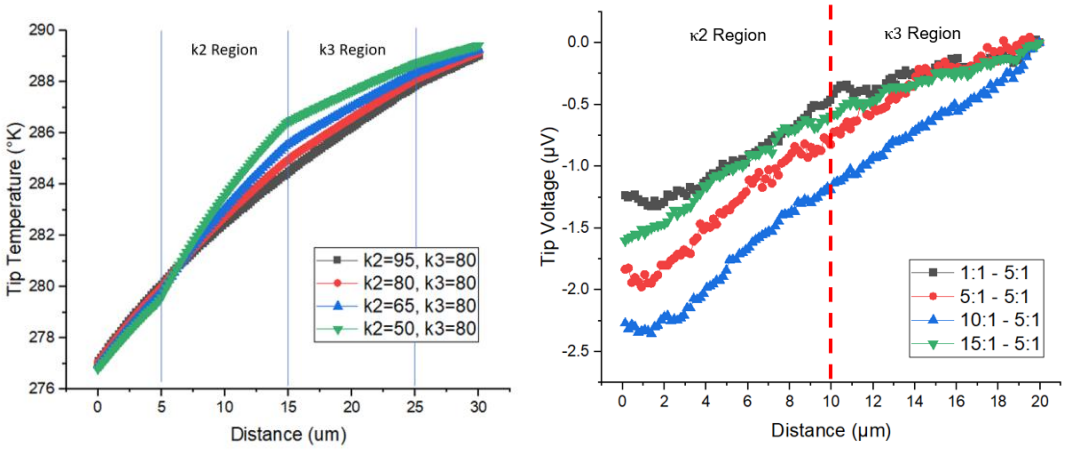

Figure-7.29: Graph comparing computational results (Left) and 6V MARF experimental results (Right) of deliberately similar experiments.

The most likely reason is that the κ change experienced by the physical sample is not sufficient to cause a visible change. The change is also not seen across the other temperatures of MARF experiments or the MDF experiments shown in Figure-7.30.

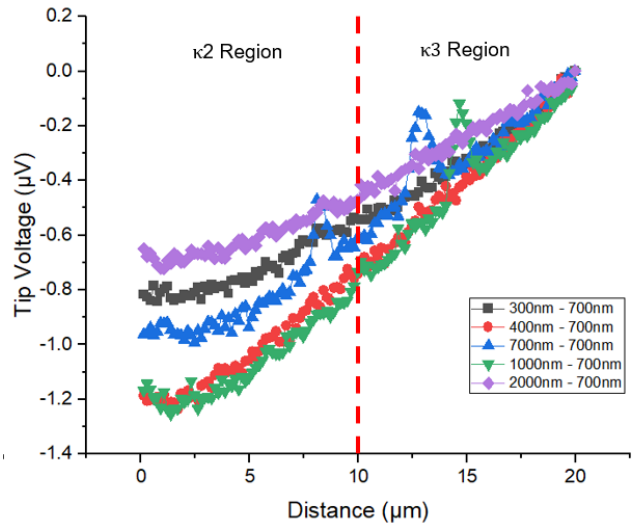

Figure-7.30: Graph of 6V MDF thermal results also showing lack of significant difference between the two different regions.

Whilst there may be some difference seen in the thermal gradients it is thought that they are not coming from a change in thermal conductivity caused by the phononic resonators. This is because such effects can also be seen on the shaft only measurements such as Figure-7.31 which have no pillars.

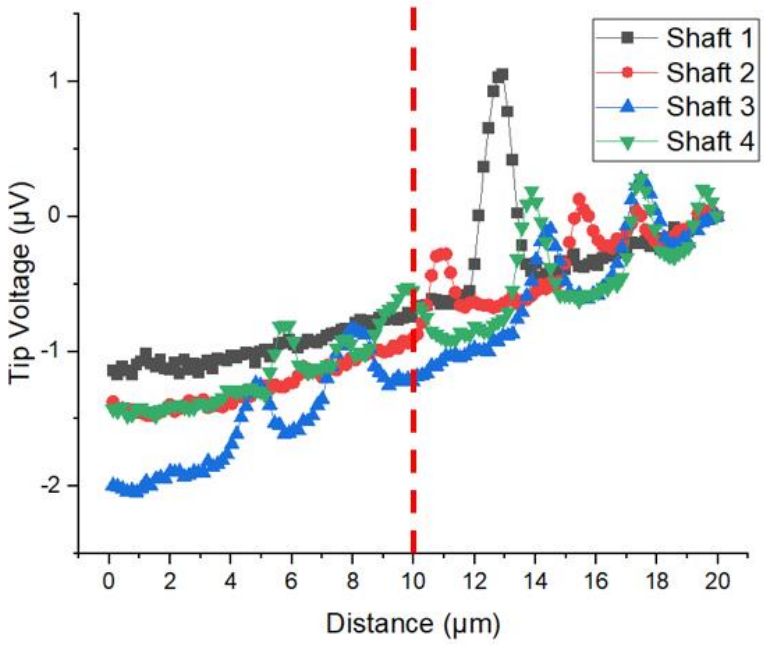

Figure-7.31: Graph of 6V shaft only thermal results showing similar differences in measurements to MDF and MARF examinations.

7.5 Interpretation of Shaft Bowing

Initially the shaft bowing had been a huge concern. It is well known that the thermal signal from an SThM is heavily influenced by topography. Due to material constraints the bowing was not a problem that was possible to be completely solved and the only measure able to be taken to reduce it was to produce multiple chips and select for those that showed the least bowing. It was also clear from examinations such as Figure-7.32 that there was a significant influence from the topography.

Whilst COMSOL simulations such as Figure-6.39 show that the curved signal across the shaft of the fishbone was an expected result, further COMSOL simulations showed that the expected influence of the measured curved topography on the thermal signal across the shaft may be negligible.

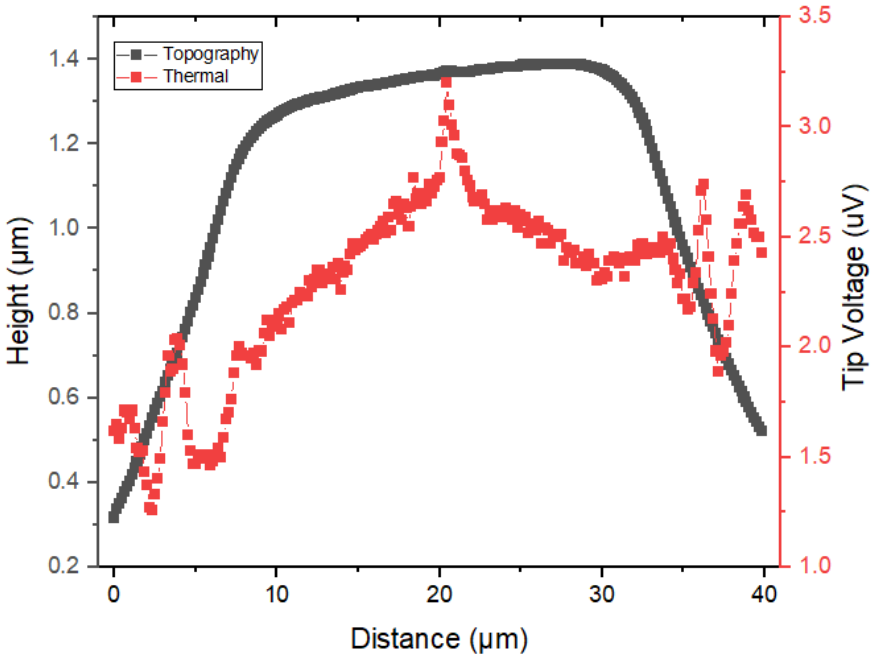

Figure-7.32: Comparison between line averaged topography and thermal signal for 2V 1:1 – 5:1 VLS-80 scan.

Whilst the possibility of the experimental results being impacted by the bowing of the shafts should not be discounted it seems that the effect is relatively small and should not be a serious impediment to examinations.

7.6 Interpretation of Too Small κ Change

It had been thought that in measuring the MARF/MDFs that there would be a clear change in the thermal gradient at the midpoint of the shaft when the barb properties changed. This was clearly shown in the COMSOL modelling of a changing thermal conductivity across a shaft. However, this gradient change was not seen in the experimental results.

It seems that the experiment has potentially returned a null result. A potential for the lack of seeing a change is that whilst there was a difference in the thermal conductivity of the shaft the SThM analysis was unable to measure this change.

7.6.1 Required Thermal Change

In order to examine this we first have to consider what change in the thermal gradient would be required in order to be statistically significant. Figure-7.33 is used as an example.

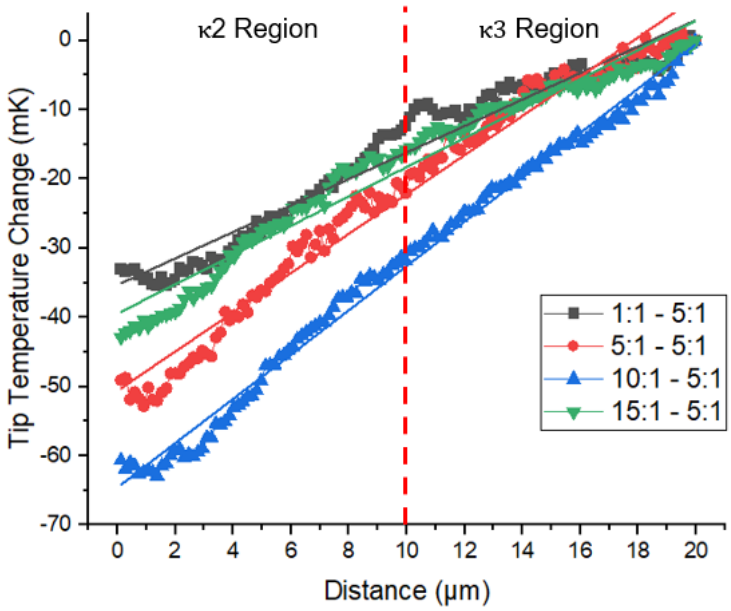

Figure-7.33: 6V MARF Experimental data across barbed area showing regions with different expected κ values and thermal gradients.

Examining Figure-7.33 we find the following gradients and errors as shown in Table-7.4.

Fishbone	Gradient (mK./μV)	Error (mK/μV)
1:1 – 5:1	1.91	0.04
5:1 – 5:1	2.84	0.04
10:1 – 5:1	3.20	0.03
15:1 – 5:1	2.12	0.04

Table-7.4: Si fishbone thermal gradients and errors taken from Figure-7.33

In examining that data we can consider the effect of thermal conductivity in a couple of different ways. Firstly as a simple statistical (5σ) difference we would expect to need to see only a 0.2mK/μm (~7.5%) change in the thermal gradient. However, as previously discussed, the impact of conductivity change increases as the initial thermal conductivity decreases (i.e. a 10W/m.K change from 150-140W/m.K would result in a smaller temperature change than for 50-40W/m.K). As the thermal conductivity of the shaft without barbs is not known, but is almost certainly lower than bulk due to geometric constraints, converting the thermal gradient change into a required κ change is not simple but is explored in section 7.8.

An examination of the modelling data shows that the difference in the thermal gradient caused by the κ change alone (i.e. with the influence of the curve removed) to be 37% for 80-50W/m.K and 28% for 80-65W/m.K. These would be easily visible in the experimental data. More readily comparable are the trends in the data. It would be expected that the 5:1 – 5:1 MARF would have no difference between the two regions (beyond any remaining influence from the curving). Whereas the 10:1 – 5:1 and 15:1 – 5:1 would have the gradient change and the 1:1 – 5:1 which should result in a higher thermal conductivity on the left-hand side should even have a reduction in the gradient (all of which is seem in the COMSOL modelling). However none of this is seen which further suggests that no influence of the phononic resonating effect is seen in these structures.

7.6.2 Modelling Predicted Change

An examination of the computer simulations both by others and those used for simulations in this project show very high thermal conductivity changes even for very small resonant structures. Figure-7.34 which shows the results of the modelling performed for this project discussed early in chapter 4 shows that adding even very small resonant structures results in at least an 80% reduction in the thermal conductivity of the membrane. The further changes caused by the difference in the resonator parameters are then much smaller.

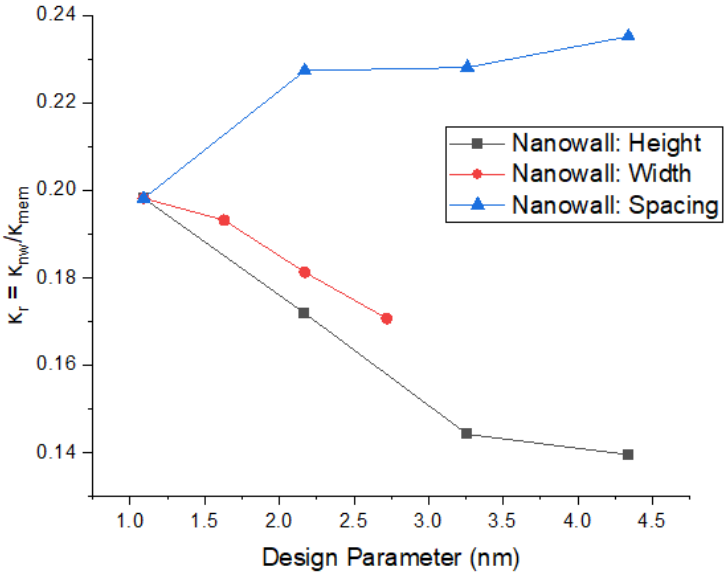

Figure-7.34: Graph of normalised effect of varying design parameters of nanowalls in the CASTEP/ShengBTE simulation of the κ_r. Note that except where mentioned the parameters are a 1CC (1.09nm) and the membrane is 1.63nm thick. Simulations take place at 300K and κ_{mem} = 10.81W/m.K. (Repeat of Figure-4.15).

From Chapter 4 the modelling data was used to make a number of predictions:

- An increased aspect ratio/height of the resonators will decrease κ
- An increased density/lower spacing between resonators will decrease κ
- An increased fill factor/resonator width will decrease κ

These predictions are consistent with the work of others.

Figure-7.34 also shows that increasing the height of the nanowalls from a 1:1 ratio to a 4:1 ratio decreases the thermal conductivity by a further 6% for a κ change between the two of 30%. Increasing the fill factor from 50% to 72% by increasing the width from 1.09nm to 2.72nm decreased the thermal conductivity by a further 17% and reducing the fill factor from 50% to 20% by increasing the spacing between the resonators increased the thermal conductivity by 19%.

7.6.3 Model to Experimental Difficulties

Whilst the simulation data might suggest very clear trends with large thermal conductivity changes which should be easily noticeable in the experimental data there are a number of possibilities why the simulations may not be applicable.

Model Membrane Size

The size of the membrane in the simulations is very small at only 1.63nm (or 1.5 cubic cells) thick. This has a number of different consequences. Firstly the intrinsic thermal conductivity of the structure within the simulation will already be massively reduced purely by geometric constraint.

Additionally at such a size scale the simulated material is not truly comparable to bulk silicon. The entire material is within one cubic cell of the surface which would make the entire material act like surface silicon. This is important because phonons interact differently within surface silicon to bulk silicon. For example surface phonons would be expected to scatter against the resonators which would not occur for phonons within the bulk. This could lead to a significant increase in the effect caused by the geometry of the resonators which might not be seen in a thicker sample.

At this very small size, when a resonator is added to the simulation it increases the volume of the structure by a minimum of 25% for the smallest resonators. This means that introducing any of the resonators causes a large change to the structure. This could result in a significant change in the phonon modes and scattering within the material without there being any of the intended resonance effects. Neither of these two effects would occur for the experimental sample as it is orders of magnitude larger. Although the addition of the pillars to the physical sample does change the volume significantly, the larger size means that the increase in surface effects do not match.

Non-Phonon Contribution to Thermal Conductivity

Silicon is a semiconductor and as such its thermal transport is dominated by phonons. The simulated models only consider the phonon contribution to thermal conductivity. However, if this is reduced by more than 80% the electron contribution to thermal conductivity could once again become a relevant factor.

This is especially true in this project as in the case of the resonators causing a reduction in the phonon group velocity as this has been designed not to affect the electron transport. This will reduce the overall efficiency of the thermal conductivity reduction measured in a physical sample. It is unlikely that this is the case for the experimental data however, as there was not a significant difference seen between the 'shaft only' and pillared samples.

Scaling Issues

It is also unclear how the thermal conductivity change will scale between the two orders of magnitude from the model to the physical sample. Some of the effects in Figure-7.34 already look to potentially be plateauing at relatively low values of aspected ratio, for example, compared to experimental samples.

Sample Impurities

Whilst the Si used in the construction of the samples is device grade this does not mean that it is perfect. The Si is P-doped at a $1x10^{15}cm^{-3}$ (1Ωcm) which will add some additional complexity into the material and whilst it is assumed to be single crystal it is not understood how it might be affected by the fabrication process.

Any impurities in the experimental sample from the Si material to how the shaft and pillars are constructed could significantly dampen the desired effects. This would affect both the electrical and thermal conductivity values.

Sample Coherency

Whilst the phonon coherence from the pillars has already been discussed the lateral phonon coherence (i.e. down the direction of travel of the shaft) has not. The model assumes that the whole system is coherent (i.e. elastic). However, we would not expect this to be the case across the length of the shaft as it is 26µm long which is many times the mean free path of phonons in Si.

The mean free path of silicon in bulk can be estimated to be around 1µm meaning that phonons travelling down the shaft would be expected to scatter a number of times. This effect is increased by the geometric restrictions of the shaft which will cause the mean free path to be lower. This will interfere with the lateral thermal conductivity of the shaft compared to the model which can be measured and is explored in section 7.8.

7.7 Interpretation of No κ Change

It is possible that there was no change in the thermal conductivity of the shafts. The design of the pillars may not have been able to resonate to produce the desired effect. This seems unlikely given that Maire et al. (90) were able to see results using similarly designed structures. Instead, it may be that a change in the dimensions have caused the lack of resonance. This would likely be due to a lack of phonon coherence. It had been assumed that phonons would remain coherent up to around 3µm based on bulk calculations.

However it is known from examinations on silicon nanowires (94) that the mean free path of the phonons is reduced and thus too will the coherence length. A comparison between the used dimensions in the Maire et al. paper and in this project is found in Table-7.5

Fishbone Part	Maire et al. Dimensions	This Project Dimensions
Neck/Shaft Width	40-135nm	1µm
Wing/Pillar Width	75-230nm	125nm
Wing Depth/Pillar Length	50-300nm	200nm-3µm

Table-7.5: Parameters used in phononic nanostructure in both (90) and this project.

Whilst many of the pillar parameters overlap and as such a result might be expected there is a very large difference between the width of the neck/shaft between the two structures. Both the experimental work of Maire et al. and phononic resonator computational work (95) show that reducing the width of the shaft is the largest contributor to reducing the thermal conductivity. However, what is not clear is what the main contributor to this. It could be due to geometric constraint within the structure (which at 1µm may have already been expected to cause a 50% κ change from in the shaft (59)) which is not due to the phononic resonance, or it could be because of the effects of the pillars.

It is from both the experimental and computational work that increasing the amount of the shaft which is covered by pillars increases the thermal conductivity reduction. This suggests that the thermal conductivity reduction caused by phononic resonance from a given pillar has a decaying 'effective radius'.

It is possible then that for the wider shaft, the coupling between the pillars is not able to affect a large enough section of the shaft to result in a significant overall change. This may result in only localised thermal conductivity changes which are not possible to see as part of the overall gradient and are too small to be seen by the resolution of the SThM tip.

7.8 Alternative Method of Determining κ Change

Whilst analysing the data it was realised that there could be an additional method for examining the thermal conductivity of the Si fishbones. The COMSOL simulations as shown in Figure-7.35 suggest that as the thermal conductivity of a shaft changes, the applied thermal gradient across that shaft remains relatively small compared to the tip temperature. However, the SThM tip's response to this is significant and could be used to measure the thermal conductivity change as a function of the peak height.

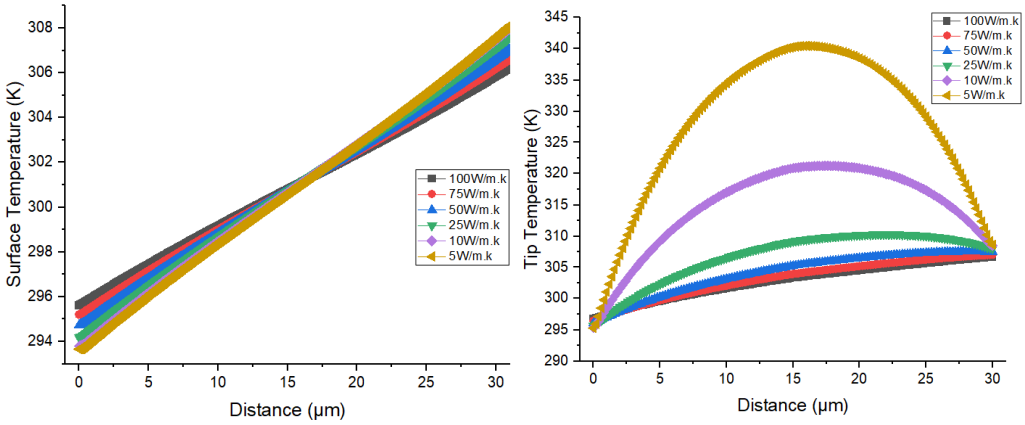

Figure-7.35 Graph showing result of 2D COMSOL model of curved shaft with applied thermal gradient at different shaft values surface temperature values (Left) and tip temperature values (Right). (Repeat of Figure-6.47).

Whilst comparing the shafts had initially been considered before the design of the MARF/MDFs, the peaked shape (even without the influence of the curved shafts) had not been expected. This method can be used on the data in this project, whilst the MARFs and MDFs may have a split thermal conductivity with one side remaining constant it would be expected that this will still result in an overall thermal conductivity reduction across the shaft which might be measurable.

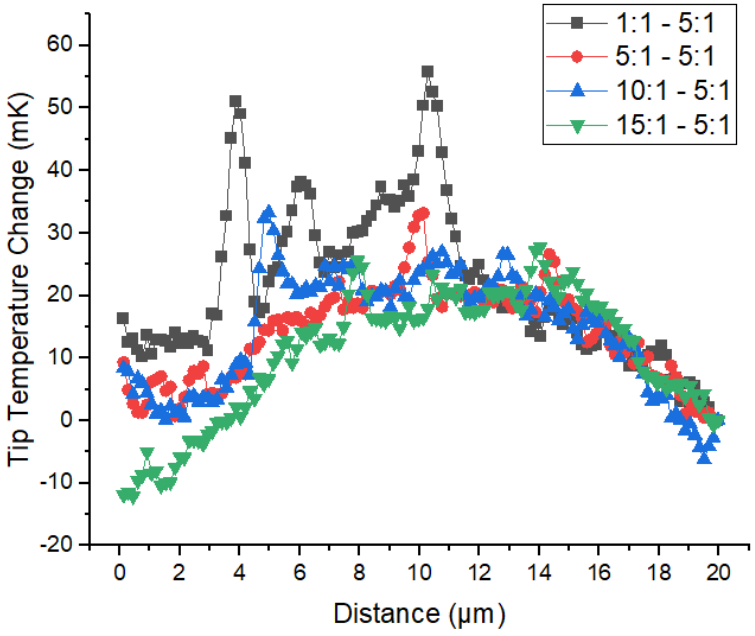

Figure-7.36: 0V MARF thermal scans across central shaft.

However, as can be seen in Figure-7.36 this does not seem to produce results. It would be expected that as 1:1 – 5:1 would have an overall higher thermal

conductivity than 15:1 – 5:1, it would result in a lower tip voltage across the shaft due to more efficient cooling. However all of the scans, regardless of the pillar parameters are similar and the differences are more likely due to noise. It seems likely that the lack of a result with this method is for the same reasons as discussed in sections 7.6 and 7.7.

7.9 Summary

The measurements of the fishbones proved possible to achieve despite some continuing issues with the fabrication of the samples. Scans were taken across MARF, MDF and shaft only samples across a range of applied heater voltages including no applied voltage.

There are remaining concerns about the reproducibility of scans across an extended time period but scans performed within a short time span showed excellent consistency.

The applied thermal gradient as well as the expected thermal curve along the Si fishbone shafts were both measurable and clearly visible. However, attempts to reproduce such results under vacuum conditions were not successful.

The main issue is that the expected change in the thermal gradient caused by a change in thermal conductivity was not seen. Data analysis suggests that any effect above a 7.5% gradient change should be detectable which would be well within the expected range of results due to predicted thermal conductivity changes.

It is not clear why this occurred but it has been suggested that this is either because the thermal conductivity change did not occur or was too small to produce a detectable change.

Chapter 8

Conclusions and Further Work

This work has examined the use of SThM as a measurement technique across two different types of samples, a multilayered structure of thin film materials and a phononic resonator.

The VLS-80 proved a successful and versatile instrument which was able to measure all of the desired samples. The used resolutions for measurements were ~100nm spatial and <10mK thermal in air.

The COMSOL simulations also proved to be successful. Whilst computational limits required many of these to be simplified to 2D structures they were still able to produce reasonable results and functioned well. The tip/surface interaction was especially important and work on allowing the tip to contact and follow the surface provided useful insight for analysing the experimental work.

Multilayer Work

Both of the tried preparation methods of 'cut and polish' and 'ion beam drilling' produced suitable surfaces for examining using SThM and were found to be suitable. The 'cut and polish' work found that both the hand polish and the ion beam polish were required and that a 30 second ion beam polish resulted in the smoothest surface as a trade-off between the polish and preferential etching. The ion beam drilling resulted in a rougher surface than the 'cut and polish' method due to the ion beam caused ridges. However, the significantly larger surface area over which the examinations can be performed result in it being the preferable sample preparation method as it can expose thinner layers and resulted in ~50% less thermal measurement noise. COMSOL simulations were also performed which mimicked the preparation methods and were found to have good agreement despite the modelling limitations.

Using the SThM to examine the multilayers' thermal properties was of mixed success. It is relatively easy to use the SThM thermal data to determine the difference between the multilayers and to make qualitative statements about the relative thermal conductivity of the materials. However, attempting to make more

quantitative statements using a comparative method does not provide reasonable answers. This is largely because of the use of SiO_2 as a baseline but difference in the roughness causes significant issues.

The COMSOL work showed a good relation between the theory and the experimental work in Figure-5.31 but further emphasised the importance of a smooth surface.

Si Fishbones

The production of the Si fishbones was a considerable success. They proved easy to scan and could have the parameters easily changed for experimentation. Ahead of the project there were concerns as to what sizes of pillars could be successfully fabricated. These were ultimately fabricated at widths of 115nm and up to aspect ratios of 26:1 which are both much better than had been expected. The fishbones also proved to have a low operational and production failure rate.

Multi-Aspect Ratio Fishbones (MARF) and Multi-Density Fishbones (MDF) were designed to attempt to circumvent some of the difficulties seen in comparing different scans. These proved to be possible to fabricate and did not seem to have a significant impact upon the topography of the shaft itself.

The presence of the Si bowing of up to 100nm was initially a large concern considering the known effect of the topography on the resulting thermal signals. However, with the aid of COMSOL modelling in Figure-6.39 it was determined that across the Si fishbones it will not have likely had a significant impact.

The fishbones were able to be successfully and repeatedly scanned using SThM. These scans were able to reveal clear applied thermal gradients from the heaters across the shafts of up to 4mK/μm and identify other thermal effects independent of the topography.

Reproducibility examinations of the fishbones raised some concerns. Whilst the scans performed sequentially had good agreement returning to a scan after a period of time could result in a significant difference whilst examining the same object. It is not clear why this is the case but is thought to be linked to the degradation of the SThM tip.

The fishbone system was then modelled using COMSOL and the effects which would be seen due to a significant change in the thermal conductivity of the material were simulated, this showed clear and significant (above 20%) changes in the modelled thermal gradient. Calculations suggested that a 0.2mK/µV (~7.5% change) should be visible in the experimental work, however such effects were not seen. A number of reasons as to why this occurred have been considered.

More than this the computational work performed by collaborators and the work of others suggested that the introduction of pillars onto the fishbones should reduce the thermal conductivity by as much as 80% which would cause a significant thermal gradient change. Further to this increasing the pillar parameters could cause up to a further 25% change in the thermal conductivity. None of which was seen.

Attempts to perform the experiments under vacuum conditions were also largely unsuccessful as it was not possible to create a thermal gradient across the fishbones. This is likely due to not being able to properly disperse the generated heat under the vacuum conditions. Examinations of the unpowered shaft under vacuum conditions were also hampered by a highly changeable calibration which was at least an order of magnitude less sensitive than in air and was more susceptible to noise.

8.1 Further Work

Multilayer Work

With the ion drilling method selected as the most suitable sample preparation technique, the examinations within this thesis could be used to further refine the milling parameters to attempt to produce an even smoother surface by working to reduce the ion mill ridging.

Some further experiments could be performed in altering the milling dwell time to attempt to decrease the milled gradient in order to expose even more of the materials surface and make it possible to examine even thinner multilayers.

The main area for improvement comes from the attempt to calculate thermal conductivities using the gained SThM thermal data. This examination has revealed further steps which need to be taken (such as an air calibration) which were not previously used in order to make a reasonable determination. Additionally, using

materials for which there is a clearer understanding of the thermal conductivity in the thin film form as comparisons within the material later is crucial for future experiments. The roughness remains a significant issue which emphasises why continuing the work using methods such a Menges-Gotsmann method is important. Additionally the oxidation was a significant issue which would benefit from being able to perform the work in situ.

Si Fishbones

As the exact reasons why the thermal conductivity change was not seen is not fully understood making recommendations for future work becomes trickier. The most significant factor which has been identified is the width of the shaft. Future fabrication should aim to reduce the width of the shaft as much as possible whilst still allowing the fishbone to remain stable. Further examinations to attempt to increase the fill factor by reducing the spacing and increasing the width should also be performed as this is expected to increase the thermal conductivity change.

The vacuum experiments also need considerable reworking. A new design for the heating and cooling of the sample whilst under vacuum conditions needs to be found which allows for a temperature gradient across the surface to be created. Additionally further experimentation needs to be performed to understand how the tip calibration functions under vacuum conditions in order to try and improve it. Other experiments such as performing scans more slowly or at higher set points might also be tried to see if the noise levels under vacuum can be reduced.

List of Acronyms and Abbreviations

AFM – Atomic Force Microscope

SThM – Scanning Thermal Microscope

HAMR – Heat Assisted Magnetic Recording

STM – Scanning Tunnelling Microscope

SEM – Scanning Electron Microscope

RMS – Root Mean Square

LBTE – Linearised Boltzmann Transport Equation

IFC – Interatomic Force Constant

TOF-Sims – Time of Flight Secondary Ion Mass Spectroscopy

GNR – Graphene Nanoribbons

GNPM - Graphene Nanopillared Material

References

1. Lees J. Physics in 50 Milestone Moments. 1st ed. Brighton: Quad Books; 2017. 188 p.
2. Arfken GB, Griffing DF, Kelly DC, Priest J. HEAT TRANSFER. Int Ed Univ Phys. 1984;430–43.
3. Cahill DG, Braun P V., Chen G, Clarke DR, Fan S, Goodson KE, et al. Nanoscale thermal transport. II. 2003–2012. Appl Phys Rev. 2014 Mar 14;1(1):011305.
4. Kryder MH, Gage EC, Mcdaniel TW, Challener WA, Rottmayer RE, Ju G, et al. Heat assisted magnetic recording. Proc IEEE. 2008;96(11):1810–35.
5. Weller D, Parker G, Mosendz O, Champion E, Stipe B, Wang X, et al. A HAMR Media Technology Roadmap to an Areal Density of 4 Tb/in^2. IEEE Trans Magn. 2014 Jan;50(1):1–8.
6. Vaqueiro P, Powell A V. Recent developments in nanostructured materials for high-performance thermoelectrics. J Mater Chem. 2010 Nov 21;20(43):9577–84.
7. Wang S, Hui S, Peng K, Bailey TP, Zhou X, Tang X, et al. Grain boundary scattering effects on mobilities in p-type polycrystalline SnSe. J Mater Chem

C. 2017 Oct 12;5(39):10191–200.

8. Binnig G, Quate CF, Gerber C. Atomic force microscope. Phys Rev Lett. 1986;56(9):930–3.

9. Quate C. The AFM as a tool for surface imaging. Surf Sci. 1994 Jan 1;299–300:980–95.

10. Tasharrofi S, Hassani SS, Sobat Z. Encyclopedia of Nanotechnology. CRC Press Taylor & Francis Group; 2015.

11. Williams CC, Wickramasinghe HK. Scanning thermal profiler. Appl Phys Lett. 1986 Dec 8;49(23):1587–9.

12. Zhang Y, Zhu W, Hui F, Lanza M, Borca-Tasciuc T, Muñoz Rojo M. A Review on Principles and Applications of Scanning Thermal Microscopy (SThM). Advanced Functional Materials. Wiley-VCH Verlag; 2019.

13. Aigouy L, Tessier G, Mortier M, Charlot B. Scanning thermal imaging of microelectronic circuits with a fluorescent nanoprobe. Appl Phys Lett. 2005 Oct 31;87(18):184105.

14. Weaver JMR, Walpita LM, Wickramasinghe HK. Optical absorption microscopy and spectroscopy with nanometre resolution. Nature. 1989;342(6251):783–5.

15. Majumdar A, Lai J, Chandrachood M, Nakabeppu O, Wu Y, Shi Z. Thermal imaging by atomic force microscopy using thermocouple cantilever probes. Rev Sci Instrum. 1995 Jun 9;66(6):3584–92.

16. Luo K, Herrick RW, Majumdar A, Petroff P. Scanning thermal microscopy of a vertical-cavity surface-emitting laser. Appl Phys Lett. 1997 Sep 22;71(12):1604–6.

17. Gimzewski JK, Gerber C, Meyer E, Schlittler RR. Observation of a chemical reaction using a micromechanical sensor. Chem Phys Lett. 1994 Jan 28;217(5–6):589–94.

18. Lai J, Perazzo T, Shi Z, Majumdar A. Optimization and performance of high-resolution micro-optomechanical thermal sensors. Sensors Actuators A Phys. 1997 Feb 28;58(2):113–9.

19. Majumdar A, Varesi J. Nanoscale Temperature Distributions Measured by Scanning Joule Expansion Microscopy. J Heat Transfer. 1998 May

1;120(2):297.

20. Dazzi A, Prazeres R, Glotin F, Ortega JM. Local infrared microspectroscopy with subwavelength spatial resolution with an atomic force microscope tip used as a photothermal sensor. Opt Lett. 2005 Sep 15;30(18):2388.
21. Gomès S, Assy A, Chapuis P-O. Scanning thermal microscopy: A review. Phys status solidi. 2015 Mar 1;212(3):477–94.
22. Majumdar A. Scanning Thermal Microscopy. Annu Rev Mater Sci. 1999 Aug 28;29(1):505–85.
23. Gomès S, Consortium QH. QUANTIHEAT project: Main results and products. In: THERMINIC 2017 - 23rd International Workshop on Thermal Investigations of ICs and Systems. Institute of Electrical and Electronics Engineers Inc.; 2017. p. 1–6.
24. Despont M, Brugger J, Drechsler U, Dürig U, Häberle W, Lutwyche M, et al. VLSI-NEMS chip for parallel AFM data storage. Sensors Actuators, A Phys. 2000 Mar 10;80(2):100–7.
25. Kittel A, Müller-Hirsch W, Parisi J, Biehs SA, Reddig D, Holthaus M. Near-field heat transfer in a scanning thermal microscope. Phys Rev Lett. 2005 Nov 25;95(22):224301.
26. Bodzenta J, Juszczyk J, Kaźmierczak-Bałata A, Firek P, Fleming A, Chirtoc M. Quantitative Thermal Microscopy Measurement with Thermal Probe Driven by dc+ac Current. Int J Thermophys. 2016 Jul 31;37(7):73.
27. Umatova Z, Zhang Y, Rajkumar R, Dobson PS, Weaver JMR. Quantification of atomic force microscopy tip and sample thermal contact. Rev Sci Instrum. 2019 Sep 1;90(9):095003.
28. Nazarenko M, Rosamond MC, Gallant AJ, Kolosov O V., Dubrovskii VG, Zeze DA. A simplified model to estimate thermal resistance between carbon nanotube and sample in scanning thermal microscopy. J Phys D Appl Phys. 2017 Nov 15;50(49).
29. Spièce J, Evangeli C, Robson AJ, El Sachat A, Haenel L, Alonso MI, et al. Quantifying thermal transport in buried semiconductor nanostructures via cross-sectional scanning thermal microscopy. Nanoscale. 2021 Jun 24;13(24):10829–36.

30. Assy A, Gomès S. Heat transfer at nanoscale contacts investigated with scanning thermal microscopy. Appl Phys Lett. 2015 Jul 27;107(4):043105.

31. Vitorino M V., Vieira A, Marques CA, Rodrigues MS. Direct measurement of the capillary condensation time of a water nanobridge. Sci Rep. 2018 Dec 1;8(1).

32. Gomès S, Trannoy N, Grossel P. DC thermal microscopy: study of the thermal exchange between a probe and a sample. Meas Sci Technol. 1999 Sep 1;10(9):805–11.

33. Fisher LR, Gamble RA, Middlehurst J. The Kelvin equation and the capillary condensation of water. Nat 1981 2905807. 1981;290(5807):575–6.

34. Israelachvili JN. Intermolecular and Surface Forces: Third Edition. Intermol Surf Forces Third Ed. 2011;1–676.

35. Luo K, Shi Z, Varesi J, Majumdar A. Sensor nanofabrication, performance, and conduction mechanisms in scanning thermal microscopy. J Vac Sci Technol B Microelectron Nanom Struct. 1997 Mar 4;15(2):349–60.

36. Fischer-Cripps AC. The Hertzian contact surface. J Mater Sci 1999 341. 1999;34(1):129–37.

37. Xu JB, Läuger K, Möller R, Dransfeld K, Wilson IH. Heat transfer between two metallic surfaces at small distances. J Appl Phys. 1994 Dec 4;76(11):7209–16.

38. Hwang G, Kwon O. Quantitative temperature profiling across nanoheater on silicon-on-insulator wafer using null-point scanning thermal microscopy. Int J Therm Sci. 2016;108.

39. Chung J, Kim K, Hwang G, Kwon O, Choi YK, Lee JS. Quantitative temperature profiling through null-point scanning thermal microscopy. Int J Therm Sci. 2012 Dec 1;62:109–13.

40. Menges F, Riel H, Stemmer A, Gotsmann B. Quantitative Thermometry of Nanoscale Hot Spots. Nano Lett. 2012 Feb 8;12(2):596–601.

41. Menges F, Riel H, Stemmer A, Gotsmann B. Nanoscale thermometry by scanning thermal microscopy. Rev Sci Instrum. 2016 Jul 14;87(7):074902.

42. Menges F, Mensch P, Schmid H, Riel H, Stemmer A, Gotsmann B. Temperature mapping of operating nanoscale devices by scanning probe

thermometry. Nat Commun. 2016 Dec 3;7(1):10874.

43. AFM Probes | Kelvin Nanotechnology [Internet]. [cited 2022 Feb 16]. Available from: https://www.kntnano.com/probes/

44. Nečas D, Klapetek P. Gwyddion: An open-source software for SPM data analysis. Cent Eur J Phys. 2012 Feb 1;10(1):181–8.

45. Ober CK, Müllen K. Introduction – Applications of Polymers. Polym Sci A Compr Ref 10 Vol Set. 2012 Jan 1;8:1–8.

46. Janarthanan B, Thirunavukkarasu C, Maruthamuthu S, Manthrammel MA, Shkir M, AlFaify S, et al. Basic deposition methods of thin films. J Mol Struct. 2021 Oct 5;1241:130606.

47. Microchem LOR Information Sheet [Internet]. [cited 2021 Nov 16]. Available from: https://amolf.nl/wp-content/uploads/2016/09/datasheets_LOR_datasheet.pdf

48. Damodara S, Shahriari S, Wu W-I, Rezai P, Hsu H-H, Selvaganapathy R. Materials and methods for microfabrication of microfluidic devices. Microfluid Devices Biomed Appl. 2021 Jan 1;1–78.

49. Pal P, Sato K. A comprehensive review on convex and concave corners in silicon bulk micromachining based on anisotropic wet chemical etching. Micro Nano Syst Lett. 2015 Dec 1;3(1):1–42.

50. Mohammed A. Scanning Electron Microscopy (SEM): A Review. Proceedings of International Conference on Hydraulics. 2018.

51. Bhatt G, Patel K, Suryavanshi P, Panchal C. Optimization of Ultrasonic and Thermosonic Wire-Bonding Parameters on Au/Ni Plated PCB Substrate. Natl Laser Symp. 2015;

52. COMSOL - Software for Multiphysics Simulation [Internet]. [cited 2022 Feb 21]. Available from: https://www.comsol.com/

53. Sinha SK. Phonons in semiconductors. C R C Crit Rev Solid State Sci. 1973;3(3):273–334.

54. File:Brillouin Zone (1st, FCC).svg - Wikimedia Commons [Internet]. [cited 2022 Feb 3]. Available from: https://commons.wikimedia.org/wiki/File:Brillouin_Zone_(1st,_FCC).svg

55. Shanks HR, Maycock PD, Sidles PH, Danielson GC. Thermal Conductivity of

Silicon from 300 to 1400°K. Phys Rev. 1963 Jun 1;130(5):1743.

56. Zhou WX, Cheng Y, Chen KQ, Xie G, Wang T, Zhang G. Thermal Conductivity of Amorphous Materials. Adv Funct Mater. 2020 Feb 1;30(8):1903829.

57. Zhang P, Yuan P, Jiang X, Zhai S, Zeng J, Xian Y, et al. A Theoretical Review on Interfacial Thermal Transport at the Nanoscale. Small. 2018 Jan 1;14(2):1702769.

58. Liang Z, Sasikumar K, Keblinski P. Thermal transport across a substrate-thin-film interface: Effects of film thickness and surface roughness. Phys Rev Lett. 2014 Aug 8;113(6):065901.

59. Jeong C, Datta S, Lundstrom M. Thermal conductivity of bulk and thin-film silicon: A Landauer approach. J Appl Phys. 2012 May 1;111(9):093708.

60. Bai SY, Tang ZA, Huang ZX, Yu J, Wang JQ. Thermal Conductivity Measurement of Submicron-Thick Aluminium Oxide Thin Films by a Transient Thermo-Reflectance Technique. Chinese Phys Lett. 2008 Feb 1;25(2):593.

61. Nath P, Chopra KL. Thermal conductivity of copper films. Thin Solid Films. 1974 Jan 1;20(1):53–62.

62. Yamane T, Nagai N, Katayama SI, Todoki M. Measurement of thermal conductivity of silicon dioxide thin films using a 3ω method. J Appl Phys. 2002 May 30;91(12):9772.

63. Schafft HA, Suehle JS, Mirel PGA. Thermal conductivity measurements of thin-film silicon dioxide. 1989;121–5.

64. Pizzagalli L, Godet J, Guénolé J, Brochard S, Holmstrom E, Nordlund K, et al. A new parametrization of the Stillinger-Weber potential for an improved description of defects and plasticity of silicon. J Phys Condens Matter. 2013 Feb 6;25(5).

65. Omini M, Sparavigna A. An iterative approach to the phonon Boltzmann equation in the theory of thermal conductivity. Phys B Condens Matter. 1995 Jul 1;212(2):101–12.

66. Li W, Carrete J, Katcho NA, Mingo N. ShengBTE: A solver of the Boltzmann transport equation for phonons. Comput Phys Commun. 2014 Jun

1;185(6):1747–58.

67. Clark SJ, Segall MD, Pickard CJ, Hasnip PJ, Probert MIJ, Refson K, et al. First principles methods using CASTEP. Zeitschrift fur Krist. 2005;220(5–6):567–70.

68. Anufriev R, Maire J, Nomura M. Reduction of thermal conductivity by surface scattering of phonons in periodic silicon nanostructures. Phys Rev B. 2016 Jan 12;93(4):045411.

69. Fu B, Tang G, Li Y. Electron–phonon scattering effect on the lattice thermal conductivity of silicon nanostructures. Phys Chem Chem Phys. 2017 Nov 1;19(42):28517–26.

70. Honarvar H, Hussein MI. Two orders of magnitude reduction in silicon membrane thermal conductivity by resonance hybridizations. Phys Rev B. 2018 May 9;97(19):195413.

71. Maris H, Tanaka Y. Phonon group velocity and thermal conduction in superlattices. Phys Rev B. 1999 Jul 15;60(4):2627.

72. Xie G, Ding D, Zhang G. Phonon coherence and its effect on thermal conductivity of nanostructures. Vol. 3, Advances in Physics: X. Taylor and Francis Ltd.; 2018. p. 720–55.

73. Honarvar H, Yang L, Hussein MI. Thermal transport size effects in silicon membranes featuring nanopillars as local resonators. Appl Phys Lett. 2016 Jun 27;108(26):263101.

74. Ma D, Wan X, Yang N. Unexpected thermal conductivity enhancement in pillared graphene nanoribbon with isotopic resonance. Phys Rev B. 2018 Dec 26;98(24).

75. Thompson AP, Aktulga HM, Berger R, Bolintineanu DS, Brown WM, Crozier PS, et al. LAMMPS - a flexible simulation tool for particle-based materials modeling at the atomic, meso, and continuum scales. Comput Phys Commun. 2022 Feb 1;271:108171.

76. Rajasekaran G, Kumar R, Parashar A. Tersoff potential with improved accuracy for simulating graphene in molecular dynamics environment. Mater Res Express. 2016 Mar 18;3(3):035011.

77. Durham B. Designing Nano-Structured Silicon Membranes To Reduce Lattice

Thermal Conductivity For Better Thermoelectric Properties. The University of York; 2020.

78. Touloukian, Y. S. Powell, R. W. Ho, C. Y. Klemens PG. Thermophysical Properties of Matter - The TPRC Data Series. Thermophysical Properties of Matter - The TPRC Data Series. Volume 2. Thermal Conductivity - Nonmetallic Solids. The TPRC Data Series. 1971. p. 1286.

79. Ma R. Examination Of Callaway-Holland-Based Thermal Conductivity Calculation. 2018.

80. Sojo Gordillo JM, Gadea Diez G, Pacios Pujadó M, Salleras M, Estrada-Wiese D, Dolcet M, et al. Thermal conductivity of individual Si and SiGe epitaxially integrated NWs by scanning thermal microscopy. Nanoscale. 2021 Apr 23;13(15):7252–65.

81. Lim J, Hippalgaonkar K, Andrews SC, Majumdar A, Yang P. Quantifying surface roughness effects on phonon transport in silicon nanowires. Nano Lett. 2012 May 9;12(5):2475–82.

82. Pennelli G, Elyamny S, Dimaggio E. Thermal conductivity of silicon nanowire forests. Nanotechnology. 2018 Oct 22;29(50):505402.

83. Maire J, Anufriev R, Hori T, Shiomi J, Volz S, Nomura M. Thermal conductivity reduction in silicon fishbone nanowires. Sci Rep. 2018 Dec 1;8(1).

84. Weaver L. Cross-Section TEM Sample Preparation of Multilayer and Poorly Adhering Films. Microsc Res Tech. 1997;36:368–71.

85. Spièce J, Evangeli C, Robson AJ, El Sachat A, Haenel L, Alonso MI, et al. Quantifying thermal transport in buried semiconductor nanostructures via cross-sectional scanning thermal microscopy. Nanoscale. 2021 Jun 24;13(24):10829–36.

86. IONTOF - TOF-SIMS (time of flight secondary ion mass spectrometry) - LEIS (low energy ion scattering). Ion beam technology products for surface spectrometry, surface analysis, depth profiling, surface imaging, 3D analysis, retrospective analysis [Internet]. [cited 2022 Mar 22]. Available from: https://www.iontof.com/tof-sims-5-product-version-100mm-200mm-300mm.html

87. Nan LK, Lung LM. Study of FIB milling induced damage and contamination

on ex-situ lift-out TEM specimen and methodology to reduce the artifacts. Proc Int Symp Phys Fail Anal Integr Circuits, IPFA. 2013;404–7.

88. Jeong C, Datta S, Lundstrom M. Thermal conductivity of bulk and thin-film silicon: A Landauer approach. J Appl Phys. 2012 May 3;111(9):093708.

89. Ruiz F, Sun WD, Pollak FH, Venkatraman C. Determination of the thermal conductivity of diamond-like nanocomposite films using a scanning thermal microscope. Appl Phys Lett. 1998 Sep 28;73(13):1802–4.

90. Maire J, Anufriev R, Hori T, Shiomi J, Volz S, Nomura M. Thermal conductivity reduction in silicon fishbone nanowires. Sci Rep. 2018 Dec 1;8(1):4452.

91. Xie G, Ding D, Zhang G. Phonon coherence and its effect on thermal conductivity of nanostructures. 2018 Jan 1;3(1):720–55.

92. Grover R, McCarthy B, Sarid D, Guven I. Mapping thermal conductivity using bimetallic atomic force microscopy probes. Appl Phys Lett. 2006 Jun 5;88(23):233501.

93. Khurshudov AG, Kato K, Koide H. Nano-wear of the diamond AFM probing tip under scratching of silicon, studied by AFM. Tribol Lett 1996 24. 1996;2(4):345–54.

94. Chen R, Hochbaum AI, Murphy P, Moore J, Yang P, Majumdar A. Thermal Conductance of Thin Silicon Nanowires. Phys Rev Lett. 2008 Sep 2;101(10):105501.

95. Hussein MI, Tsai C, Honarvar H. Thermal Conductivity Reduction in a Nanophononic Metamaterial versus a Nanophononic Crystal: A Review and Comparative Analysis. Adv Funct Mater. 2020 Feb 4;30(8):1906718.